The Pennsylvania State University

The Graduate School

EXTRINSIC CONTRIBUTIONS IN LEAD ZIRCONATE TITANATE FILMS: FROM DEFECTS TO DEVICES

A Dissertation in

Materials Science and Engineering

by

Travis Lee Peters

Submitted in Partial Fulfillment
of the Requirements
for the Degree of

Doctor of Philosophy

May 2023

The dissertation of Travis Lee Peters was reviewed and approved by the following:

Susan Trolier-McKinstry
Evan Pugh University Professor and Flaschen Professor of Ceramic Science and Engineering and Electrical Engineering
Dissertation Advisor
Chair of Committee

Clive A. Randall
Distinguished Professor of Materials Science and Engineering

Long-Qing Chen
Hamer Professor of Materials Science and Engineering

Ramakrishnan Rajagopalan
Associate Professor of Engineering

Liam Collins
R&D Staff Scientist, Center for Nanophase Materials Science, Oak Ridge National Laboratory
Special Member

John C. Mauro
Graduate Program Head, Professor of Materials Science and Engineering

ABSTRACT

This thesis probes how extrinsic contributions affect the dielectric, piezoelectric, and ferroelectric properties of morphotropic phase boundary lead zirconate titanate (PZT) films. Secondly, the influence of grain and grain boundary microstructure on domain behavior under an electric field was investigated. Domain wall mobility via the Rayleigh Law was locally probed to investigate avalanche characteristics and the width of influence of individual grain boundaries on the nonlinear piezoelectric response. This was coupled with macroscopic characterization showing the dependence of the domain structure on the thermal stress induced from substrate clamping effects. The results guided an attempt to fabricate a self-powered, wireless PZT thin film insole sensor for applications involving balance detection to assist the elderly population. A novel lead-free flexoelectric array was also prototyped for eventual use in a self-powered force sensing device, that can harvest energy from a heel-strike via the direct flexoelectric effect.

In undoped lead zirconate-titanate (PZT) films 1-2 μm thick, domain walls move in clusters with a correlation length of ~ 0.5–2 μm. Mapping of the piezoelectric nonlinearity via band excitation piezoresponse force microscopy (BE-PFM) showed that doping with niobium (Nb) increases the average concentration or mobility of domain walls *without* changing the cluster area of correlated domain wall motion. In contrast, manganese (Mn) doping reduces the contribution of mobile domain walls to the dielectric and piezoelectric responses without changing the cluster area for correlated motion. In both Nb and Mn doped films, cluster area increases as film thicknesses rise from 250 to 1250 nm while cluster density drops; this can be seen in spatial maps generated from the analysis of irreversible to reversible ratios of the Rayleigh coefficients.

Next, the effect of microstructural features such as grain boundaries and triple points on the pinning of domain wall motion in perovskite PZT films was investigated. Spatial variability in

the collective domain wall dynamics was assessed using non-linearity mapping via BE-PFM. Collocating the non-linearity maps with triple point locations (visualized by electron back scatter diffraction) allowed for exploration of the effect that local microstructure (e.g., grain boundary) has on domain wall motion. It was found that the extrinsic behavior varied with both the misorientation angle and the proximity to the grain boundary. The width of influence of individual grain boundaries on the motion of domain walls was a function of the character of the grain boundary; random grain boundaries exhibit deeper minima in $\alpha_d/d_{33,initial}$ and larger widths of influence (up to 905 nm) compared to coincident site lattice (CSL) boundaries (up to 572 nm). Additionally, triple points containing larger numbers of random boundaries exhibited non-Rayleigh behavior to greater distances, suggesting that the triple point provides either a deep potential minimum or a region where domain wall motion is unfavorable.

Piezoelectric thin films were dip coated onto flexible metal substrates to investigate the dependence of macroscopic dielectric and ferroelectric properties on the coefficient of thermal expansion mismatch and substrate thickness. The bending stiffness was controlled by the thickness of the substrate. Grazing incidence x-ray diffraction displayed distinct peak splitting for Nb-doped PZT on flexible Pt, Ni, Ag, and stiff Ni substrates, where the out-of-plane d-spacing and integrated peak area for *c*-domains was highest with the largest film compressive stress. As expected, PZT films on stiff Si were under tensile stress and contained more in-plane domains. The dielectric permittivity was highest in PZT on stiff Si and lowest for PZT on thick Ni, while remanent polarization displayed the opposite trend, commensurate with the residual stress state as well as the resistance to bending in thick substrates as a strain-relief mechanism. The irreversible Rayleigh coefficient decreased dramatically upon poling for PZT on flexible substrates compared to PZT on stiff substrates; the $\alpha_e/\varepsilon_{initial}$ ratio was 56% higher in PZT on a flexible Ni substrate relative to a stiff Ni substrate at 100 Hz prior to electrical poling. This investigation distinguishes

the impact of substrate flexibility from thermal expansion on ferroelectric domain mobility and provides dip coating conditions for high quality piezoelectric films on any substrate.

The resulting PZT films on metal foils were employed in the fabrication of a low power insole embedded force sensor array attempting to monitor a patient's balance and weight distribution while standing, walking, or running. Flexible piezoelectric films as force sensors eliminate the need for standby energy, providing high sensitivity and flexibility in sensor array design. Lead zirconate-titanate piezoelectric films 1 μm thick were dip coated onto a 25 μm thick stainless steel flexible metal foil. The film displayed a 47% Lotgering factor for the <100> crystallographic direction and exhibited a high-density granular perovskite structure with little pyrochlore near the middle and bottom of the dip cast film. The films showed high remanent polarization values of +28.2 $\mu C/cm^2$ and -24.3 $\mu C/cm^2$ and typical coercive fields of 59.4 kV/cm and -56.7 kV/cm. This piezoelectric sensing array with 24 photolithographically-defined electrodes enabled the simulation of a single toe response, the ball of the foot rolling during a step response, and a heel-strike emulation response. Voltage measurements extracted from cyclic applied forces from 0 to 30 N showed a linear response with a sensitivity of -9.76 mV/N between 0 to 12 N and a nonlinear response between 12 to 30 N. The roll test provided ~100 mV responses when expected during a perpendicular and diagonal roll on four individual sensors, each with fast response times and some mixture of bending and compressive stresses. The heel-strike emulation above a single electrode exhibited a response of ~300 mV with 60 N compressive force, ~100 mV from a nearby electrode, and minimal response from electrodes further from the applied force. A discrete circuit was designed and tested on a printed circuit board for multi-channel sensing, digitization, amplification, and wireless transmission of the activation signal.

Finally, a lead-free flexoelectric device was fabricated in an attempt to provide a power-source for the electronics associated with the PZT film insole sensor. Flexoelectric polarization

output scales with dielectric permittivity and strain gradient; thus, it is proposed that a barrier layer capacitor with doped silicon as the conducting medium will enhance the flexoelectric coefficient via space charge polarizability. A cantilever beam was fabricated as proof of concept, which displayed a flexoelectric coefficient of 4.9 ± 0.4 μC/m. Furthermore, a centrosymmetric <100> silicon wafer was processed with an anisotropic wet etchant into truncated pyramid arrays varying in size from 100s of microns to tens of microns. A dielectric passivation layer acted as the insulating region within the asymmetric barrier layer capacitor, and interfacial space charge polarizability generated effective permittivities that exceed those possible with paraelectrics. The novel centrosymmetric flexoelectric fabrication procedure exhibited here generated the capability to decrease the structure size by orders of magnitude as well, thereby increasing the flexoelectric polarization response in proportion. A scanning probe-based methodology was developed to directly measure the local converse flexoelectric response of a single pyramid with a height of 70 μm. The feasibility of ferroelectric material-free flexoelectricity was analyzed via both direct and converse flexoelectric measurements at the macro-scale and nano-scale.

TABLE OF CONTENTS

LIST OF FIGURES

LIST OF TABLES

ACKNOWLEDGEMENTS

I am sincerely grateful for the time and energy Professor Susan Trolier-McKinstry provided to me during my doctoral studies. Her guidance and support equipped me with the confidence to pursue and fulfill the goals we outlined when I began in her research group. Her assistance, feedback, and expertise during group, individual, and team meetings enabled critical thinking, which I believe resulted in high quality peer-reviewed manuscripts. She placed an emphasis on collaboration in areas that were not her expertise, an aspect of research not every PI is comfortable with. Her love for teaching is palpable, and I admire her commitment to both the students that she teaches as well as her graduate students. Additionally, I want to thank her for her patience and flexibility during my time at Oak Ridge; she gave me the opportunity to grow as a researcher while experiencing a different environment outside of graduate research at a university.

The STM group was an absolute tremendous help for me. They integrated me into PhD level research, guided me through fabrication processes, stayed patient while explaining difficult concepts, and provided support within and outside of the lab. Specifically, I would like to thank Dixiong Wang, Kathleen Coleman, and Tianning Liu for their help in training me during my first year of studies. I thank Chris Cheng for being my desk partner, staying late with me in the nanofab and sol-gel labs to work out kinks in a process. Thank you to Mike Haun for training me on the flexoelectric measurement setup and fun PSU gameday activities. I'd like to thank Nathon Bishop for his help in discussing the meaning of my early results and optimization processes for sputter deposition. I want to thank Haley Jones and Yeongwoo Son for their conversations where our research projects overlapped. I appreciate the interactions and collaboration I've had with Shruti Gupta and Leonard Jacques. The post docs in our group (Smitha Shetty, Wanlin Zhu, Betul Akkopru-Akgun, Jung In Yang, and Fan He) were an incredible support for me, and I thank them

dearly. I sincerely appreciate Gavin Hennessey for his time, effort, support, and friendship during our two years together. Last but certainly not least is Pannawit Tipsawat, who began his PhD the same August 2019 term that I did. I'd like to thank him for his friendship, passion for producing excellent research, and inspiration for working incredibly difficult and long hours to achieve his goals.

Without the Materials Research Institute staff members, several research projects would have been nearly impossible to complete on time. For this, I'd like to thank them dearly. Specifically, thank you to Beth Jones, Bill Drawl, and Andy Fitzgerald for help not only in the cleanroom, but for being true friends of mine. I thank Guy Lavallee, Michael Labella, Kathleen Gehoski, Bangzhi Liu, Bill Mahoney, and Jaime Reish for their help with lithography processes, ALD, sputter and PECVD depositions, and finicky budget detail support, respectively. I'd like to sincerely thank Damian Richards for his help with developing the dip-coating station now permanently embedded in the PZT bay. Finally, I'd like to thank Jeff Long and Steve Perini for their help and support in my electrical measurements, providing answers and suggestions to experimental setups that they may or may not have been frustrated with.

During my time at Oak Ridge National Lab, I was given a tremendous amount of support to help achieve the goals I laid out in the proposal. I want to thank each and every member that helped me produce high-quality research, including the nanofab staff Kevin Lester, Dayrl Briggs, Bernadeta Srijanto, Dale Hensley, Leslie Wilson, Nick Lavrik, and Scott Retterer. My time as a "temporary member" of the Functional Atomic Force Microscopy Group was absolutely invaluable to me, and I'd like to thank Rama Vasudevan, Yongtao Liu, Sabine Neumayer, Olya Popova, Shiva Raghuraman, and Wan-Yu for integrating me into the group. They helped train me on the SPM tools, talked to me about the experimental procedures, and provided guidance on data interpretation. I want to thank Kyle Kelley for his help in diagnosing issues I encountered during my PFM reservations as well as being a supportive friend of mine while I lived 10 hours away

from home. Thank you to Neus Domingo and Stephen Jesse for being excellent leaders, as I learned so many technical and professional growth skills from you. Most dearly, I thank Liam Collins and Marti Checa. I cannot repay to them what they provided for me in only a 10-month span: excellent research skills, patience, commitment to the projects I brought, support, tool-training, manuscript advise, and a deep friendship are only a few. I thank Marti Checa for being my best friend during those 10 months.

Thank you to my thesis committee, Professor Clive Randall, Long-Qing Chen, Ramakrishnan Rajagopalan, and Liam Collins who have supported and challenged me throughout my Ph.D. I am extremely grateful for their commitment to the quality of my thesis, education, and research.

My family has been incredibly supportive of my pursuits in academia. They've encouraged me to move where I needed in order to develop my career and specifically, perform the research I wanted in the right research group. My brother, sister, mother, and father have always encouraged me to pursue the career I've dreamed of, and they were in full support when I told them a Ph.D. was what I needed to place me in the best position for success. My parents always provided a warm-welcoming home to visit whenever I had time to, and my brother and sister made an effort to meet me there to spend what little time they could as they pursued their own degrees. Their availability for a phone call was 24/7, anytime I needed. I am also extremely thankful for my girlfriend, whom I met at Penn State in the Spring of 2021. She has been wholly supportive, sympathetic, understanding and encouraging, especially when I needed it most. For these reasons, and many others, I am forever grateful for them.

Specific to each chapter, and subsequent peer-reviewed manuscripts, within this thesis, certain portions were a highly collaborative effort, and I would be remiss if I did not detail the contributions from each author. From chapter 2, all sample fabrication was performed by Wanlin Zhu. Additionally, Liam Collins and Marti Checa trained me and further assisted with the

experimental setup, data analysis, and data interpretation. From chapter 3, Gavin Hennessey performed the majority of the experimental work, including sample preparation, PZT deposition, EBSD analysis, and initial manuscript drafting. Pannawit Tipsawat helped with photomask design and photolithography steps. PFM experimental setup and data interpretation was assisted by Liam Collins and Marti Checa, and Gavin Hennessey generated the Rayleigh ratio vs. distance from grain boundary figures. In chapter 4, Chris Cheng helped with PZT solution preparation and grazing incidence XRD analysis, while George Rossetti assisted in the interpretation of XRD peak separation and its meaning on our films. Ke Wang in the Materials Research Institute at Pennsylvania State University performed the TEM/EDS analysis. Within chapter 5, Issak Allaire-MacDonald and Shad Roundy at the University of Utah manufactured the “squishy tup” and performed the Instron compression tests along with the “roll tests”. Sujay Hosur fabricated the microelectronic chip which demonstrated successful wireless data acquisition and voltage amplification. XPS measurements were performed by Jeffrey Shallenberger in the Materials Research Institute at The Pennsylvania State University. Finally, chapter 6 would not have been possible without the help of Guy Lavallee in the Materials Research Institute Nanofabrication facility at The Pennsylvania State University. He worked incredibly hard to help overcome processing issues that risked project termination.

I gratefully acknowledge funding from the National Science Foundation from the Center for Advanced Self-Powered Systems of Integrated Sensors and Technologies (ASSIST) (EEC-1160483) and DMR-2025439, Flaschen Professorship, U.S. Naval Department (N00014-18-1-2471) a 3M Fellowship from Pennsylvania State University, and an Oak Ridge National Laboratory SCGSR Fellowship corresponding to CNMS user proposal CNMS2022-B-999. PFM research was supported by the Center for Nanophase Materials Sciences (CNMS), which is a US Department of Energy, Office of Science User Facility at Oak Ridge National Laboratory.

CHAPTER 1

Introduction and thesis organization

Piezoelectric thin films are found in several microelectromechanical systems, such as biomedical sensors, hard disk drives, scanning probe microscopy, and microrelay applications [1][2]. Morphotropic phase boundary lead zirconate titanate ($Pb(Zr_{0.52}Ti_{0.48})O_3$) is one of the most common piezoelectric films because it exhibits a large piezoelectric d_{33} coefficient and is chemically and mechanically robust; however, an understanding of the mechanisms that control domain wall movement is critical in designing devices with a stable response [3]. The piezoelectric coefficient in PZT is reliant on several factors, which include defect chemistry, grain size, grain boundary density, film orientation, domain wall density, domain orientation, domain wall mobility, intrinsic stress, and electrical imprint, among others. These factors influence the two key contributions to the observed piezoelectric response: intrinsic and extrinsic contributions. Intrinsic contributions refer to the displacement of the center of positive and negative charge within a single PZT domain, resulting in the distortion of the unit cell. At sub-coercive AC fields, the relationship between polarization and an electric field is linear and reversible for intrinsic contributions. In contrast, extrinsic contributions to the piezoelectric coefficient may be reversible or irreversible, where both involve the motion of domain walls. The relationship between low AC fields and polarization is nonlinear for irreversible extrinsic contributions. Equation 1.1 shows the relationship between the piezoelectric coefficient d_{33} and domain contributions at low fields, where α_{d33} represents irreversible extrinsic and $d_{33,\ initial}$ represents intrinsic and reversible extrinsic contributions: this is the Rayleigh Law.

$$d_{33}=d_{33,initial}+\alpha_{d33}E_{AC} \qquad \text{Equation 1.1}$$

The difference between reversible and irreversible extrinsic contributions is that reversible domain wall motion may induce local bowing of the wall under an applied field but

returns to its original position after field removal; irreversible domain wall motion overcomes the potential energy barrier required to move that domain wall into a different locally stable position. In both cases, the density and structure of domain walls remain unchanged as the field is cycled [3]. The primary purpose of this thesis was to investigate irreversible domain wall motion in films with dopants (donor and acceptor), defects (grain boundaries and triple points) and thermal stresses (clamped and released) by comparing a "nonlinearity ratio", calculated as the piezoelectric Rayleigh coefficient ratio of $\alpha_{d33}/d_{33,initial}$, between domains in different states.

In Chapter 2, domain wall avalanche characteristics are investigated as a function of PZT dopant and thickness. The piezoelectric nonlinearity ratio was locally measured as a spectroscopic map using nonlinear band excitation piezoresponse force microscopy at sub-coercive field conditions. Domain cluster areas were then correlated to films with different dopant types to determine if lead and oxygen vacancy defects alter domain wall avalanche behavior. Cluster areas were also compared for films with varying thickness.

Chapter 3 provides a first of its kind report on triple point radial influence of domain wall mobility measured by local nonlinear band excitation piezoresponse force microscopy. This chapter shows the dependence of the domain wall mobility on the distance from two different types of grain boundaries: coincident site lattice and random boundaries. The width of influence and pinning potentials of grain boundaries with several misorientation angles provides evidence of extrinsic suppression up to 905 nm away, depending on the type of grain boundary.

Chapter 4 discusses the effect of substrate flexibility and substrate coefficient of thermal expansion on *dielectric* nonlinearity ratios. Grazing incidence XRD and Rayleigh analysis reveal how the dependence of thermal stress and substrate clamping of PZT films on substrate properties can alter the domain wall mobility and ultimately, the performance of a device.

Chapter 5 gives a detailed fabrication procedure for insole embedded force sensors utilizing flexible PZT films. The lessons learned from Chapters 2 and 4 were implemented in an

attempt to maximize the sensitivity of the device. The sensitivity, dielectric properties, film structure, and force sensor application tests were examined.

Chapter 6 shows a creative flexoelectric device design, utilizing a barrier layer capacitor structure with doped silicon as the conducting region and HfO_2 or Al_2O_3 as the insulating layer. The flexoelectric device, in theory, has the potential to act as an energy harvester to power the electronics associated with the PZT-based insole force sensor array. Fabrication routes, dielectric data, and flexoelectric results for both cantilever beams and micro-sized truncated pyramid arrays are given.

Chapter 7 summarizes the significant findings from this study. A proposed future work section, based on the conclusions from Chapter 3 and Chapter 6 of this thesis, describes possible pathways for more efficient PFM measurements around grain boundaries and methods to understand various barrier layer capacitor flexoelectric effects in further detail.

1.1 References

[1] Muralt, Paul. "PZT thin films for microsensors and actuators: Where do we stand?." *IEEE Transactions on Ultrasonics, Ferroelectrics, and Frequency Control* 47.4 (2000): 903-915.

[2] Kueppers, H., Leuerer, T., Schnakenberg, U., Mokwa, W., Hoffmann, M., Schneller, T., Boettger, U. and Waser, R. "PZT thin films for piezoelectric microactuator applications." *Sensors and Actuators A: Physical* 97 (2002): 680-684.

[3] Damjanovic, Dragan, and Marlyse Demartin. "The Rayleigh law in piezoelectric ceramics." *Journal of Physics D: Applied Physics* 29.7 (1996): 2057-2060.

CHAPTER 2

Influence of doping and thickness on domain avalanches in lead zirconate titanate thin films

Chapter 2 of this thesis is in progress as a manuscript: Peters, T., Zhu, W., Checa, M., Collins, L., Trolier-McKinstry, S., Influence of doping and thickness on domain avalanches in lead zirconate titanate thin films. *Advanced Functional Materials.*

2.1 Introduction

Morphotropic phase boundary composition lead zirconate titanate (PZT) is widely utilized in sensing, actuation, and transducing applications due to its high piezoelectric coefficients, low dissipation factor, comparatively temperature-stable performance, and facile processing of ceramics. PZT is modified for specific applications to control the relative amount of domain wall motion at electric fields well below the coercive field [1]–[4]. Donor doping of PZT ceramics, for example by substituting Nb^{5+} and Ta^{5+} on the $(Zr/Ti)^{4+}$ site, is charge compensated largely by lead-site vacancies in the crystal lattice, along with a smaller population of electrons. Donor doping produces “soft PZT”. Conversely, acceptor additives such as Mn^{3+} and Fe^{3+} on the $(Zr/Ti)^{4+}$ site produce “hard PZT” by generating oxygen vacancies in the lattice and a smaller population of holes.

Accompanying these changes in the defect chemistry are changes in the domain wall contributions to the permittivity, piezoelectric coefficients, and elastic stiffness. In hard PZT, the domain walls are “hard” to move, such that the extrinsic contribution to the macroscopic response is modest. In contrast, in soft PZT, the domain contributions to the functional properties are more substantive [5]–[12].

While the importance of domain wall motion is widely documented, there are still numerous unknowns about how to best describe the macroscopic responses quantitatively in terms of microscopic responses, including the interactions between domain walls, microstructural features, and point defects. For example, it is now well established that in both single crystal and polycrystalline samples, that domain walls move collectively during the switching process, such that motion of one domain wall often triggers an avalanche of correlated motion. These avalanches have been reported to be favored at kinks or junctions of different types of domain walls [13]–[19]. Correlated switching has also been linked to the existence of a random distribution of defects with widely varying pinning potentials [20].

Boser demonstrated that a uniform distribution of restoring forces induces Rayleigh-like responses of the domain walls at fields well below the coercive field [21]. Rayleigh behavior of the dielectric and piezoelectric responses are widely observed in macroscopic measurements of lead-based films clamped to Si substrates [9]–[11],[22]–[30]. Rayleigh behavior in the piezoelectric response even at very local scales is, in and of itself, an indication that domain wall motion must be correlated, such that a Gaussian distribution of restoring forces can be sampled over the correlation volume. Bintachitt et al. experimentally demonstrated collective motion of domain walls in ferroelectric films, as opposed to the motion of noninteracting walls, via nonlinear band excitation piezoresponse force microscopy (BE-PFM) measurements of undoped PZT films. It was found that the correlation length for motion of domain walls was typically ~ 500 – 2000 nm in films clamped to their underlying substrate, where this dimension was much larger than either the grain size or the domain size [31]. Marincel et al. found that individual microstructural features (e.g. grain boundaries) produce pinning sites that also affect domain wall motion for length scales up to ~800 nm [32]–[34].

Given this background, it is interesting to ask whether donor and acceptor doping of PZT films influences not just the mobility of domain walls, but their correlation length over which clusters of domain walls move cooperatively. That is the goal of this chapter.

2.2 Experimental procedure

2.2.1 Sample Fabrication

Two sets of samples were created in order to investigate the influence of thickness and dopants on the domain clusters in PZT films on silicon substrates: (1) 2 mol% Nb doped $Pb(Zr_{0.52}Ti_{0.48})O_3$ (PNZT) films with thickness from 288 nm to 1210 nm; (2) 2 mol% Mn doped $Pb(Zr_{0.52}Ti_{0.48})O_3$ (PMZT) films from 222 nm to 1265 nm. Table 2.1 shows each PNZT and PMZT film thickness. The commercial chemical solutions (PZT-E1, Mitsubishi Materials Corporation, Tokyo, Japan) used for the seed layer, bulk layer and top layer are described in detail elsewhere [35]. ϕ500 μm, 100 nm thick platinum top electrodes were deposited by DC-sputtering and patterned by a standard lift-off process for electrical characterization.

Table 2.1: PNZT and PMZT films.

Film	Thickness (nm)	Film	Thickness (nm)
2mol% Nb-PZT	288	2mol% Mn-PZT	222
	528		498
	775		773
	1022		1085
	1210		1265

2.2.2 Piezoresponse force microscopy

The AFM used in this study was a commercial Cypher AFM (Asylum Research, Santa Barbara, CA). All PFM measurements were taken with Pt-coated cantilevers (PPP-EFM) with nominal spring constants of ~3 N/m and resonance frequencies of ~75 kHz. BE-PFM was performed using external data acquisition electronics based on a NI-6115 fast DAQ card

controlled by Labview software. The voltage signal (which combined chirp and sync waveforms) excited the capacitor to enable quantitative *local* measurements of piezoelectric nonlinearity via non-linear BE-PFM as previously described [31]. The signals were stored and post-processed using python scripts [36]. The measurements were performed on separate 2% Nb-doped and 2% Mn-doped PZT films with thicknesses ranging from 250 nm to 1250 nm. Prior to PFM measurements, each capacitor was poled with a probe station at 150^{o}C for 15 minutes at 3x the average coercive voltage (V_c). Table A.1 (Appendix A) shows the coercive fields and poling voltages for each PZT film. PFM measurements were initiated no sooner than 60 minutes after DC bias removal to reduce artefacts from aging.

Nonlinear BE-PFM experiments were conducted by linearly increasing the excitation amplitude from 0 to ~1/2 V_c, where V_c is the coercive voltage of the material under test. It is common in standard scanning probe methodologies for several artifacts to complicate data interpretation. These include effects such as topographic crosstalk, electrostatic signals, and complex cantilever dynamics. In this work attempts were made to minimize all of these. First, band excitation was employed to overcome topographic crosstalk common in single frequency PFM by measuring in a frequency range that tracks the contact resonance peak (~ 325-360 kHz) [37-38]. Topographic changes or artifacts will change the resonance frequency position. Measuring the amplitude response in a band of frequencies enables 'resonance tracking', which eliminates the frequency dependence of phase, maximum amplitude, and mechanical quality factor. Second, the conductive probe and top electrode were driven with the same excitation function, which largely mitigated electrostatic contributions to the signal, while the bottom electrode was grounded [39-40]. Thus, the capacitor structures were excited individually with known electric fields, and the AFM cantilever detected local displacement [41]. Third, it is essential in these measurements to detect the material nonlinearity, rather than mechanical nonlinearities associated with the tip-electrode contact. Nonlinear cantilever dynamics were

minimized by chirping up in frequency space, then chirping down in frequency, as described previously [41], and measuring peak asymmetry. The phase of the chirp wave was tuned closer to a sync, so that chirp up and chirp down frequency sweeps produced symmetric peaks. The frequency was therefore independent on the direction of the chirp and cantilever non-linearities were thereby significantly reduced. Spectral images were collected on a two-dimensional grid on the top electrode surface; the resultant multidimensional data measured was a function of frequency, excitation voltage, and two spatial coordinates.

2.2.3 Data analysis

A simple harmonic oscillator equation (SHO) was used to fit the cantilever deflection as a function of frequency, voltage step and position, obtaining the amplitude at resonance (A_{max}), the resonant frequency (ω_o), and the mechanical quality factor (Q). The nonlinear function of A_{max} was described with a second-order polynomial $A_{max}=A_0+A_1*E_{AC}+A_2*E_{AC}^2$; differentiation with respect to the electric field yielded the Rayleigh law given in Equation 1.1 [31]. The ratio of the Rayleigh coefficients associated with irreversible contributions (α_{d33}) to the reversible contributions ($d_{33,initial}$) is given by $2A_2/A_1$ where A_2 is the quadratic coefficient, A_1 is the linear coefficient, and A_0 is the intercept of the second-order polynomial. As previously noted, A_0 was assigned to 0 [31]. Piezoelectric amplitude responses below the Rayleigh voltage regime showed little to no resonance. The coefficient of determination (R^2) for the simple harmonic oscillator (SHO) fit was therefore low, enabling an exclusion of such datapoints from the polynomial fit.

K-means clustering [42] was performed on each $\alpha_{d33}/d_{33,initial}$ spatial map to group datapoints with similar response into three clusters: low, medium, and high response. The k-means clustered spatial map was binarized so that each pixel containing a Rayleigh ratio in the highest bin received a value of 1 and all other pixels were 0. A median filter was applied to the binary image, and a python label “blobbing” function [43] determined the number of clusters and

the area of each cluster (in μm^2). An identical analysis was repeated for all ten PZT film nonlinear BE-PFM measurements.

2.3 Results and discussion

All PZT films showed <100> preferred orientation (See Figure A.1 in Appendix A for Bragg-Brentano X-ray diffraction patterns of 500 nm thick Nb and Mn-doped PZT films). Figure 2.1 contrasts the x-ray diffraction data of Mn-doped and Nb-doped PZT films around the 100 PZT peak. The Shannon-Prewitt effective ionic radii of Nb^{5+} and Mn^{3+} in octahedral coordination are 64 pm and 58 pm, respectively [44]. The 100 XRD peak in Nb-doped PZT shifted to a lower 2θ value corresponding to a larger out of plane unit cell lattice spacing. There was no observed thickness dependence in the lattice parameters for a given dopant.

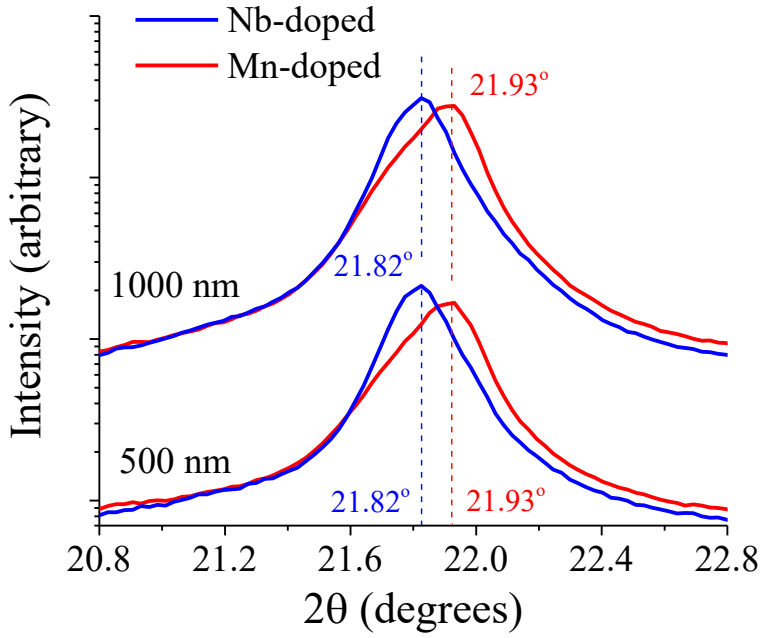

Figure 2.1: Bragg-Brentano x-ray diffraction analysis of 500 nm and 1000 nm thick PZT films doped with Mn and Nb near the 100 PZT peak.

Figure 2.2a displays the experimental setup for nonlinearity measurements using BE-PFM. The measurements were made on capacitors, such that the probe acted as a strain sensor and the electric field distribution across the film was homogeneous and quantifiable. The piezoresponse at each point was captured across the frequency band centered on the resonant frequency of the cantilever (~345 kHz) for both chirp directions (Figure 2.2b). The resultant SHO maximum amplitude (A_{max}) is plotted as a function of applied AC electric field in Figure 2.2c for a single pixel, which was fitted with the quadratic polynomial $A_{max}=A_1*E_{AC}+A_2*E_{AC}^2$ shown as the blue curve. The voltage steps below the Rayleigh regime (black data points in Figure 2.2c) were excluded from the quadratic fit due to poor SHO R^2 values ($R^2<0.5$).

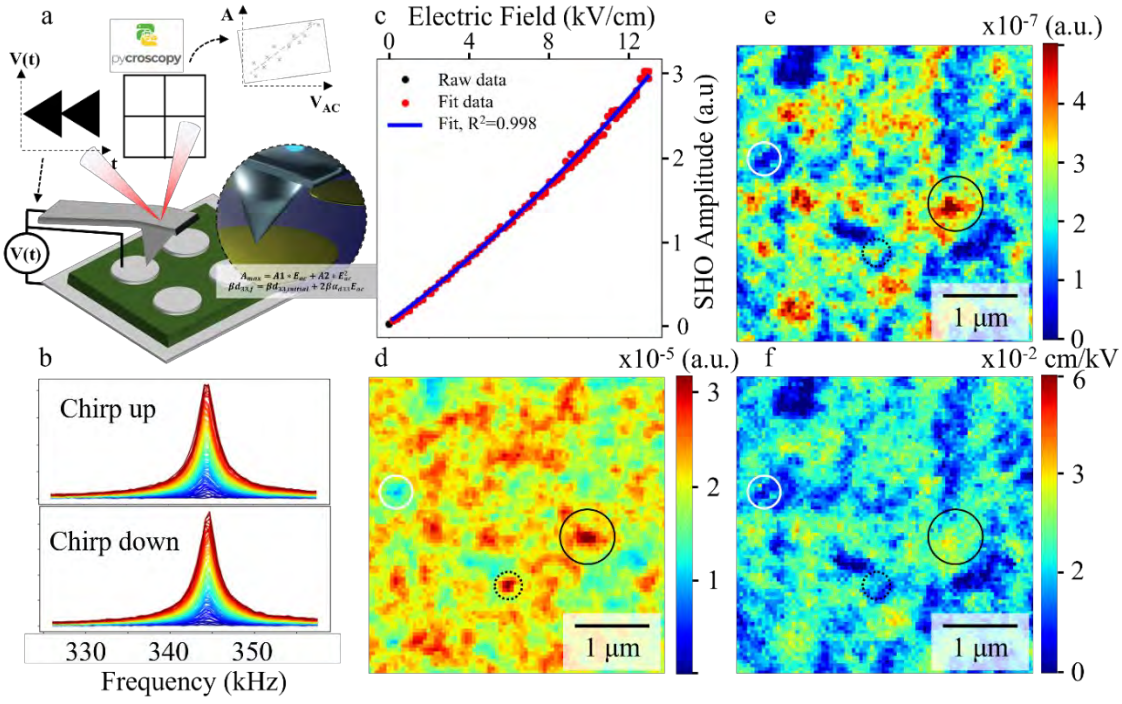

Figure 2.2: Mn-doped 500 nm thick PZT film BE-PFM results. (a) Schematic of experimental setup. (b) Alignment of peak amplitude at resonance by optimization of the phase variation parameter (c) Example of the fitted response for one pixel; black data points with poor SHO fit ($R^2<0.5$) were excluded. (d) Map of A_2 (proportional to $d_{33,initial}$) (e) Map of the A_3 (proportional to α_{d33}) (f) Ratio of α_{d33} / $d_{33,initial}$.

Piezoelectric amplitude is directly proportional to sample displacement h, $A_{max}=\beta h$, where β is the cantilever sensitivity [31]. The Rayleigh law is extracted by the differentiation of A_{max}: $\beta d_{33,f} = \beta d_{33,initial} + 2\beta\alpha_{d33} E_{AC}$, where $d_{33,f}$ is the piezoelectric coefficient, $A_1 \propto d_{33,initial}$ and $2A_2 \propto \alpha_{d33}$. Evidence of domain wall clustering is displayed in Figure 2.2d, which shows the spatial map of Rayleigh coefficient $d_{33,initial}$. Similarly, Figure 2.2e shows clusters with higher α_{d33}, or irreversible domain wall contributions, compared to the lower α_{d33} matrix. The $\alpha_{d33}/d_{33,initial}$ map displayed in Figure 2.2f shows clustering of the extrinsic responses.

The $d_{33,in}$ maps illustrate the presence of large-scale features (hundreds of nm to 2 μm), well above the grain sizes. The α_{d33} maps also illustrate micron-sized clusters. It is noted that the $d_{33,initial}$ and α_{d33} cluster maps are largely decoupled from one another. This is visualized in Figure 2.2 (d-f), where the solid black circles show a region of high $d_{33,initial}$ and high α_{d33} coefficients and the dotted black circle shows a region of high $d_{33,initial}$ but low α_{d33} coefficients. The white circle highlights a region where both $d_{33,initial}$ and α_{d33} responses are low.

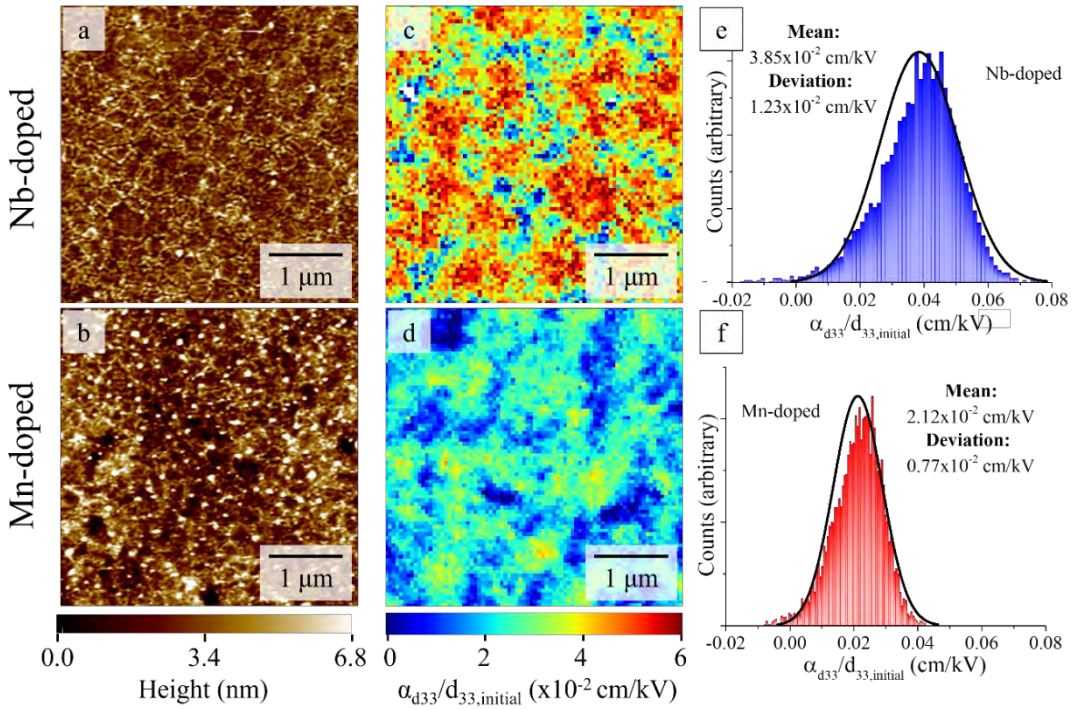

Figure 2.3: Topography maps of 500 nm thick PZT films doped with Nb (a) and Mn (b). Spectroscopic nonlinear Rayleigh ratio map for 500 nm thick PZT films doped with Nb (c) and Mn (d). Histogram of nonlinear Rayleigh ratio maps (c/d) for Nb (e) and Mn (f) doped PZT films, with the black lines as Gaussian fits.

Figure 2.3 (a,b) shows the topography of the 500 nm thick Nb and Mn doped PZT film surfaces measured with contact mode AFM, respectively. The average in-plane grain area for the 500 nm thick Nb-doped film was $33\times10^{-3} \pm 7\times10^{-3}$ μm^2 and $20\times10^{-3} \pm 2\times10^{-3}$ μm^2 for the Mn-doped film. Grain area analysis is shown in Figure A.2 of Appendix A. The average surface roughness for both films does not exceed 1.3 nm. Additionally, it should be noted that there were small differences between the electrical conductivity of the donor and acceptor doped films; as is typical in PZT, the majority of the doping was ionically compensated, rather than electronically compensated [45-47]. A comparison of spatially resolved nonlinear Rayleigh ratio maps from BE-PFM are displayed in Figure 2.3 (c,d) for Nb and Mn-doped films, respectively. Figure 2.3 (c,d) clearly display high response clusters with areas 0.1 to 1 μm^2, much larger than the average grain area in each film. Histograms of the nonlinear Rayleigh ratios for Nb and Mn doped films

are shown in Figure 2.3 (e,f), respectively, with average $\alpha_{d33}/d_{33,initial}$ ratios of 38.5x10^{-3} cm/kV and 21.2x10^{-3} cm/kV, respectively. The black lines in Figure 2.3 (e,f) are Gaussian fits to the Rayleigh ratio histograms which do not fully fit the spatial distribution of $\alpha_{d33}/d_{33,initial}$ ratios. There is a slight skew of the histogram data to a smaller ratio in both films. The higher nonlinearities in the Nb-doped PZT film are related to reduced domain wall pinning, as is typical in bulk donor doped PZT ceramics [11].

Importantly, the cluster areas are similar between the two films even though the $\alpha_{d33}/d_{33,initial}$ ratio is very different. The $\alpha_{d33}/d_{33,initial}$ maps for Nb and Mn doped PZT films displayed in Figure 2.3 (c,d) were processed to calculate individual high response cluster areas. The image processing was performed with the scikit learn [42] and scikit image [43] analysis tools in Python, and the individual steps are shown in Figure A.3 in Appendix A. The image processing software is available on Github.

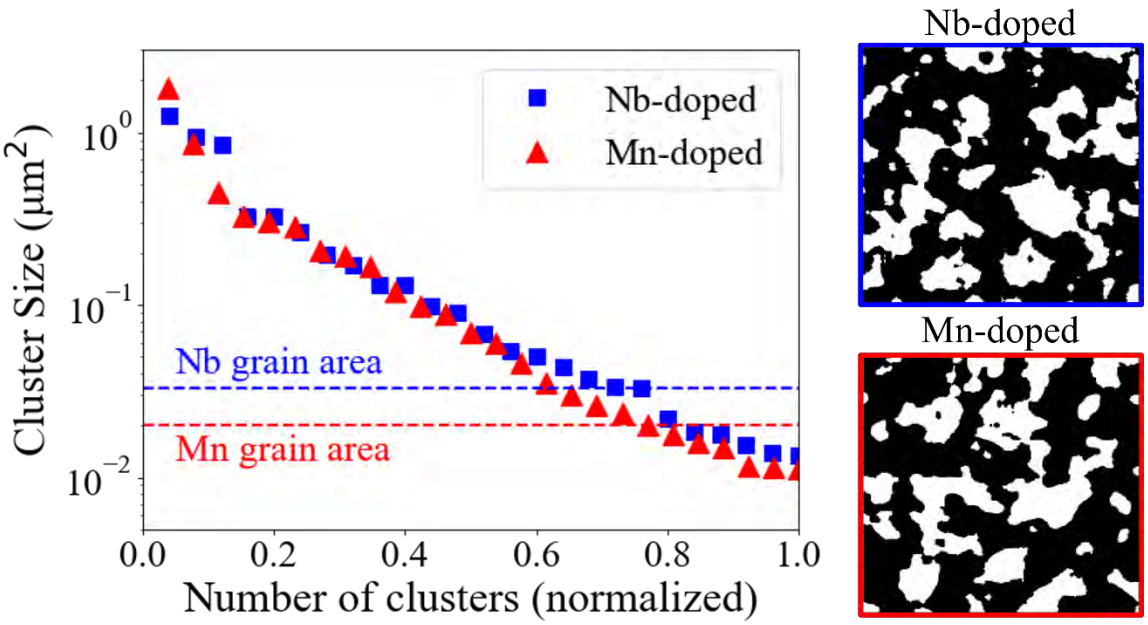

Figure 2.4: High mobility cluster areas in Nb-doped and Mn-doped PZT films 500 nm thick. The white regions in the figures at the right are regions which had high response.

A closer examination of the individual cluster areas for 500 nm thick Nb-doped (blue) or Mn-doped (red) PZT films is shown in Figure 2.4. The horizontal lines in the left-side plot are the average grain areas for the two films. The right-side images are the binary spectroscopic maps of high response Rayleigh clusters in white; both medium and low response regions are shown in black. Of the twenty-five clusters larger than 0.01 μm^2, 76% are bigger than the average grain area in Nb-doped PZT and 77% are bigger than the grain area in Mn-doped PZT. More than 75% of the high Rayleigh response clusters in each film are larger than the average grain area, demonstrating domain avalanches across grain boundaries.

Furthermore, clusters in the range of 0.01 μm^2 to 2 μm^2 are independent of dopant type, displayed by the overlapping trend of cluster area vs. the normalized cluster number. Thus, the correlation length for motion of domain walls is comparable for both donor and acceptor-doped films. This suggests that domain avalanche sizes are unaffected by lead or oxygen vacancies at the 2% dopant levels in 500 nm thick PZT films. The combination of the data in Fig. 2.3 and 2.4 suggests that extrinsic contributions are suppressed everywhere (e.g. at very small volumes) in the Mn-doped films and enhanced at very small volumes in the Nb-doped films. That is, point defects do not govern the spatial extent of correlated motion of domain walls, just their local mobility.

An identical analysis of the spectroscopic $\alpha_{d33}/d_{33,initial}$ ratios for each Nb doped and Mn doped PZT film between 250 nm and 1250 nm thick enabled evaluation of cluster characteristics in films of varying thickness. Figure 2.5 shows the binary Rayleigh response clusters (with white regions as the high response clusters) for each film thickness. As PZT film thickness increased, the total number of clusters greater than 0.01 μm^2 in size within a 4x4 μm^2 scan size decreased. This trend is also shown in the right-most plot in Figure 2.5. There is no clear difference in the number of clusters between the films with different dopant types, as the Nb-doped and Mn-doped results largely superimpose in the range of film thicknesses investigated.

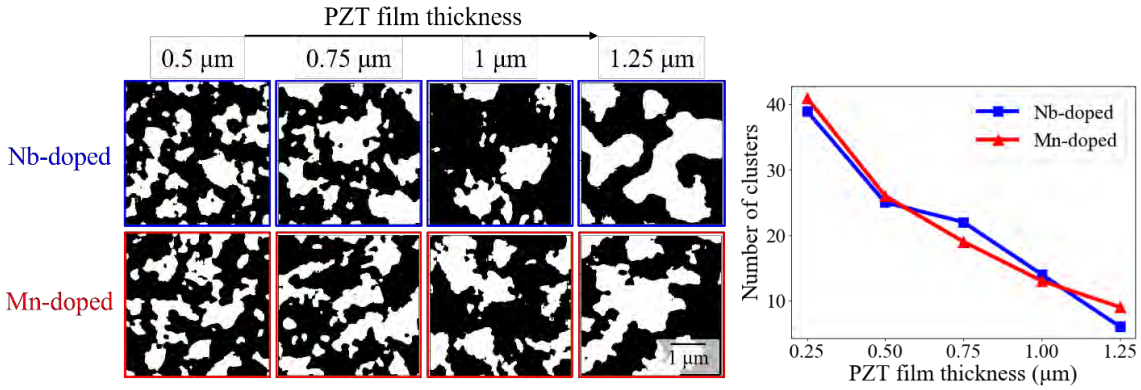

Figure 2.5: Binarized cluster maps showing regions of high nonlinearity (white) in a matrix of medium and low nonlinearity (black) for a 4x4 μm^2 scan size. The right-most figure shows the number of clusters counted as a function of film thickness for Nb-doped (blue) and Mn-doped (red) PZT films.

An evaluation of the cluster areas in each PZT film thickness is shown in Figure 2.6 (a) and (b) for Nb-doped and Mn-doped films, respectively. The bar charts represent trends between individual cluster area and PZT film thickness. First, in both Nb and Mn doped films, the thinner films contain more clusters in a 4x4 μm^2 area, visualized by the long tails extending to 0.01 μm^2 cluster area for the 250 nm thick film (red). The thicker films (e.g. 1250 nm film in grey) have relatively few clusters, each one larger than the majority of clusters in the thinner films. Second, the total cluster area and number of clusters for each film is independent of dopant type but is dependent on film thickness. The high response clusters represent 32% and 33% of the 16 μm^2 scan region for the Nb-doped and Mn-doped 500 nm thick films, respectively. However, the 250 nm Mn-doped film contains 8% high response (clustered) regions compared to 42% high response regions for the Mn-doped 1250 nm (Figure 2.6b).

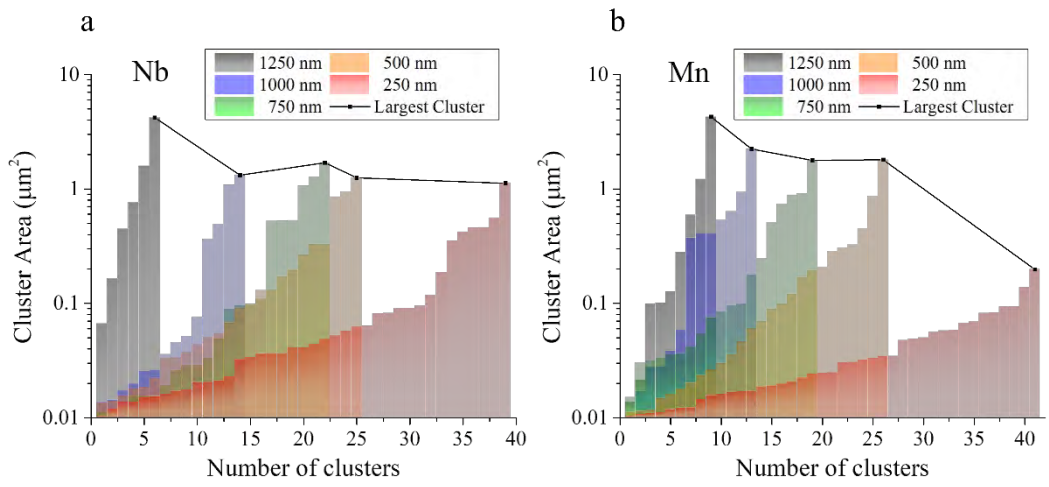

Figure 2.6: Bar charts for Nb-doped (a) and Mn-doped (b) PZT films from 250 nm to 1250 nm thick, showing the cluster area for each identified cluster.

Finally, as film thickness increases for films with both dopant types, the largest cluster observed in the analysis increases, which is visualized with the black lines in Figure 2.6. Bassiri-Gharb et al. [9] and Denis et al. [48] reported that for PZT films near ~1 μm thick, domain mobility increased in films of increasing thickness because, either, the potential energy profile for moving domain walls contains increasingly shallow wells, the concentration of pinning sites due to substrate clamping is lower, or the mobility of existing domain walls increases [9]. Here, as film thickness increases from 250 nm to 1250 nm, the avalanche characteristics indicate more collective irreversible motion of domain walls, possibly because with increased thickness, there is a higher probability of a region which couples well to adjacent regions laterally.

2.4 Conclusions

This work describes how dopants and film thickness affect clustering of irreversible domain wall motion in Nb- and Mn-doped PZT films that are 250 nm to 1250 nm in thickness. Nonlinearity measurements via band-excitation piezoresponse force microscopy enabled local

spectroscopic mapping of irreversible to reversible Rayleigh ratios in 4x4 μm^2 regions. It was found that domain clustering exists in both Nb- and Mn-doped PZT films in this thickness regime, with cluster areas as small as PZT grains (~$20x10^{-3}$ μm^2) and as large as 4.2 μm^2 in the ~1250 nm thick films with each dopant type. Cluster areas and avalanche characteristics were found to *not* depend on dopant type and subsequent crystalline vacancy defects; however, individual cluster areas increased with increasing PZT film thickness. Also, as film thickness increased, cluster density decreased and the percent of high response regions in a 4x4 μm^2 scan area increased.

2.5 References

[1] B. Jaffe, W. R. Cook, and H. Jaffe, *Piezoelectric Ceramics*. London, 1971. doi: 10.5772/45784.

[2] D. Berlincourt, "Piezoelectric ceramic compositional development," *J. Acoust. Soc. Am.*, vol. 91, no. 5, pp. 3034–3040, 1992, doi: 10.1121/1.402938.

[3] D. Berlincourt, "Piezoelectric crystals and ceramics," in *Ultrasonic Transducer Materials*, Boston, MA: Springer, 1971, pp. 63–124.

[4] S. Trolier-McKinstry, S. Zhang, A. J. Bell, and X. Tan, "High-performance piezoelectric crystals, ceramics, and films," *Annu. Rev. Mater. Res.*, vol. 48, pp. 191–217, 2018, doi: 10.1146/annurev-matsci-070616-124023.

[5] S. Li, W. Cao, and L. E. Cross, "The extrinsic nature of nonlinear behavior observed in lead zirconate titanate ferroelectric ceramic," *J. Appl. Phys.*, vol. 69, no. 10, pp. 7219–7224, 1991, doi: 10.1063/1.347616.

[6] D. Damjanovic and M. Demartin, "Contribution of the irreversible displacement of domain walls to the piezoelectric effect in barium titanate and lead zirconate titanate

ceramics," *J. Phys. Condens. Matter*, vol. 9, no. 23, pp. 4943–4953, 1997, doi: 10.1088/0953-8984/9/23/018.

[7] D. A. Hall, "Rayleigh behaviour and the threshold field in ferroelectric ceramics," *Ferroelectrics*, vol. 223, no. 1–4, pp. 319–328, 1999, doi: 10.1080/00150199908260586.

[8] D. A. Hall, "Nonlinearity in piezoelectric ceramics," *J. Mater. Sci.*, vol. 36, pp. 4575–4601, 2001.

[9] N. Bassiri-Gharb, I. Fujii, E. Hong, S. Trolier-McKinstry, D. V. Taylor, and D. Damjanovic, "Domain wall contributions to the properties of piezoelectric thin films," *J. Electroceramics*, vol. 19, no. 1, pp. 47–65, 2007, doi: 10.1007/s10832-007-9001-1.

[10] W. Zhu, I. Fujii, W. Ren, and S. Trolier-McKinstry, "Influence of Mn doping on domain wall motion in $Pb(Zr_{0.52}Ti_{0.48})O_3$ films," *J. Appl. Phys.*, vol. 109, no. 6, pp. 0–6, 2011, doi: 10.1063/1.3552298.

[11] W. Zhu, I. Fujii, W. Ren, and S. Trolier-McKinstry, "Domain wall motion in A and B site donor-doped $Pb(Zr_{0.52}Ti_{0.48})O_3$ films," *J. Am. Ceram. Soc.*, vol. 95, no. 9, pp. 2906–2913, 2012, doi: 10.1111/j.1551-2916.2012.05243.x.

[12] T. Rojac and D. Damjanovic, "Domain walls and defects in ferroelectric materials," *Jpn. J. Appl. Phys.*, vol. 56, no. 10, pp. 1–5, 2017, doi: 10.7567/JJAP.56.10PA01.

[13] W. Cao and C. A. Randall, "Grain size and domain size relations in bulk ceramic ferroelectric materials," *J. Phys. Chem. Solids*, vol. 57, no. 10, pp. 1499–1505, 1996, doi: 10.1016/0022-3697(96)00019-4.

[14] C. A. Randall, N. Kim, J. P. Kucera, W. Cao, and T. R. Shrout, "Intrinsic and extrinsic size effects in fine-grained morphotropic-phase-boundary lead zirconate titanate ceramics," *J. Am. Ceram. Soc.*, vol. 81, no. 3, pp. 677–688, 1998, doi: 10.1111/j.1151-2916.1998.tb02389.x.

[15] J. Y. Li, R. C. Rogan, E. Üstündag, and K. Bhattacharya, "Domain switching in

polycrystalline ferroelectric ceramics," *Nat. Mater.*, vol. 4, no. 10, pp. 776–781, 2005, doi: 10.1038/nmat1485.

[16] B. Casals, G. F. Nataf, D. Pesquera, and E. K. H. Salje, "Avalanches from charged domain wall motion in $BaTiO_3$ during ferroelectric switching," *APL Mater.*, vol. 8, no. 1, 2020, doi: 10.1063/1.5128892.

[17] B. Casals, G. F. Nataf, and E. K. H. Salje, "Avalanche criticality during ferroelectric/ferroelastic switching," *Nat. Commun.*, vol. 12, no. 1, pp. 1–7, 2021, doi: 10.1038/s41467-020-20477-6.

[18] J. Schultheiß, L. Liu, H. Kungl, M. Weber, L.K. Venkataraman, S. Checchia, D. Damjanovic, J.E. Daniels, and J. Koruza, "Revealing the sequence of switching mechanisms in polycrystalline ferroelectric/ferroelastic materials," *Acta Mater.*, vol. 157, pp. 355–363, 2018, doi: 10.1016/j.actamat.2018.07.018.

[19] J. Schultheiß, S. Checchia, H. Uršič, T. Frömling, J. E. Daniels, B. Malič, T. Rojac, and J. Koruza, "Domain wall-grain boundary interactions in polycrystalline $Pb(Zr_{0.7}Ti_{0.3})O_3$ piezoceramics," *J. Eur. Ceram. Soc.*, vol. 40, no. 12, pp. 3965–3973, 2020, doi: 10.1016/j.jeurceramsoc.2020.03.054.

[20] E. K. H. Salje, D. Xue, X. Ding, K. A. Dahmen, and J. F. Scott, "Ferroelectric switching and scale invariant avalanches in $BaTiO_3$," *Phys. Rev. Mater.*, vol. 3, no. 1, p. 14415, 2019, doi: 10.1103/PhysRevMaterials.3.014415.

[21] O. Boser, "Statistical theory of hysteresis in ferroelectric materials," *J. Appl. Phys.*, vol. 62, no. 4, pp. 1344–1348, 1987, doi: 10.1063/1.339636.

[22] L. M. Denis, G. Esteves, J. Walker, J. L. Jones, and S. Trolier-McKinstry, "Thickness dependent response of domain wall motion in declamped {001} $Pb(Zr_{0.3}Ti_{0.7})O_3$ thin films," *Acta Mater.*, vol. 151, pp. 243–252, 2018, doi: 10.1016/j.actamat.2018.03.046.

[23] L. M. Denis-Rotella, G. Esteves, J. Walker, H. Zhou, J. L. Jones, and S. Trolier-

McKinstry, “Residual stress and ferroelastic domain reorientation in declamped {001} $Pb(Zr_{0.3}Ti_{0.7})O_3$ films,” *IEEE Trans. Ultrason. Ferroelectr. Freq. Control*, vol. 68, no. 2, pp. 259–272, 2021, doi: 10.1109/TUFFC.2020.2987438.

[24] N. B. Gharb and S. Trolier-McKinstry, “Dielectric nonlinearity of $Pb(Yb_{1/2}Nb_{1/2})O_3$-$PbTiO_3$ thin films with {100} and {111} crystallographic orientation,” *J. Appl. Phys.*, vol. 97, no. 6, 2005, doi: 10.1063/1.1857054.

[25] S. Trolier-McKinstry, N. B. Gharb, and D. Damjanovic, “Piezoelectric nonlinearity due to motion of 180° domain walls in ferroelectric materials at subcoercive fields: A dynamic poling model,” *Appl. Phys. Lett.*, vol. 88, no. 20, 2006, doi: 10.1063/1.2203750.

[26] N. B. Gharb, S. Trolier-McKinstry, and D. Damjanovic, “Piezoelectric nonlinearity in ferroelectric thin films,” *J. Appl. Phys.*, vol. 100, no. 4, 2006, doi: 10.1063/1.2266235.

[27] W. Zhu, W. Ren, H. Xin, P. Shi, and X. Wu, “Enhanced ferroelectric properties of highly (100) oriented $Pb(Zr_{0.52}Ti_{0.48})O_3$ thick films prepared by chemical solution deposition,” *J. Adv. Dielectr.*, vol. 03, no. 02, p. 1350011, 2013, doi: 10.1142/s2010135x13500112.

[28] F. Griggio, S. Jesse, W. Qu, A. Kumar, O. Ovchinnikov, D.S. Tinberg, S.V. Kalinin, and S. Trolier-McKinstry, “Composition dependence of local piezoelectric nonlinearity in $(0.3)Pb(Ni_{0.33}Nb_{0.67})O_3$-$(0.7)Pb(Zr_xTi_{1-x})O_3$ films,” *J. Appl. Phys.*, vol. 110, no. 4, pp. 0–10, 2011, doi: 10.1063/1.3622312.

[29] F. Griggio, S. Jesse, A. Kumar, O. Ovchinnikov, H. Kim, T.N. Jackson, D. Damjanovic, S.V. Kalinin, and S. Trolier-McKinstry, “Substrate clamping effects on irreversible domain wall dynamics in lead zirconate titanate thin films,” *Phys. Rev. Lett.*, vol. 108, no. 15, pp. 1–5, 2012, doi: 10.1103/PhysRevLett.108.157604.

[30] R. Keech, C. Morandi, M. Wallace, G. Esteves, L. Denis, J. Guerrier, R.L. Johnson-Wilke, C.M. Fancher, J.L. Jones, and S. Trolier-McKinstry, “Thickness-dependent domain wall reorientation in 70/30 lead magnesium niobate- lead titanate thin films,” *J. Am. Ceram.*

Soc., vol. 100, no. 9, pp. 3961–3972, 2017, doi: 10.1111/jace.14927.

[31] P. Bintachitt, S. Jesse, D. Damjanovic, Y. Han, I.M. Reaney, and S. Trolier-McKinstry, "Collective dynamics underpins Rayleigh behavior in disordered polycrystalline ferroelectrics," *Proc. Natl. Acad. Sci. U. S. A.*, vol. 107, no. 16, pp. 7219–7224, 2010, doi: 10.1073/pnas.0913172107.

[32] D. M. Marincel, H. Zhang, A. Kumar, S. Jesse, S.V. Kalinin, W.M. Rainforth, I.M. Reaney, C.A. Randall, and S. Trolier-McKinstry, "Influence of a single grain boundary on domain wall motion in ferroelectrics," *Adv. Funct. Mater.*, vol. 24, no. 10, pp. 1409–1417, 2014, doi: 10.1002/adfm.201302457.

[33] D. M. Marincel, H. Zhang, S. Jesse, A. Belianinov, M.B. Okatan, S.V. Kalinin, W.M. Rainforth, I.M, Reaney, C.A. Randall, and S. Trolier-McKinstry, "Domain wall motion across various grain boundaries in ferroelectric thin films," *J. Am. Ceram. Soc.*, vol. 98, no. 6, pp. 1848–1857, 2015, doi: 10.1111/jace.13535.

[34] D. M. Marincel, H.R. Zhang, J. Britson, A. Belianinov, S. Jesse, S.V. Kalinin, L.Q. Chen, W.M. Rainforth, I.M. Reaney, C.A. Randall, and S. Trolier-McKinstry, "Domain pinning near a single-grain boundary in tetragonal and rhombohedral lead zirconate titanate films," *Phys. Rev. B - Condens. Matter Mater. Phys.*, vol. 91, no. 13, 2015, doi: 10.1103/PhysRevB.91.134113.

[35] W. Zhu, B. Akkopru-Akgun, J.I. Yang, C. Fragkiadakis, K. Wang, S.W. Ko, P. Mardilovich, and S. Trolier-McKinstry, "Influence of graded doping on the long-term reliability of Nb-doped lead zirconate titanate films," *Acta Mater.*, vol. 219, p. 117251, 2021, doi: 10.1016/j.actamat.2021.117251.

[36] Somnath, S., Smith, C.R., Laanait, N., Vasudevan, R. K., & Jesse, S. "USID and pycroscopy-Open source frameworks for storing and analysing imaging and spectroscopy data." *Microscopy and Microanalysis* 25.S2, pp. 220-221, 2019. doi:

10.1017/S1431927619001831

[37] Jesse, S., Kumar, A., Rodriguez, B.J., Proksch, R., and Kalinin, S.V., "Resolution theory, and static and frequency-dependent cross-talk in piezoresponse force microscopy," *Nanotechnology*, vol. 21, 405703, 2010.

[38] Yang, S.M., Mazet, L., Okatan, M.B., Jesse, S., Niu, G., Schroeder, T., Schamm-Chardon, S., Dubourdieu, C., Baddort, A.P., and Kalinin, S.V., "Decoupling indirect topographic cross-talk in band excitation piezoresponse force microscopy imaging and spectroscopy," *Appl. Phys. Lett.,* vol. 108, 252902, 2016.

[39] Qiao, H., Kwon, O., and Kim, Y., "Electrostatic effect on off-field ferroelectric hysteresis loop in piezoelectric force microscopy," *Appl. Phys. Lett.*, vol. 116, 172901, 2020.

[40] Collins, L., Liu, Y., Ovchinnikova, O.S., Proksch, R., "Quantitative electromechanical atomic force microscopy," *ACS Nano,* vol. 13, pp. 8055-8066, 2019.

[41] F. Griggio, S. Jesse, A. Kumar, D.M. Marincel, D.S. Tinberg, S.V. Kalinin, and S. Trolier-McKinstry, “Mapping piezoelectric nonlinearity in the Rayleigh regime using band excitation piezoresponse force microscopy,” *Appl. Phys. Lett.*, vol. 98, no. 21, pp. 98–101, 2011, doi: 10.1063/1.3593138.

[42] F. Pedregosa, G. Varoquaux, A. Gramfort, V. Michel, B. Thirion, O. Grisel, M. Blondel, P. Prettenhofer, R. Weiss, V. Dubourg, and J. Vanderplas*,* "Scikit-learn: Machine learning in Python," *JMLR* 12, pp. 2825-2830, 2011.

[43] Stefan an der Walt, Johannes L. Schonberger, Juan Nunez-Iglesias, Francois Boulogne, Joshua D. Warner, Neil Yager, Emmanuelle Gouillart, Tony Yu and the scikit-image contributors. "Scikit-image: Image processing in Python," *PeerJ,* 2:e453, 2014, doi: 10.7717/peerj.453

[44] R. D. Shannon, “Revised effective ionic radii and systematic studies of interatomic distances in halides and chalcogenides,” *Acta Crystallogr. Sect. A*, vol. 32, no. 5, pp. 751–

767, 1976, doi: 10.1107/S0567739476001551.

[45] Donnelly, N.J. and Randall, C.A., "Pb loss in Pb(Zr,Ti)O_3 ceramics observed by *in situ* ionic conductivity measurements," *J. Appl. Phys.,* vol. 109, 104107, 2011.

[46] Akkpru-Akgun, B., Marincel, D.M., Tsuji, K., J.M. Bayer, T., Randall, C.A., Lanagan, M.T., and Trolier-McKinstry, S., "Thermally stimulated depolarization current measurements on degraded lead zirconate titanate films," *J. Am. Ceram. Soc.,* vol. 104, pp. 5270-5280, 2021.

[47] Koh, D., Ko, S.W., Yang, J.I., Akkopru-Akgun, B., and Trolier-McKinstry, S., "Effect of Mg-doping and Fe-doping in lead zirconate titanate (PZT) thin films on electrical reliability," *J. Appl. Phys.,* vol. 132, 174101, 2022.

[48] Denis, L. M., Esteves, G., Walker, J., Jones, J. L., & Trolier-McKinstry, S. "Thickness dependent response of domain wall motion in declamped {001} Pb($Zr_{0.3}Ti_{0.7}$)O_3 thin films." *Acta Materialia*, 151, pp: 243-252, 2018, doi: 10.1016/j.actamat.2018.03.046

CHAPTER 3

Domain wall motion across microstructural features in polycrystalline ferroelectric films

Chapter 3 of this thesis has been previously submitted for publication (as of January 10th, 2023) as: Hennessey, G., Peters, T., Tipsawat, P., Checa, M., Collins, L., Trolier-McKinstry, S., (2023). Domain Wall Motion Across Microstructural Features in Polycrystalline Ferroelectric Films. *Acta Materialia,* (awaiting review). Additional details are found in the Master Thesis of Gavin Hennessey.

3.1 Introduction

The piezoelectric response of ferroelectric materials can be divided into intrinsic and extrinsic sources, where the intrinsic response corresponds to the appropriate average of the single domain single crystal response; extrinsic contributions are those due to motion of mobile interfaces such as phase boundaries or domain walls [1–5]. The macroscopic properties of polycrystalline perovskites are the ensemble average of many grains and even more domain walls. Calculating the response of ceramics is challenging, however, due to the grain-to-grain coupling, the interactions between the intrinsic and extrinsic contributions, the inherent anisotropy of the piezoelectric response, and incomplete knowledge about how local elastic and electric fields influence domain wall motion. It is thus interesting to explore somewhat simplified systems where the effect of single factors on extrinsic contributions can be quantified. This paper focuses on the characteristics of individual grain boundaries and triple points on the extrinsic piezoelectric response in lead zirconate titanate (PZT) films, as a model system.

Extrinsic contributions have been reported to decrease near grain boundaries in ferroelectric films and ceramics. Randall et al. demonstrated that the piezoelectric properties of PZT ceramics decreased with decreasing grain size, which was attributed to a change in the domain structure and a reduction in domain wall contributions [6]. Similarly, Griggio et al. reported that an average grain size increase from 110 nm to 270 nm in PZT-based films was accompanied by a doubling of the irreversible dielectric Rayleigh coefficient α_d from 5.3 ± 0.1 cm/kV to 10.6 ± 0.1 cm/kV [7]. α_d is associated with the irreversible motion of domain walls. Grain boundaries have also been reported to influence the ferroelectric switching characteristics [8–11].

Marincel et al. measured the local impact of single grain boundaries on the irreversible to the reversible Rayleigh coefficient ratios using band excitation piezoresponse force microscopy (BE-PFM). Both reversible $d_{33,initial}$ and irreversible α_d Rayleigh coefficients were calculated from the nonlinear dependence of out-of-plane deflection on increasing applied AC voltage. The ratio of $\alpha_d/d_{33,initial}$ suggested increased pinning of domain wall motion within 476 nm of a 24 ° tilt grain boundary in a $PbZr_{0.52}Ti_{0.48}O_3$ (PZT 52/48) film on a bicrystal substrate [12]. The width of influence of the reduced response at grain boundaries was found to be dependent on both the misorientation angle and the tilt/twist characteristics of the boundary [13].

Among the factors thought to affect the width of influence of a particular grain boundary is the connectivity of the domain structure across the structural discontinuity. Following seminal work by Tsurekawa [14], Mantri reported that for random grain-grain misorientations, domain continuity is dependent on the ability of the material to compensate strain mismatch and minimize the polarization charge at the grain boundary [15]. It was found that a larger uncompensated charge and/or bigger spontaneous polarizations make continuity less energetically favorable.

Fousek et al. studied permissible orientations of ferroelectric domain walls in detail. He noted that, in theory, uniform strain states should only yield domain walls along planes of

mechanical compatibility in the absence of external stress [16]. When no additional elastic strain develops, the domain wall is deemed a "permissible wall" [16]. If two non-permissible domains meet along a stressed boundary, domain switching is expected to be restricted, as has been noted in grain boundary pinning [16,17]. The domain structure is thus a developing system that acts in response to strain and charge from differently oriented polarizations.

To date, quantitative evaluations of the role of individual grain boundaries on the motion of domain walls are limited, with most of the data pertaining to symmetrical grain boundaries. A more comprehensive set of data is required to better understand the role that grain boundaries exert in pinning extrinsic contributions to the properties. It is speculated that grain boundaries with a shared axis of rotation, i.e., Coincident Site Lattice (CSL) boundaries, may facilitate domain wall motion across the grain boundary relative to random grain boundaries. Thus, in this work, the intrinsic and extrinsic contributions to the piezoelectric response were assessed for PZT films deposited onto polycrystalline large-grained $SrRuO_3/SrTiO_3$ substrates. The substrates allowed many grain boundary orientations to be isolated by Electron Backscatter Diffraction (EBSD) and categorized based on grain boundary angle and shared orientation axes. BE-PFM imaging was used to quantify the local piezoelectric nonlinearities.

3.2 Experimental Procedure

3.2.1 Sample fabrication

Strontium titanate ($SrTiO_3$) ceramic substrates, obtained from Knowles Precision Devices, were cleaned, mechanically polished, and annealed prior to depositing the strontium ruthenate ($SrRuO_3$) bottom electrodes. The final substrate polishing parameters and anneal conditions are given in Appendix B. Epitaxial $SrRuO_3$ bottom electrodes were deposited on the

$SrTiO_3$ substrates by pulsed laser deposition (PLD) following the conditions listed in Table B.1 in Appendix B. The detailed procedure for $SrRuO_3$ deposition via PLD is also given in Appendix B.

The samples were cleaned with acetone, ethanol, and isopropyl alcohol, then annealed at 750°C for 1 min in a rapid thermal annealer (Allwin21 Corp AW 810 RTP). A modification of the processes reported by Borman and Zhu was used for chemical solution deposition of the PZT films [18,19]. A Mitsubishi Materials Corporation 114/52/48/2 PZTNb solution of $PbZr_{0.52}Ti_{0.48}O_3$ with 14 mol% excess Pb and 2 mol% Nb was utilized for PZT film growth. Sol-gel PZT deposition conditions are given in Appendix B. There is an explicit assumption that the PZT film grain boundaries grew perpendicular the substrate surface.

Layers of LOR 5A (Microchem) and SPR3012 (Dow Electronic Materials) photoresist were spin coated, soft-baked, then exposed at 180 mJ/cm^2 using 405 nm laser MLA150 advanced maskless aligner (Heidelberg, Germany). The exposed areas of patterned resist were circles with a diameter of 200 μm. MF CD-26 developer (1-5% Tetramethylammonium hydroxide (TMAH) in water – Dow Electronic Materials) was then utilized to develop the exposed photoresist areas and reveal the underlying PZT. An oxygen plasma ash step using an M4L RF Gas Plasma System (PVA TePla Corona, California) with gas flow rates of 50 sccm He and 150 sccm O_2, at a pressure of 550 mTorr, and an RF power of 200 W for 1 min then served to remove any remaining resist in the patterned areas.

3.2.2 Electron backscatter diffraction

Electron Backscatter Diffraction (EBSD) was used to analyze the films for crystallographic orientations and grain boundary locations, as demonstrated in Figure B.1 in Appendix B. The angle between any two grains was calculated using the Aztec crystal software. Crystallographic orientation of the 200 μm diameter lithographically defined circular electrode area was mapped before top electrode deposition, as shown in Figure B.2 (a,b) in Appendix B. Top platinum electrodes 50 nm thick were sputter deposited (Kurt Lesker CMS-18, Pittsburgh

PA) with an Ar chamber pressure of 2.5×10^{-3} Torr at room temperature. The plasma was struck through the application of 200 W DC. Post-deposition photoresist lift-off resulted in circular top electrodes for electrical measurements. Finally, to improve adhesion of the top electrode to the PZT surface, each sample underwent an RTA step at 550 °C for 1 min with a heating rate of 4 °C/s and ambient chamber conditions (no gas flow).

Using a secondary photolithography step, a set of crosshairs was created around the platinum electrodes to act as cardinal directions for PFM scan alignment, shown in Figure B.2 (a,c) in Appendix B. Square bonding pads were also added during this step, as shown in Figure B.2c. Approximately 200 nm of gold was sputtered onto the exposed areas of each sample (Kurt Lesker CMS-18, Pittsburgh PA) using a power supply setpoint of 200 W and a chamber pressure of 4.7 mTorr at 22°C for 400 seconds.

3.2.3 Piezoresponse force microscopy

BE-PFM [20] was performed using a commercial atomic force microscope (AFM), namely a Cypher AFM (Asylum Research an Oxford Instruments Company, Santa Barbara, CA) equipped with PXI architecture, based on National Instruments NI-6124 fast arbitrary waveform generator and data acquisition cards controlled using custom labview software. All measurements were performed using Pt/Ir-coated cantilevers (BudgetSensors Multi75E-G) with a nominal spring constant of ~3 N/m and resonance frequency of ~75 kHz. Quantitative local measurements of piezoelectric nonlinearity in the Rayleigh regime were acquired via nonlinear BE-PFM, as previously described [21]. Nonlinear BE-PFM experiments were conducted by varying the excitation amplitude from 0 to ~1/2 the coercive voltage in the frequency range of 300 to 400 kHz, around the contact resonance of the probe. To separate material non-linearities from cantilever non-linearities, the AC driving voltage was swept up and down in frequency, and the phase content of the chirp wave was adjusted to keep the cantilever dynamics in the linear regime, as described previously [22]. The deflection amplitude as a function of frequency was fit

to a simple harmonic oscillator (SHO) model and the amplitude at resonance (A_{max}), resonance frequency and Q factor were extracted for each applied AC electric field (E_{AC}). Spectral images were collected on a dense grid of points on the top electrode, providing a 3-dimensional dataset containing information on spatial (x,y) and E_{AC} dependence, A_{max} (x,y,E_{AC}). Spatial maps of the Rayleigh coefficients were extracted by fitting A_{max} vs E_{AC}, for each spatial location, with a second order polynomial $A_{max}=A2*E_{AC}+A3*E_{AC}^2$, where $d_{33,initial} \propto A2$ and $2*A3 \propto \alpha_d$.

Prior to BE-PFM measurements, the samples were poled at three times the coercive field at 150°C for 15 minutes. Care was taken to ensure that the piezoelectric phase was uniform across the scan area. Using the EBSD map, grain boundaries of interest were located. From BE-PFM, the piezoresponse amplitudes varied between grains, as expected, due to their different grain orientations. BE-PFM nonlinearity measurements were acquired within a scan area of either 4x4 μm^2 measuring 80x80 $pixels^2$ or 5x5 μm^2 with 100x100 $pixels^2$, keeping the pixel separation constant at 50 nm (on the order of magnitude of the probe radius). EBSD orientation and PFM Rayleigh ratio ($\alpha_d/d_{33,initial}$) maps were correlated with respect to each other, aided using the fiduciary marks, which enabled the direct comparison of $\alpha_d/d_{33,initial}$ responses at and around precise grain boundary locations of interest. Individual grains were color-coded with respect to the orientation key in all EBSD maps.

3.3 Results and Discussion

A method adopted from Marincel et al. (Method 3), which utilized clustered response behavior, was implemented to analyze the width of influence of individual grain boundaries on the motion of domain walls [12]. In particular, the average nonlinear response was calculated parallel to the grain boundary in 50 nm (BE-PFM pixel size) increments away from the boundary

as the distance from the grain boundary. The average and standard deviation of the nonlinear response in each grain was then determined far from the grain boundary, where the $\alpha_d/d_{33,initial}$ appeared to be independent of the distance from the boundary. The width of influence was determined from the collective nonlinear response of the grain far from the grain boundary. The width of influence standard deviation was calculated as 25% of the standard deviation of each grain's nonlinear response. Given the different orientations of the grains, a separate mean and standard deviation for each grain were collected on both sides of each grain boundary. The following discussion describes several triple point regions in the film and characterizes their response.

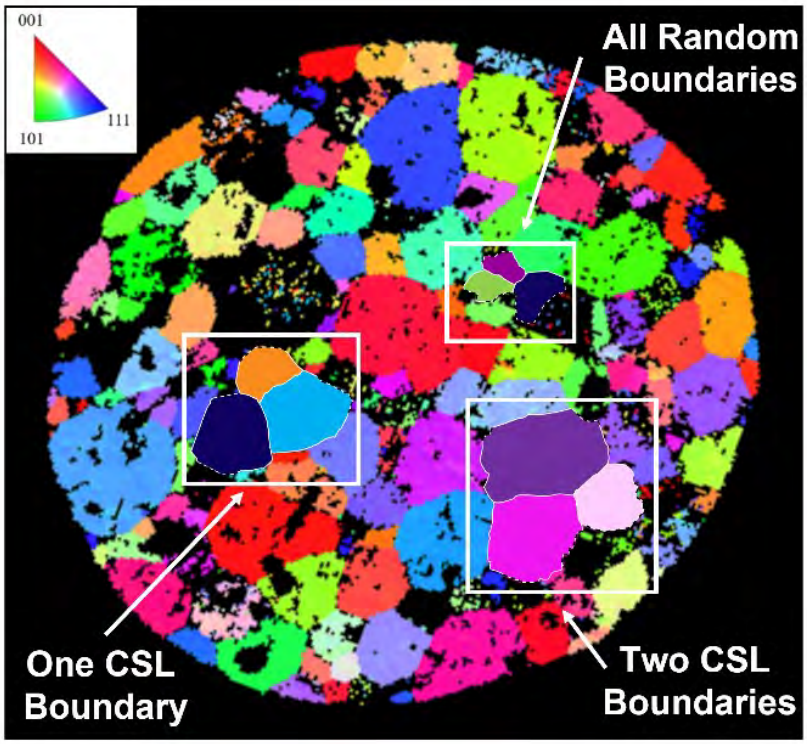

Figure 3.1: EBSD orientation map of the capacitor structure with three triple points under investigation highlighted. Also shown is the crystallographic orientation color map (top left corner).

The capacitor used in this investigation is displayed in the EBSD map in Figure 3.1. A sample tilt of 70° during SEM and EBSD measurements resulted in the circular electrode

appearing eliptical. The three triple points highlighted were selected for investigation based on having a different number of CSL vs random boundaries. The selected triple points exhibit two CSL, one CSL, and entirely random boundaries.

3.3.1 Extrinsic response near grain boundaries

The first triple point investigated corresponds to the map in Figure 3.2a with two CSL boundaries and one random boundary present. For the following analysis, the lower left grain will be referred to as fuchsia, the lower right grain as pink, and the top grain as purple, where the color was assigned based on the EBSD grain orientation. The location of the PFM scan region is the white box at the triple point of these three grains. The topography of the 5x5 μm^2 scan size is displayed in Figure 3.2b, showing a relatively smooth electrode with a few large (> 30 nm) contamination features. The BE-PFM $\alpha_d/d_{33,initial}$ map of the approximate 5x5 μm^2 region is shown in Figure 3.2c. Here, the large topographic artifacts display a piezoelectric response with a negative A3 coefficient, indicative of non-Rayleigh like behavior. Outside of the artifacts, there are distinct regions of high nonlinear response in the grains and lower responses near the grain boundaries, which are indicated by white lines in Figure 3.2c. Figure B.3 in Appendix B shows the quadratic A2 coefficient and A3 coefficient maps.

The average response vs. grain boundary position for the three grain boundaries is shown in Figure 3.2 (d-f). Figure 3.2d shows the results for the purple-fuchsia 60.9° CSL grain boundary, which displays a pinning influence that stretches 379 ± 76 nm into the purple grain and 193 ± 295 nm into the fuchsia grain for a total width of influence of 572 ± 371 nm. The thicker horizontal red dotted line represents the average $\alpha_d/d_{33,initial}$ far from the boundary, and the other two red dotted lines represent 25% of the standard deviation away from that mean; the black vertical dotted line marks the Σ17b grain boundary. The fuchsia grain has an average $\alpha_d/d_{33,initial}$ that goes through a shallow maximum of $1.4x10^{-3} \pm 0.5x10^{-4}$ cm/kV (error is 25% of the grain response standard deviation) while the purple grain has an average $\alpha_d/d_{33,initial}$ that reaches a larger

steady state value of $3.5x10^{-3} \pm 0.1x10^{-3}$ cm/kV. The vertical purple and pink lines indicate the respective pinning distances away from the grain boundary, and the distance between the colored vertical lines is labeled with the entire grain boundary width of influence.

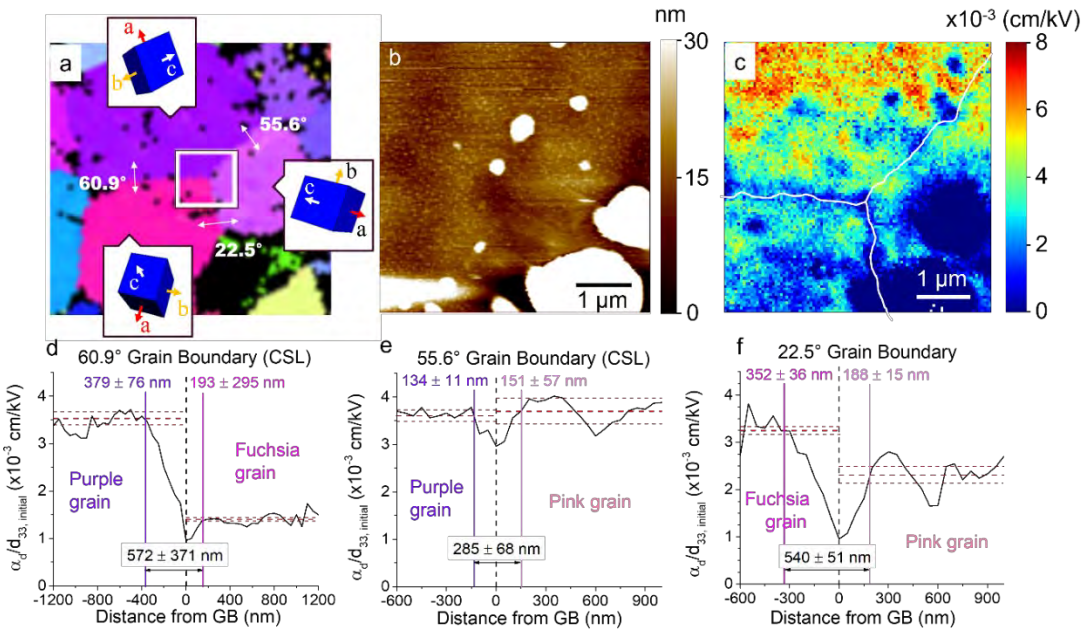

Figure 3.2: Analysis of the grain boundaries separating purple, pink, and fuchsia grains. (a) EBSD schematic of the three grains with each grain boundary misorientation angle labeled, the crystallographic orientation of each grain is shown, and approximate size of the BE-PFM scan given within the white box. (b) Contact mode AFM scan of a 5x5 μm^2 region around the triple point. (c) BE-PFM nonlinear $\alpha_d/d_{33,initial}$ Rayleigh ratio spectroscopic map showing the relative magnitude of domain wall mobility. White lines are overlaid on the grain boundary regions. (d-f) Average $\alpha_d/d_{33,initial}$ ratios with respect to grain boundary proximity for (d) fuchsia/purple 60.9° grain boundary, (e) purple/pink 55.6° grain boundary and (f) fuchsia/pink 22.5° grain boundary. The grain boundaries are marked as the center dashed black vertical lines, the thick red horizontal dashed lines represent an average $\alpha_d/d_{33,initial}$ far from the grain boundary. Thinner dashed red lines mark 25% of the standard deviation from the mean grain response, and the domain wall pinning distance into each grain, along with the total grain boundary width of influence, are labeled.

For comparison, the 55.6° boundary that separates purple and pink is a Σ3 CSL boundary, as shown in Figure 3.2e. The purple grain reaches a steady state $\alpha_d/d_{33,initial}$ value of $3.6x10^{-3} \pm 0.1x10^{-3}$ cm/kV away from this pink-purple boundary. This is similar to the average response of the purple grain away from the purple/fuschia boundary, though the local minimum of $3.0x10^{-3}$ cm/kV at the grain boundary position in purple-pink exceeds the $0.9x10^{-3}$ cm/kV minimum for

the fuchsia-purple boundary. This result suggests stronger local pinning (or a lower density of domain walls) for the Σ17b 60.9° grain boundary. The width of influence is also found to be greater for the 60.9° boundary, despite similar steady state behavior far into the grain from both grain boundaries. Steady state behavior in the purple grain for the 55.6° boundary occurs at 134 ± 11 nm from the grain boundary, compared to 379 ± 76 nm for the 60.9° grain boundary.

Considering just these two coincident site lattice boundaries, the larger degree of misorientation and deeper minima led to an increased width of influence on domain wall motion; however, as is shown in Figure 3.2f, this is not always the case. The final boundary of this triple point is the fuchsia-pink boundary, displayed in Figure 3.2f. This is a random boundary (not CSL) with a misorientation angle of 22.5°. Relatively symmetric behavior can be seen on either side of the boundary up to ~150-200 nm. Beyond this distance, neither the pink nor the fuchsia grain reached the same average $\alpha_d/d_{33,initial}$ as the CSL boundaries. While the reason for this is not fully known, it is speculated that differences in the domain structures across a grain may depend on the matching conditions across the adjacent grain boundary. It should be noted that of the three grain boundaries intersecting at this triple point, the random grain boundary demonstrated the deepest minima in $\alpha_d/d_{33,initial}$ at the grain boundary position. Random grain boundaries were found to exhibit the largest total width of influence and deepest minima in $\alpha_d/d_{33,initial}$.

A large number of topographical defects notably induced a dip in $\alpha_d/d_{33,initial}$ some 500 nm into the pink grain. Despite these points being eliminated from the averages, the $\alpha_d/d_{33,initial}$ ratios of the surrounding material may be affected; a distribution of strong pinning sites may drive variability in the average $\alpha_d/d_{33,initial}$ maps adjacent to these points.

The pinning influence of the 22.5° boundary, shown in Figure 3.2f, was estimated to stretch 352 ± 36 nm into the fuchsia grain and 188 ± 15 nm into the pink grain for a total width of influence of 540 ± 51 nm. The larger individual width of influence for both the fuchsia and pink grains were found in the random grain boundary compared to the CSL boundary. This trend of

CSL boundaries pinning less than random boundaries held true for all the investigated triple points; the largest triple point width of influence appears in the cases where more random boundaries are present. The only exception to this arises in the case of the two boundaries involved with the pink grain. The unique response of the 22.5° and 55.6° boundaries are thought to be connected to the large topological features which influenced neighboring measurements deep into the pink grain, despite the removal of affected $\alpha_d/d_{33,initial}$ data when calculating averages.

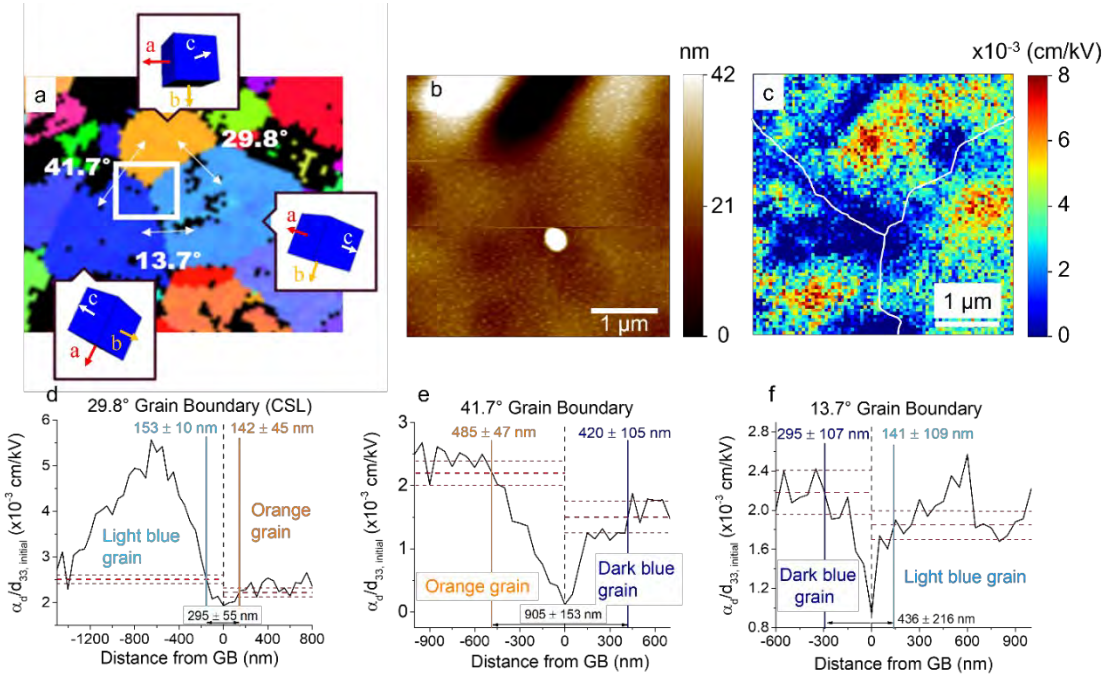

Figure 3.3: Analysis of the three grain boundaries separating the light blue, dark blue, and orange grains. (a) Schematic of the triple point. (b) Contact AFM scan of a 4x4 μm^2 region around the triple point. (c) BE-PFM Rayleigh ratio spectroscopic map of the same approximate region. (d-f) Average Rayleigh ratio $\alpha_d/d_{33,initial}$ with respect to the grain boundary position for (d) the light blue/orange 29.8° grain boundary, (e) the orange/dark blue 41.7° grain boundary, and (f) the dark blue/light blue 14.7° grain boundary.

The second triple point within this investigation contained only a single CSL grain boundary. For the orange - light blue - dark blue triple point, the CSL grain boundary was between the light blue and orange grains, displaying a misorientation angle of 29.8 ° which corresponds to a rotation around {111}. Figure 3.3a shows the EBSD schematic of all three grains

with each Euler angle and approximate grain orientation. Figure 3.3b shows the 4x4 μm^2 contact AFM scan around the triple point, and Figure 3.3c shows the local nonlinear Rayleigh ratios in the same region. Figure B.4 in Appendix B shows the individual PFM quadratic A2 and A3 coefficients. It should be noted that the 29.8° CSL boundary had both the shallowest minima and lowest width of influence for this triple point: 295 ± 55 nm, which is shown in Figure 3.3d. The largest reported influence in this investigation was 905 ± 152 nm for the random 41.7° boundary within the same triple point, shown in Figure 3.3e. The 41.7° boundary had a relatively asymmetric response. It is notable that the minimum was more than an order of magnitude different between the dark blue-orange ($\alpha_d/d_{33,initial}$ value of $0.12x10^{-3}$ cm/kV) and light blue-orange ($\alpha_d/d_{33,initial}$ value of $1.9x10^{-3}$ cm/kV) grain boundaries. Steady state was approached at 485 ± 47nm and 420 ± 105 nm into the orange and dark blue grains, respectively. The total width of influence for the dark blue-orange grain boundary was therefore 905 ± 152 nm. In some cases, random grain boundaries demonstrated a width of influence of ~ 1 μm, while the largest recorded CSL boundary influence of all the triple points was 572 ± 371 nm. The final random 13.7° boundary that separated dark blue and light blue is shown in Figure 3.3f. Like the other reported random boundaries, it was found to exhibit more symmetric $\alpha_d/d_{33,initial}$ behavior near the boundary than the adjacent CSL light blue-orange grain boundary. Similar to the purple-pink-fuchsia triple point region, the random boundaries exhibited deeper minima of $\alpha_d/d_{33,initial}$ compared to their associated CSL boundary neighbors. The light and dark blue areas reached their steady state at 141 ± 109 nm and 295 ± 107 nm into the grain, respectively, for a total width of influence of 436 ± 216 nm.

Uncovering local structural features tied to decreased pinning is also fundamental to this work; it is shown here in the case of the green-blue-pink triple point consisting of entirely random boundaries as is displayed in Figure 3.4. Despite the presence of a 45.1 ° grain boundary, shown

in Figure 3.4d, no evidence of pinning correlates with proximity to the blue-pink grain boundary. Instead, a minimum is found some 500 nm into the pink grain.

All three blue-pink-green boundaries show $\alpha_d/d_{33,initial}$ minima at the grain boundary an order of magnitude smaller than the others. Again, the individual A2 and A3 (associated with $d_{33,initial}$ and α_d, respectively) quadratic coefficients are given in Figure B.5 in Appendix B. Additionally, all three of the boundaries in this region correspond to random boundaries. This has been correlated with the deepest pinning levels of all three triple points in this investigation. It is thought that a triple point of three random boundaries may exacerbate this finding and contribute to low reported $\alpha_d/d_{33,initial}$ minima and comparatively large widths of influence. The 37.8° blue-green boundary, shown in Figure 3.4e, had the second largest total influence, at 859 ± 186 nm.

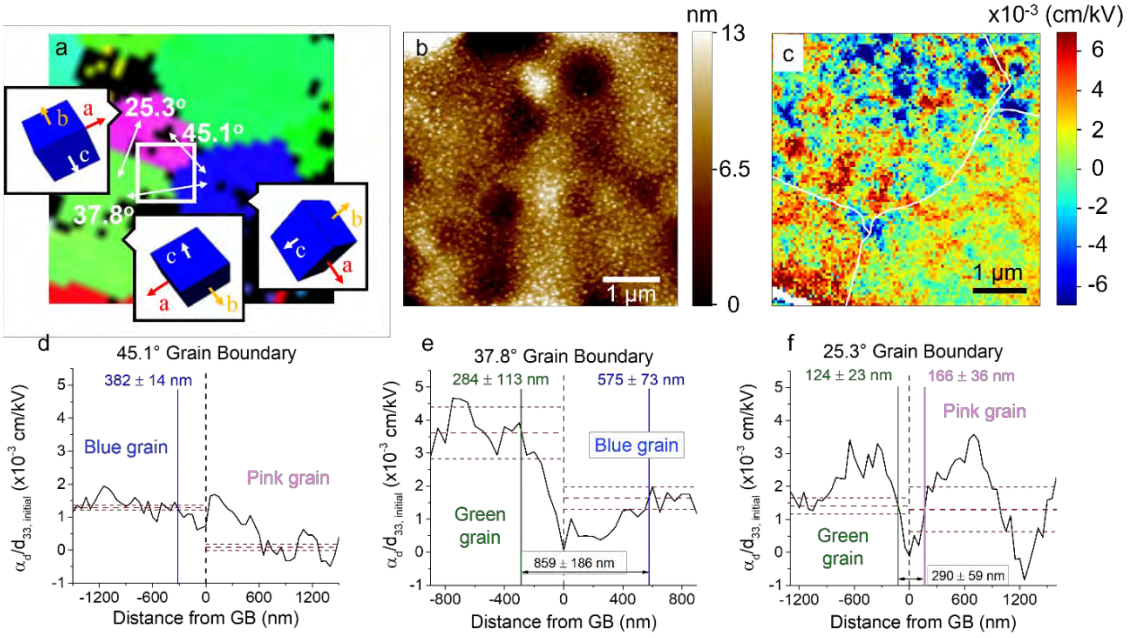

Figure 3.4: Analysis of the grain boundaries separating the blue/pink/green grains, where all were random grain boundaries. (a) The EBSD schematic (b) topographic 5x5 μm^2 contact AFM scan (c) BE-PFM spectroscopic Rayleigh coefficient ratios and (d-f) the average Rayleigh ratio $\alpha_d/d_{33,initial}$ with respect to grain boundary position for the (d) 45.1° blue/pink grain boundary, (e) 37.8° green/blue grain boundary, and (f) 25.3° green/pink grain boundary.

The random 25.3° boundary was the only investigated boundary that showed a negative value for $\alpha_d/d_{33,initial}$, as seen in Figure 3.4f. The negative $\alpha_d/d_{33,initial}$ at position zero suggests a

non-Rayleigh behavior that could be the result of a non-uniform distribution of restoring forces due to either an anomalously strong pinning site or the absence of domain walls. Assessing whether this difference is correlated with comparatively smaller $SrTiO_3$ grain areas is of interest in future work. Grain sizes were 45 μm^2, 138 μm^2, and 83 μm^2 for pink, green and blue areas, respectively. Figure 3.4 (d-f) shows the pinning distances and width of influence values for the green-blue-pink triple point. Table 3.1 summarizes the grain boundary angle, width of influence and $\alpha_d/d_{33,initial}$ response at the grain boundary for all nine boundaries in this investigation.

Table 3.1: Grain boundary (g.b.) angle, total width of influence, and $\alpha_d/d_{33,initial}$ nonlinearity response at the grain boundary for all nine grains boundaries.

	CSL Grain Boundary			**Random Grain Boundary**					
g.b. angle (°)	60.9	55.6	29.8	22.5	41.7	13.7	45.1	37.8	25.3
Width of influence (nm)	572 ± 371	285 ± 68	298 ± 55	540 ± 51	905 ± 153	436 ± 216	-	859 ± 186	290 ± 59
$\alpha_d/d_{33,initial}$ at g.b. ($x10^{-3}$ cm/kV)	0.96	2.96	1.93	0.95	0.12	0.94	0.74	0.06	-0.15

3.3.2 Extrinsic response near triple points

Next, the circular width of influence at each triple point location was studied. It should be noted that the triple 'point' denoted here is perhaps better described as a triple 'line'; just as the grain boundaries grew perpendicular to the substrate surface, so did the triple points. The radius from the triple point was used as a guideline, and the points at each concentric perimeter were averaged. An example of a circular radius of influence is shown in Figure 3.5a for the purple/pink/fuchsia triple point. The BE-PFM nonlinear Rayleigh ratio map is overlain with the grain boundary locations and the approximate radius of influence as a concentric circle around the triple point in white. The radius of influence was determined from data in Figure 3.5b. It was found that triple points typically serve as deep pinning sites, for which irreversible domain wall motion can be degraded hundreds of nm away on any side of the triple point. At the triple points, the nonlinear piezoelectric response was often non-Rayleigh-like in character, suggesting that the

domain walls locally experience a non-Gaussian set of restoring forces or that there are few domain walls at the triple point [23]. The average distance of non-Rayleigh behavior was 220 ± 170 nm in any direction across all investigated triple points; it increased as the number of random grain boundaries increased.

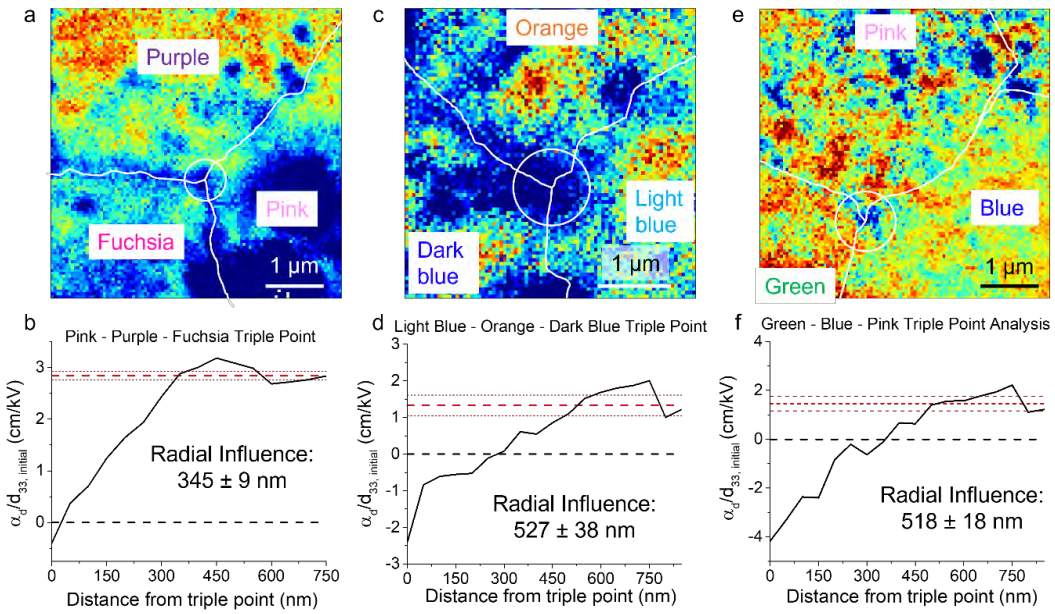

Figure 3.5: (a) BE-PFM spectroscopic map of $\alpha_d/d_{33,initial}$ Rayleigh ratios for the Purple/Pink/Fuchsia triple point. In white are the grain boundaries and circular width of influence around the triple point with a radius of 345 ± 9 nm. (b) Rayleigh ratio as a function of the distance away from the triple point in the pink-purple-fuchsia triple point. (c) Light blue-orange-dark blue $\alpha_d/d_{33,initial}$ spectroscopic map with the 527 ± 38 nm radial influence shown and (d) corresponding Rayleigh ratio vs. distance from the triple point. (e) Green-blue-pink triple point spectroscopic map with 518 ± 18 nm radial influence and (f) Rayleigh ratio vs. distance from triple point. The horizontal black lines in (b,d,f) represent the point where $\alpha_d/d_{33,initial}$ becomes positive with respect to the distance. Horizontal red lines represent the mean and 25% of the standard deviation from the mean.

It was found that triple points with a larger number of random boundaries corresponded to deeper minima in $\alpha_d/d_{33,initial}$ and greater distances of non-Rayleigh like behavior. The Pink-Purple-Fuchsia triple point shown in Figure 3.5 (a,b) had two CSL boundaries. This led to the smallest area of non-Rayleigh behavior and the shallowest minima of the interrogated triple points. Non-Rayleigh behavior was observed for the first 24 nm from the triple point and a radius of influence of 345 ± 9 nm was found. The triple point with one identified CSL boundary is

shown in Figure 3.5 (c,d); an increased area of non-Rayleigh behavior and deeper minima was observed. Non-Rayleigh behavior was seen up to 279 nm from the triple point and the largest radius of influence of 527 ± 38 nm from the triple point was recorded. This large width of influence is reasonable given the pinning demonstrated by the strongly negative $\alpha_d/d_{33,initial}$ minima. The final triple point, displayed in Figure 3.5 (e,f), had no identified CSL boundaries; it showed the lowest recorded $\alpha_d/d_{33,initial}$ minima and the largest area of non-Rayleigh behavior, which was 370 nm. A radius of influence of 518 ± 18 nm from the triple point was determined. The -4.0×10^{-3} cm/kV minima and large distance of non-Rayleigh behavior suggest that increased pinning from random grain boundaries drove a non-Gaussian set of restoring forces or the absence of domain walls further into the grains.

3.4 Conclusions

The influence of assorted grain boundaries and triple points on the motion of domain walls was studied in $PbZr_{0.52}Ti_{0.48}O_3$ films. It was found that the character of the grain boundary affected the way in which domain walls moved. In particular, coincident site lattice grain boundaries exhibited shallower minima in $\alpha_d/d_{33,initial}$ than was observed for random grain boundaries. It is speculated that regularity in the crystalline arrangement of the two grains may facilitate collective domain wall movement between grains. In contrast, a triple point with three random boundaries exacerbated pinning and contributed to low $\alpha_d/d_{33,initial}$ minima. The width of influence on domain wall motion scaled better with the difference between the minima and the steady state $\alpha_d/d_{33,initial}$ than it did with the value of $\alpha_d/d_{33,initial}$ at the grain boundary. That is, wider widths of influence were observed with larger differences between the minima and the steady state $\alpha_d/d_{33,initial}$. Different grain boundaries influenced the mobility of domain walls on length scales from 124 ± 23 nm to 905 ± 153 nm normal to their respective grain boundary. The largest

width of influence (905 ± 153 nm) occurred near a random boundary in the triple point region with one CSL boundary, while the largest recorded width of influence for a CSL boundary was 572 nm. Further studies in static domain structures around random and CSL boundaries with different shared rotation axes is of interest.

This study also provides the first quantitative measurements of the effects of triple points on the motion of domain walls. It was found that immediately adjacent to the triple points, a region of material which did not show Rayleigh-like characteristics was observed, i.e. $\alpha_d/d_{33,initial}$ was negative. This could be a result of either a non-Gaussian distribution of restoring forces (perhaps due to very strong pinning associated with the triple point itself) and/or a reduction in the number of domain walls at the triple point. At larger diameters, a region of material with suppressed (but positive) $\alpha_d/d_{33,initial}$ was observed, before the material reached steady state at still longer distances. As the number of random boundaries within a given triple point is increased, the distance from the triple point where Rayleigh-like behavior occurs increased and the radial influence of the triple point on domain wall motion also increased.

3.5 References

[1] A. Pramanick, D. Damjanovic, J.E. Daniels, J.C. Nino, J.L. Jones, Origins of electro-mechanical coupling in polycrystalline ferroelectrics during subcoercive electrical loading, J. Am. Ceram. Soc. 94 (2011) 293–309. https://doi.org/10.1111/j.1551-2916.2010.04240.x.

[2] D.A. Hall, Nonlinearity in piezoelectric ceramics, J. Mater. Sci. 36 (2001) 4575–4601.

[3] Q.M. Zhang, H. Wang, N. Kim, L.E. Cross, Direct evaluation of domain-wall and intrinsic contributions to the dielectric and piezoelectric response and their temperature dependence on lead zirconate-titanate ceramics, J. Appl. Phys. 75 (1994) 454–459.

https://doi.org/10.1063/1.355874.

[4] D. Damjanovic, M. Demartin, The Rayleigh law in piezoelectric ceramics, J. Phys. D. Appl. Phys. 29 (1996) 2057–2060. https://doi.org/10.1088/0022-3727/29/7/046.

[5] N. Bassiri-Gharb, I. Fujii, E. Hong, S. Trolier-McKinstry, D. V. Taylor, D. Damjanovic, Domain wall contributions to the properties of piezoelectric thin films, J. Electroceramics. 19 (2007) 47–65. https://doi.org/10.1007/s10832-007-9001-1.

[6] C.A. Randall, N. Kim, J.P. Kucera, W. Cao, T.R. Shrout, Intrinsic and extrinsic size effects in fine-grained morphotropic-phase-boundary lead zirconate titanate ceramics, J. Am. Ceram. Soc. 81 (1998) 677–688. https://doi.org/10.1111/j.1151-2916.1998.tb02389.x.

[7] F. Griggio, S. Trolier-McKinstry, Grain size dependence of properties in lead nickel niobate-lead zirconate titanate films, J. Appl. Phys. 107 (2010). https://doi.org/10.1063/1.3284945.

[8] W. Cao, C.A. Randall, Grain size and domain size relations in bulk ceramic ferroelectric materials, J. Phys. Chem. Solids. 57 (1996) 1499–1505. https://doi.org/10.1016/0022-3697(96)00019-4.

[9] G. Arlt, The influence of microstructure on the properties of ferroelectric ceramics, Ferroelectrics. 104 (1990) 217–227. https://doi.org/10.1080/00150199008223825.

[10] A. Gruverman, O. Auciello, H. Tokumoto, Nanoscale investigation of fatigue effects in $Pb(Zr,Ti)O_3$ films, Appl. Phys. Lett. 69 (1996) 3191–3193. https://doi.org/10.1063/1.117957.

[11] S. Choudhury, Y.L. Li, C. Krill, L.Q. Chen, Effect of grain orientation and grain size on ferroelectric domain switching and evolution: Phase field simulations, Acta Mater. 55 (2007) 1415–1426. https://doi.org/10.1016/j.actamat.2006.09.048.

[12] D.M. Marincel, H.R. Zhang, J. Britson, A. Belianinov, S. Jesse, S. V. Kalinin, L.Q. Chen,

W.M. Rainforth, I.M. Reaney, C.A. Randall, S. Trolier-McKinstry, Domain pinning near a single-grain boundary in tetragonal and rhombohedral lead zirconate titanate films, Phys. Rev. B - Condens. Matter Mater. Phys. 91 (2015) 1–12. https://doi.org/10.1103/PhysRevB.91.134113.

[13] D.M. Marincel, H. Zhang, S. Jesse, A. Belianinov, M.B. Okatan, S. V. Kalinin, W.M. Rainforth, I.M. Reaney, C.A. Randall, S. Trolier-McKinstry, Domain wall motion across various grain boundaries in ferroelectric thin films, J. Am. Ceram. Soc. 98 (2015) 1848–1857. https://doi.org/10.1111/jace.13535.

[14] S. Tsurekawa, K. Ibaraki, K. Kawahara, T. Watanabe, The continuity of ferroelectric domains at grain boundaries in lead zirconate titanate, Scr. Mater. 56 (2007) 577–580. https://doi.org/10.1016/j.scriptamat.2006.12.029.

[15] S. Mantri, J. Oddershede, D. Damjanovic, J.E. Daniels, Ferroelectric domain continuity over grain boundaries, Acta Mater. 128 (2017) 400–405. https://doi.org/10.1016/j.actamat.2017.01.065.

[16] J. Fousek, Permissible domain walls in ferroelectric species, Czechoslov. J. Phys. B. 21 (1971) 955–968.

[17] J. Sapriel, Domain-wall orientations in ferroelastics, Phys. Rev. B. 12 (1975) 5128–5140.

[18] T.M. Borman, {001} Textured growth of doped, gradient free, lead zirconate titanate thin films by chemical solution deposition, The Pennsylvania State University, 2016.

[19] W. Zhu, I. Fujii, W. Ren, S. Trolier-McKinstry, Domain wall motion in A and B site donor-doped $Pb(Zr_{0.52}Ti_{0.48})O_3$ films, J. Am. Ceram. Soc. 95 (2012) 2906–2913. https://doi.org/10.1111/j.1551-2916.2012.05243.x.

[20] S. Jesse, S. V. Kalinin, R. Proksch, A.P. Baddorf, B.J. Rodriguez, The band excitation method in scanning probe microscopy for rapid mapping of energy dissipation on the nanoscale, Nanotechnology. 18 (2007). https://doi.org/10.1088/0957-4484/18/43/435503.

[21] P. Bintachitt, S. Jesse, D. Damjanovic, Y. Han, I.M. Reaney, S. Trolier-McKinstry, S. V. Kalinin, Collective dynamics underpins Rayleigh behavior in disordered polycrystalline ferroelectrics, Proc. Natl. Acad. Sci. U. S. A. 107 (2010) 7219–7224. https://doi.org/10.1073/pnas.0913172107.

[22] F. Griggio, S. Jesse, A. Kumar, D.M. Marincel, D.S. Tinberg, S. V. Kalinin, S. Trolier-McKinstry, Mapping piezoelectric nonlinearity in the Rayleigh regime using band excitation piezoresponse force microscopy, Appl. Phys. Lett. 98 (2011) 98–101. https://doi.org/10.1063/1.3593138.

[23] T. O'Reilly, K. Holsgrove, A. Gholinia, D. Woodruff, A. Bell, J. Huber, M. Arredondo, Exploring domain continuity across $BaTiO_3$ grain boundaries: Theory meets experiment., Acta Mater. 235 (2022) 118096. https://doi.org/10.1016/j.actamat.2022.118096.

CHAPTER 4

Thermal stress accommodation in dip cast lead zirconate-titanate ferroelectric films on flexible substrates

Chapter 4 of this thesis has been previously published as: Peters T, Cheng C, Rossetti GA, Trolier-McKinstry S. Thermal stress accommodation in dip cast lead zirconate-titanate ferroelectric films on flexible substrates. J Am Ceram Soc. 2022;1-13. https://doi.org/10.1111/jace.18355

4.1 Introduction

Piezoelectric microelectromechanical systems (MEMS) on flexible metal foils enable an array of applications not possible with stiff substrates, such as robust energy harvesters exposed to high strains [1–5], ambulatory sensing [6–9], and biomedical monitoring [5, 10, 11]. Lead zirconate titanate (PZT) films on metal foils provide an alternative to PVDF when higher piezoelectric coefficients are needed. In particular, niobium-doped lead zirconate titanate [$Pb_{0.99}\blacksquare_{0.01}(Zr_{0.52}Ti_{0.48})Nb_{0.02}O_3$] has considerable commercial relevance due to its high piezoelectric coefficient, dielectric constant, and remanent polarization values (where ■ denotes a vacancy on the Pb site).

Chemical solution deposition (CSD) is often used to deposit high quality piezoelectric thin films on flexible substrates, via spin coating, dip coating, microcontact printing [12], or ink jet printing [13, 14]. The spin coating enables excellent uniformity of film thickness on flat, circular substrates [15]. Complications arise in the spin coating process however, when substrates are non-circular, flexible, and/or have non-planar surface topography. In the case of flexible foils susceptible to plastic deformation, the vacuum hold during spin coating can produce a permanent dimple in the substrate, rendering the center unusable. Additionally, a large fraction of excess

precursor is spun off the wafer and wasted during mass production via spin coating [15]. In dip coat CSD, a substrate is withdrawn vertically from a solution reservoir at a constant speed. The moving substrate entraps the liquid in a fluid mechanical boundary layer that splits into two layers above the liquid bath and returns the outer layer to the bath [15]. Depositions can be conducted simultaneously on both foil surfaces, avoiding unbalanced stress that induces bending of the foils associated with single side deposition [16]. Dip coating also simplifies production of bimorphs and conserves precursor solution. Takahashi et al. reported on the dip coating of piezoelectric thin films onto stiff substrates such as glass, platinum, and single-crystal plates [17, 18]. He et al. investigated the effects of solution ionic concentration, substrate roughness, and withdrawal speed on the resulting films' crystalline structure, single layer thickness, and electrical properties [19]. Hida et al. investigated the dielectric and piezoelectric properties of bimorphs with high flexibility produced by dip-coating PZT films onto flexible stainless steel metal foils [20]. Dip coating of a humidity-insensitive chemical solution was selected for this work, as it will allow for mass manufacture of high-quality piezoelectric films on flexible or oddly shaped substrates that are not amenable to spin coating, for example, cylinders, rods, pyramids or flexible foils.

It is well-established that the substrate coefficient of thermal expansion has a strong influence on the domain state of thick PZT films [21–25]. Upon cooling PZT films from the crystallization temperature, domains form to minimize elastic or electrical energy and release stress buildup between the film and substrate. The volume fraction of the domains depends on the magnitude of the substrate coefficient of thermal expansion (CTE), specifically at and above the Curie temperature (T_c) [21]. If the substrate CTE is smaller than that of the piezoelectric film, the film will be placed under tensile stress upon cooling and preferentially align domains in-plane, since the unit cell of many of the ferroelectric perovskites elongates parallel to the polarization direction [21, 22]. Conversely, if the substrate CTE exceeds that of the ferroelectric film, domains align out-of-plane. Assuming that the film is strain-free at the crystallization temperature, the

resulting thin film in-plane biaxial stress is a function of film (f) and substrate (s) coefficient of thermal expansion (α_{CTE}), elastic modulus (Y), thickness (t), and Poisson's ratio (ν). The residual stress is approximated with Equation 4.1 [26]. As described by the Funakubo group [24, 25], in cases where the substrate CTE exceeds the film CTE, the out-of-plane domain volume fraction increases, where PZT at the morphotropic phase boundary has a lower dielectric relative permittivity with a higher remanent polarization along the polar direction [27]. Specifically, the dielectric relative permittivity for a single domain oriented parallel to the film surface is approximately 1721 at room temperature; for a domain oriented perpendicular to the surface it is 382 [27].

$$\sigma_t = \frac{\int_{T_c}^{T_{max}} (\alpha_{CTE,f} - \alpha_{CTE,s}) dT}{\left(\frac{1-\nu_f}{Y_f}\right) + \left(\frac{1-\nu_s}{Y_s}\right) * \left(4\frac{t_f}{t_s}\right)} \qquad \text{Equation 4.1}$$

In addition to the substrate coefficient of thermal expansion, substrate thickness is hypothesized to influence stress relief during PZT film cooling. Thick, rigid substrates both apply stresses to the ferroelectric film and resist the electromechanical deformation associated with application of electric fields. This acts to clamp both the intrinsic and the extrinsic contributions to the piezoelectric properties. Griggio et al. showed that the most significant factors reducing the irreversible motion of domain walls in PZT films on Si is a combination of residual stress and substrate rigidity [28]. They attributed a large increase in irreversible domain wall motion of a released PZT film to partial release of the residual in-plane tensile stress developed from CTE mismatch, compared to the clamped film [28]. Residual stresses are known to mechanically suppress domain mobility or domain wall motion, and the release of a film from a rigid substrate will enhance domain mobility during the poling process [28].

Rayleigh analysis is utilized to investigate the contributions of reversible and irreversible domain response to electrical properties. Equation 4.2 describes the linear dependence of relative dielectric permittivity on the electric field, where ε_r is relative dielectric permittivity, $\varepsilon_{initial}$ is the

reversible dielectric Rayleigh coefficient, α_ε is the irreversible Rayleigh coefficient, and E_0 is the electric driving field. Reversible extrinsic contributions and intrinsic contributions are characterized by $\varepsilon_{initial}$, whereas α_ε describes irreversible motion of interfaces such as domain walls or phase boundaries [28]. If a large enough field is applied to a piezoelectric film, domain wall motion can switch from pinned reversible oscillation to depinning.

$$\varepsilon_r = \varepsilon_{initial} + \alpha_\varepsilon E_0 \qquad \text{Equation 4.2}$$

One factor that has not been widely discussed in the literature is the interplay between substrate clamping and residual stresses in controlling the dielectric and ferroelectric thin film properties. Of particular interest is whether stresses can be relieved through substrate bending in a way that influences the resulting behavior. Here, the adopted approach is to hold the substrate coefficient of thermal expansion (CTE) constant while varying the substrate thickness, and hence its bending rigidity. Several metal foils with different thermal expansion coefficients but constant thicknesses were also explored. Rayleigh analysis was then used in conjunction with other electrical characterization techniques to assess the dependence of domain clamping and motion on film residual stress. For this purpose, a humidity insensitive acetic acid-based PZT solution was developed and deposited onto substrates of various thicknesses and CTE via dip coating. A thickness of 2 μm PZT was deposited on all substrates. It is demonstrated that the flexibility of the substrate can have a higher effect on the film domain structure than the thermal expansion coefficient mismatch with the substrate.

4.2 Experimental procedure

Figure 4.1 displays the coefficient of thermal expansion of PZT and the substrate materials selected in this study, which are silicon, platinum, nickel, and silver, from room temperature to the PZT crystallization temperature of 923K. Table 4.1 illustrates the calculated

stresses from Equation 4.1 for PZT on five different substrates, where the CTE integration was from the PZT T_c to the T_{max} used in this study, which was 650ºC. To explore the effect of substrate thickness, 25 µm thick Ni foil was compared to a Ni plate of 500 µm in thickness. Throughout the balance of the paper, the substrates will be referred to by the composition and thickness, such that Ni-500 denotes a 500 µm thick Ni substrate.

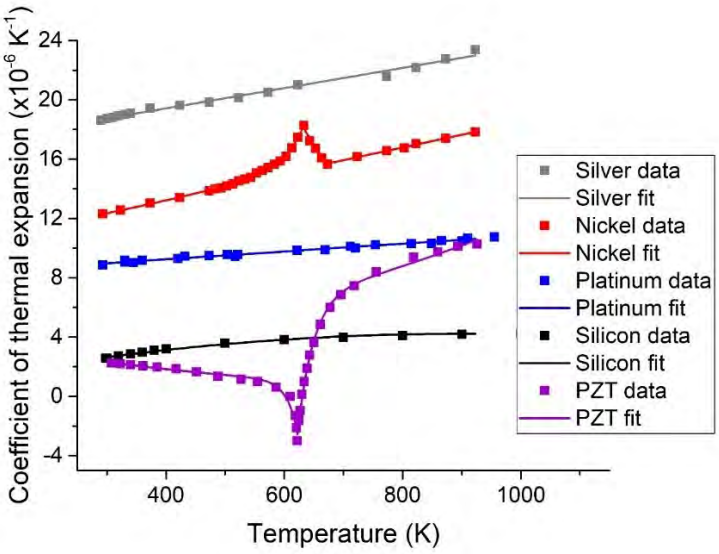

Figure 4.1: Coefficient of thermal expansion (CTE) for lead zirconate titanate (PZT), silicon, platinum, nickel, and silver from room temperature to PZT crystallization temperature. Data extracted from [29] for Si, [30] for Pt, Ni, and Ag, and [31] for PZT.

Table 4.1: Thermal stress calculated for 2 µm lead zirconate titanate (PZT) deposited on substrates of varying CTE and thickness following Equation 4. 1.

	PZT on Si-500	PZT on Pt-25	PZT on Ni-25	PZT on Ni-500	PZT on Ag-25
Thermal Stress	158 MPa	-102 MPa	-342 MPa	-368 MPa	-529 MPa

4.2.1 Sample Preparation

Three thin metal foils, one thick metal plate, and a platinized silicon wafer (all 25 mm x 25 mm) were selected as substrates according to their coefficient of thermal expansion, resistance

to oxidation, and thickness. Table 4.2 displays the five substrates with their thickness, purity, Young's modulus (E), CTE, and manufacturer selected for this study. The calculated thermal stress values displayed in Table 4.1 used a PZT Young's modulus of 90 GPa[32] and a Poisson's ratio of 0.38, extracted from the work of Cook et al.[31]. The three 25 μm foils and 500 μm Ni plate were polished on both surfaces with an ALLIED High Tech Products MetPrep automatic polishing tool, as shown in Table C.1 in Appendix C. To remove the ambient surface oxide formed on the Ni substrates, they were annealed in an H_2/N_2 reducing gas atmosphere at 900ºC for 1 hour. An insignificant amount of surface oxide was verified on all four metal substrates using a Woolam M2000X spectroscopic ellipsometer. The four metal substrates were blanket coated with 50 nm amorphous HfO_2 via atomic layer deposition (Lesker ALD System 150LE) at 200ºC (515 cycles). The chemical precursor for Hf was Tetrakis (Dimethylamido) Hafnium ($Hf(NMe_2)_4$) and the oxidant used was H_2O. To provide a consistent bottom electrode for each substrate, 30 nm Ti was sputtered at room temperature as an adhesion layer followed by 100 nm platinum sputter deposited at 550ºC onto both sides of the substrates. The substrate mounting plate is shown in Figure C.1 of Appendix C. The silicon wafer used in this study was double-side polished 500 μm thick P-type Si <100> oriented with 300 nm SiO_2 wet thermal oxide, 10 nm sputtered Ti, and 150 nm sputtered Pt oriented (111). A PZT (20% excess Pb, 44/56 Zr/Ti ratio, 2% Nb) sol-gel Mitsubishi seed solution was spin coated at 3500 rpm for 45 seconds, pyrolyzed at 200ºC for 2.5 minutes on a hotplate, and annealed at 700ºC for 1 minute in a rapid thermal annealer (RTA) with 2 SLPM O_2 gas flow. This seed layer was deposited to attempt to preferentially orient the dip coated PZT layers along the {100} axis.

Table 4.2: Substrate properties. The coefficients of thermal expansion are given at 624 K, the Curie temperature of lead zirconate titanate (PZT) films used in the study.

Substrate	Thickness (µm)	Purity	E (GPa)	Poisson's ratio	CTE at 624 K (ppm/K)	Supplier
Silver (Ag)	25	99.9%	80.0 (annealed)	0.37	21.0	Sigma-Aldrich
Nickel (Ni)	25	99.98%	196 (annealed)	0.32	17.5	Hpulcas
Nickel (Ni)	500	99.98%	196 (annealed)	0.32	17.5	Sigma-Aldrich
Platinum (Pt)	25	99.99%	170 (annealed)	0.44	9.8	Alfa Aesar Premion
Silicon (Si)	500	1-10 Ω cm		0.278	3.9	KO Tech

4.2.2 Solution chemistry

An inverted mixing order (IMO) solution preparation procedure was adapted from Olding et al. to reduce the humidity sensitivity of the solution relative to 2-methoxyethanol based routes [33]. An acetic acid-based PZT (52/48) solution with 2% niobium dopant was prepared following the procedure outlined in Table C.2 in Appendix C. Precursors for zirconium (Zirconium (IV) butoxide solution (80 wt. % in 1-butanol)), titanium (Titanium (IV) butoxide (>97% gravimetric)), niobium (Niobium n-butoxide), lead (Lead(II) acetate trihydrate), and glacial acetic acid were purchased from Sigma-Aldrich. An excess of 14 mol% Pb was added to minimize non-ferroelectric pyrochlore (or fluorite) formation during crystallization. A molarity of 0.6 was found to enable a uniform film thickness during dip coat deposition.

4.2.3 Sol gel dip coat deposition

Dip coating was conducted using a home-built apparatus pictured in Figure C.2 of Appendix C. The dip and withdrawal rates were controlled with an automated user interface panel. The system was installed in a low-humidity (20% relative humidity) class 1000 cleanroom. Each substrate was dipped and withdrawn at either 30 or 40 mm/min rate and held in the solution bath for 1 second. The film was dried at 250°C for 30 seconds, pyrolyzed on a hotplate at 400°C

for 1 minute, then heated in an RTA at a rate of 6.25ºC/s to 650ºC and held for 2 minutes using a flow of 2 SLPM O_2 gas to crystallize the film. The RTA script is displayed in Table C.3 in Appendix C. The procedure was repeated 18-20 times to reach a film thickness of 2 μm on both surfaces of all five substrates.

4.2.4 Crystallographic and microstructure characterization

A Zeiss Merlin field emission scanning electron microscope (FESEM) equipped with a Gemini II column was utilized to image the surface of all five PZT films and the cross section of PZT on Si-500. An operating voltage of 5 kV was used with a working distance of 5 mm and an in-lens secondary electron detector. Analysis included verifying film density, pyrochlore content, cracking, and relative grain size. X-ray diffraction was performed with a Malvern Panalytical Empyrean III with a generator voltage of 45 V and a tube current of 40 A in two modes: Bragg-Brentano with a scan range of 10º to 70º and a scanning rate of 0.0673º/s, and grazing incidence with a scan range of 42º to 48º, a scanning rate of 0.0026º/s, and an incident angle of 1º. Bragg-Brentano allowed for overall film orientation and minor substrate peak analysis while the grazing incidence mode probed near the surface of the sample in the 2θ range of the (002)/(200) peaks.

4.2.5 Electrical characterization

Circular electrodes ranging from 200 to 1000 μm in diameter were patterned via a standard photolithographic spin, expose, develop process, followed by 100 nm platinum sputter deposition and a photoresist liftoff process. A post anneal was performed at 600ºC for 1 minute in 2 SLPM O_2 gas flow in an RTA to improve adhesion between the PZT and Pt electrodes. Prior to dielectric frequency sweeps and ferroelectric measurements, the capacitance and loss of 15-20 electroded structures on each sample were measured at 1 kHz with 30 mV AC voltage. The capacitance varied between electrodes on each sample due to thickness variation of the film, with the edge having larger PZT thicknesses than the center (<300 nm difference). Loss values ranged from 0.02 to 0.10. A Nanometrics Nanospec Thin Film Thickness System was utilized to search

for capacitor structures that had a thickness closest to 2 μm (± 0.05 μm). Capacitors with this thickness range and electrode diameter between 400 μm and 1000 μm varied in dielectric permittivity less than 1.5%. Additionally, capacitors with the same shape and size displayed a variation of 8.1% in remanent polarization, 3.3% in coercive field, and 1.0% in maximum polarization. For dielectric and ferroelectric data published in this report, a single representative electrode was measured for each sample.

Dielectric permittivity and loss tangent were measured 30 minutes after the post-anneal with an HP 4284A Precision LCR Meter in the range of 100 Hz – 100 kHz with 30 mV applied AC voltage. Rayleigh coefficients were established by applying an electric field in the range of 0 to 12.5 kV/cm and measuring the dielectric permittivity with the same instrument. Linear least-square fitting was performed on Rayleigh data at 100, 200, 500, and 1000 Hz for each sample in the electric field range of 2.5 to 7.5 kV/cm. The reversible and irreversible domain wall motion contributions were extracted from the linear fit with Equation 4.2. Polarization-electric field (P–E) hysteresis loops were measured with a Radiant Technologies Precision Multiferroic tester from -600 to +600kV/cm. Poling was performed on the electrodes at 5x the measured coercive field (~35V) at 150^{o}C for 30 minutes in the poled-up direction (where voltage was applied to the bottom electrode), then allowed to cool to room temperature for 1 hour. Dielectric permittivity/loss tangents and Rayleigh coefficients were measured after the poling procedure.

4.3 Results and discussion

4.3.1 Structural analysis

Bragg-Brentano X-ray diffraction data are plotted in Figure 4.2 for PZT films deposited on all five substrates. The (100)/(001) peaks are clearly visible; their relative intensities depend on orientation of the hot sputtered platinum and PZT Mitsubishi seed layer. XRD scans for PZT

on Ni display NiO peaks from residual oxidation of the substrate, while all substrates except Si show small HfO_2 passivation layer peaks. All five PZT films show partial (100)/(001) orientation, while PZT on Si displays a high intensity (111) peak. Figure C.3 in Appendix C contains a Bragg-Brentano XRD plot showing the variation in platinum (111) intensity between the platinum coated Si wafer (100% volume fraction) and the hot sputtered platinum on Ni-25 substrate (85.17% volume fraction). Similarly, Brennecka et al. reported the formation of a Pt_3Ti intermetallic layer below the PZT film prepared using the inverted mixing order process; this promoted (111) PZT growth [34]. Figure 4.3 displays grazing incidence x-ray diffraction data near the PZT 200/002 peak.

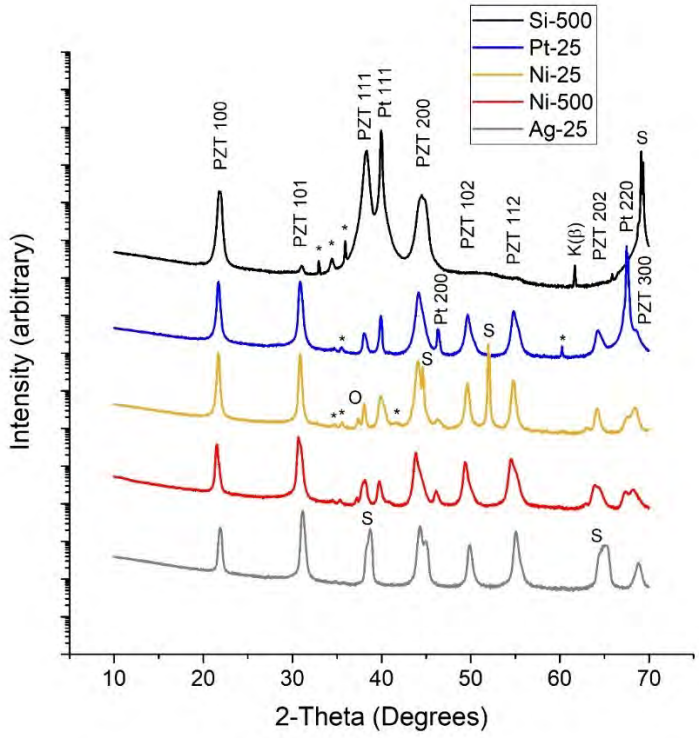

Figure 4.2: Bragg-Brentano X-ray diffraction (XRD) analysis of 2 μm lead zirconate titanate (PZT) on all five substrates. Labeled in the figure is S for substrate, O for NiO, and * for HfO_2. The ICDD inorganics database pdf file for PZT (52/48) [01-070-4060] was utilized as the reference.

Background intensity was subtracted from the observed data and LIPRAS[35] was used to fit each peak with an asymmetric pseudo-Voigt function, holding peak breadth as the constraint. LIPRAS provided each peak's constrained full width half maximum (FWHM, f), 2θ at maximum peak intensity (x#), asymmetry (a#), and intensity of each peak (N#), where # indicates the peak number in each fit. The peak profile coefficients and their errors are given in Table C.4 in Appendix C, as well as the overall R^2 value and root-mean-square deviation (rmse). A Matlab script was written to calculate the integrated intensity from peak fitting parameters, which is given at the end of Appendix C.

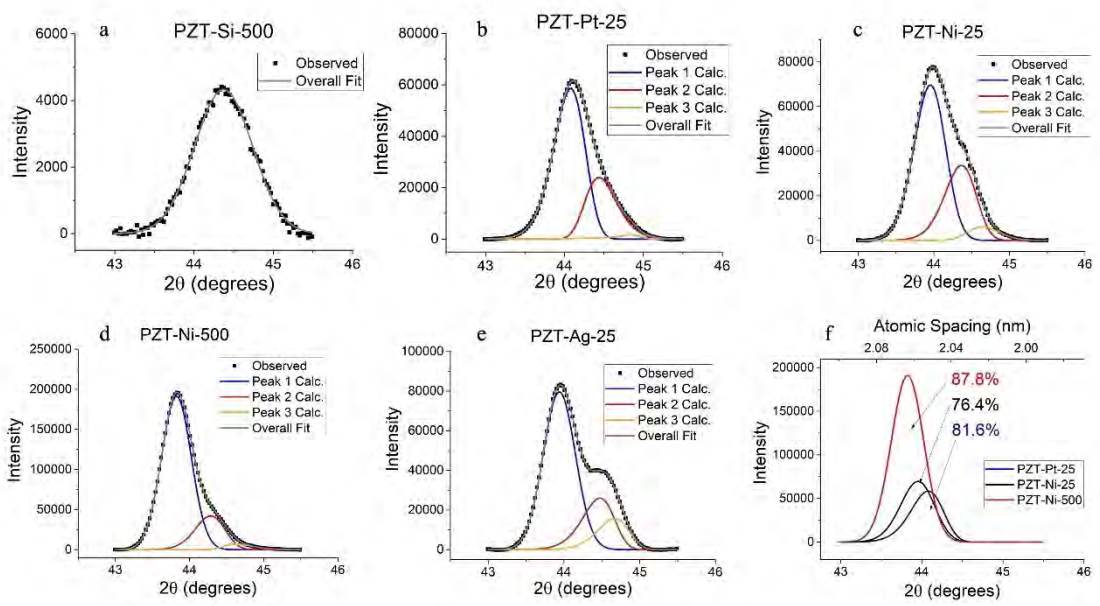

Figure 4.3: Grazing incidence x-ray diffraction (XRD) near the 200/002 lead zirconate titanate (PZT) peaks on all five substrates: (a) PZT-Si-500, (b) PZT-Pt-25, (c) PZT-Ni-25, (d) PZT-Ni-500, (e) PZT-Ag-25, and (f) LIPRAS (002) peak (peak 1) fit for PZT-Pt-25, PZT-Ni-25, and PZT-Ni-500. The labels show the volume fraction of tetragonal (002) domains to the total integrated intensity, calculated with Equation 4. 3.

A single discernable peak was found for PZT on Si, and the calculated FWHM was 0.863 ± 0.013°. This FWHM value was significantly larger than all other peaks for PZT on metal substrates, for which the FWHM were all 0.486 ± 0.013°. Due to the tensile stress in the PZT film on cooling through T_c, it is inferred that the film on Si had a higher volume fraction of in

plane domains rather than out of plane. Peak splitting is observed for PZT on the other four substrates, as illustrated in Figure 4.3 (b-e). In each figure, the black data points are the observed data, the blue curve fits the tetragonal (002) peak, the red curve fits the (024) rhombohedral peak, the orange curve fits the tetragonal (200) peak, and the grey curve shows the overall fit. The (002) peak intensity is significantly larger than the other two peaks for all four PZT films on metal substrates. Figure 4.3f displays the fit results for the tetragonal (002) peaks (peak 1) in PZT on Pt, PZT on Ni-25 and PZT on Ni-500; the volume fraction of (002) domains was calculated with Equation 4.3 and is labeled next to each peak. I_{002} is the integrated intensity of peak 1, I_{024} is the integrated intensity of peak 2, I_{200} is the integrated intensity of peak 3, and I'_{hkl} is the reference intensity of the powder diffraction file ($I'_{002,tet.}$=107, $I'_{024,\ rhomb.}$ =435, $I'_{200,\ tet.}$=260) [36]. The (002) peak area is representative of the c-domain volume fraction and is expected to be directly dependent on the magnitude of film compressive stress, which is largest for the PZT film on the 500 μm thick nickel plate. As shown in Figure 4.3f, PZT on Ni-500 displays the highest (002)-domain volume fraction of 87.6%, whereas PZT on Pt-25 and Ni-25 were 81.6% and 76.4%, respectively. Aruchamy et al. reported a ratio of 0.79:0.21 for out-of-plane to in-plane (002):(200) peak area for 52/48 PZT on a stiff sapphire substrate; the PZT film had a compressive stress of 100 MPa.[37] This is comparable to the data shown here for PZT on the flexible Pt-25 substrate, which had a calculated compressive stress of 102 MPa and a (002):(200) ratio of 0.82:0.18.

$$\nu_{002} = \frac{\frac{I_{002}}{I'_{002}}}{\frac{I_{002}}{I'_{002}} + 2\frac{I_{200}}{I'_{200}} + 2\frac{I_{024}}{I'_{024}}} \qquad \text{Equation 4.3}$$

As the compressive stress of the PZT film increases in magnitude, the out of plane spacing of c-oriented domains increases. The lattice parameters were computed from the 2θ at maximum intensity generated from LIPRAS and are plotted in Figure 4.4 at the 52/48 PZT composition. The black data points are the lattice parameters vs. PZT composition extracted from the study by Shirane, et al.[38] The three lattice parameters calculated from the (002) peak for PZT

on Pt-25, Ni-25, and Ni-500 in Figure 4.3f fall near the tetragonal c-axis lattice parameter line in Figure 4.4, and increase with film compressive stress magnitude. The lattice parameters calculated from the (200) peaks for the same three samples fall slightly above the reported tetragonal a-axis lattice parameter. Extracted lattice parameters from the (024) rhombohedral peaks appear to lay along an extrapolation from the low Ti concentration rhombohedral region in Figure 4.4. This data suggests that the (200) tetragonal peak and the (024) rhombohedral peak may not be fully deconvoluted. All three lattice parameters increase as film compressive stress increases in magnitude.

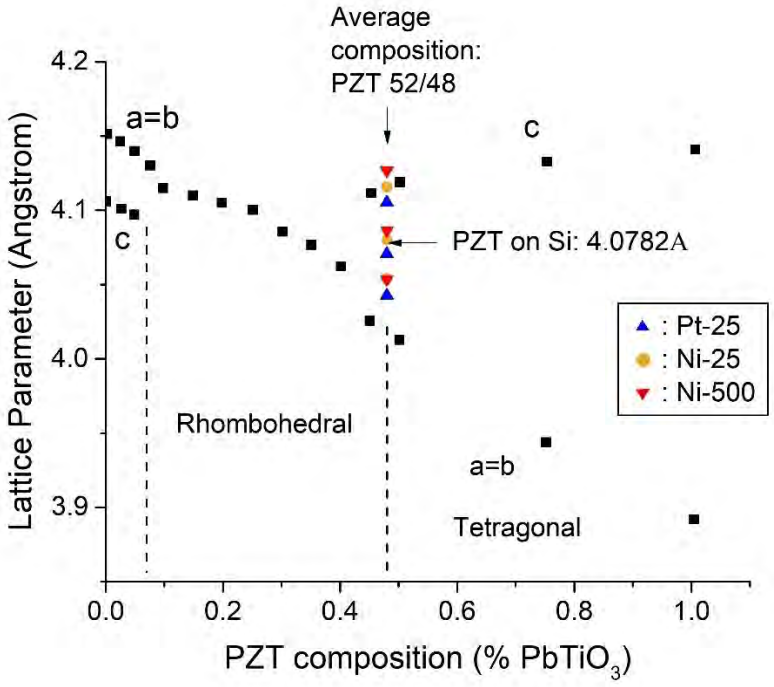

Figure 4.4: Lead zirconate titanate (PZT) lattice parameter versus composition. Black data points extracted from Shirane et al.[38] Data points placed at 48% $PbTiO_3$ composition show rhombohedral, tetragonal a, and tetragonal c lattice parameters extracted from Figure 4.3 (b-d).

Some of the variation from the expected in-plane tetragonal lattice parameter may be explained with energy dispersive x-ray spectroscopy (EDS) via high-angle annular dark field transmission electron microscopy (TEM). An analysis of the Zr/Ti composition gradient was

performed on a ~2 μm thick 52/48 PZT with 2% Nb film that was spun coat on a platinized Si wafer. The PZT solution was fabricated identically to the solution used for the dip coating experiments. Prior to film growth, a 44/56 Zr/Ti ratio PZT with 20% excess Pb Mitsubishi seed layer was spun coat and crystallized. Figure 4.5 displays the EDS results overlain on the TEM image with all 26 layers shown with orange tick marks signifying each layer boundary.

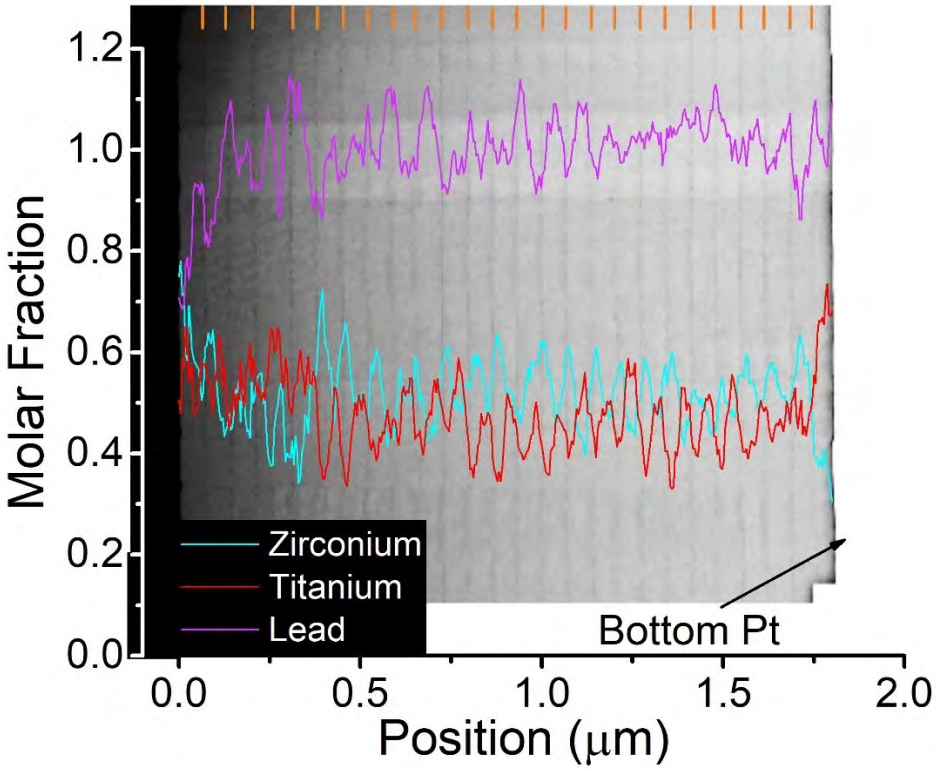

Figure 4.5: Transmission electron microscopy image overlain with energy dispersive x-ray spectroscopy results for zirconium, titanium, and lead content in a 2 μm PZT 52/48 thin film.

As described earlier [39], some PZT films are characterized by strong Zr/Ti gradients through the film thickness. The Ti-rich seed layer provides a higher concentration of Ti near the electrode/film interface and reduces lead loss to the bottom electrode. As the second PZT layer nucleates from the first seed layer (right side of Figure 4.5), the Ti-rich tetragonal phase nucleates preferentially and is shown by a high Ti fraction near the start of the layer. Zr is excluded towards the top of each crystallized layer, such that the Zr concentration exceeds 0.52, resulting in a larger

volume fraction of the rhombohedral phase[40]. It is also noted that the lead concentration is lower at the surface of each crystallized layer, as lead oxide is volatile at the crystallization temperature. This process repeats for each layer, resulting in composition gradients throughout the thickness of each PZT layer, as reported by Calame et al. [40] It is likely that these gradients help stabilize the rhombohedral distortion in these films.

Field emission scanning electron microscopy (SEM) was utilized to visualize the surface microstructure of the 2 μm thick PZT films. Figure 4.6 displays the PZT grain structure on platinized silicon (a), platinum foil (b), nickel foil (c), thick nickel plate (d), and silver foil (e). A cross-section image of PZT on Si is displayed in Figure 4.6f. Each PZT film contained limited amounts of non-ferroelectric pyrochlore (or fluorite) decorated near the grain boundaries; the films displayed high density with little to no porosity. It is notable that the grain sizes shown in the bottom right of each SEM scan tended to be smaller for the thicker substrates. This effect may be linked to the processing conditions; where the thick nickel plate and thick silicon plate rested directly on a silicon carrier wafer during pyrolysis and crystallization steps, the three thin metal foils were propped up by their four corners (See Figure C.4 in Appendix C). For all samples, the same side was facing up for each anneal step; this was the side onto which the electrodes were deposited. Thermal transfer to the thick plates was expected to be different than that of the foils, where a difference in surface temperature could affect the nucleation density of PZT on foils and hence the grain sizes. Figure 4.6e displays PZT film blistering on the silver foil substrate, presumably due to the high compressive stresses experienced by the film. Coupeau reported that above a critical equibiaxial compressive stress, buckling above a circular separation near the film/substrate interface is likely [41]. The buckled area may occur as a straight-sided wrinkle, a circular blister or as a dendritic, brain-like, or telephone cord-like shape and may result in full delamination of the film in some areas [41]. This is likely when a stiff film such as PZT is placed under a large compressive stress on a soft substrate, such as a flexible Ag foil [42].

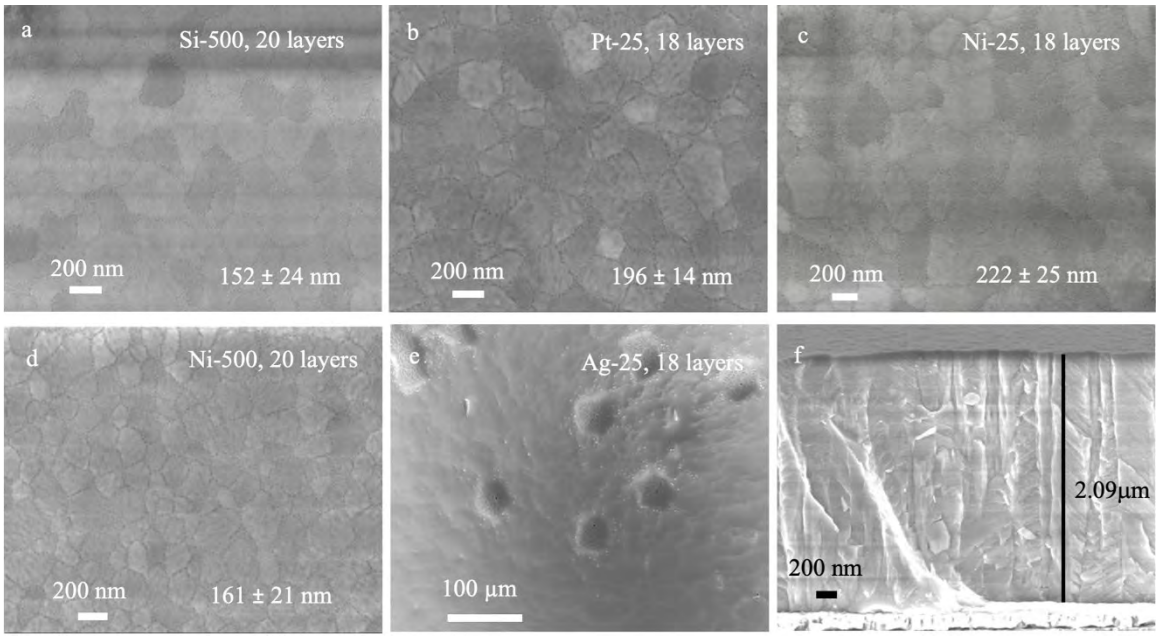

Figure 4.6: Field emission scanning electron microscopy images of thin film lead zirconate titanate (PZT) on 500 µm Si (a), 25 µm Pt (b), 25 µm Ni (c), 500 µm Ni (d), low magnification 25 µm Ag (e), and cross-section PZT on 500 µm Si (f).

4.3.2 Characterization of dielectric and ferroelectric properties

Dielectric permittivity and loss tangent were measured as a function of frequency before and after poling. Due to the buckling and subsequent cracking of the PZT film on Ag foil, electrical measurements were unattainable. Figure 4.7 displays the dielectric properties of PZT films on silicon, platinum, and both nickel substrates at 30mV AC from 100 Hz to 100 kHz, where each PZT film displays loss tangents below 0.06. The dielectric permittivity was highest for PZT on silicon and lowest for PZT on the thick nickel plate. This effect was expected due to the thermal stress in the films, where a large volume fraction of in plane polarization developed in the PZT on Si-500 due to tensile stress. PZT on Pt-25 displayed the next largest dielectric permittivity followed by PZT on Ni-25 and Ni-500, respectively. Increasing film compressive stress forced a larger volume fraction of domains out of plane, which reduced the dielectric permittivity [27].

On poling, it was found that the dielectric permittivity of films on flexible foils dropped considerably more than the films on thicker, more rigid substrates, and the loss tangent decreased for all four films. After poling, the permittivity was hardly affected for PZT on silicon, consistent with prior reports of limited ferroelastic switching [43, 44]. In contrast, poled PZT on Pt-25 almost overlaps the permittivity of the as-processed PZT on Ni-25, indicating that domain reorientation on poling is less dependent on the CTE of the substrate when the substrate is flexible.

This effect is exemplified in Figure 4.8, which displays dielectric permittivity at 1 kHz vs. film stress for PZT calculated with Equation 4.1 prior to and after poling. As compressive film stress increased, the dielectric permittivity decreased due to the higher volume fraction of out-of-plane domains. The trend is not linear and appears to depend on whether the substrate is stiff or flexible, as seen in comparing the permittivity between the two nickel substrates. There was a steep drop in permittivity for the stiff nickel substrate, indicating a significantly higher volume fraction of c-domains compared to the flexible nickel substrate. Prior to poling, the difference between the permittivity of the PZT on Ni-25 and Ni-500 was larger than that between PZT on Ni-25 and Pt-25. This result shows that although the CTE of the substrate is critical in domain configuration after processing, substrate clamping of domain re-alignment may exceed the effect of the CTE difference.

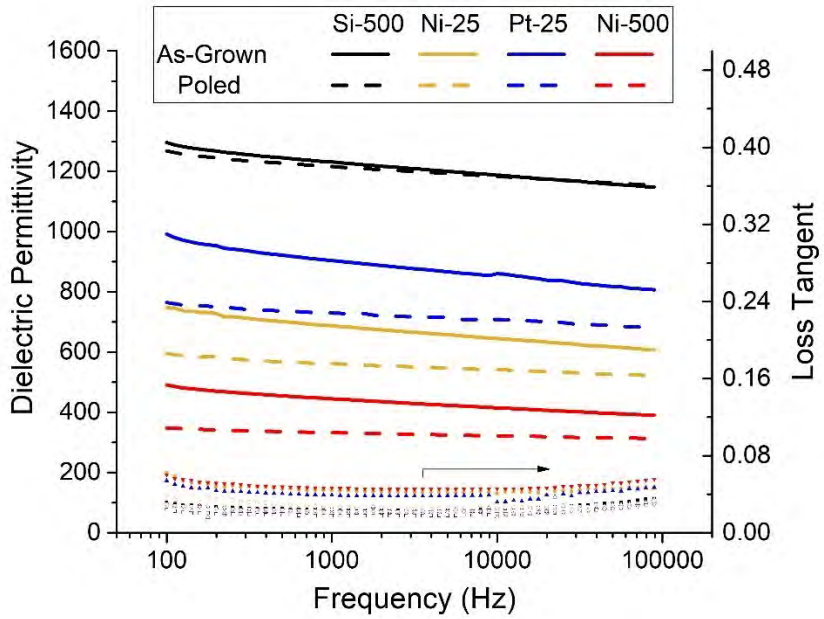

Figure 4.7: Dielectric permittivity and loss tangent versus frequency for lead zirconate titanate (PZT) films on four substrates. Loss tangent for as-grown capacitors displayed with closed symbols (■ for Si-500) and open symbols for poled capacitors (□ for Si-500).

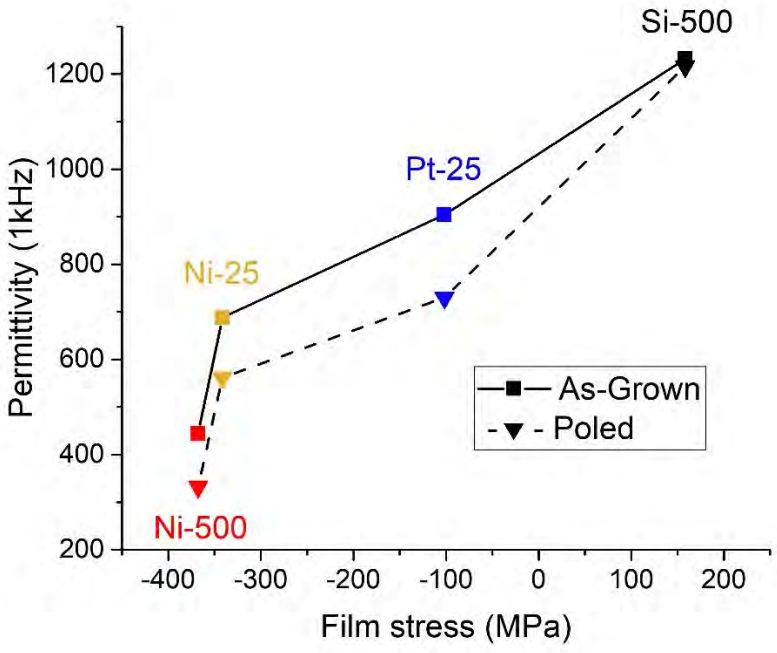

Figure 4.8: Dielectric permittivity at 1 kHz versus calculated films stress for 2 μm thick lead zirconate titanate (PZT) on four substrates prior to and after poling.

Ferroelectric properties of the films were measured via P–E hysteresis loops for PZT on silicon, platinum, and both nickel substrates, as shown in Figure 4.9. The inset shows a magnified view of the positive remanent polarization values, where PZT on the thick nickel plate is highest and PZT on silicon is lowest. PZT on flexible platinum and nickel are essentially equivalent. Coercive fields for the PZT on all four substrates are comparable, as stress does not control the field required to switch domain polarization [45].

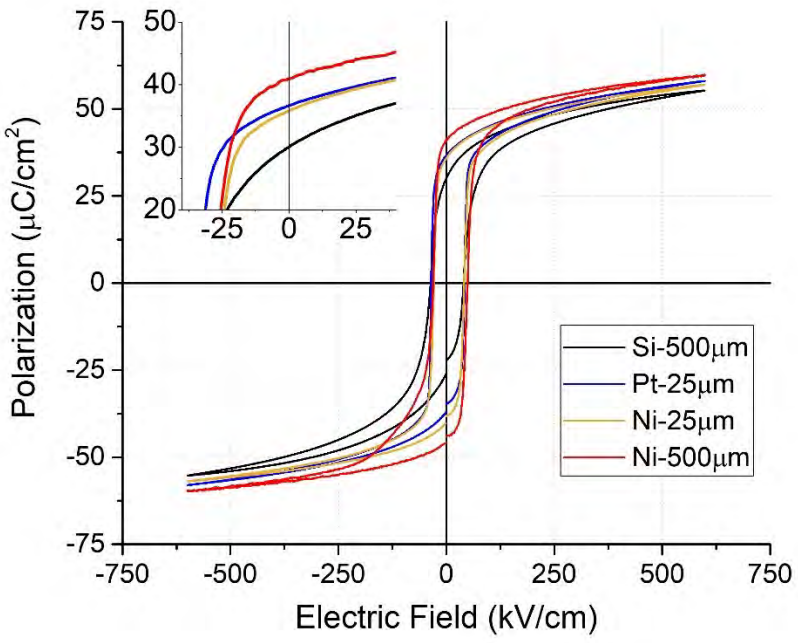

Figure 4.9: Polarization versus Electric Field hysteresis loops at 600 kV/cm field for lead zirconate titanate (PZT) films on four substrates.

Figure 4.10 displays both positive and negative remanent polarization values for PZT on silicon, platinum, and both nickel substrates. An inverse relationship is displayed between P_r and dielectric permittivity; as film compressive stress increases, P_r increases. This is attributed to the domain population variation for PZT on the four substrates. The sharp difference in P_r for PZT on Ni-25 and Ni-500 follows the same rapid, but inverse trend to dielectric permittivity, where a higher volume fraction of out-of-plane domains in PZT on Ni-500 produces a significantly higher

P_r. PZT on silicon displays the lowest P_r while PZT on platinum shows an intermediate value, consistent with mixed in and out-of-plane domain populations. None of the films show significant imprint. An unexpected result is the very small variation in P_r between PZT on Ni-25 and PZT on Pt-25 based on their calculated stress values. It is proposed that this is a result of the improved ferroelastic domain reorientation in films on flexible substrates, relative to more rigid substrates.

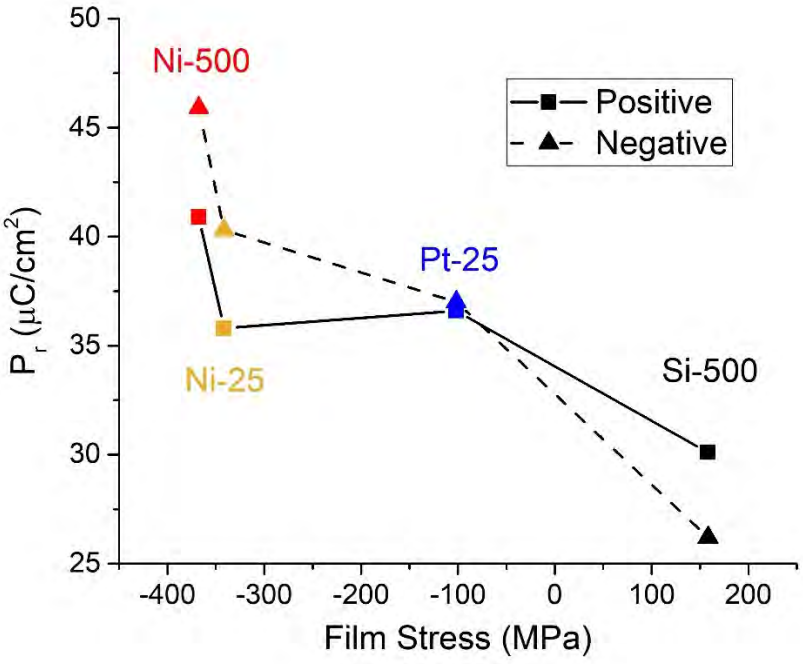

Figure 4.10: Positive and negative remanent polarization for lead zirconate titanate (PZT) versus film stress for four substrates.

Coleman et al. deposited thin film PZT onto a 50 μm nickel foil to investigate the effect of applied stresses on dielectric, piezoelectric, and ferroelectric properties [26]. Subsequent grazing incidence XRD measurements performed near the (200)/(002) peaks on those samples yielded lattice parameters of 4.111 Angstroms and 4.066 Angstroms. These values match the lattice parameters calculated for PZT on Ni-25 in this work (4.116, 4.080, and 4.054 Angstroms for (002), (024) and (200), respectively), indicating that both PZT films on Ni foils contained mixed tetragonal and rhombohedral phases. Figure 4.11 shows the results obtained from [26] for remanent

polarization vs film stress for PZT on Ni foil and on Si substrate, where a significant gap in P_r developed between tensile and compressive stress states. The large gap may be a function of the higher volume fraction of the rhombohedral phase in the film on silicon.

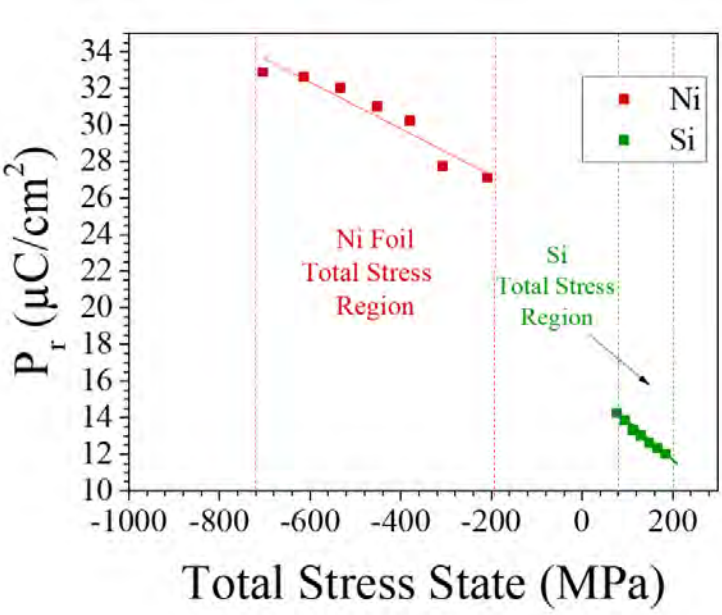

Figure 4.11: Working total stress ranges for PZT films on nickel foil (red) and silicon substrate (green). Figure reproduced from [26].

Rayleigh analysis was used to probe reversible and irreversible contributions to the dielectric response to further investigate the effect of substrate clamping on domain mobility. Figure 4.12 shows the irreversible contributions as a function of frequency for PZT on silicon, platinum foil, nickel foil, and on a nickel plate. Prior to poling, PZT on platinum shows the highest irreversible contributions at all frequencies followed by PZT on nickel foil, PZT on silicon, and PZT on a thick nickel plate. The drop in α_ε after poling suggests either a lower population of domain walls or a reduced wall mobility.

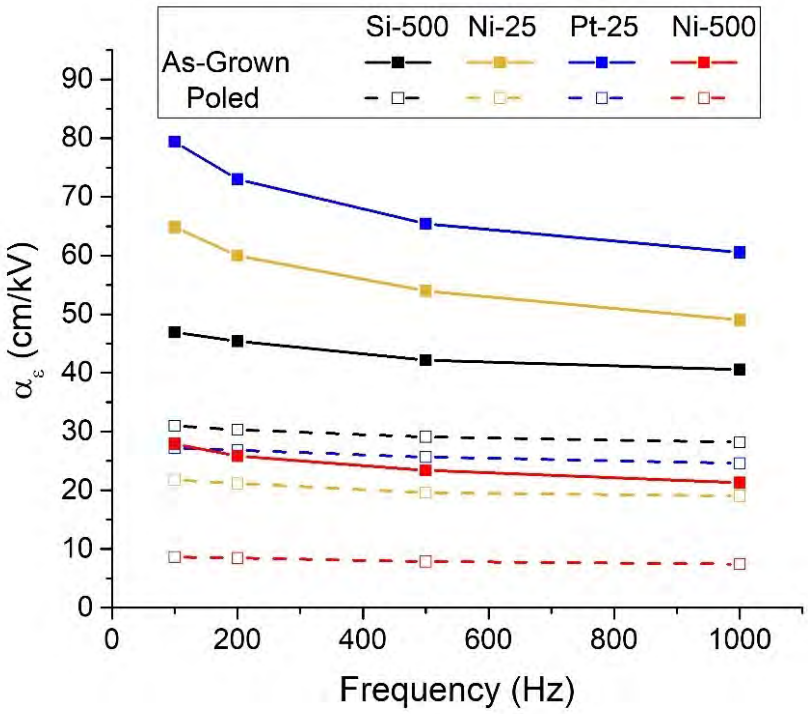

Figure 4.12: Irreversible Rayleigh coefficient at 100, 200, 500, and 1000 Hz for lead zirconate titanate (PZT) on four substrates prior to and after poling.

The decreases in α_ε for PZT on thick silicon and nickel after poling are significantly smaller than the decreases for PZT on flexible platinum and nickel, which would be consistent with the reduced ferroelastic domain reorientation on more rigid substrates. It is speculated that the flexibility of a metal foil may relieve residual film stress developed during cooling from the crystallization temperature by bending, such that the resulting PZT films possess more in-plane domains than estimated from the calculated residual stress from Equation 4.1. This is clearly seen in the dielectric permittivity and P_r plots vs film stress, where the permittivity is significantly lower and P_r is much higher for PZT on the thick nickel plate compared to the flexible nickel foil. Thus, a second contribution to the lower permittivity change on poling for the PZT on the thick nickel plate would be the larger extent of pre-existing out-of-plane oriented domains in the as-prepared films. That is, the substrate flexibility enhances irreversible domain wall motion upon

PZT poling while the CTE of the substrate determines the initial post-fabrication domain structure.

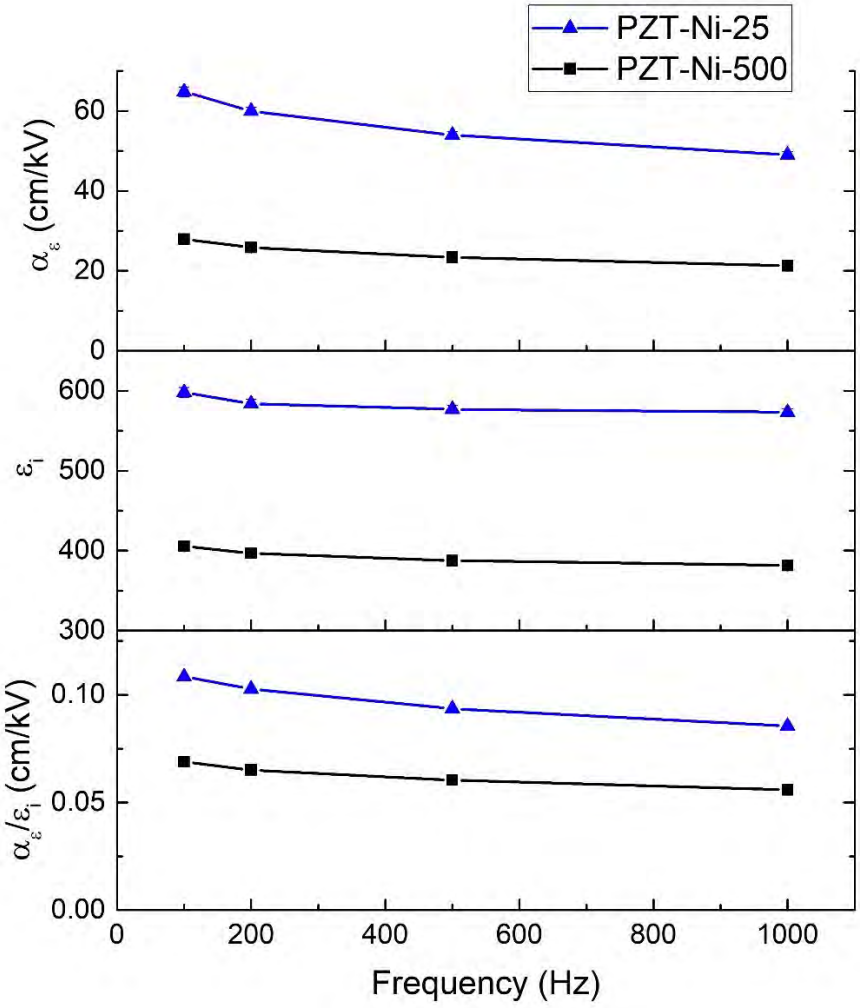

Figure 4.13: Rayleigh coefficients of lead zirconate titanate (PZT) on Ni-25 and Ni-500 substrates in the as-grown condition. Irreversible Rayleigh coefficient (top), reversible Rayleigh coefficient (middle), and the ratio of the irreversible to reversible Rayleigh coefficients (bottom).

Figure 4.13 displays Rayleigh coefficients for PZT on flexible and stiff Ni substrates in the as-grown condition. The irreversible and reversible coefficients are significantly higher for PZT on flexible foils, consistent with the clamping effect of thick substrates, as well as a higher population of in-plane domains in the PZT on thinner Ni. The bottom plot in Figure 4.13 shows the ratio of irreversible to reversible Rayleigh coefficients. Presuming that the Ni foil allows PZT

to behave more like an unclamped film than the one on thick nickel, then the trend shown here is opposite of the results displayed by Griggio et al., where after PZT release the $\alpha_e/\varepsilon_{initial}$ ratio was higher in the clamped PZT film [28]. However, the released PZT film in their study was under a significant amount of tensile stress and domains remained predominantly in their as-grown condition.

To summarize, nickel has a higher CTE than platinum at the PZT crystallization temperature, both of which are higher than the CTE for PZT; silicon has a lower CTE than PZT. The two flexible substrates relieve stress developed in the PZT film upon cooling by bending, but PZT on stiff Si is placed in tension upon cooling, arranging the majority of domains parallel (or nearly so) to the film surface. The film on the Ni plate is in compression, and domains are arranged predominantly perpendicular to the film surface upon cooling. The stress in the film on platinum is partially relieved by bending, but the film contains less out of plane domains than the film on flexible Ni due to Pt's lower CTE than Ni. Ferroelastic domain wall and/or phase boundary motion is reduced in films on stiff substrates; therefore, poling provides only modest changes in the as-grown ferroelastic domain configuration. In contrast, on flexible substrates, domain reorientation (including ferroelastic domains), is easier. As a result, the irreversible Rayleigh coefficient decreases significantly after poling PZT films on foils.

One consideration excluded from this investigation is the yield strength of each metal substrate. The yield stress of metals depends on their purity, defect concentration, grain size, grain boundary concentration, and thermal history. Without direct measurement of yield strength for each metal substrate, it is unknown whether the calculated compressive thermal stresses for PZT in Table 4.1 on the metal exceeds the tensile yield strength. Evidence that this can occur, however, is shown in Figure 4.14, where the thick nickel plate is bent after 20 heating and cooling PZT crystallization cycles. Thus, for the 25 μm flexible metal foils, it is possible that local

permanent substrate plastic deformation or recrystallization of the foils can occur during the PZT heat treatment steps. Substrate plastic deformation may, in principle, affect the domain orientation, domain wall density, and domain wall motion activation energy.

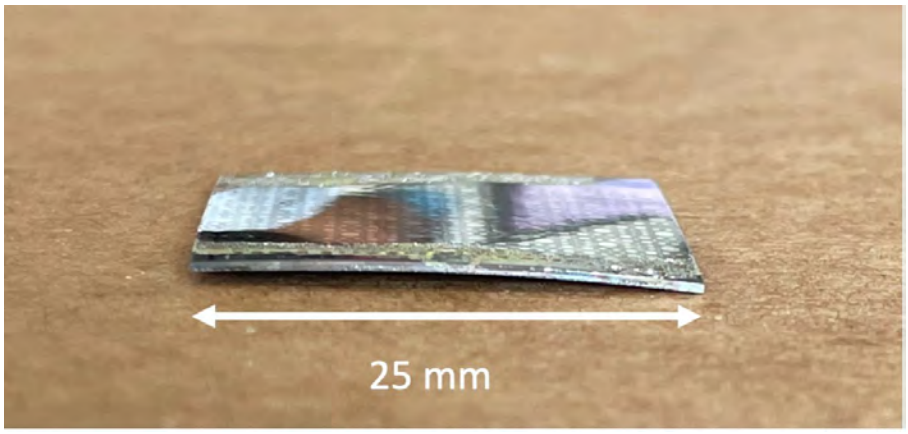

Figure 4.14: Plastic deformation observed for lead zirconate titanate (PZT) on Ni-500.

4.4 Conclusions

Thin film (2 μm) PZT was deposited via dip coat deposition onto five substrates with varying thickness and CTE to investigate the dependence of thermal stress on dielectric and ferroelectric properties of the films. It was found through grazing incidence XRD that with higher thermal compressive stresses, the films displayed larger volume fractions of out-of-plane domains. The lattice parameter determined from the position of the (002) peak matched well with existing literature for the c-domain of the tetragonal phase; however, the positions of the rhombohedral (024) and tetragonal (200) peaks matched poorly with the expected lattice parameters, indicating mixture of the two phases. Dielectric permittivity and P-E hysteresis loops showed a large dependence on substrate thickness, where with the same substrate material and CTE, PZT on 500 μm Ni had 35% lower permittivity and 12% higher remanent polarization than PZT on 25 μm Ni. Rayleigh coefficients displayed a similar trend, where the $\alpha_\varepsilon/\varepsilon_{initial}$ ratio was

56% higher in PZT on a flexible Ni substrate relative to a stiff Ni substrate at 100 Hz prior to electrical poling. It is concluded that substrate flexibility enhances irreversible domain wall and/or phase boundary motion upon PZT poling while the CTE of the substrate determines the initial post-fabrication domain structure.

4.5 References

1. Yeo HG, Ma X, Rahn C, Trolier-McKinstry S. Efficient piezoelectric energy harvesters utilizing (001) textured bimorph PZT films on flexible metal foils. *Adv Funct Mater*. 2016;26(32):5940–5946. https://doi.org/10.1002/adfm.201601347
2. Won SS, Seo H., Kawahara M, Glinsek S, Lee J, Kim Y, Jeong CK, Kingon AI Kim SH. Flexible vibrational energy harvesting devices using strain-engineered perovskite piezoelectric thin films. *Nano Energy*. 2019;55(September 2018):182–192. https://doi.org/10.1016/j.nanoen.2018.10.068
3. Kang L, An HL, Park JY, Hong MH, Nahm S, Lee CG. La-doped p-type ZnO nanowire with enhanced piezoelectric performance for flexible nanogenerators. *Appl Surf Sci*. 2019;475(January):969–973. https://doi.org/10.1016/j.apsusc.2019.01.025
4. Delnavaz A, Voix J. Flexible piezoelectric energy harvesting from jaw movements. *Smart Mater Struct*. 2014;23(10). https://doi.org/10.1088/0964-1726/23/10/105020
5. Hwang GT, Byun M, Jeong CK, Lee KJ. Flexible piezoelectric thin-film energy harvesters and nanosensors for biomedical applications. *Adv Healthc Mater*. 2015;4(5):646–658. https://doi.org/10.1002/adhm.201400642
6. Cha Y, Kim H, Kim D. Flexible piezoelectric sensor-based gait recognition. *Sensors (Switzerland)*. 2018;18(2):1–10. https://doi.org/10.3390/s18020468
7. Proto A, Fida B, Bernabucci I, Bibbo D, Conforto S, Schmid M, Vlach K, Kasik V,

Penhaker M. Wearable PVDF transducer for biomechanical energy harvesting and gait cycle detection. *IECBES 2016 - IEEE-EMBS Conf Biomed Eng Sci*. 2016;62–66. https://doi.org/10.1109/IECBES.2016.7843415

8. Cha Y, Song K, Shin J, Kim D. Gait analysis system based on slippers with flexible piezoelectric sensors. *2018 IEEE Int Conf Robot Biomimetics, ROBIO 2018*. 2018;2479–2484. https://doi.org/10.1109/ROBIO.2018.8664872
9. Lei KF, Lee KF, Lee MY. Development of a flexible PDMS capacitive pressure sensor for plantar pressure measurement. *Microelectron Eng*. 2012;99:1–5. https://doi.org/10.1016/j.mee.2012.06.005
10. Liu T, Dangi A, Kim JN, Kothapalli SR, Choi K, Trolier-McKinstry S, Jackson T. Flexible thin-film PZT ultrasonic transducers on polyimide substrates. *Sensors*. 2021;21(1014):1–9.
11. Jackson N, Keeney L, Mathewson A. Flexible-CMOS and biocompatible piezoelectric AlN material for MEMS applications. *Smart Mater Struct*. 2013;22(11). https://doi.org/10.1088/0964-1726/22/11/115033
12. Nagata H, Ko SW, Hong E, Randall CA, Trolier-McKinstry S, Pinceloup P, Skamser D, Randall M, Tajuddin A. Microcontact printed $BaTiO_3$ and $LaNiO_3$ thin films for capacitors. *J Am Ceram Soc*. 2006;89(9):2816–2821. https://doi.org/10.1111/j.1551-2916.2006.01137.x
13. Godard N, Glinšek S, Matavž A, Bobnar V, Defay E. Direct patterning of piezoelectric thin films by inkjet printing. *Adv Mater Technol*. 2019;4(2):1–8. https://doi.org/10.1002/admt.201800168
14. Kuscer D, Noshchenko O, Uršič H, Malič B. Piezoelectric properties of ink-jet-printed lead zirconate titanate thick films confirmed by piezoresponse force microscopy. *J Am Ceram Soc*. 2013;96(9):2714–2717. https://doi.org/10.1111/jace.12532

15. Schneller T, Waser R, Kosec M, Payne D. Chemical Solution Deposition of Functional Oxide Thin Films. Springer; 2013 https://doi.org/10.1021/cm970286f

16. Yeo HG, Xue T, Roundy S, Ma X, Rahn C, Trolier-McKinstry S. Strongly (001) oriented bimorph PZT film on metal foils grown by rf-sputtering for wrist-worn piezoelectric energy harvesters. *Adv Funct Mater*. 2018;28(36):1–9. https://doi.org/10.1002/adfm.201801327

17. Takahashi Y, Matsuoka Y, Yamaguchi K, Matsuki M, Kobayashi K. Dip coating of PT, PZ and PZT films using an alkoxide-diethanolamine method. *J Mater Sci*. 1990;25(9):3960–3964. https://doi.org/10.1007/BF00582467

18. Takahashi Y, Yamaguchi K. Dip-coating conditions and modifications of lead titanate and lead zirconate titanate films. *J Mater Sci*. 1990;25:3950–3955.

19. He XY, Ding AL, Zheng X Sen, Qiu PS, Luo WG. Preparation of PZT(53/47) thick films deposited by a dip-coating process. *Microelectron Eng*. 2003;66(1–4):865–871. https://doi.org/10.1016/S0167-9317(02)01013-4

20. Hida H, Hamamura T, Nishi T, Tan G, Umegaki T, Kanno I. Piezoelectric characterization of $Pb(Zr,Ti)O_3$ thin films deposited on metal foil substrates by dip coating. *Jpn J Appl Phys*. 2017;56(10). https://doi.org/10.7567/JJAP.56.10PF08

21. Tuttle BA, Voigt JA, Garino TJ, Goodnow DC, Schwartz RW, Lamppa DL, Headley TJ, Eatough MO. Chemically prepared $Pb(Zr,Ti)O_3$ thin films: The effects of orientation and stress. *ISAF 1992 - Proc 8th IEEE Int Symp Appl Ferroelectr*. 1992;344–348. https://doi.org/10.1109/ISAF.1992.300703

22. Tuttle BA, Garino TJ, Voigt JA, Headley TJ, Dimos D, Eatough MO. Relationships between ferroelectric 90 degree domain formation and electrical properties of chemically prepared $Pb(Zr,Ti)O_3$ thin films. *Sci Technol electroceramic thin Film*. 1995;284:117–132.

23. Tuttle B, Headley T, Drewien C, Michael J, Voigt J, Garino T. Comparison of ferroelectric domain assemblages in $Pb(Zr,Ti)O_3$ thin films and bulk ceramics. *Ferroelectrics*. 1999;221(1):209–218.

24. Yamada T, Yasumoto J, Ito D, Sakata O, Imai Y, Kiguchi T, Shiraishi T, Shimizu T, Funakubo H, Yoshino M, Nagasaki T. Negligible substrate clamping effect on piezoelectric response in (111)-epitaxial tetragonal $Pb(Zr, Ti)O_3$ films. *J Appl Phys*. 2015;118(7). https://doi.org/10.1063/1.4927810

25. Miyoshi T, Nakajima M, Funakubo H. Effects of substrate clamping on electrical properties of polycrystalline piezoelectric films. *Jpn J Appl Phys*. 2009;48(9 Part 2). https://doi.org/10.1143/JJAP.48.09KD09

26. Coleman K, Walker J, Beechem T, Trolier-McKinstry S. Effect of stresses on the dielectric and piezoelectric properties of $Pb(Zr_{0.52}Ti_{0.48})O_3$ thin films. *J Appl Phys*. 2019;126(3):0–8. https://doi.org/10.1063/1.5095765

27. Haun MJ, Furman E, Jang SJ, Cross LE. Thermodynamic Theory of The Lead Zirconate-Titanate Solid Solution System, Part V: Theoretical Calculations. *Ferroelectrics*. 1989;99:63–86.

28. Griggio F, Jesse S, Kumar A, Ovchinnikov O, Kim H, Jackson TN, Damjanovic D, Kalinin SV, Trolier-McKinstry, S. Substrate clamping effects on irreversible domain wall dynamics in lead zirconate titanate thin films. *Phys Rev Lett*. 2012;108(15):1–5. https://doi.org/10.1103/PhysRevLett.108.157604

29. Okada Y, Tokumaru Y. Precise determination of lattice parameter and thermal expansion coefficient of silicon between 300 and 1500 K. *J Appl Phys*. 1984;56(2):314–320. https://doi.org/10.1063/1.333965

30. Touloukian YS, Kirby RK, Taylor RE, Desai PO. Thermophysical Properties of Matter-The TPRC Data Series -- Vol. 12. Thermal Expansion Metallic Elements and Alloys. New

York - Washington: IFI/Plenum; 1975

31. Cook WR, Berlincourt DA, Scholz FJ. Thermal expansion and pyroelectricity in lead titanate zirconate and barium titanate. *J Appl Phys*. 1963;34(5):1392–1398. https://doi.org/10.1063/1.1729587

32. Das D, Sanchez L, Martin J, Power B, Isaccson S, Polcawich RG, Chasiotix I. Control of mechanical response of freestanding $PbZr_{0.52}Ti_{0.48}O_3$ films through texture. *Appl Phys Lett*. 2016;109(13):0–5. https://doi.org/10.1063/1.4963348

33. Olding T, Leclerc B, Sayer M. Processing of multilayer PZT coatings for device purposes. *Integr Ferroelectr*. 1999;26(1):225–241. https://doi.org/10.1080/10584589908215624

34. Brennecka GL, Huebner W, Tuttle BA, Clem PG. Use of stress to produce highly oriented tetragonal lead zirconate titanate (PZT 40/60) thin films and resulting electrical properties. *J Am Ceram Soc*. 2004;87(8):1459–1465. https://doi.org/10.1111/j.1551-2916.2004.01459.x

35. Esteves G, Ramos K, Fancher C, Jones J. LIPRAS: Line-Profile Analysis. 2017. https://doi.org/10.13140/RG.2.2.29970.25282/3

36. Frantti J, Ivanov S, Eriksson S, Lappalainen J, Latto V, Kakihana M, Rundlöf H. Neutron diffraction and bond-valence calculation studies of $Pb(Zr_xTi_{1-x})O_3$ ceramics. *Ferroelectrics*. 2002;272(1):51–56. https://doi.org/10.1080/00150190211594

37. Aruchamy N, Schenk T, Kovacova V, Glinsek S, Defay E, Granzow T. Influence of tensile vs. compressive stress on fatigue of lead zirconate titanate thin films. *J Eur Ceram Soc*. 2021;(June). https://doi.org/10.1016/j.jeurceramsoc.2021.07.010

38. Shirane G, Suzuki K. Crystal structure of $Pb(Zr,Ti)O_3$. *J Phys Soc Japan*. 1952;7(3):333.

39. Ihlefeld J.F., Kotula P.G, Gauntt B.D. Gough D.V., Brennecka G.L., Lu P., Spoerke E.D. Solution chemistry, substrate, and processing effects on chemical homogeneity in lead zirconate titanate thin films. *J Am Ceram Soc.* 2015;98(7):2028-2038.

https://doi.org/10.1111/jace.13576

40. Calame F, Muralt P. Growth and properties of gradient free sol-gel lead zirconate titanate thin films. *Appl Phys Lett*. 2007;90(6):2–4. https://doi.org/10.1063/1.2472529

41. Coupeau C. Atomic force microscopy study of the morphological shape of thin film buckling. *Thin Solid Films*. 2002;406(1–2):190–194. https://doi.org/10.1016/S0040-6090(01)01772-2

42. Boijoux R, Parry G, Faou JY, Coupeau C. How soft substrates affect the buckling delamination of thin films through crack front sink-in. *Appl Phys Lett*. 2017;110(14). https://doi.org/10.1063/1.4979614

43. Denis-Rotella LM, Esteves G, Walker J, Zhou H, Jones JL, Trolier-McKinstry S. Residual stress and ferroelastic domain reorientation in declamped {001} $Pb(Zr_{0.3}Ti_{0.7})O_3$ films. *IEEE Trans Ultrason Ferroelectr Freq Control*. 2021;68(2):259–272. https://doi.org/10.1109/TUFFC.2020.2987438

44. Esteves G, Wallace M, Johnson-Wilke R, Fancher CM, Wilke RH, Trolier-McKinstry S, Jones JL. Effect of mechanical constraint on domain reorientation in predominantly {111}-textured lead zirconate titanate films. *J Am Ceram Soc*. 2016;99(5):1802–1807. https://doi.org/10.1111/jace.14159

45. Lee JW, Park CS, Kim M, Kim HE. Effects of residual stress on the electrical properties of PZT films. *J Am Ceram Soc*. 2007;90(4):1077–1080. https://doi.org/10.1111/j.1551-2916.2007.01610.x

CHAPTER 5

Insole embedded lead zirconate-titanate film force sensor array

Chapter 5 of this thesis has been previously published as: Peters, T., Hosur, S., Kiani, M., Roundy, S., & Trolier-McKinstry, S. (2022) Insole embedded lead zirconate-titanate film force sensor array. *Sensors and Actuators A: Physical,* 114097. https://doi.org/10.1016/j.sna.2022.114097

5.1 Introduction

The CDC reports that falls are the leading cause of fatal and nonfatal injuries among adults aged ≥ 65 years; approximately 3 million older adults were treated in emergency departments for fall-related injuries in 2018 [1-2], where the estimated medical costs attributable to falls is ~ $50 billion [3]. Within a clinical environment, strategies for reducing the number of falls incorporate balance assessment, strength and balance exercises, and medication review [1]. While some medical assessments can be performed remotely, accurate appraisal of balance is challenging to do away from a clinician's office. Therefore, a low-power balance detection sensing system could ease the burden on outpatient caretakers and aging adults who have experienced a fall. Insole embedded force sensors (IEFCs) within footwear can realize balance detection and the temporal characteristics of gait, as they cause little discomfort and strain penalty to the patient. The focus of this study is to improve the current IEFC state of the art for a sole sensing application.

Essential characteristics of IEFCs include lightweight design, flexibility, thickness minimization, low to zero power consumption, moderate sensitivity, and electrical/mechanical robustness. Several existing force sensors achieve some of these attributes, but few succeed to

fulfill all conditions [4]. Table D.1 in Appendix D summarizes the sensitivity, flexibility, power requirement, and force/pressure ranges of comparable force sensor devices. If wired battery charging or replacement is necessary, the patient must remove the shoe insole; if the batteries are wirelessly charged, the shoes must sit stationary throughout charging. In both cases, the quantity of interpretable patient data is reduced. Capacitive [5], resistive [6], triboelectric [7], and piezoresistive [8] pressure sensors require power input, thus they were not considered. Piezotronic sensors are gaining popularity in the strain and pressure sensing communities; however, they are not considered here [9]. Piezoelectric sensors take advantage of the direct piezoelectric effect, where a voltage is generated with the application of a stress or strain. Several designs have been developed that utilize bulk ceramic-based piezoelectrics, which exhibit d_{33} coefficients of several hundred pm/V, to achieve some of the IEFC requirements. Yi and Tian et al. utilized a chemical mechanical polishing (CMP) process to thin bulk PZT down to 50 μm [10-11]. This process enables sensor development with high sensitivity and flexibility, but in some cases, CMP processed ceramics display a low strain tolerance and may fracture beyond 0.1% strain [11-12]. Liu et al. fabricated a flexible piezoelectric micromachined ultrasonic transducer with 5x5x1 mm^3 PZT elements sandwiched by flexible electrical interconnects and polydimethylsiloxane (PDMS) [13]. Although their device could be stretched by 25%, the large bulk PZT units may affect comfort within a shoe sole. Piezoelectric thin films offer an improvement in flexibility, mass control, and comfortability over bulk piezoelectric ceramics for this application.

Piezoelectric films in a pressure sensing application contain the desirable characteristics necessary for IEFCs; they are lightweight, inherently thin, require zero input power besides the applied pressure, are highly sensitive, and are both electrically and mechanically robust. One limitation is flexibility; ceramic piezoelectric films are commonly placed on a stiff substrate. Choi and Lee et al. fabricated PDMS/PZT multilayer structures for biomedical force sensing

applications; however, their devices remain stiff due to the rigid silicon substrate [14-15]. Poly(vinylidene fluoride-trifluoroethylene) (PVDF-TrFE) piezoelectric polymer films have been proposed to overcome this limitation; however, their d_{33} coefficient of ~14 pm/V limits sensor response in low pressure regions of the foot [16-17].

Although limited, some methods exist to fabricate flexible ceramic piezoelectric films. Among the reported routes for preparation of high quality piezoelectric films on flexible substrates are laser lift-off (LLO) processing [18-19], etching of a sacrificial layer such as SiO_2 [20-21], $(La,Sr)MnO_3$ [22], or ZnO [23], and direct deposition on a flexible substrate. The first two approaches deposit the ferroelectric films on a substrate compatible with a high temperature crystallization step (typically >550°C); the resulting film is then transferred to a flexible substrate such as a polymer. Alternatively, thin, oxidation-resistant metal foils have been used as flexible substrates. Ferroelectric films can be directly deposited onto these substrates via sputter deposition [24], sol-gel spin coating [25], or dip-coat deposition [26]. Dip, or immersion coating is a promising route to directly deposit bilayer piezoelectric ceramic films on a wide range of substrate geometries.

In this study, a 1 μm thin lead zirconate titanate film on a 25 μm thick stainless steel (SS) foil is proposed as a novel, flexible insole embedded force sensor. Dip coating was employed to directly deposit the piezoelectric films onto the oxidation-resistant SS foil. Photolithographic processing enabled a high density of electrodes to be placed on the piezoelectric film surface, and the entire sensor structure was embedded in a layer of PDMS for improved mechanical resilience. Five individual sensors were tested for voltage output with direct compression to imitate a single toe response, a roll-test to simulate the ball of the foot rolling during a step, and a test utilizing a squishy “tup,” or indenter in the rough shape of a heel, to emulate a heel-strike. Various electrodes displayed an output voltage of nearly 200 mV with less than 60 N applied force. The signal was amplified, wirelessly transmitted, and recorded on a nearby computer to demonstrate

real-time, wireless, and low-power application feasibility. Previous ceramic piezoelectric films have not exhibited the flexibility, mechanical resilience, power-free capability, or data processing strategies to successfully track weight distribution remotely.

5.2. Experimental procedure

5.2.1 Piezoelectric film growth and structural characterization

Piezoelectric films were deposited onto a 50x50 mm^2 stainless steel 304 (SS-304) metal-foil substrate, 25 μm thick, purchased from TDC Corporation. Preparation of the substrate and the PZT solution, as well as the dip coat deposition parameters have been described previously [27]. Briefly, a thin 50 nm HfO_2 film was deposited onto both surfaces of the pre-polished foil via atomic layer deposition to act as a passivation layer. $LaNiO_3$ films were sputter deposited (99.9% pure lanthanum nickel oxide target, Kurt J. Lesker) onto both surfaces of the foil to a thickness of 100 nm at a chamber temperature of 275ºC, 90W RF power, an Ar/O_2 gas ratio of 3:1, and a chamber pressure of 7 mTorr. The $LaNiO_3$ films acted as both a bottom electrode and an orienting seed layer for the PZT film growth. The $LaNiO_3$ sample was annealed at 500ºC for one minute in a rapid thermal annealer (RTA) with 2 sccm O_2 gas flow after sputter deposition to better crystallize the film.

Dip coat chemical solution deposition enabled simultaneous film growth of $[Pb_{0.98}■_{0.01}(Zr_{0.52}Ti_{0.48})Nb_{0.02}O_3]$, where ■ denotes a lead vacancy, onto both substrate surfaces. A 0.6 M acetic-acid based Nb-doped PZT (52/48) solution was prepared according to Peters et al. [27], and the SS-304 substrate was dipped, held for 1 second in solution, and withdrawn at a rate of 30 mm/min. The depositions were performed in a fume hood with circulating airflow, and a withdrawal distance of at least twice the length of the substrate above the solution bath prior to thermal processing. After each “dip,” the sample was placed on two consecutive hotplates, 300ºC

and 420ºC respectively, to pyrolyze the film, followed by a crystallization step in a rapid thermal annealing (RTA) furnace at 650ºC for 2 minutes with 2 sccm O_2 gas flow. The hotplate setup is displayed in Figure D.1 in Appendix D. Single layer PZT thicknesses were measured as 88.4 ± 2.0 nm with a Nanometrics Nanospec Thin Film Thickness System, and the process was repeated 12 times with the same substrate dip direction to achieve a thickness of approximately 1 μm. The PZT film is expected to be under compressive stress; based on Equation 4.1, ν_s=0.265, Y_s=190 GPa, t_s=25 μm, and thermal film stress (σ_{CTE}) ≈ -481.4 MPa. This value is between the thermal stress calculated for PZT on Ni and PZT on Ag, as the CTE of SS-304 falls between these two substrates near ~17.3 x10^{-6} K^{-1}.

The film surface was imaged with a Zeiss Merlin field emission scanning electron microscope (FESEM) equipped with a Gemini II column. An operating voltage of 5 kV was implemented with a working distance of 5 mm and an in-lens secondary electron detector. Film surface characteristics were compared between eight different regions on the sample with FESEM analysis and energy dispersive x-ray spectroscopy (EDS). X-ray diffraction (XRD) was performed on the center region of the sample with a Malvern Panalytical Empyrean III, operating with a generator voltage of 45 V and a tube current of 40 A. The scan range of the Bragg-Brentano XRD mode was 20-70º with a scanning rate of 0.0673º. Of interest was the $LaNiO_3$ and PZT film crystallinity, orientation, and the underlying substrate oxide and passivation layer growth.

5.2.2 Sensor fabrication

The process flow for the sensor fabrication is shown in Figure 5.1. Twelve circular electrodes both 1 and 2 mm in diameter, 24 electrodes in total, were patterned with a standard dual-layer photolithography procedure (Figure 5.1, steps 2-3). Platinum was sputter deposited to 100 nm, followed by lift-off in a 70ºC bath of 1165 PR remover to enable dielectric characterization (Figure 5.1, step 4). The sample was annealed at 600ºC for 1 minute in 2 sccm

O_2 gas flow in an RTA to improve adhesion between the PZT and Pt electrodes prior to electrical measurements. The real and imaginary parts of capacitance were measured with 30 mV AC from 10 to 10^6 Hz with a Solartron Modulab XM. Polarization-electric field (P-E) hysteresis loops were measured with a Radiant Technologies Precision Multiferroic tester at ±200, ±400, and ±600 kV/cm applied electric fields. A 2:1 volume ratio of photopatternable Bis-Benzocyclobutene (BCB): mesitylene was then deposited, pre-exposure baked, exposed, post-exposure baked, developed, cured, and descummed (Figure 5.1, steps 5-6). The photolithographic parameters for BCB processing have been described previously [28] and resulted here in a BCB film approximately 1 μm thick. The photomask contained circular patterns ~5% smaller than the 1- and 2-mm diameter platinum electrodes. Then, the surface was patterned with dual-layer LOR-5A and SPR-3012 positive photoresist to create 500 μm wide leads connecting to larger 3 x 7.5 mm^2 pads (Figure 5.1, steps 7-8). Sputter deposition was used to coat the film with a 30 nm Ti adhesion layer and 100 nm Au (Figure 5.1, step 9). Lift-off was performed with a 70ºC bath of 1165 PR remover, and the gold leads and pads remained on the BCB surface (Figure 5.1, step 9 top). Next, gold-plated brass crimps were placed on each gold pad and mechanically secured with a 2-part conducting silver epoxy. Individual 20-gauge wires were placed and secured within each crimp (Figure 5.1, step 10). The whole structure was embedded in polydimethylsiloxane (PDMS) by mixing the base and curing agents at a volume ratio of 10:1, de-airing in a vacuum desiccator to remove trapped air bubbles, pouring the bubble-free PDMS into a plastic petri-dish containing the sensor array, and curing the PDMS in a curing oven at 65ºC for 240 minutes (Figure 5.1, step 11). The PDMS thickness was several millimeters and provided some structural rigidity to the PZT sensing device. Then, each electrode was poled through the 20-gauge wires at 70ºC and 180 kV/cm electric field for 15 minutes with the DC voltage supply positive terminal connected to the top electrode and the negative terminal connected to the common ground $LaNiO_3$ layer.

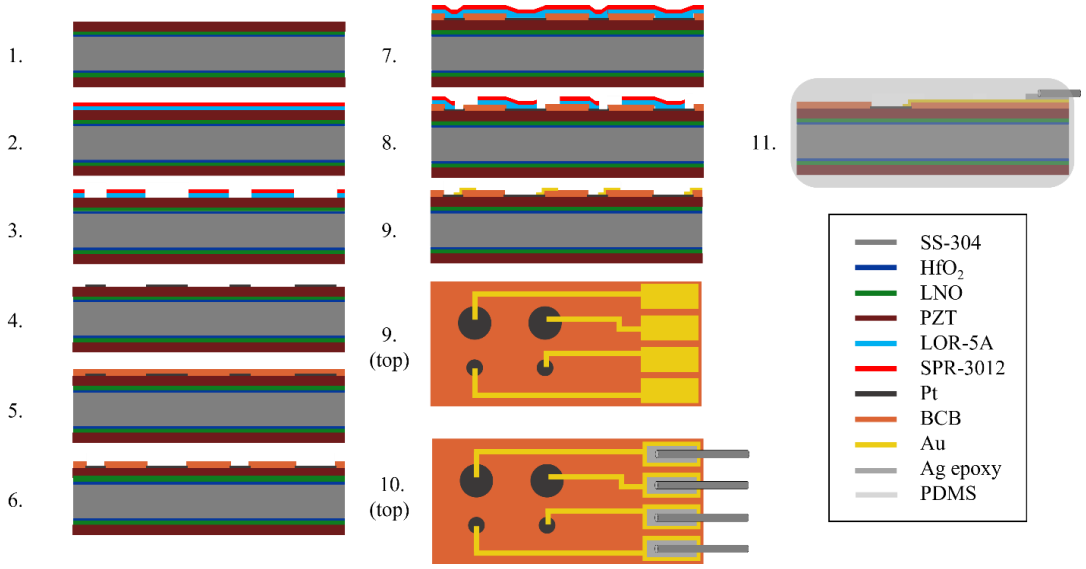

Figure 5.1: Flexible piezoelectric force sensor fabrication flow. Step 1: Start with a PZT/LNO/HfO_2/SS-304 sample. Step 2: Spin coat and cure LOR5A and SPR-3012 dual layer photoresist. Step 3: Expose/develop electrode pattern. Step 4: Sputter 100 nm platinum and lift-off photoresist. Step 5: Spin coat & cure BCB. Step 6: Expose, bake, develop, cure, and descum BCB. Step 7: Spin coat and cure LOR-5A and SPR-3012 dual layer photoresist. Step 8: Expose/develop gold electrode pattern. Step 9: Sputter 30 nm Ti and 100 nm Au electrodes. Lift off photoresist. Step 10: Place and cure crimps with silver epoxy. Crimp 20-gauge wires. Step 11: Embed structure in PDMS layer.

5.2.3 Sensor performance testing

Initial testing of the sensing array was performed by manually pressing on 1 mm and 2 mm diameter electrodes separately and measuring the voltage response with an oscilloscope. Measurements to approximate the sensitivity of a single capacitor were performed on an Instron 5969 Universal Testing Machine with a machined circular head 20 mm in diameter. A schematic of the setup is shown in Figure D.2a in Appendix D, where a unity gain buffer circuit was connected directly to the top electrode. The output of the unity gain buffer was connected to a Tektronix MDO 3014 oscilloscope connection. To roughly simulate the ball of the foot rolling over the pressure sensing array, an 8 cm diameter roll of electrical tape was rolled under moderate pressure over the pressure sensing array. The cylinder was first rolled in a diagonal direction such that the cylinder rolled over electrode K2 first, then over electrodes G2 and L2, and finally over electrode H2. The cylinder was then rolled straight over electrodes K2 and L2 and then over

electrodes G2 and H2. These four electrodes were connected to a Tektronix MDO 3014 oscilloscope with high impedance (10 MΩ) probes. A 4th order Butterworth bandpass filter, with low and high cutoff frequencies of 5 and 100 Hz, respectively, was applied to the raw open circuit voltage to remove DC bias and noise. Then an IIR notch filter centered at 60 Hz was applied to remove noise from the mains.

To simulate the heel pressing down on the pressure sensing array, the foil was tested on an Instron 5969 Universal Testing Machine. A "tup" or indenter in the rough shape of a heel was machined per the specifications of ASTM F1975-13: a flat, circular surface 45 mm in diameter with a 1 mm edge fillet radius. A "squishy tup" made of elastomer was attached to this machined tup to observe the effect of a softer surface pressing down on the pressure sensor array. A schematic of the setup is displayed in Figure D.2b in Appendix D. The squishy tup pressed down on the pressure sensor array in a triangle wave with 3 mm amplitude. The displacement rate of the Instron was 10 mm/sec. The test was performed centered above electrode H2, activating H2 first, followed by G2 (which is closest) and finally L2 and K2. The data acquisition and data processing procedures were like those used for the laboratory tests.

5.3 Results and discussion

X-ray diffraction analysis of the underlying $LaNiO_3$ (LNO) seed layer and subsequent PZT layer were necessary to verify the crystallinity and orientation of the piezoelectric thin film. Figure 5.2 displays Bragg-Brentano X-ray diffraction data of the LNO and crystallized 1 μm PZT. The sputtered LNO shows random crystallographic orientation and low peak intensities. The poor {001} orientation of the LNO was attributed to mediocre thermal transfer between the substrate holder and the substrate. The PZT film templated from the random crystallographic orientation of the LNO. LIPRAS [29] software was utilized to fit each PZT peak with an

asymmetric Pseudo-Voigt function and background intensity was subtracted to extract the integrated intensity. The Lotgering factor for <001> orientation was calculated as LF=$(p-p_o)/(1-p_o)$ where p denotes the fractional sum of <001> peaks and p_o is p of the material with a random particle distribution [30]. The {100} Lotgering factor for the 1 µm thick PZT film was 47%. In addition to the perovskite peaks, the XRD scan shows peaks from the passivation HfO_2 layer, Cr_2O_3 from the stainless-steel substrate oxidation during multiple anneal steps at 650°C, and the stainless-steel substrate.

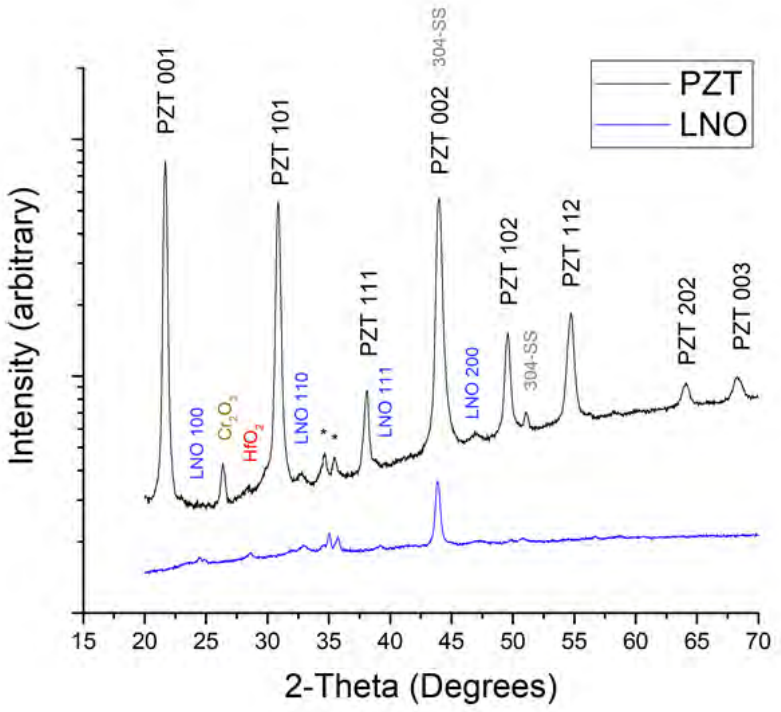

Figure 5.2: X-ray diffraction of $LaNiO_3$ film (blue) and 1 µm PZT (black). The HfO_2 (red) peak and stainless-steel substrate (grey) peaks are displayed in both scans, but Cr_2O_3 (gold) is present only in the PZT scan.

Figure 5.3 displays the scanning electron microscopy (SEM) images of eight separate regions of the dip cast PZT thin film. The center image shows an optical image of the 50 mm x 50 mm sample, and the red circles indicate approximately where each SEM image was taken on the surface. The blue arrow indicates the down direction during dip casting; a common orientation

was maintained for all 12 dipping steps. The middle image shows a yellow region near the base of the sample which was the last surface of the foil to leave the sol-gel bath. Surface tension of the liquid led to accumulation at the bottom of the substrate, causing cracking in the PZT film. The cracked region grew up the film after each dip. Thus, the bottom 10% of the substrate was removed post-processing to eliminate this cracked area.

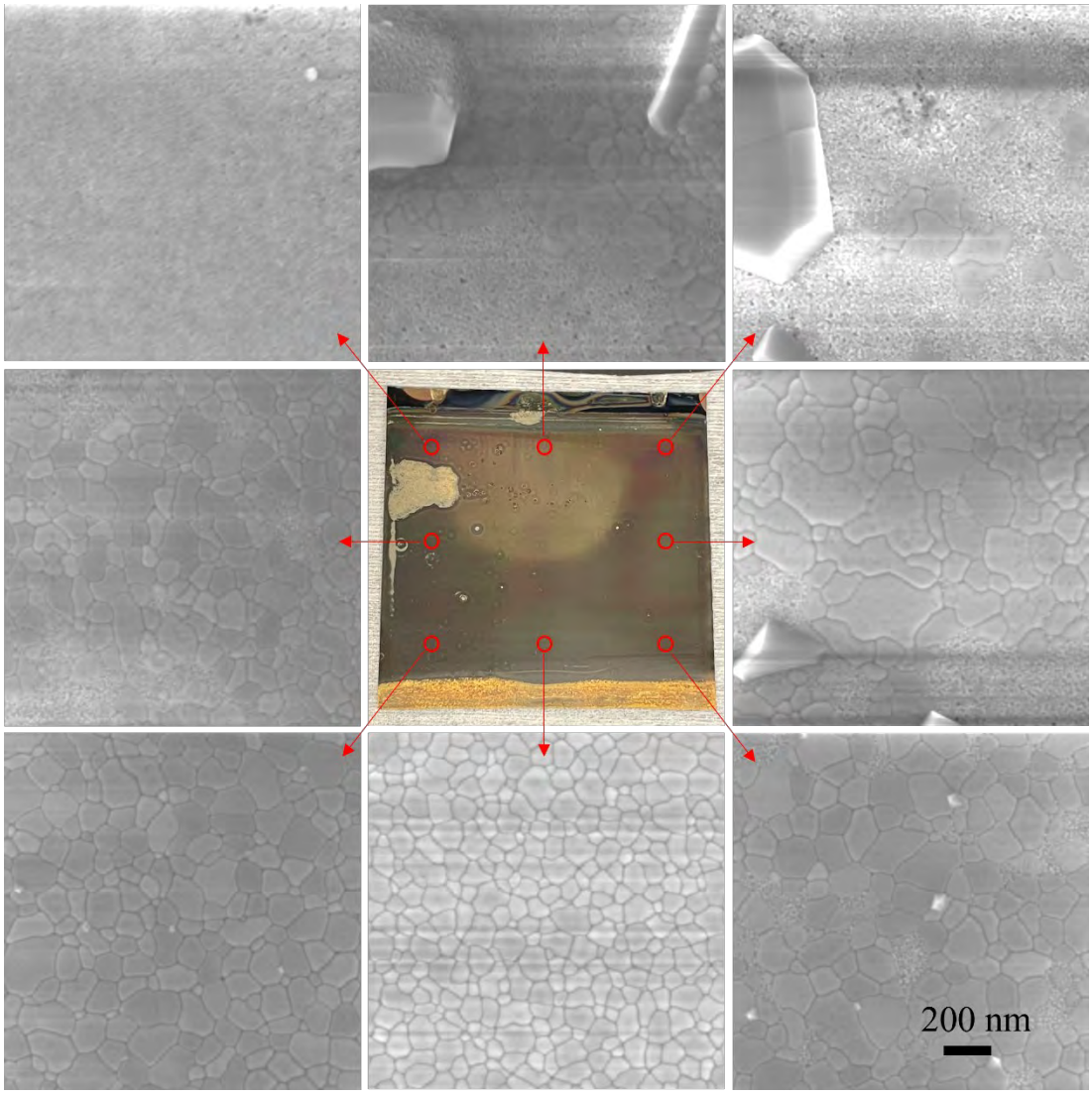

Figure 5.3: Scanning electron microscopy; 8 regions of the 50 mm x 50 mm PZT film.

The three rows of SEM scans display variation in the surface structure of the 1 μm thick PZT film. The first row displays a significant amount of non-ferroelectric pyrochlore and large

hexagonally shaped inclusions. Energy-dispersive X-ray spectroscopy analysis revealed that these inclusions were lead-rich chromium oxide growth from the underlying stainless-steel substrate. The 50 nm HfO_2 passivation layer reduced the growth of Cr_2O_3; most of the film surface does not show inclusions. The second row shows more perovskite grains than the first row, with some pyrochlore remaining. The final row, closest to the bottom of the substrate, displays very little pyrochlore in a high-density perovskite matrix. X-ray photoelectron spectroscopy (XPS) enabled the direct measurement of surface lead content down the film surface. Figure D.3 in Appendix D displays optical ellipsometry paired with XPS measurements prior to the high temperature crystallization step. Thickness and lead content appear inversely related, with %Pb increasing towards the base of the sample. Figure D.4 in Appendix D shows the XPS and ellipsometry results after a 650°C anneal for 2 minutes in an RTA. Lead content decreases down the length of the film and appears to match the microstructural variation from SEM analysis in Figure 5.3.

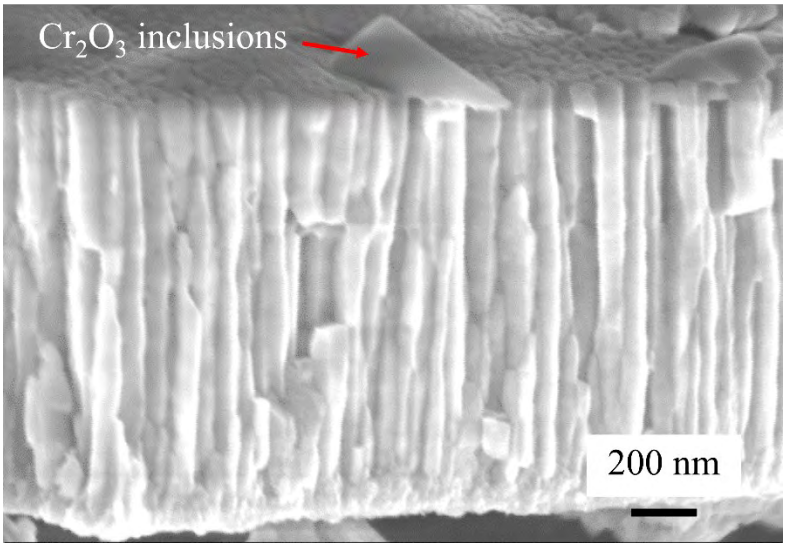

Figure 5.4: Cross-section SEM of ~1 μm PZT

A columnar grain structure of the film is depicted in the cross-sectional SEM image in Figure 5.4. This image was taken near the base of the film, in the region with minimal pyrochlore. The lead rich Cr_2O_3 inclusions are shown by the red arrow. Further evidence of the Cr_2O_3

inclusion growth is displayed in Figure D.5 in Appendix D, showing energy dispersive spectroscopy mapping. Figure D.6 shows an additional cross-section SEM image.

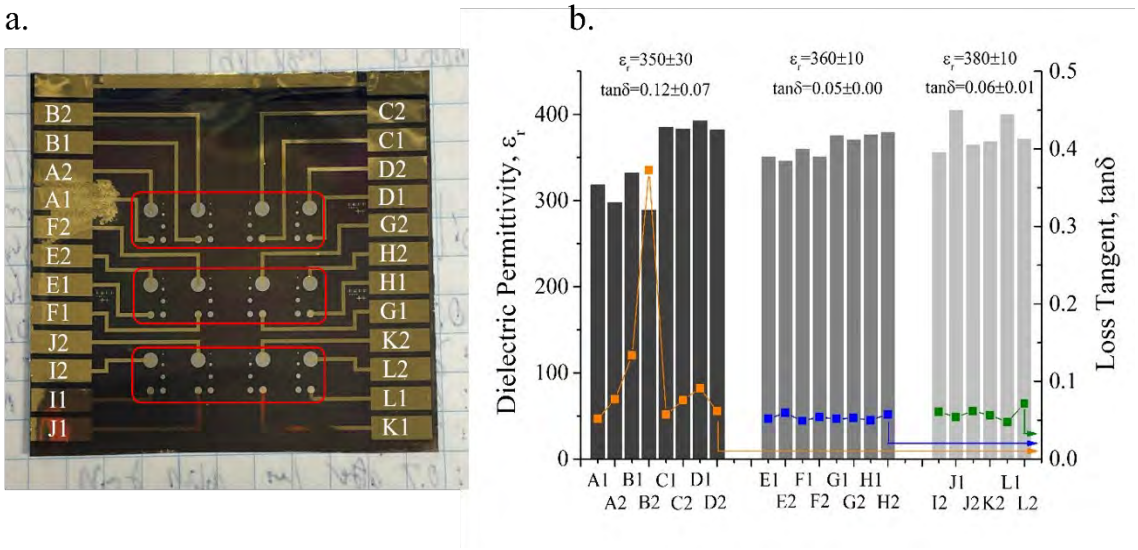

Figure 5.5: (a) Electrode map of PZT film on SS-304 foil, where the letter denotes the region on the sample (top row is A-D left to right, middle row E-H etc.) and the number shows the electrode diameter (in mm). (b) Dielectric permittivity and loss tangent for each capacitor in (a) at 100 Hz for the top (dark grey), middle (grey), and bottom (light grey) rows of electrodes circled in red. Orange, blue, and green datapoints indicate loss tangents.

Dielectric capacitance and loss tangents were measured with 30 mV AC voltage on electrodes distributed across the surface of the PZT film. Figure 5.5a shows a map of the 24 electrodes measured. Figure 5.5b shows the permittivity (bar chart) and loss tangent (scatter plot) at *100 Hz* frequency of 22 capacitors, separated by row on the PZT film. Figure 5.5b shows a lower permittivity with high variation (average ε_r=350±30) and higher losses (average tanδ=0.12±0.07) for the top row of capacitors (dark grey); two capacitors show a permittivity below 300 at 100 Hz, which can be explained by the pyrochlore and Cr_2O_3 inclusions. The middle row of capacitors (grey) in Figure 5.5b shows a tighter distribution of dielectric permittivity (average ε_r=360±10) and losses near 0.05±0.00. The consistent low loss and high permittivity of the electrodes in this row can be attributed to decreased pyrochlore and Cr_2O_3 inclusion growth. The final row (light grey) contains six capacitors with an average loss tangent of 0.06±0.01 and

an average dielectric permittivity of 380±10. Electrodes I1 and K1 displayed high dielectric loss at and below 100 Hz, and thus were removed from the dataset. Dielectric permittivity and loss tangents appear to match the microstructural variation in Figure 5.3 and XPS analysis of lead content variation. Overall average dielectric permittivity was 360 ± 3.5% with an average loss tangent of 0.08.

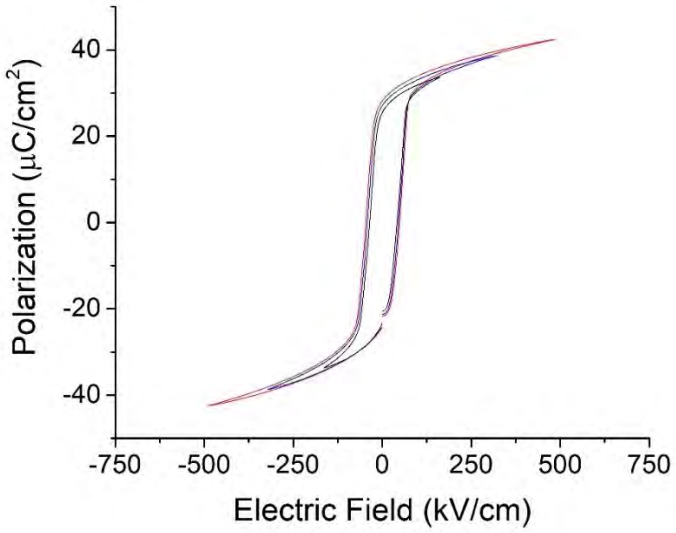

Figure 5.6: Nested P-E hysteresis loops of 1 mm diameter electrode near the middle of the film.

Figure 5.6 displays polarization electric-field hysteresis loops measured at 200, 400, and 600 kV/cm. The loops show high remanent polarization values of +28.2 μC/cm^2 and -24.3 μC/cm^2 and typical coercive fields of 59.4 kV/cm and -56.7 kV/cm, showing little to no imprint. It is assumed, based on the high remanent polarization and low dielectric permittivity values, that the majority of <001> domains are aligned out-of-plane. This is in agreement with the thermal expansion coefficient mismatch between the stainless-steel substrate and PZT film; upon cooling from the crystallization temperature, the film was placed in compression, forcing many domains out-of-plane [27], [31-33].

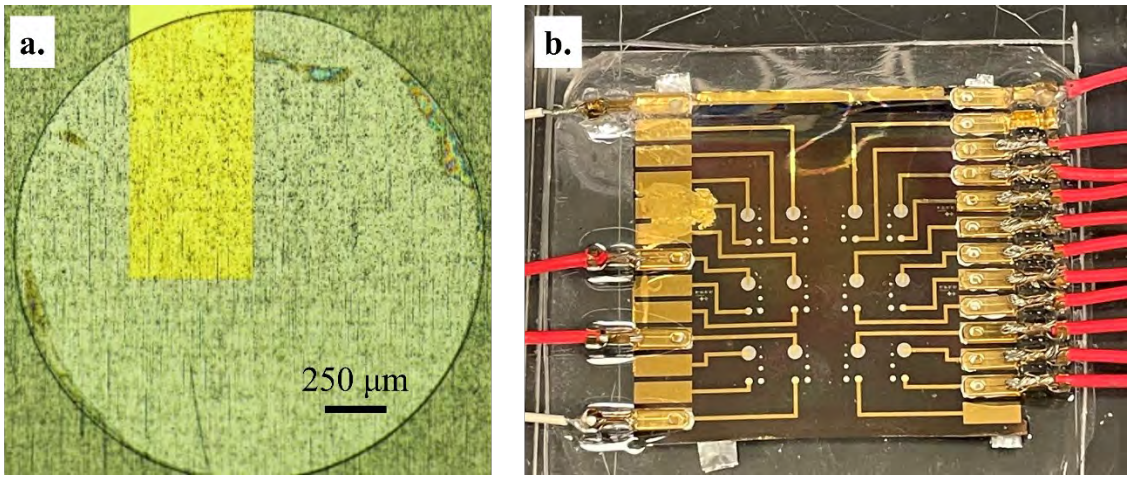

Figure 5.7: (a) Lithographically defined 2 mm diameter platinum electrode, BCB photoresist outside of the circle, and 500 μm wide gold leads connecting the Pt electrode to the gold pad. (b) Final device structure embedded in PDMS with epoxied crimps attaching 20-gauge wires to each gold pad.

Figure 5.7a shows an optical microscope image of a single 2 mm diameter capacitor; the bottom layer is the circular platinum electrode, outside of the circle is an insulating BCB layer, and the top layer is the patterned gold lead connecting the electrode to a pad on the edge of the sample. The vertical lines correspond to the original roll marks of the foil. Figure 5.7b displays the final device, with brass-plated crimps connected via conductive silver epoxy to each gold pad, and 20-gauge wires individually crimped. The device is embedded in a PDMS layer. The top left white wire is connected to the bottom $LaNiO_3$ layer, acting as the ground electrode for all capacitors.

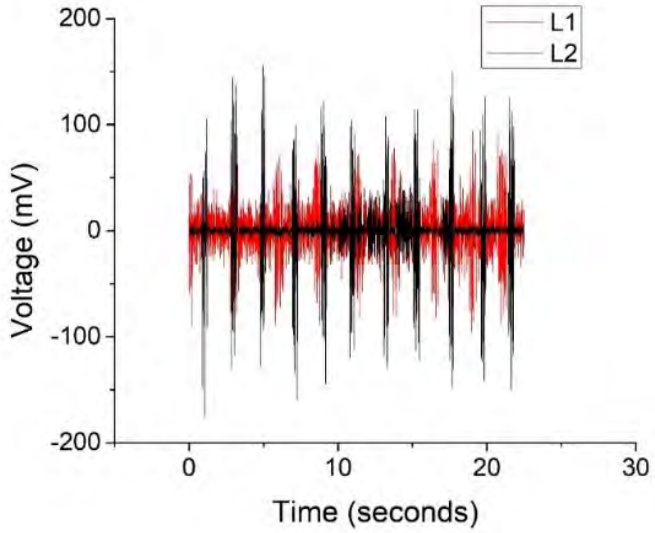

Figure 5.8: Voltage output measured on an oscilloscope when manually pressing on a 2 mm diameter electrode (L2) and a 1 mm diameter electrode (L1).

Five electrodes were selected for sensor application analysis: G2, H2, K2, L2, and L1 (labeled in Figure 5.5a, Figure 5.10, and Figure 5.11). Table D.2 in Appendix D shows the capacitance, loss, and permittivity at *1 kHz* and 30 mV applied AC voltage at three different stages of the fabrication process. A parasitic capacitance of 890 ± 150 pF originated from the gold lead areas on the surface of the BCB. After poling each capacitor individually, the permittivity decreased to nearly the value that was measured prior to BCB deposition. To test device functionality, a short pressure pulse was applied with a capped pen directly onto electrodes L1 and L2. The signal was measured with an oscilloscope for 22 seconds, applying a pressure every 2 seconds. Figure 5.8 shows the signal of the 2 mm diameter capacitor (L2) in black and the 1 mm diameter capacitor (L1) in red. The larger electrode displays a higher signal for each pulse, the smaller electrode shows a higher noise signal, and both electrodes experience fast response and recovery times.

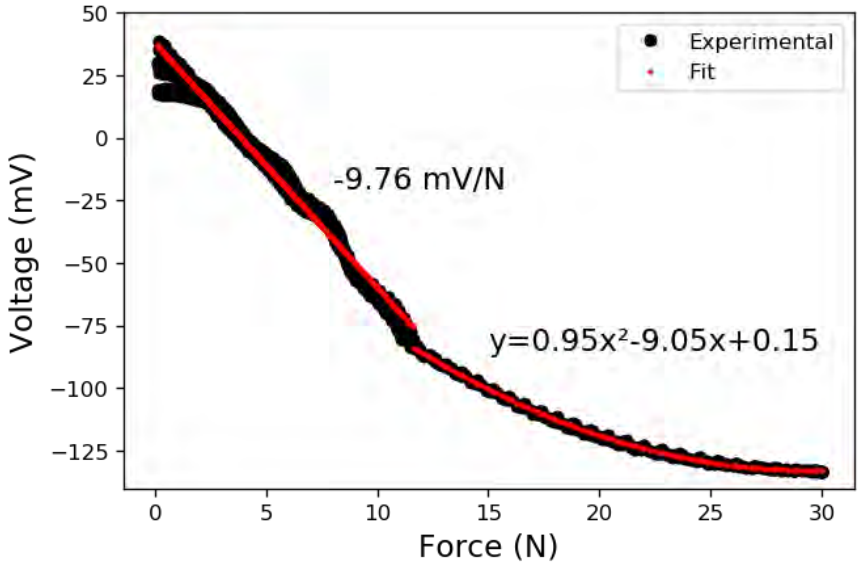

Figure 5.9: Output voltage vs applied force for electrode G2. The low force regime (0-12 N) shows a linear sensitivity of -9.76 mV/N and the high force regime (12-30 N) shows a nonlinear voltage response.

To measure the sensitivity of the sensor array, ten cycles of 30 N were applied to electrode G2. Figure D.2a in Appendix D shows a schematic of the setup and Figure D.7 displays the measurement analysis of the voltage response and force cycles with time. The voltage output with applied force, shown in Figure 5.9, displays a piecewise response with increasing applied force from 0 to 30 N; this is attributed to the mechanical response of the protective PDMS shell. The strain response of PDMS with an applied stress is best modeled with a nonlinear second-order Ogden model [34]. At low stresses, PDMS displays a low elastic modulus and transfers strain to the embedded PZT film. At forces below ~12 N, the piezoelectric capacitor displays a sensitivity of -9.76 mV/N and a linear regression R^2 value of 0.98. At higher forces, the elastic modulus of PDMS increases and supports more of the applied stress. The response is a nonlinear function of output voltage with applied force and exhibits a best fit 2nd order polynomial function of $y=0.95x^2-9.05x+0.15$ mV/N and an $R^2=0.98$.

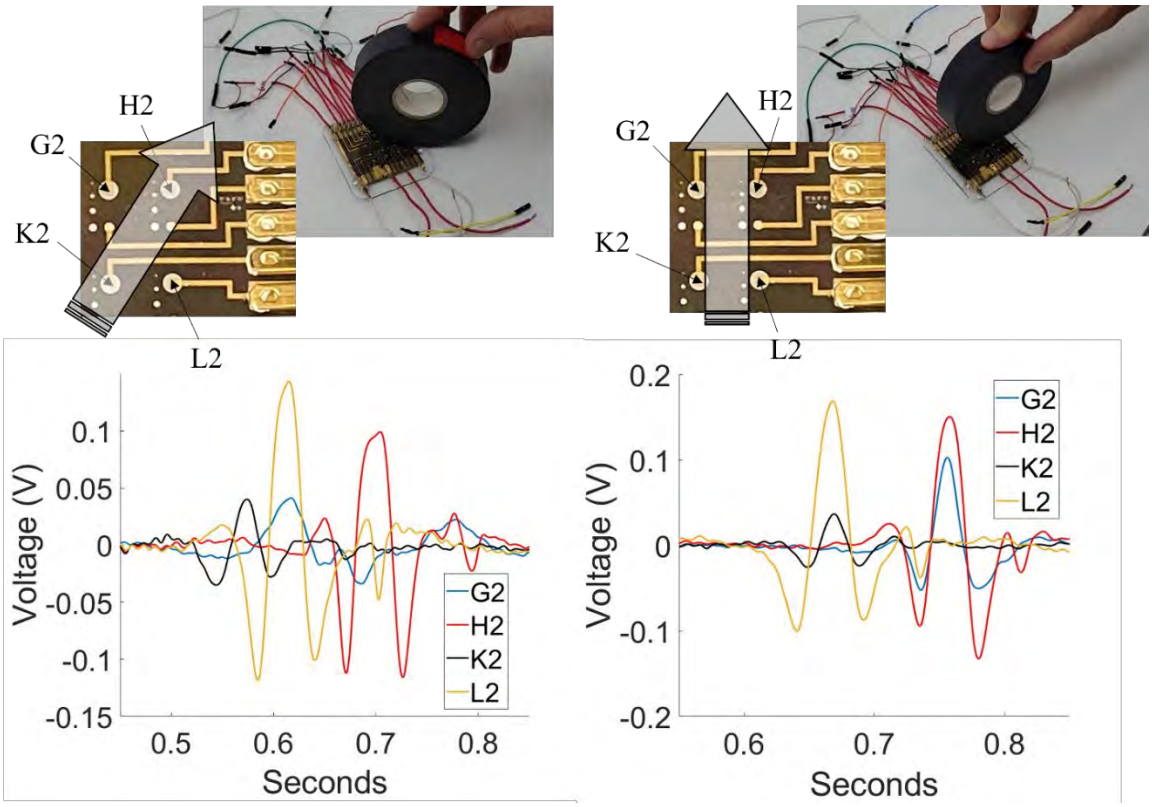

Figure 5.10: Open circuit voltages from "roll test" in which a cylinder was rolled over the pressure sensing array. The left-side images show the cylinder rolling diagonally over the sensing foil in the direction of the arrow. Open circuit voltages for the "diagonal roll" are displayed in the bottom left. The right-side images show the cylinder rolling straight over the sensing foil, where the bottom right plot displays open circuit voltages from the "straight roll".

An imitation of the "roll" that occurs during a single step from the ball of the foot was investigated. Figure 5.10 shows the open circuit voltage output from diagonal and straight roll tests performed in the lab. Note that the force on the pressure sensing foil was not controlled in this experiment. The pressure sensors' ability to locate the center of pressure from the activation time of different electrodes was tested. The shape of the signal, resulting from something rolling over the pressure sensors, was also evaluated. Electrode K2 was expected to be activated first for the diagonal roll, followed by electrodes G2 and L2, and finally, electrode H2. For the straight roll, electrodes K2 and L2 were expected to show activation first, followed by electrodes G2 and H2. The activation of the voltage signal from each electrode occurred with the expected timing. Note that electrode K2 had a lower sensitivity in this experiment, so its voltage output is lower.

Electrodes G2, H2, and L2 exhibited similar voltage amplitudes to the applied forces, estimated as 20 – 30 N. Given the poling direction of the piezoelectric material, a compressive force should result in a negative voltage. The reason for the potential shape of each voltage signal (trough-peak-trough) as it rolls over the electrode is not immediately clear. The foil was likely subjected to some level of bending and compression during this test. It is also possible that the electrode was subjected to shear forces. Mechanical crosstalk will exist between individual sensors on the same flexible metal substrate due to mechanical coupling; however, there is no electrical coupling between individual sensors. The voltage response at capacitors away from the applied force may provide additional information if the data is properly documented and analyzed. To limit the applied force on the device during operation to only compressive, either a supporting structure or a more sophisticated post-processing is necessary.

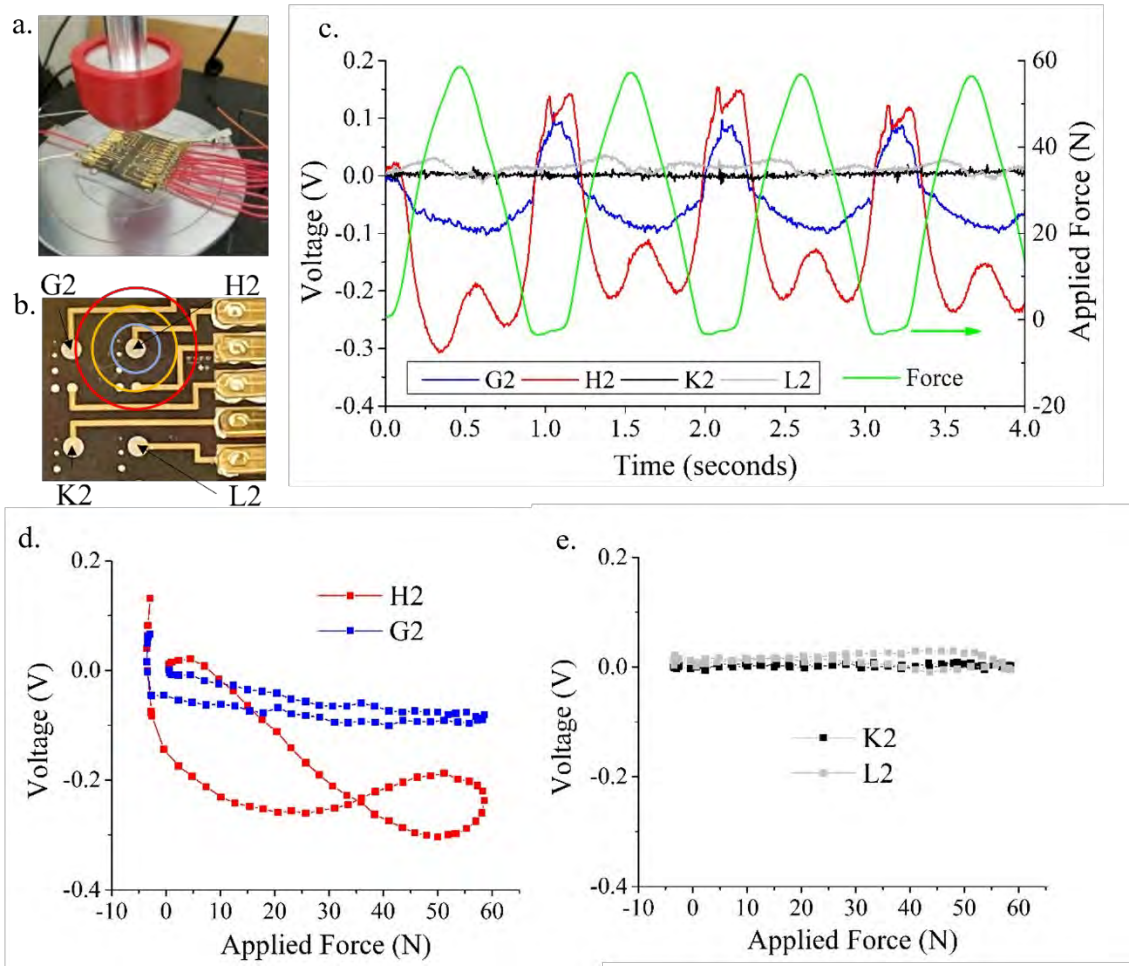

Figure 5.11: (a) Image of pressure sensing array mounted on the material testing machine with a squishy tup to imitate a heel strike. (b) Location of the center of tup over the top of electrode H2. (c) Open circuit voltage and force applied during compression tests on material testing machine. (d) Output voltage of H2 and G2 electrodes vs applied force for the first force cycle (e) Output voltage of K2 and L2 electrodes for the first force cycle.

An Instron 5969 Universal Testing System was equipped with a silicone-based cup (tup) to imitate a heel strike. This is displayed in Figure 5.11a. The tup location is shown in Figure 5.11b, centered over electrode H2 and interacting with G2. Figure 5.11c shows the open circuit voltage from the four electrodes and the applied force from the Instron at a compression speed of 10 mm/s. Note that the Instron was equipped with a "squishy tup" which means that the contact area between the tup and the pressure sensing foil increased as the Instron moved down. Therefore, the pressure on any given electrode at a specific time is not exactly known. Electrode

H2 had the largest response, followed by G2 (the electrode closest to H2); this is shown in Figure 5.11d in the voltage response vs applied force figure. A small response was recorded from K2 and L2, displayed in Figure 5.11e. From this experiment, the location of the center of pressure of the tup was deduced. However, as with the cylinder roll tests, the electrodes were likely exposed to a combination of bending and compressive stresses and therefore the compressive force cannot be directly back calculated from these voltage signals.

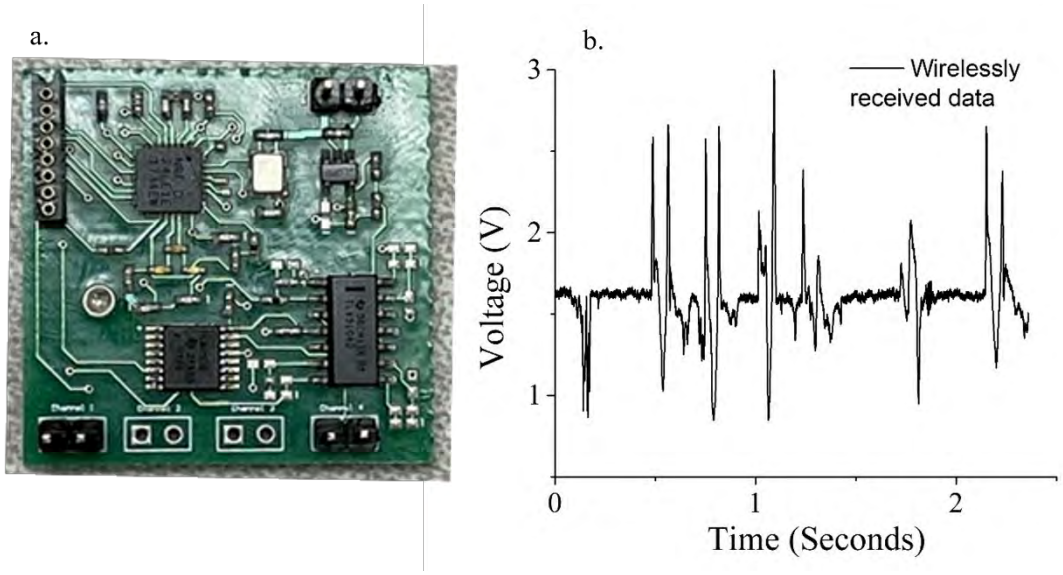

Figure 5.12: (a) Discrete circuit prototype for multi-channel sensing, digitization, and wireless transmission of the activation signal. (b) Wirelessly logged data from channel 1 when the flexible sensor was connected to it and the electrode D2 was pressed by a capped pen.

For practical applications in a remote balance sensor, the raw data from the flexible sensor should be recorded and wirelessly transmitted to a device (e.g., a PC or smartphone) for further signal processing and data storage. This would enable real-time monitoring. As a proof of concept, a discrete circuit was designed, developed, and tested using off-the-shelf components on a printed circuit board (PCB). The PCB supported multi-channel (up to 4 channels) data sensing, which included amplification, digitization, and wireless data transmission. Signals from each channel were first amplified using a trans-impedance amplifier (TLV9104IDR, Texas Instruments, Dallas, TX) with a feedback resistor of 10 MΩ. An analog multiplexer chip

(CD4052BPW, Texas Instruments, Dallas, TX) was used to multiplex the amplified signals from the four channels. The multiplexer select lines were controlled by a microcontroller (nRF24LE1, Nordic Semiconductor, Trondheim, Norway), and its built-in analog-to-digital converter (ADC) was used for digitization of the signal into 8-bit data at a sampling rate of 4k samples/second. The digitized data was then wirelessly transmitted using the microcontroller's built-in RF wireless transceiver operating at 2.4 GHz with a data rate of 2 Mbps (Megabits per second). Figure 5.12a shows an image of the fabricated circuit prototype. Figure 5.12b displays the wirelessly received data on channel 1 when connected to the flexible sensor and the corresponding electrode (D2) pressed with a capped pen. The spikes indicate the instances when the electrode was pressed, where the signal is biased at about 1.65 V.

5.4 Conclusions

A ~1 μm thin PZT film was dip cast via sol gel chemical solution deposition directly onto a flexible 25 μm thick stainless-steel foil. The PZT film displayed dielectric permittivities of 360 ± 10 with losses of 0.07 ± 0.03 at 100 Hz and remanent polarizations of 26.3 ± 3.8 $\mu C/cm^2$. Photolithography enabled the fabrication of individual capacitor structures designed in an array structure around the surface of the film. A nonlinear voltage output at forces higher than 12 N originated from the thicker PDMS layer and is a cause for concern, as real forces applied to the film from a footstep are more than an order of magnitude higher than those reported here (albeit spread out over a wider area). To combat this and retain a highly sensitive, linear response at higher applied forces, a layered structure involving a stiffer polymer closer to the sensor array and flexible PDMS for user comfort near the shoe sole is of interest for the next generation of this device. Five capacitors displayed fast response times, high sensitivity, as well as high mechanical and electrical robustness. In addition, they are inherently thin, flexible, lightweight, and require

zero external power input to operate. Flexible PZT films were demonstrated here to successfully operate as insole-embedded pressure sensing films.

5.5 References

[1] G. Bergen, M. R. Stevens, and E. R. Burns, "Falls and fall injuries among adults aged ≥65 Years — United States, 2014," *MMWR. Morb. Mortal. Wkly. Rep.*, vol. 65, no. 37, pp. 993–998, 2016, doi: 10.15585/mmwr.mm6537a2.

[2] B. Moreland, R. Kakara, and A. Henry, "Trends in nonfatal falls and fall-related injuries among adults aged ≥65 years — United States, 2012–2018," *MMWR. Morb. Mortal. Wkly. Rep.*, vol. 69, no. 27, pp. 875–881, 2020, doi: 10.15585/mmwr.mm6927a5.

[3] C. S. Florence, G. Bergen, A. Atherly, E. Burns, J. Stevens, and C. Drake, "Medical costs of fatal and nonfatal falls in older adults," *J. Am. Geriatr. Soc.*, vol. 66, no. 4, pp. 693–698, 2018, doi: 10.1111/jgs.15304.

[4] M. Cheng, G. Zhu, F. Zhang, W.L Tang, S. Jianping, J.Q. Yang, and L.Y. Zhu, "A review of flexible force sensors for human health monitoring," *J. Adv. Res.*, vol. 26, pp. 53–68, 2020, doi: 10.1016/j.jare.2020.07.001.

[5] M. Ntagios, S. Dervin, and R. Dahiya, "3D printed capacitive pressure sensing sole for anthropomorphic robots," *FLEPS 2021 - IEEE Int. Conf. Flex. Printable Sensors Syst.*, pp. 1–4, 2021, doi: 10.1109/FLEPS51544.2021.9469839.

[6] S. Gong, W. Schwalb, Y. Wang, Y. Chen, Y. Tang, J. Si, B. Shirinzadeh, W. Cheng, "A wearable and highly sensitive pressure sensor with ultrathin gold nanowires," *Nat. Commun.*, vol. 5, pp. 1–8, 2014, doi: 10.1038/ncomms4132.

[7] J. Yu, X. Hou, M. Cui, S. Shi, J. He, Y. Sun, C. Wang, and X. Chou, "Flexible PDMS-based triboelectric nanogenerator for instantaneous force sensing and human joint

movement monitoring," *Sci. China Mater.*, vol. 62, no. 10, pp. 1423–1432, 2019, doi: 10.1007/s40843-019-9446-1.

[8] X. Liu, M. Mwangi, X. Li, M. O'Brien, and G. M. Whitesides, "Paper-based piezoresistive MEMS sensors," *Lab Chip*, vol. 11, no. 13, pp. 2189–2196, 2011, doi: 10.1039/c1lc20161a.

[9] K. Jenkins, V. Nguyen, R. Zhu, and R. Yang, "Piezotronic effect: An emerging mechanism for sensing applications," *Sensors (Switzerland)*, vol. 15, no. 9, pp. 22914–22940, 2015, doi: 10.3390/s150922914.

[10] Z. Yi, H. Yang, Y. Tian, X. Dong, J. Liu, and B. Yang, "Self-powered force sensor based on thinned bulk PZT for real-time cutaneous activities monitoring," *IEEE Electron Device Lett.*, vol. 39, no. 8, pp. 1226–1229, 2018, doi: 10.1109/LED.2018.2846184.

[11] Y. Tian, P. He, B. Yang, Z. Yi, L. Lu, and J. Liu, "A flexible piezoelectric strain sensor array with laser-patterned serpentine interconnects," *IEEE Sens. J.*, vol. 20, no. 15, pp. 8463–8468, 2020, doi: 10.1109/JSEN.2020.2985063.

[12] T. A. Ring, P. Feeney, D. Boldridge, J. Kasthurirangan, S. Li, and J. A. Dirksen, "Brittle and ductile fracture mechanics analysis of surface damage caused during CMP," *J. Electrochem. Soc.*, vol. 154, no. 3, p. H239, 2007, doi: 10.1149/1.2426877.

[13] H. Liu, J. Geng, Q. Zhu, L. Zhang, F. Wang, T. Chen, and L. Sun, "Flexible ultrasonic transducer array with bulk PZT for adjuvant treatment of bone injury," *Sensors*, vol. 20, no. 1, p. 86, 2019.

[14] W. Choi, J. Lee, Y. Kyoung Yoo, S. Kang, J. Kim, and J. Hoon Lee, "Enhanced sensitivity of piezoelectric pressure sensor with microstructured polydimethylsiloxane layer," *Appl. Phys. Lett.*, vol. 104, no. 12, 2014, doi: 10.1063/1.4869816.

[15] J. Lee, W. Choi, Y.K. Yoo, K.S. Hwang, S.M Lee, S. Kang, J. Kim, J.H. Lee, "A micro-fabricated force sensor using an all thin film piezoelectric active sensor," *Sensors*

(Switzerland), vol. 14, no. 12, pp. 22199–22207, 2014, doi: 10.3390/s141222199.

[16] C. C. Hong, S. Y. Huang, J. Shieh, and S. H. Chen, "Enhanced piezoelectricity of nanoimprinted sub-20 nm poly(vinylidene fluoride-trifluoroethylene) copolymer nanograss," *Macromolecules*, vol. 45, no. 3, pp. 1580–1586, 2012, doi: 10.1021/ma202481t.

[17] S. Gao, J. L. Chen, Y. N. Dai, R. Wang, S. B. Kang, and L. J. Xu, "Piezoelectric-based insole force sensing for gait analysis in the internet of health things," *IEEE Consum. Electron. Mag.*, vol. 10, no. 1, pp. 39–44, 2021, doi: 10.1109/MCE.2020.2986828.

[18] H. S. Lee, J. Chung, G.T. Hwang, C.K. Jeong, Y. Jung, J.H. Kwak, H. Kang, M. Byun, W.D. Kim, S. Hur, and S.H. Oh, "Flexible inorganic piezoelectric acoustic nanosensors for biomimetic artificial hair cells," *Adv. Funct. Mater.*, vol. 24, no. 44, pp. 6914–6921, 2014, doi: 10.1002/adfm.201402270.

[19] M. Yao, Y. Cheng, Z. Zhou, and M. Liu, "Recent progress on the fabrication and applications of flexible ferroelectric devices," *J. Mater. Chem. C*, vol. 8, no. 1, pp. 14–27, 2019, doi: 10.1039/c9tc04706a.

[20] C. Dagdeviren, Y. Shi, P. Joe, R. Ghaffari, G. Balooch, K. Usgaonkar, O. Gur, P.L. Tran, J.R. Crosby, M. Meyer, and Y. Su, "Conformal piezoelectric systems for clinical and experimental characterization of soft tissue biomechanics," *Nat. Mater.*, vol. 14, no. 7, pp. 728–736, 2015, doi: 10.1038/nmat4289.

[21] T. Yamashita, S. Takamatsu, H. Okada, T. Itoh, and T. Kobayashi, "Development of flexible piezoelectric strain sensor array," *Electr. Eng. Japan (English Transl. Denki Gakkai Ronbunshi)*, vol. 204, no. 1, pp. 52–58, 2018, doi: 10.1002/eej.23084.

[22] S. R. Bakaul, C.R. Serrao, M. Lee, C.W. Yeung, A. Sarker, S.L. Hsu, A.K. Yadav, L. Dedon, L. You, A.I. Khan, and J.D. Clarkson, "Single crystal functional oxides on silicon," *Nat. Commun.*, vol. 7, no. 1, pp. 1–5, 2016, doi: 10.1038/ncomms10547.

[23] T. Liu, M. Wallace, S. Trolier-McKinstry, and T. N. Jackson, “High-temperature crystallized thin-film PZT on thin polyimide substrates,” *J. Appl. Phys.*, vol. 122, no. 16, 2017, doi: 10.1063/1.4990052.

[24] H. G. Yeo, X. Ma, C. Rahn, and S. Trolier-McKinstry, “Efficient piezoelectric energy harvesters utilizing (001) textured bimorph PZT films on flexible metal foils,” *Adv. Funct. Mater.*, vol. 26, no. 32, pp. 5940–5946, 2016, doi: 10.1002/adfm.201601347.

[25] H. G. Yeo and S. Trolier-McKinstry, “{001} Oriented piezoelectric films prepared by chemical solution deposition on Ni foils,” *J. Appl. Phys.*, vol. 116, no. 1, 2014, doi: 10.1063/1.4886597.

[26] H. Hida, T. Hamamura, T. Nishi, G. Tan, T. Umegaki, and I. Kanno, “Piezoelectric characterization of $Pb(Zr,Ti)O_3$ thin films deposited on metal foil substrates by dip coating,” *Jpn. J. Appl. Phys.*, vol. 56, no. 10, 2017, doi: 10.7567/JJAP.56.10PF08.

[27] T. Peters, C. Cheng, G. A. Rossetti, and S. Trolier-McKinstry, “Thermal stress accommodation in dip cast lead zirconate-titanate ferroelectric films on flexible substrates,” *J. Am. Ceram. Soc.*, vol. 105, no. 6, pp. 4058–4070, 2022, doi: 10.1111/jace.18355.

[28] T. Liu, “Thin-film PZT on polymer and glass substrates: Breaking the rules,” Ph.D. Thesis, The Pennsylvania State University, 2020.

[29] G. Esteves, K. Ramos, C. M. Fancher, and J. L. Jones, “LIPRAS: Line-profile analysis software.” 2017. doi: 10.13140/RG.2.2.29970.25282/3.

[30] R. Furushima, S. Tanaka, Z. Kato, and K. Uematsu, “Orientation distribution-Lotgering factor relationship in a polycrystalline material - as an example of bismuth titanate prepared by a magnetic field,” *J. Ceram. Soc. Japan*, vol. 118, no. 1382, pp. 921–926, 2010, doi: 10.2109/jcersj2.118.921.

[31] K. Coleman, J. Walker, T. Beechem, and S. Trolier-McKinstry, “Effect of stresses on the

dielectric and piezoelectric properties of $Pb(Zr_{0.52}Ti_{0.48})O_3$ thin films," *J. Appl. Phys.*, vol. 126, no. 3, pp. 0–8, 2019, doi: 10.1063/1.5095765.

[32] G. L. Brennecka, W. Huebner, B. A. Tuttle, and P. G. Clem, "Use of stress to produce highly oriented tetragonal lead zirconate titanate (PZT 40/60) thin films and resulting electrical properties," *J. Am. Ceram. Soc.*, vol. 87, no. 8, pp. 1459–1465, 2004, doi: 10.1111/j.1551-2916.2004.01459.x.

[33] B. A. Tuttle, J. Voigt, T.J. Garino, D.C. Goodnow, R.W. Schwartz, D.L. Lamppa, T.J. Headley, and M.O. Eatough, "Chemically prepared $Pb(Zr,Ti)O_3$ thin films: The effects of orientation and stress," *ISAF 1992 - Proc. 8th IEEE Int. Symp. Appl. Ferroelectr.*, pp. 344–348, 1992, doi: 10.1109/ISAF.1992.300703.

[34] T. K. Kim, J. K. Kim, and O. C. Jeong, "Measurement of nonlinear mechanical properties of PDMS elastomer," *Microelectron. Eng.*, vol. 88, no. 8, pp. 1982–1985, 2011, doi: 10.1016/j.mee.2010.12.108.

CHAPTER 6

Flexoelectricity induced from interfacial polarization in silicon-based barrier layer capacitors

6. 1 Introduction

United States military troops commonly carry 15-20 pounds of lithium-ion batteries, as of 2021, to power their portable equipment [1]. If the insole sensor arrays proposed in Chapter 5 are utilized in the shoes of troops traversing miles in a foreign country, adding lead may not benefit their mission, and would actually fulfill the taunting phrase of "lead-foot" for slow moving soldiers. The motivation for this chapter was to create an alternative material that is lead-free, lightweight, displays a potential for heel-strike energy harvesting, and may act as its own sensor array for insole shoe sensors. The fundamental mechanism that enables these properties is flexoelectricity, an exciting frontier of research that has experienced a resurgence due to Ma and Cross's seminal work in the early 2000s [2].

Flexoelectricity is a fourth-rank tensor property found in all insulators, whose direct effect relates polarization to a strain gradient (Equation 6.1) and converse effect relates a mechanical stress to electric polarization gradient [3]. In Equation 6.1, P_l is polarization, μ_{ijkl} is the flexoelectric coefficient, and $\partial\epsilon_{ij}/\partial x_k$ is the strain gradient. The flexoelectric response of simple ionic solids was first proposed to exhibit coefficients on the order of the ratio of elementary charge to the unit cell lattice dimension [4][5]. Experimental analysis of this prediction proved an underestimation on the order of 10^6 C/m, i.e., in paraelectric barium strontium titanate [2]. Tagantsev suggested that the flexoelectric coefficient may be directly proportional to dielectric permittivity, which is shown in Equation 6.2 where γ_{ij} is a constant of value close to unity, χ_{kl} is dielectric susceptibility (which is approximately equal to dielectric permittivity for high k dielectrics), e is the charge of an electron and a is the lattice constant [6].

The majority of flexoelectric research has involved polar ferroelectric materials in their paraelectric regime, for example barium titanate or barium strontium titanate in order to maximize the dielectric permittivity [2][7][8]. Table 6.1 summarizes several flexoelectric coefficients achieved in ferroelectric materials near their paraelectric state at room temperature.

$$P_l = \mu_{ijkl} \frac{\partial \epsilon_{ij}}{\partial x_k} \quad \text{Equation 6.1}$$

$$\mu_{ijkl} = \gamma_{ij} \chi_{kl} \frac{e}{a} \quad \text{Equation 6.2}$$

Table 6.1: Flexoelectric coefficients at room temperature for various ferroelectric materials

Material	Dielectric permittivity	Flexoelectric coefficient (μC/m)	Sample type	Reference
$SrTiO_3$	~300-400	0.006	3-point bend	[9]
$Pb(Zr_{0.52}Ti_{0.48})O_3$	~2100	1.4	Cantilever	[10]
PMN	~12700	4.5	Cantilever	[11]
$BaTiO_3$	~2400	10	Cantilever	[8]
$Ba_{0.67}Sr_{0.33}TiO_3$	~16000	100	Cantilever	[2]

In ferroelectrics, the maximum dipolar polarizability contribution to dielectric permittivity is ~30,000. Space charge polarizability, the macroscopic motion of charge carriers until blocked by an insulating interface, may increase the permittivity well above 50,000 and enable significantly higher flexoelectric coefficients than those in ferroelectrics [12]. Barrier layer capacitors (BLC) consist of a central conductive region and an exterior insulating region, where the effective permittivity is proportional to the insulating material permittivity multiplied by a factor of $h/2h_o$ (h is the total thickness and h_o is the insulating layer thickness) [13]. Barrier layer capacitors have been utilized commercially for decades, largely based on inhomogeneously reduced titanate ceramics, as shown in Figure 6.1 [14-16]. A typical approach would be to reduce the grains, such that they conduct by electron hopping between Ti^{3+} and Ti^{4+}. More insulating grain boundaries serve as the blocking layers. The permittivity in BLC remains high until the charge carriers can no longer keep up with the oscillating electric field, and the space charge polarizability relaxes.

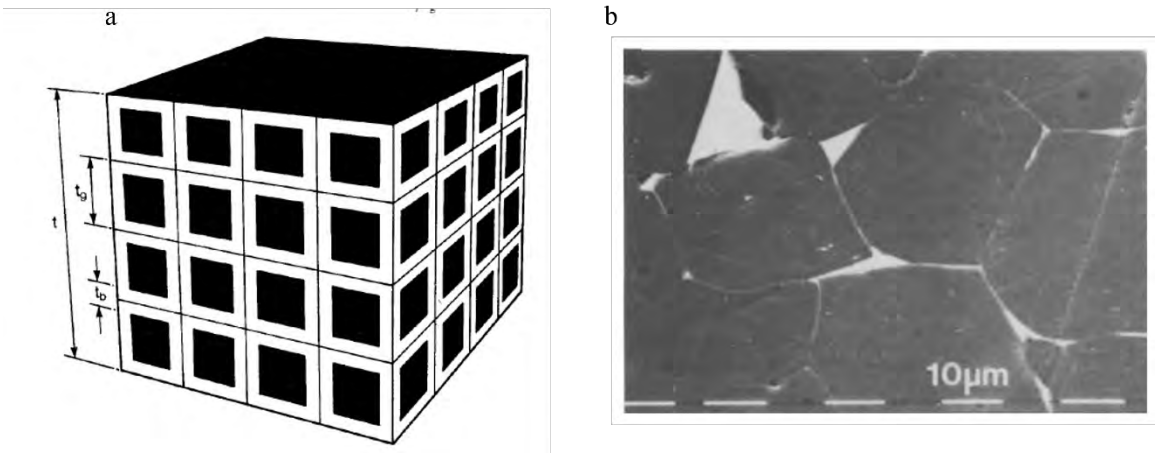

Figure 6.1: (a) Schematic diagram of an internal barrier-layer capacitor, where t is overall thickness, t_g is individual grain thickness, and t_b is grain boundary thickness. Black regions are semi-conducting and white regions are insulating. Reprinted with permission from [17]. (b) Scanning electron micrograph of a polished surface of $SrTiO_3$ boundary-layer capacitor, reprinted with permission from [13].

Narvaez et al., investigated the effect of space charge polarizability on the flexoelectric coefficient with Nb-doped TiO_2 or reduced $BaTiO_3$ as the conducting region [7]. The flexoelectric coefficient for a Nb-doped TiO_2 conducting region with a thickness of ~525 μm was three orders of magnitude higher than an insulating TiO_2 ceramic when bent to induce an inhomogeneous strain (4 μC/m vs. 1.5 nC/m), as shown in Figure 6.2. Further, they discovered an effective flexoelectric coefficient of ~900 μC/m for oxygen vacancy doped $BaTiO_3$, which demonstrates the feasibility and potential of this approach. To date, however, there are no devices which utilize this method.

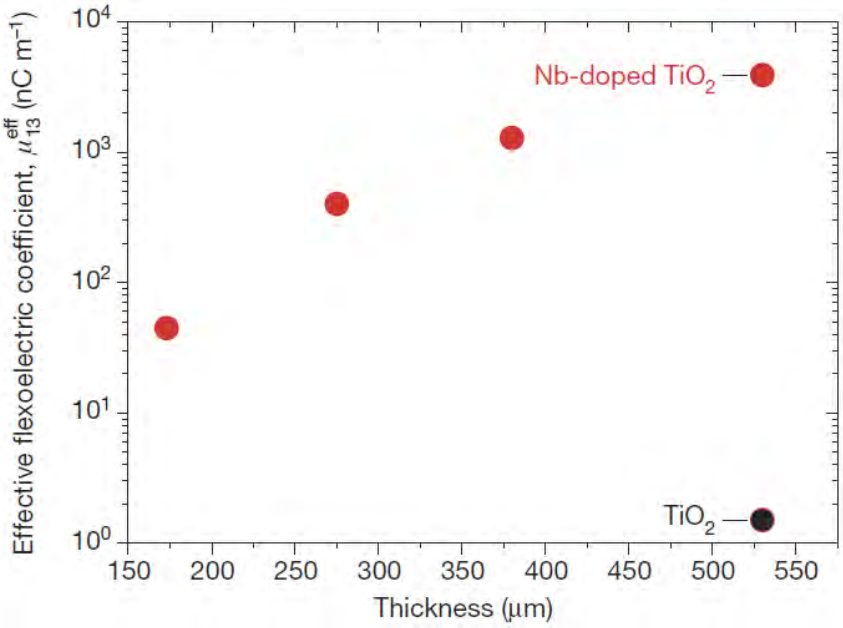

Figure 6.2: Effective flexoelectricity of TiO_2 (black) and 0.05% Nb-doped TiO_2, reprinted with permission from [6].

It is thus interesting to imagine a practical geometry for utilization of the space-charge-based flexoelectrics. Flexure of cantilever beams to induce a large strain gradient, the most common substrate geometry for achieving a strain gradient in flexoelectrics, produces a tensile stress on one side of the beam. Tensile stress degrades device integrity, as cracks initiate and propagate at defects. Thus, the achievable strain gradients in bulk cantilever beams are limited. One flexoelectric device design suggested by Ma and Cross to overcome this limitation is truncated pyramid arrays [18]. Decreasing the scale of a truncated pyramid will decrease ∂x_k and increase $\partial \epsilon_{ij}/\partial x_k$ in Equation 6.1, which is directly proportional to the polarization output in the direct flexoelectric effect. That is, the strain gradient is inversely proportional to the height *(h)* and the height dependent cross-sectional area *(S(h))* for a simply supported top or bottom constrained truncated pyramid (Equation 6.3) [19]. Thus, if flexoelectric truncated pyramids are scaled down several orders of magnitude, larger polarization outputs are possible. Indeed,

Očenášek et al. predicted a "flexoelectric size effect" where the flexoelectric coefficient is impacted by the strain gradient magnitude [20].

$$\left(\frac{\partial \varepsilon_{11}}{\partial x_1} = \frac{F}{E}\frac{\partial}{\partial h}\left(\frac{1}{S(h)}\right)\right) \qquad \text{Equation 6.3}$$

In the seminal work by Ma and Cross, the minimum truncated pyramid height and edge length were 760 μm and 1130 μm, respectively [18]; these parts were made by cutting into the flat face of a BST ceramic sheet. Thus, maximizing strain gradients via nanoscale effects is not compatible with bulk ceramic machining. However, the use of silicon in promising. Silicon is currently utilized in microelectronic cleanroom processing, an industry with a market cap of $437.1 billion as of 2021 [21]. Silicon as the bulk conducting region in a BLC truncated pyramid design provides several advantages: (1) common anisotropic silicon etching techniques can shrink device sizes down to the micron level, providing large strain gradients (2) heavily doped silicon may contain electrons and holes as free carriers at concentrations as high as 10^{21} cm^{-3}, enhancing space charge polarizability, and (3) silicon processing is well documented. Potassium hydroxide (KOH) is an anisotropic etchant for single crystal silicon, where the {111} planes show the slowest etch rate, and the <100> direction the fastest etch rate. This difference in etch rate defines truncated pyramid walls at a constant angle of 54.7°, the angle between [111] and [100] in single crystal silicon, independent of the starting top square edge length. It is proposed here that silicon-based barrier layer capacitor devices in the shape of micro-sized truncated pyramid arrays with amorphous hafnia and alumina as thin insulating layers will display a flexoelectric polarization output competitive with current devices, for example those listed in Table 6.1.

6.2 Cantilever beam method to assess the flexoelectric coefficient of Si-based barrier layer capacitors

The first goal of the flexoelectric research was to make a measurement of the flexoelectric coefficient of a Si-based barrier layer capacitor. Towards this end, Si beams with insulating layers and electrical contacts were prepared for bending measurements. All cantilever beams were fabricated using 100 mm diameter (ϕ), from 500-550 μm thick, <100> oriented, double side polished p-doped Si wafers (NOVA Wafers) with a resistivity of 1-10 Ω-cm. This required that thin dielectric layers be deposited on both surfaces. In this work, both Al_2O_3 and HfO_2 were explored as dielectric layers. Atomic layer deposition was chosen as the deposition method, since it deposits conformally (including over the pyramid geometry explored subsequently).

6.2.1 Al_2O_3-based beam fabrication

Amorphous Al_2O_3 films were grown via atomic layer deposition (Kurt Lesker, ALD-150LE) at 200°C for 319 cycles; 31.63 ± 0.02 nm Al_2O_3 was deposited on both surfaces of the Si wafer, verified via optical ellipsometry (Woolam M2000X). Bi-layer photolithography enabled photoresist patterning of 7x1.5 mm^2 rectangular electrode arrays, evenly spaced 2 mm apart. LOR 5A photoresist was spun coat at 4000 rpm for 45 seconds then baked at 180°C for two minutes. Then SPR-3012 was spun coat at the same speed and time then baked at 95°C for one minute. An exposure step (Suss MA/BA6 Gen 4) at 56 mJ/cm^2 followed by developing in CD-26 for 90 seconds patterned the 7x1.5 mm^2 electrode areas. A 100 nm thick platinum layer was sputter deposited (Pt target, Kurt J. Lesker) and all remaining photoresist was removed in a bath of PR-remover at 70°C for 10 minutes. Backside alignment was utilized to replicate an identical electrode pattern on the backside of the 100 mm ϕ wafer. The wafer was cleaved into 1 cm wide cantilevers; the electrodes were centered on each beam and were arrayed down the length of the beam.

6.2.2 HfO_2-based beam fabrication

Atomic layer deposition (ALD) was used for the growth of amorphous HfO_2 films on both surfaces of the Si wafers. Native oxide on the Si wafers were removed in BOE 10:1 solution for 30 seconds immediately prior to deposition. Four individual rectangles (4x5 cm^2) were cleaved from the wafer, and cycle counts of 103 (producing a thickness of 7.9 ± 1.1 nm), 206 (17.4 ± 1.4 nm), 309 (25.4 ± 4.1 nm), and 412 (36.7 ± 2.5 nm) enabled the approximate 10 to 40 nm HfO_2 thicknesses on different samples. Identical platinum electrodes were deposited on the 'HfO_2 beams' as the 'Al_2O_3' beams and each 4x5 cm^2 rectangular was cleaved into four 1x5 cm^2 beams. Example HfO_2 beams with top Pt electrodes are displayed in Figure 6.3.

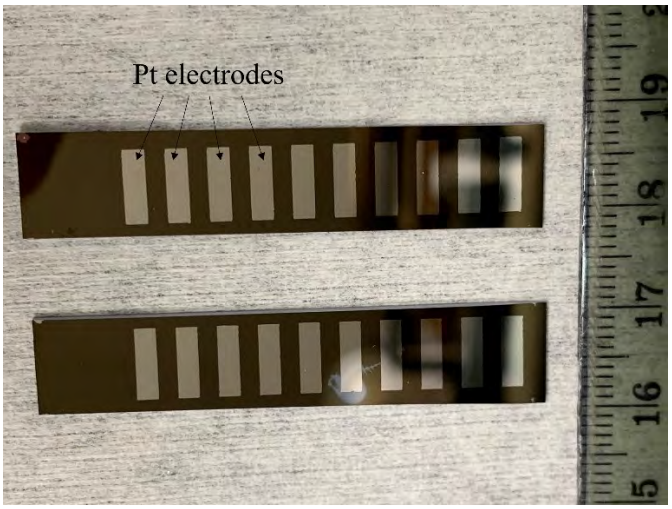

Figure 6.3: HfO_2 coated Si cantilevers with 7x1.5 mm^2 platinum electrodes on the top and bottom surface. The left side of the beams without electrodes are the clamped end for flexoelectric measurements.

6.2.3 Dielectric property measurements of Si barrier layer capacitors

Dielectric permittivity and loss tangent measurements were performed on 'Al_2O_3' beams and 'HfO_2' beams with an LCR meter (HP 4284A Precision LCR Meter) at 30 mV from 20 Hz to 200 kHz. Figure 6.4 shows the effect of HfO_2 film thickness on dielectric permittivity (a) and loss tangent (b) for different measurement frequencies. With films at and below ~20 nm, the loss tangent was near 1.0 at 100 Hz; at these frequencies the dielectric permittivity shows

contributions from conduction. Films with ~30 nm thickness had the highest dielectric permittivity over the widest range of frequencies below 10 kHz and low loss tangents. The beam with 40 nm HfO_2 displayed a smaller dielectric permittivity; its loss peak shifted to a lower frequency, compared to the 30 nm HfO_2. The 30 nm dielectric layer thickness was selected as the optimal value.

Figure 6.5 shows the dielectric permittivity and loss tangent for beams with ~30 nm Al_2O_3 and HfO_2 films. The permittivity was 29,250 ± 20 and the loss tangent was 0.12 ± 0.0007 at 100 Hz for the Al_2O_3 beam. Comparatively, the beam with ~30 nm HfO_2 at 100 Hz showed relative permittivity and loss tangent values of 34,380 ± 4,260 and 0.12 ± 0.10, respectively. This difference in relative permittivity between the two beams was due to the inherent dielectric permittivity difference between amorphous HfO_2 and Al_2O_3: 25 vs 9, respectively [22].

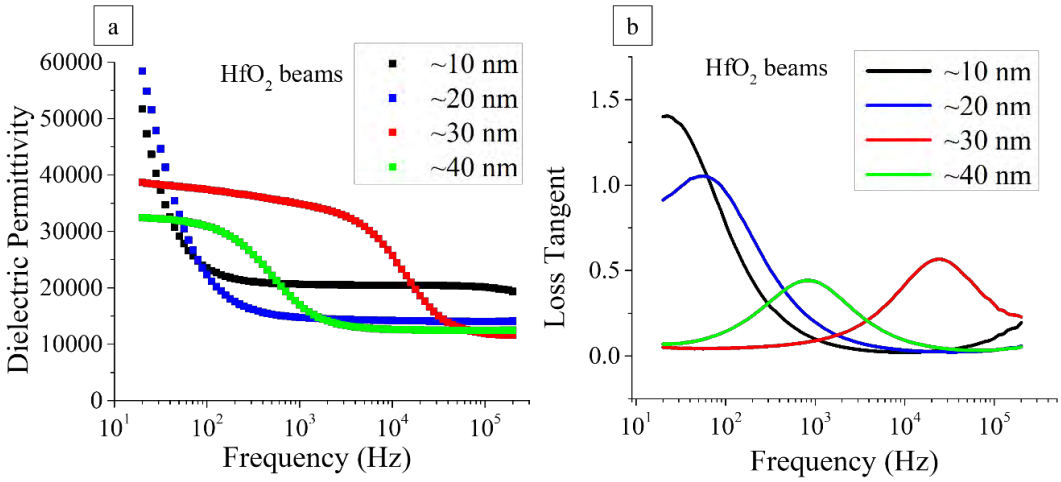

Figure 6.4: Dielectric permittivity (a) and loss tangent (b) versus frequency for the $Pt/HfO_2/Si/HfO_2/Pt$ stack with HfO_2 varying from 10 to 40 nm

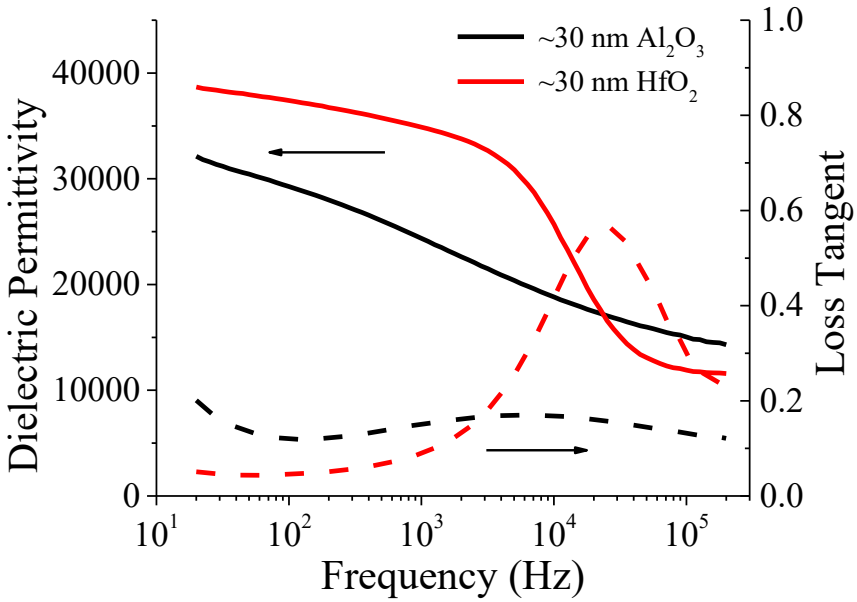

Figure 6.5: Dielectric permittivity and loss tangent versus frequency for the 'Al_2O_3' (black) and 'HfO_2' (red) beams, each with 30 nm thickness on Si.

It is hypothesized that a short anneal of the Pt/HfO_2/Si/HfO_2/Pt beam may adjust the frequency dependence on the dielectric permittivity and shift the peak in loss tangent. The ~30 nm HfO_2 beam was placed in an alumina tube furnace with 50 sccm N_2 flow for one hour prior to the anneal. The sample was annealed in the nitrogen atmosphere at 400ºC for ten minutes with a temperature ramp up rate of 5ºC/min and a ramp down naturally to room temperature. The dielectric permittivity and loss tangent were measured with a ModuLab XM MTS (Solartron Analytical) before and after the anneal. Figure 6.6 shows the 'as-grown' ~30 nm HfO_2 measurement in red and the 400ºC 'annealed' measurement in blue. After annealing for ten minutes, the dielectric permittivity increased by 2.7×, from 46,040 to 123,200, and the space-charge relaxation shifted to a lower frequency; both films remained amorphous as measured with a lab scale x-ray diffractometer. The increase in dielectric permittivity was likely due to an improvement in the contact quality between the Pt/HfO_2/Si interface. An anneal temperature of 400ºC was not expected to crystallize the film, but partial densification may have occurred, which

may have decreased the HfO_2 film thickness and increased capacitance along with effective permittivity [23]. The increased capacitance would have led to a longer RC time constant and thus a smaller roll-off frequency, as seen in Figure 6.6.

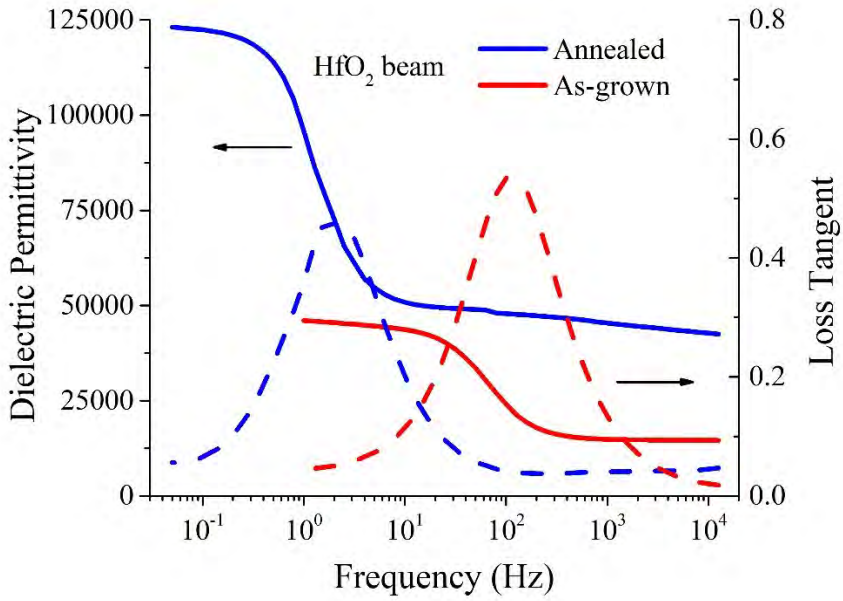

Figure 6.6: Dielectric permittivity and loss tangent of ~30 nm HfO_2 beam in the as-grown state (red) and after a ten minute anneal at 400°C in nitrogen (blue).

6.2.4 Flexoelectric measurements

A schematic (top) and image (bottom) of the electrical setup and all cantilever connections is displayed in Figure 6.7. An Omega strain gauge was glued onto the surface of the platinum electrode 1 cm from the clamped end of the cantilever. Then, a mass was placed on top and left to dry for 24 hours. The structure was placed in a homemade flexoelectric testing station surrounded by a Faraday cage, constructed as described in references [24-25]. The strain gauge was fed through a Wheatstone bridge to the strain lock-in amplifier. Wires were attached with silver paste to the top and bottom cantilever electrodes near the clamped end to make electrical connections to the charge channel of the lock-in amplifier. A 4 Hz AC voltage was applied to a piezoelectric stack placed underneath the flexoelectric structure, which placed the strain gauge

and electrode into dynamic compression. A current amplifier/converter (within the Wheatstone bridge box) measured the charge from the top electrode; the lock-in amplifier phase-matched each signal, generating an output charge. The output charge was read in mV, with the setup having a charge to voltage converter that amplifies and converts ~100 pA to ~1 mV with a 10 nF capacitor. Flexoelectric polarization was calculated as the lock-in amplifier output voltage (converted to charge) and divided by electrode area. The strain was measured simultaneously using a separate lock-in amplifier. Equation 6.4 was used to calculate the strain gradient ($\partial \epsilon_{ij}/\partial x_k$) of the beam, where s is the lock-in amplifier output (in V), $10^{-6}/V_{in}$ is the conversion factor for the Wheatstone bridge. The input voltage (V_{in}) was 4 V, GF is the strain gauge Gauge Factor = 1.95, and t is the total thickness of the cantilever beam. After several measurements at a constant AC voltage, the voltage level on the piezoelectric stack actuator was increased to induce a larger strain gradient, and the measurement was repeated.

$$\frac{\partial \epsilon_{ij}}{\partial x_k} = \frac{(s)\left(\frac{10^{-6}}{V_{in}}\right)\left(\frac{V_{in}}{GF}\right)}{\frac{t}{2}} \qquad \text{Equation 6.4}$$

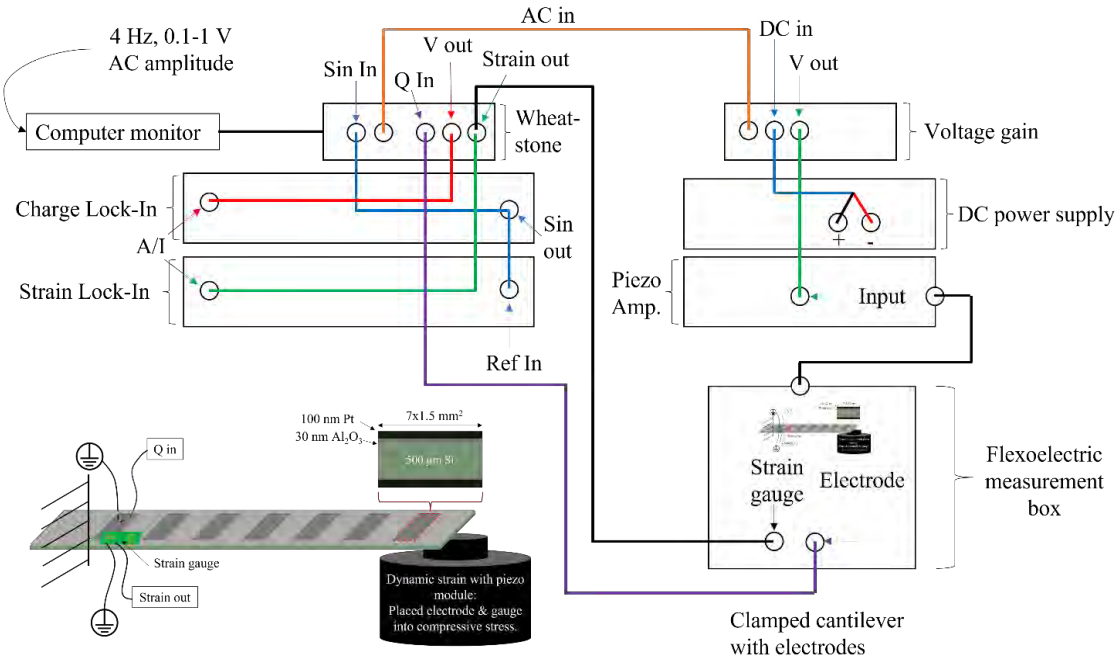

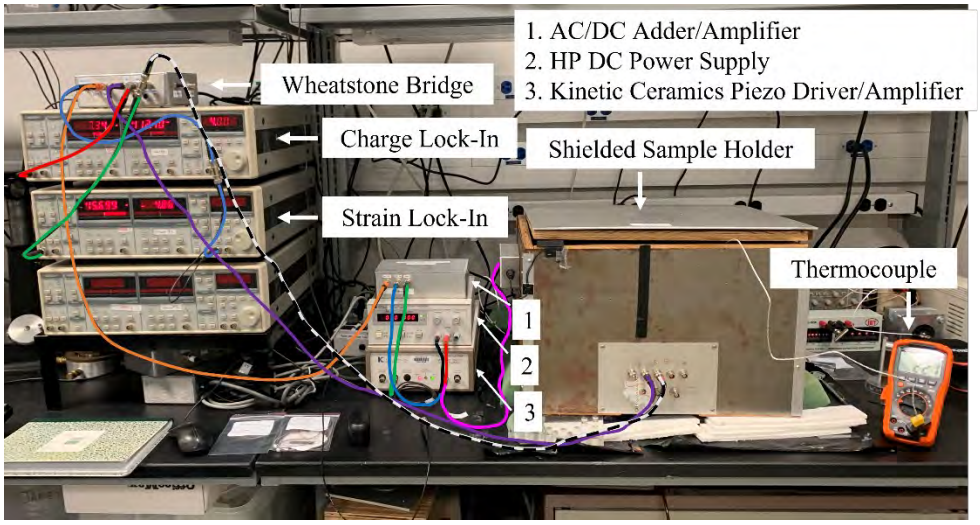

Figure 6.7: Cantilever beam flexoelectric experimental schematic. A 4 Hz AC voltage was applied with LABVIEW software from a PC connected to two separate lock-in amplifiers and a Wheatstone bridge box which contained a current amplifier. The sinusoidal wave (blue line, left) was matched between the lock-ins and the AC voltage In (orange line) went to a unity gain amplifier (voltage gain box). A DC power supply was connected to the unity gain amplifier (blue line, right) and the V output (green line, right) was fed to the piezoelectric amplifier. As the piezoelectric module placed the beam into dynamic compressive stress, the cantilever strain gauge (black line) and top electrode (purple line) fed back to the Wheatstone bridge and current amplifier (Q In and Strain out, respectively). Each signal was fed to the separate charge (red line) and strain (green line, left) lock-in amplifiers and recorded on the computer monitor. Electrical-line colors match top schematic with bottom image.

The polarization output as a function of the strain gradient is displayed in Figure 6.8 for the cantilever beam containing ~30 nm 'as grown' HfO_2. As per Equation 6.1, the flexoelectric coefficient, was μ=4.9 ± 0.4 μC/m. Comparing these results to those in Table 6.1, this coefficient is in the moderate range and provides a promising route towards space charge barrier layer capacitor designs. The cantilever beam flexoelectric measurements were highly sensitive to room vibrations, electrical noise, frequency of applied force, and some thermal variation within the Faraday cage box. Appendix E documents some of the problems encountered during these measurements.

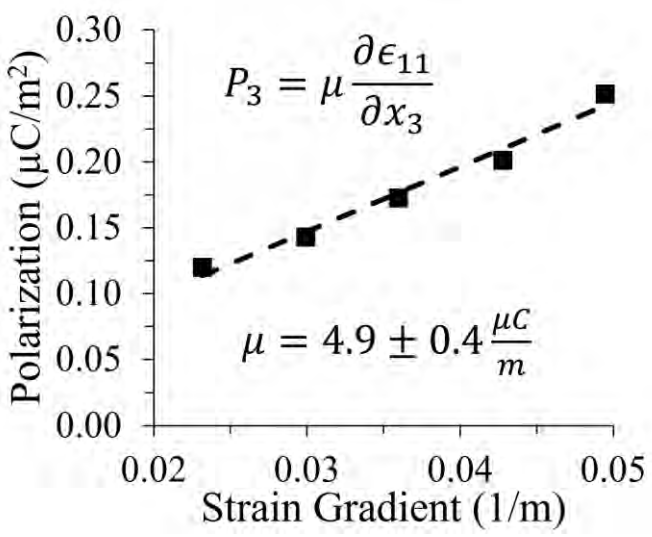

Figure 6.8: HfO_2 cantilever flexoelectric measurement. A linear least square fit extracted the flexoelectric coefficient.

A semiconducting silicon beam with an insulating layer of HfO_2 enhanced the dielectric permittivity in the space charge frequency regime. The design had a polarization output with an applied strain gradient, verifying flexoelectricity. Although promising, there is room for improvement in the device design. Cantilever beams inherently impose strain gradient limitations; as one side is place in compression, the opposite side is placed in tension. A large tensile stress placed on a semiconductor with normal surface flaw populations induces fracture [26]. Therefore, a device incorporating truncated pyramid arrays as the strain gradient source was investigated.

6.3 Truncated pyramid arrays

6.3.1 Fabrication methodology

Micron-sized truncated pyramid arrays were fabricated in a class 100/1000 cleanroom. There were several iterations of the process flow to reach a functioning flexoelectric device with multiple re-optimization steps along the way. Figure 6.9 shows the successful fabrication process to make truncated pyramids from silicon on insulator (SOI) wafers. Appendix E documents earlier iterations which returned unsuccessful results but helped optimize the final flow pattern. Future works section 7.2.5 shows an alternate process flow based on a wafer-to-wafer bonding process that may replace the SOI-based process in future device designs.

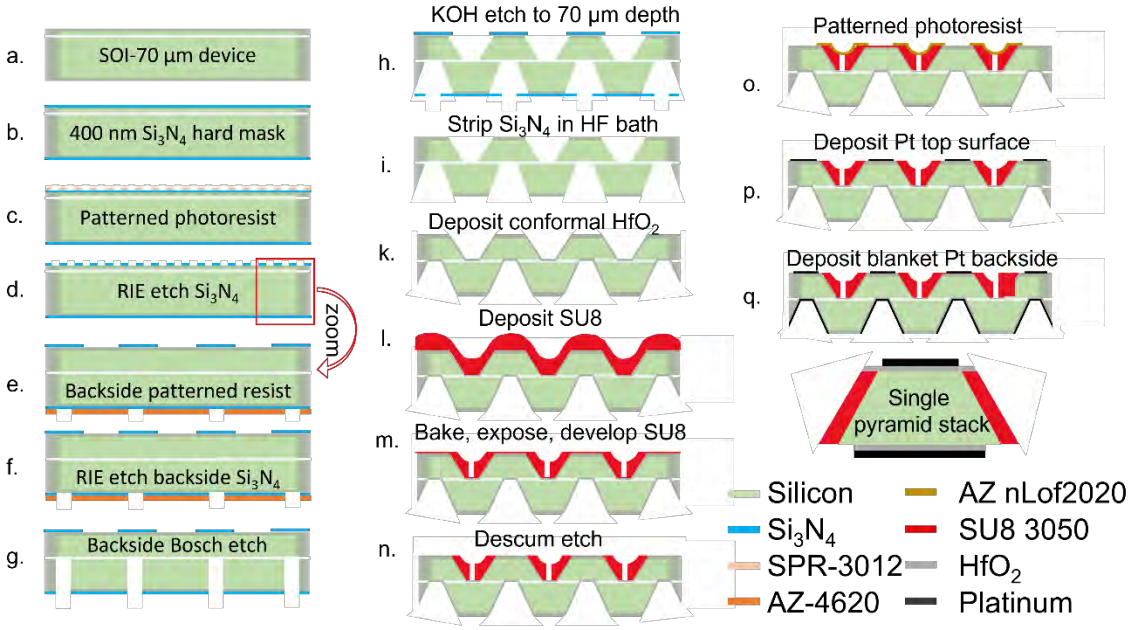

Figure 6.9: Truncated pyramid array microelectronic fabrication flow.

4" diameter silicon on insulator (SOI) wafers with a device layer thickness of 70 µm, a buried oxide (BOX) layer of 1 µm thickness, and a handle thickness of ~500 µm were used. The <100> oriented device layer was p-doped with a resistivity of 1-10 Ω-cm. An SOI wafer schematic is shown in Figure 6.9a, not to scale. 400 nm thick Si_3N_4 (nitride) layers were

deposited on both surfaces of the SOI wafer via plasma enhanced chemical vapor deposition (PECVD) (Applied Materials P-5000 PECVD Cluster Tool). This is shown in Figure 6.9b. The process variables were: chamber temperature of 350°C, chamber pressure of 650 mTorr, 5%SiH_4/Ar flow of 400 sccm, NH_3 flow of 20 sccm, N_2 flow of 600 sccm, LF power of 200 W for a pulse time of 5 seconds, RF power of 20 W for a pulse time of 15 seconds, and a deposition rate of 5.8 nm/second.

After deposition of the Si_3N_4 layer, a single SPR-3012 photoresist layer was spun on the device side of the SOI wafer at a rate of 4000 rpm for 45 seconds, then placed on a hotplate at 95°C for 60 seconds. A direct write (Heidelberg MLA 150 Direct Write) exposure step with 56 mJ/cm^2 UV power exposed the photoresist into individual squares with edge lengths ranging from 50 to 500 μm. To enable a truncated pyramid shape, bound by the {111} planes during a KOH etch, the edge of each nitride square was aligned 45° to the major flat, which was parallel to the <110> direction. A 90 second develop step in CD-26 removed the photoresist *outside* of the square patterns (Figure 6.9c). Next, the unmasked nitride was removed via reactive ion etching (ULVAC NE-550 ICP Etching System) for 70 seconds, 4 sccm O_2 flow rate, 40 sccm CF_4 flow rate, and RF power of 200 W at an etch rate of ~400 nm/minute. A 70°C heated bath of PRS 3000 removed the remaining SPR-3012 photoresist (Figure 6.9d). An example of nitride squares on the surface of the SOI device layer is shown in Figure 6.10.

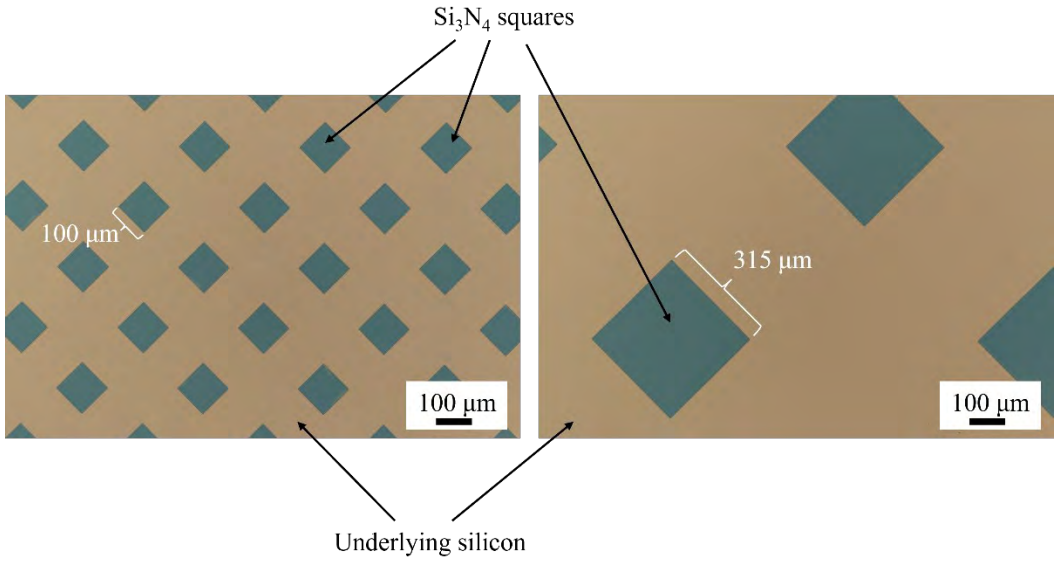

Figure 6.10: Patterned nitride squares (blue) on the SOI wafer device side surface with 100 µm edge length (left) and 315 µm edge length (right).

Next, the SOI wafer was flipped over, with the handle side up, and AZ4620 photoresist was deposited on the surface of the nitride. A spin coat of 4000 rpm for 45 seconds produced a ~7 µm thick film, which was thick enough to protect the nitride during Si handle etching. Then, a two-step bake of 60 seconds at 95°C and 180 seconds at 105°C cured the photoresist, and the direct write MLA 150 tool enabled UV exposure to small square windows (size was dependent on the front side nitride square size) which were back-side aligned to the middle of the front side squares. The exposed photoresist regions were developed in AZ 400K 4:1 until the exposed features were clear (3-5 minutes). A schematic of the remaining photoresist is shown in Figure 6.9e. Again, a 70 second dry etch (ULVAC) with the same parameters as previously described removed the uncovered nitride squares on the wafer backside (Figure 6.9f). To access the box layer behind each frontside nitride patterned square, a silicon etch Bosch process (SPTS Deep Silicon Etch Tool) was performed. Gases SF_6 and O_2 with a power of 2500 W, a chuck temperature of 10°C and 90-120 cycles etched through the openings in the AZ 400K, through the

~500 μm Si handle. The remaining AZ 400K photoresist was stripped using a 70ºC bath of PRS 3000. A schematic of the "backside vias" are shown in Figure 6.9g.

Potassium hydroxide (KOH) wet etch enables efficient anisotropic etching of silicon along the <100> direction, bound by the slowest etching <111> side walls. The addition of IPA to the KOH solution slightly reduces the etch rates of the <100> and <110> directions, but smooths the sidewalls and reduces the etch rate of some unwanted high-index planes [27–29]. A saturated solution of IPA in the KOH bath was found to produce the smoothest <111> sidewalls; thus, a 6:3:1 ratio of DI water, KOH, and IPA solution was utilized. The bath was set to 70ºC, which was found to provide the best selectivity of <100> silicon with respect to the nitride mask, and the wafer was etched for ~100 minutes, or until the BOX layer was visible. This KOH+IPA etch served several purposes: (1) the device side was patterned into truncated pyramids bound by the <111> sidewalls with a height of 70 μm, (2) the previously Bosch etched backside vertical vias took the shape of truncated pyramids, which enabled conformal backside metallization in later steps, and (3) the BOX layer became accessible for future wet etch removal. A schematic of the results after the KOH+IPA etch is displayed in Figure 6.9h. The remaining nitride masks were stripped in a room temperature bath of 49% HF solution for 60 seconds (Figure 6.9i). Scanning electron microscopy (SEM) (Zeiss Merlin field emission SEM) images are displayed in Figure 6.11 of a device after step Figure 6.9i; this array was patterned with a nitride square mask edge length of 100 μm. The SEM was equipped with a Gemini II column and the measurements were taken with an operating voltage of 5 kV and a working distance of ~5 mm with an in-lens secondary electron detector. Clearly observed are the smooth <111> sidewalls, the angle between the <001> and <111> directions, which was ~54.7º, and the periodicity and reproducibility of the truncated pyramid arrays.

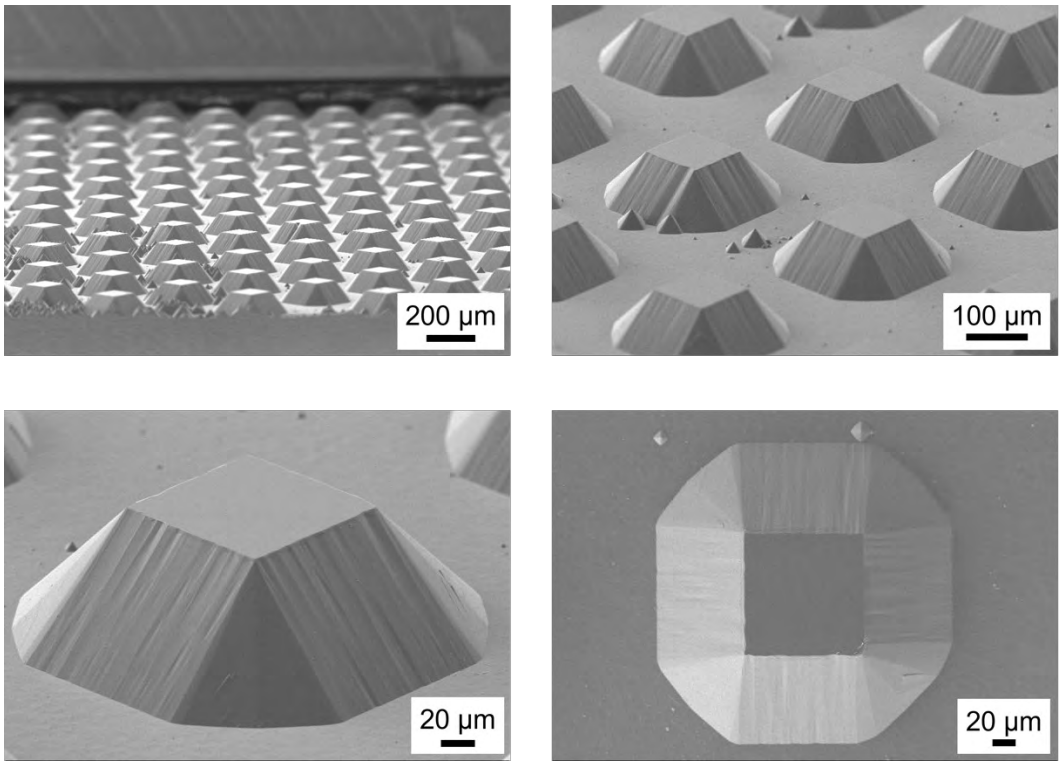

Figure 6.11: Scanning electron microscopy images showing various viewing angles of the truncated pyramid arrays. The topside width was ~100 µm, the pyramid height was ~70 µm, and the sidewall angle was ~54°.

After all nitride was removed, a thin ~30 nm layer of HfO_2 was conformally deposited via atomic layer deposition (ALD) (Kurt J. Lesker ALD150LX cluster tool) at 200°C for 309 cycles with chemical precursors Tetrakis (Dimethylamido) Hafnium ($HF(NMe_2)_4$) and H_2O [30]. Figure 6.9k shows a schematic after the HfO_2 deposition. Next, photoresist SU8-3050 was used to pattern the topside of each pyramid and electrically separate pyramid trenches from pyramid surfaces. The photoresist was spun at 1800 rpm for 60 seconds to coat the front side of the wafer, encapsulating the pyramid arrays (Figure 6.9*l*). A pre-exposure bake at 65°C for 5 minutes and 95°C for 25 minutes was followed by an exposure step (Suss MA/BA6 Gen 4) at 425 mJ/cm^2. Figure 6.12 (left) displays the mask layers used for SU8 exposure; the nitride and SU8 masks are shown. The purple dashed lines represent regions exposed to UV. Regions without SU8 after the develop step are labeled “SU8 mask opening between pyramids” and “SU8 mask size at

pyramid". Each pyramid opening was several microns larger than its top, preventing residual SU8 from remaining on the pyramid top surface. Openings were created between individual pyramids to relieve thermal stresses within the invariably stressy (~12 MPa) SU8 film [31-32]. After exposure, the wafer was baked at 65°C for 3 minutes and 95°C for 5 minutes. Then, the wafer was placed on a 65°C hotplate and allowed to gradually cool to room temperature, reducing SU8 film stress. When the wafer reached room temperature, it was placed in SU8 developer for 15 minutes to remove the unexposed SU8 regions, as shown in Figure 6.9m. An SU8 descum etch (Vision 320 RIE) for 1-2 minutes cleaned the surface of the Si pyramids (schematic in Figure 6.9n). Figure 6.12 (right) shows an optical microscopy image of the processed SOI wafer. The device-side is shown with pyramid surfaces, SU8 stress relief openings and a missing pyramid. The BOX layer under some pyramids was etched away during the 49% HF dip nitride removal step (Figure 6.9i), causing some pyramids to fall into solution.

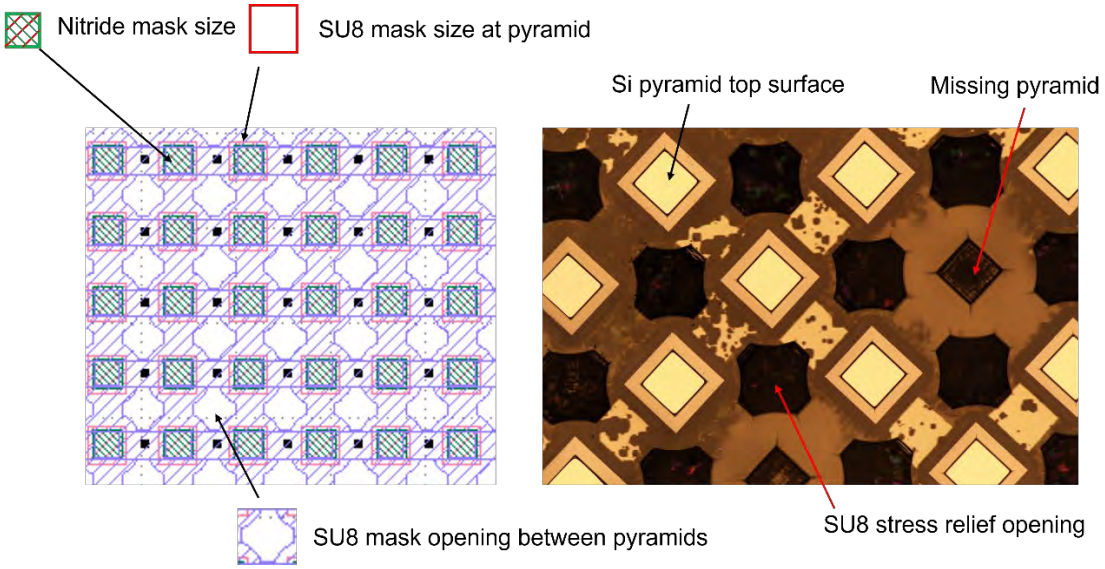

Figure 6.12: Photomask showing the nitride mask areas, SU8 masked areas surrounding each pyramid, and openings, or vias, in the SU8 film in the middle of pyramid corners (left). Optical microscopy image of the developed SU8 film with pyramid surfaces and SU8 stress relief openings labeled. Also shown is a pyramid missing from the array (right).

Finally, electrodes on the surface of each pyramid and a blanket backside metallization were patterned and deposited. For the top electrode definition, nLof2020 photoresist was spun

coat at 4000 rpm for 45 seconds on the top-side surface followed by a soft-bake at 110°C for 60 seconds. The wafer was exposed (Suss MA/BA6 Gen 4) at 90 mJ/cm^2 which polymerized photoresist outside of the chrome-masked regions. The size of the chrome-masked squares was dependent on the pyramid surface edge length and were made several microns smaller to minimize any electrode covering SU8. Table E.1 in Appendix E provides nine different final pyramid dimensions that were produced. Electrode leads were designed in the mask to electrically connect several pyramids in parallel. A post-exposure bake at 110°C for 60 seconds was then followed by a develop step in AZ 300MIF for 60 seconds. A schematic of the remaining resist is shown in Figure 6.9o. Platinum metal contacts were deposited on the patterned surface with E-beam evaporation (Temescal F-2000) to 150 nm thick at 0.2 nm/second deposition rate. The remaining photoresist was removed in PRS 3000 warmed to 70°C. The resulting platinum contacts are shown in the schematic in Figure 6.9p. The final step was backside blanket metallization via E-beam evaporation using a 10 nm Ti adhesion layer followed by 150 nm platinum. A final processed four-pyramid array schematic is shown in Figure 6.9q and below it is an isolated pyramid stack schematic.

6.3.2 Permittivity and flexoelectricity measurements

Prior to converse flexoelectric measurements, the dielectric permittivity and loss tangent of several individual pyramids were measured with varying frequency from 0.1 Hz to 100 kHz at 30 mV AC. The silicon resistivity was 1-10 Ohm-cm (p-doped with boron), the silicon pyramid thickness was 70 μm, the hafnia thickness was ~30 nm, and the top electrode area was 260x260 μm^2. The dielectric permittivity was in the tens of thousands at low frequencies. Loss increased, and permittivity decreased between 100 and 1000 Hz due to space charge polarizability relaxation. This is shown in Figure 6.13. Next, piezoresponse force microscopy was utilized to probe for a converse flexoelectric response.

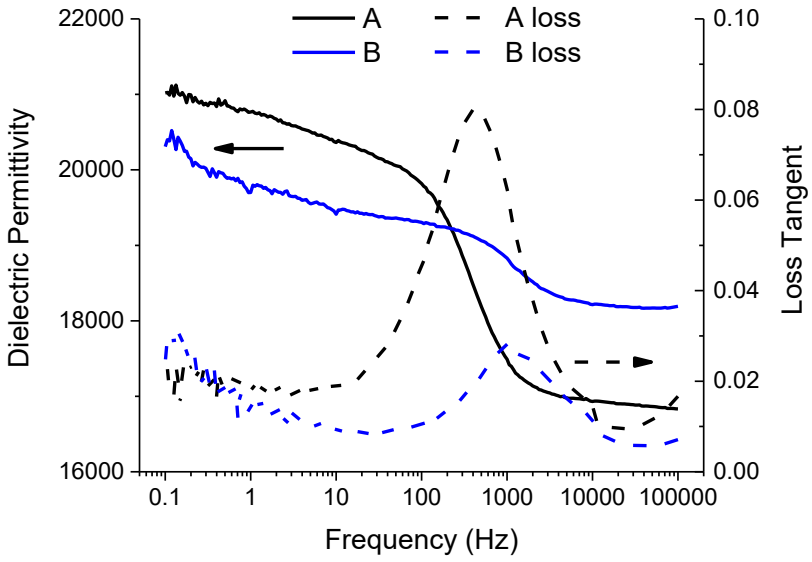

Figure 6.13: Dielectric permittivity and loss tangent of two electrically isolated truncated pyramids.

Piezoresponse force microscopy (PFM) was performed using a commercial atomic force microscope (Cypher AFM, Asylum Research an Oxford Instruments Company, Santa Barbara, CA) equipped with Pt/Ir-coated cantilevers (Nanosensors PPP-EFM-W) which had a nominal spring constant of 0.5-9.5 N/m and a resonance frequency of 45-115 kHz. Figure 6.14a shows a schematic of the PFM approach and the constitutive converse flexoelectricity equation, where ϵ_{33} is out of plane strain, μ_{3333} is the converse flexoelectric coefficient, and $\partial E_3/\partial z_3$ is the out of plane electric field gradient. A pyramid and a "planar" geometry were measured; the planar barrier layer capacitor contained a similar stack sequence as the pyramid. The stack included 100 nm Pt (area=100x100 μm^2) / 30 nm HfO_2 / 350 μm Si / 30 nm HfO_2 / 100 nm Pt from top to bottom Pt electrodes. Silver paste, shown as the granular grey material in Figure 6.14 (b,c) optical microscopy images, was applied to both pyramid and planar top electrodes, and a wire was attached to induce a global bias. An AC voltage with a triangle waveform at 1 Hz from -15 to 15 V was applied between top and bottom electrodes of each stack, and the AFM tip measured local

out of plane displacement. The electron and hole charge separation in Figure 6.14a is shown to represent space charge polarizability as the AC field gradient was applied on the pyramid structure: $\partial E_3/\partial z_3$

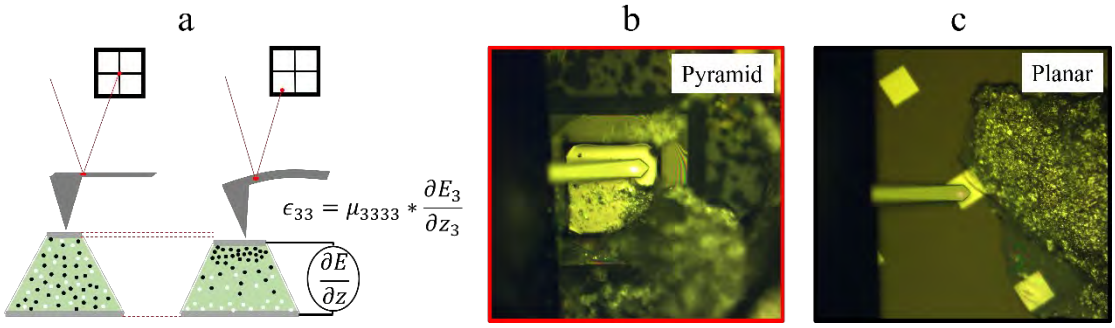

Figure 6.14: (a) Converse flexoelectric PFM measurement schematic, measuring an out of plane displacement with an applied electric field. (b) Optical microscopy image of AFM tip on the surface of the pyramid electrode. (c) Optical microscopy image of the AFM tip on the surface of the planar electrode.

Figure 6.15 (top) displays the bias field applied between top and bottom electrodes for the pyramid and planar stack geometries. Figure 6.15 (bottom) shows the out of plane displacement (in nm) of both devices. The planar stack showed zero out of plane displacement for any applied voltage, as expected. The pyramid device showed a displacement amplitude as the voltage was cycled. When displacement is plotted against applied voltage (Figure 6.16), the pyramid structure shows a hysteretic response, while the planar geometry shows zero response.

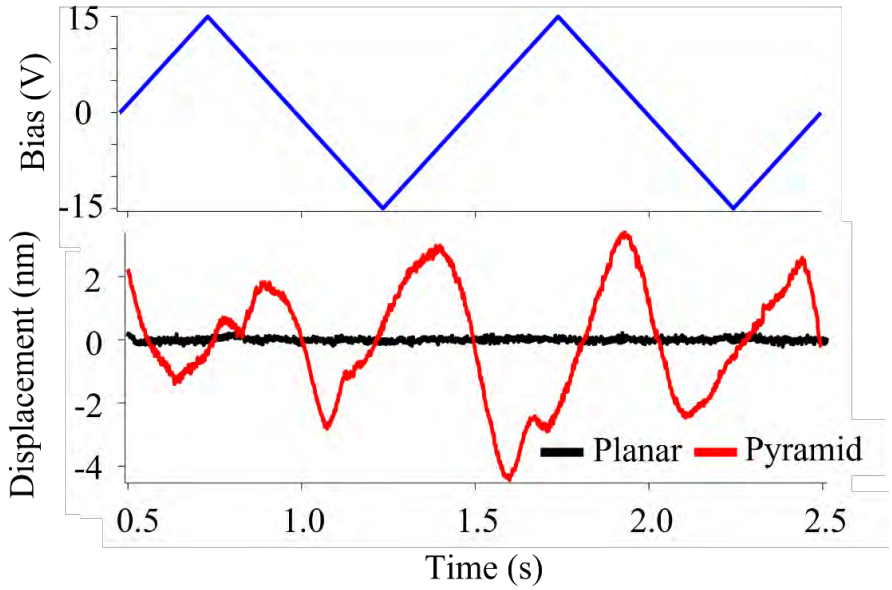

Figure 6.15: Applied DC voltage bias as a triangle wave from -15 to 15 V (top). Out of plane displacement amplitude at tip resonance for the pyramid structure (red) and planar structure (black) with time (bottom).

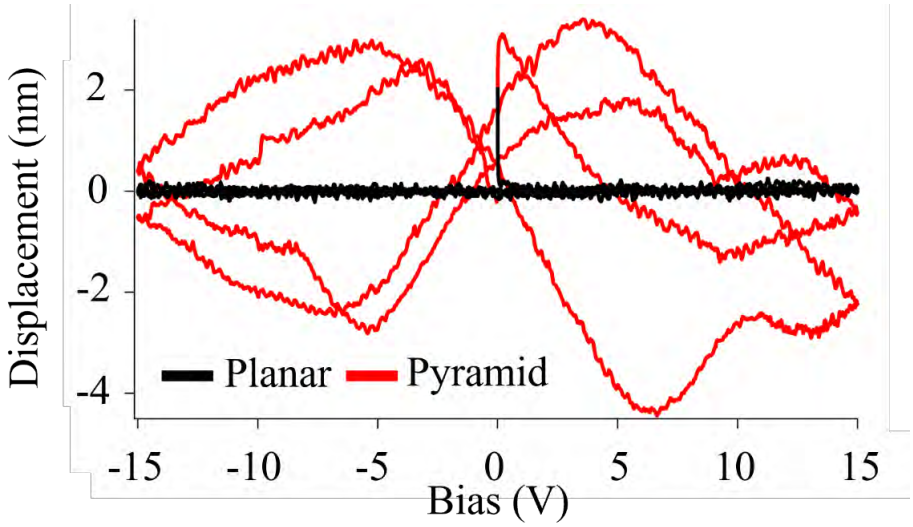

Figure 6.16: Displacement amplitude vs applied voltage for the planar and pyramid geometries.

The maximum in displacement upon each cycle may have experienced a phase delay due to the length of the PFM cables. This could explain the shift in the expected response, where the maximum applied voltage would result in the highest out of plane displacement. Notably, the

maximum in displacement amplitude (both positive and negative) is larger for the positive applied voltage, rather than the negative. In the experimental setup, the top electrode is positive (+) and the bottom negative (-), such that a positive bias will attract free holes towards the bottom interface. It is speculated that because the bottom electrode is larger than the top in the truncated pyramid geometry, the majority carrier induced a higher polarizability when attracted to the larger collecting area, increasing the local out of plane displacement.

6.4 Conclusions

Barrier layer capacitors, with doped silicon as the conductive region and HfO_2 and Al_2O_3 as insulating regions, were investigated for dielectric and flexoelectric properties. Cantilever beams were fabricated as a proof of concept, and 30 nm HfO_2 on 500 μm silicon displayed a dielectric permittivity and loss tangent of 34,380 ± 4,260 and 0.12 ± 0.10 at 100 Hz, with a space charge relaxation frequency around 10 kHz. When the film on silicon was annealed at 400ºC, below the HfO_2 crystallization temperature, the dielectric permittivity increased 2.7x and the space charge dropout loss tangent peak shifted two decades lower in frequency. The HfO_2/Si cantilever stack displayed a flexoelectric coefficient of 4.9 ± 0.4 μC/m. To increase strain gradient and therefore flexoelectric polarization output, micron-size truncated pyramids with the same HfO_2/Si stack sequence were fabricated with silicon microelectronic processing techniques. Individual pyramids displayed a dielectric permittivity and loss tangent of 20200 ± 1000 and 0.016 ± 0.006 at 1 Hz, respectively. Piezoresponse force microscopy was utilized to measure the converse flexoelectric deflection of a single pyramid and a planar device with the same stack. With an applied voltage of ±15 V, the planar device displayed zero out of plane deflection and the pyramid device deflected a maximum 4 nm out of plane. This investigation represents the first report on silicon-based barrier layer capacitor designed cantilevers and truncated pyramids that

display a flexoelectric polarizability with both an induced strain gradient and electric field gradient.

6.5 References

[1] Lithium Batteries in Defense, National Mining Association, October 20, 2021. nma.org/2021/10/20/lithium-batteries-in-defense

[2] W. Ma, L.E. Cross, Flexoelectric polarization of barium strontium titanate in the paraelectric state, Appl. Phys. Lett. 81 (2002) 3440–3442.

[3] P. Zubko, G. Catalan, A.K. Tagantsev, Flexoelectric effect in solids, Annu. Rev. Mater. Res. 43 (2013) 387–421. https://doi.org/10.1146/annurev-matsci-071312-121634.

[4] S.M. Kogan, Sov. Phys.-Solid State 5, 20169 (1964).

[5] V.L. Indenbom, E.B. Loginov, and M.A. Osipov, Kristallografiya 26, 1157 (1981). https://doi.org/10.1063/1.1518559.

[6] A.K. Tagantsev, Theory of flexoelectric effect in crystals, Sov.Phys. JETP. 61 (1985) 1246.

[7] J. Narvaez, F. Vasquez-Sancho, G. Catalan, Enhanced flexoelectric-like response in oxide semiconductors, Nature. 538 (2016) 219–221. https://doi.org/10.1038/nature19761.

[8] W. Ma, L.E. Cross, Flexoelectricity of barium titanate, Appl. Phys. Lett. 88 (2006) 2001–2004. https://doi.org/10.1063/1.2211309.

[9] P. Zubko, G. Catalan, A. Buckley, P.R.L. Welche, J.F. Scott, Strain-gradient-induced polarization in $SrTiO_3$ single Crystals, Phys. Rev. Lett. 99 (2007) 99–102.

https://doi.org/10.1103/PhysRevLett.99.167601.

[10] W. Ma, L.E. Cross, Flexoelectric effect in ceramic lead zirconate titanate, Appl. Phys. Lett. 86 (2005) 072905. https://doi.org/10.1063/1.1868078.

[11] W. Ma, L.E. Cross, Large flexoelectric polarization in ceramic lead magnesium niobate, Appl. Phys. Lett. 79 (2001) 4420–4422. https://doi.org/10.1063/1.1426690.

[12] S. Trolier-McKinstry, R.E. Newnham, Materials Engineering: Bonding, Structure, and Structure-property Relationships, Cambridge University Press, 2018.

[13] R.M. Glaister, Barrier-layer dielectrics, Proceedings of the IEE-Part B: Electronic and Communication Engineering 109 (1962) 423-431

[14] M. Fujimoto, and W.D. Kingery, Microstructures of $SrTiO_3$ internal boundary layer capacitors during and after processing and resultant electrical properties, J. Am. Ceram. Soc. 68 (1985) 169-173

[15] P.E.C. Franken, M.P.A Viegers, and A.P. Gehring, Microstructure of $SrTiO_3$ boundary-layer capacitor materials, J. Am. Ceram. Soc. 64 (1981) 687-690

[16] N. Yamaoka, M. Masuyama, M. Fukui, $SrTiO_3$-based boundary layer capacitor having varistor characteristics, Am. Ceram. Soc. Bull. 62 (1983) 698-703

[17] A.J. Moulsen and J.M. Herbert, Electroceramics: materials, properties, and applications. John Wiley & Sons, 2003.

[18] W. Zhu, J.Y. Fu, N. Li, L. Cross, Piezoelectric composite based on the enhanced flexoelectric effects, Appl. Phys. Lett. 89 (2006). https://doi.org/10.1063/1.2382740.

[19] H. Ji, S. Zhang, K. Liu, T. Wu, M. Xu, S. Shen, Flexoelectricity in pyramid compression: Decoupling from effective to intrinsic, J. Phys. D. Appl. Phys. 53 (2020).

https://doi.org/10.1088/1361-6463/ab5c50.

[20] J. Očenášek, H. Lu, C.W. Bark, C.B. Eom, J. Alcalá, G. Catalan, A. Gruverman, Nanomechanics of flexoelectric switching, Phys. Rev. B - Condens. Matter Mater. Phys. 92 (2015) 1–9. https://doi.org/10.1103/PhysRevB.92.035417.

[21] Microelectronics Market - Global Industry Assessment & Forcast, (n.d.). https://www.vantagemarketresearch.com/industry-report/microelectronics-market-1579.

[22] J. Robertson, High dielectric constant oxides, Eur. Phys. J. Appl. Phys. 28 (2004) 265–291. https://doi.org/10.1051/epjap.

[23] H. Alex Hsain, Y. Lee, G. Parsons, and J.L. Jones, Compositional dependence of crystallization temperatures and phase evolution in hafnia-zirconia $(Hf_xZr_{1-x})O_2$ thin films, Appl. Phys. Lett. 116 (2020) 192901

[24] L. Garten, Residual ferroelectricity, piezoelectricity, and flexoelectricity in barium strontium titanate tunable dielectrics, Ph.D. Dissertation, Pennsylvania State University, 2014.

[25] M. Haun, Flexoelectricity in the barium strontium titanate (BST) system for hydrophones, M.S. Thesis, Pennsylvania State University, 2020.

[26] K. Coleman, R. Bermejo, D. Leguillon, and S. Trolier-McKinstry, Thickness dependence of crack initiation and progagation in stacks for piezoelectric microelectromechanical systems, Acta Materialia 191 (2020) 245-252.

[27] I. Zubel, M. Kramkowska, The effect of alcohol additives on etching characteristics in KOH solutions, Sensors Actuators, A Phys. 101 (2002) 255–261. https://doi.org/10.1016/S0924-4247(02)00265-0.

[28] I. Zubel, M. Kramkowska, Etch rates and morphology of silicon (h k l) surfaces etched in KOH and KOH saturated with isopropanol solutions, Sensors Actuators, A Phys. 115 (2004) 549–556. https://doi.org/10.1016/j.sna.2003.11.010.

[29] I. Zubel, K. Rola, M. Kramkowska, The effect of isopropyl alcohol concentration on the etching process of Si-substrates in KOH solutions, Sensors Actuators, A Phys. 171 (2011) 436–445. https://doi.org/10.1016/j.sna.2011.09.005.

[30] R. Lo Nigro, E. Schiliro, G. Mannino, S. Di Franco, and F. Roccaforte, Comparison between thermal and plasma enhanced atomic layer deposition process for the growth of HfO_2 dielectric layers, J. Crystal Growth 539 (2020) 125624.

[31] R. Feng, and R.J. Farris, Influence of processing conditions on the thermal and mechanical properties of SU8 negative photoresist coatings, J. Micromech. Microeng. 13 (2003) 80-88.

[32] K. Wouters, and R. Puers, Characterization of the adhesion of SU-8 and Epoclad, J. Micromech. Microeng. 22 (2012) 097002

CHAPTER 7

Conclusions and Future Work

7.1 Conclusions

The primary goal of this work was investigating how extrinsic contributions affect the dielectric, piezoelectric, and ferroelectric properties of morphotropic phase boundary lead-zirconate titanate ($Pb(Zr_{0.52}Ti_{0.48})O_3$ or PZT) films. The fabrication of two different devices followed: 1) a PZT thin film insole sensor for balance detection to assist the elderly population, and 2) a novel flexoelectric device based around silicon as a potential lead-free energy harvester for this insole sensor. Combining electrical analysis (dielectric permittivity and loss tangent, polarization-hysteresis loops, and macroscopic Rayleigh measurements), with structural analysis (x-ray diffraction (XRD), scanning electron microscopy (SEM), electron backscatter diffraction (EBSD), energy dispersive spectroscopy (EDS), and transmission electron microscopy (TEM)) provided insight into the fundamental mechanisms responsible for the behavior of lead-zirconate titanate films. Additionally, piezoresponse force microscopy (PFM) measurements provided local evidence of domain wall motion.

It is known that undoped PZT films near 1 μm thick display domain clustering behavior. An applied electric field below the coercive field will move domain walls collectively, where the motion of one domain wall often triggers an avalanche of correlated motion. What was unknown prior to this report was whether donor and acceptor doping of PZT films influences the mobility of domain walls and the correlation length over which clusters of domain walls move cooperatively. Band excitation PFM was utilized to directly measure how cluster areas and local nonlinear piezoelectric responses change with a donor dopant (Nb^{5+}) and an acceptor dopant (Mn^{3+}). PFM local spectroscopic mapping of irreversible to reversible Rayleigh coefficient ratios

in 4x4 μm^2 regions showed that an Nb-doped 500 μm thick PZT film displayed a local $\alpha_{d,33}/d_{33,initial}$ ratio of 3.85x10^{-2} ± 1.23x10^{-2} cm/kV while an Mn-doped PZT film of the same thickness displayed a ratio of 2.12x10^{-2} ± 0.77x10^{-2} cm/kV. Importantly, the two films showed nearly identical cluster areas, confirming that avalanche characteristics do not depend on dopant type. Within a 4x4 μm region, it was found that ~75% of clusters detected, which were probed in sub-coercive field conditions, displayed larger areas than the in-plane grain areas of ~20x10^{-3} μm^2 (Mn-doped) and 33x10^{-3} μm^2, confirming domain wall avalanching across grain boundaries. Cluster sizes were also compared for PZT films between 250 nm and 1250 nm thick with donor and acceptor dopants. PZT film thickness was found to influence cluster size and subsequent avalanche characteristics in films with both dopant types. Thicker films displayed both a lower density of high response (high $\alpha_{d,33}/d_{33,initial}$) regions and larger overall cluster areas than thinner films.

Domain wall clustering and sub-coercive avalanche characteristics are not the only extrinsic parameter to consider when designing devices which utilize ferroelectric films. The mobility of domain walls around microstructural features such as grain boundaries and triple points must be considered for polycrystalline ferroelectric films. PZT films on silicon substrates often display an average in-plane grain size between 50 and 200 nm in diameter, which is below the limits of reliable nonlinear band excitation PFM measurements to isolate a single grain boundary. To measure single grain boundaries width of influence in ferroelectric films, PZT was epitaxially grown on $SrTiO_3$ substrates. EBSD enabled the crystallographic orientation mapping of individual PZT grains, and subsequent analysis of grain boundary misorientation angles for both coincident site lattice (CSL) boundary and random boundary types. Nonlinear band excitation PFM was utilized to directly probe the local nonlinear Rayleigh ratio ($\alpha_{d,33}/d_{33,initial}$) to measure extrinsic responses at and near the different types of grain boundaries. In addition, this study provided the first quantitative measurements of the effects of triple points on the motion of

domain walls. CSL grain boundaries were shown to exhibit a shallower minimum in $\alpha_{d,33}/d_{33,initial}$ compared to random grain boundaries, where it is speculated that the regularity in crystalline arrangement at the boundary may facilitate collective domain wall movement. Also, wider widths of influence on domain wall mobility were observed around grain boundaries that displayed a larger difference between its minimum in $\alpha_{d,33}/d_{33,initial}$ and the steady state value into the grain. CSL boundaries showed, on average, lower widths of influences than random boundaries. The largest width of influence occurred near a random boundary, which was 905 ± 153 nm, while the smallest width of influence occurred near a CSL boundary, which was 124 ± 23 nm.

It was found in the same investigation that immediately adjacent to the triple points investigated, a region of material which did not show Rayleigh-like characteristics was observed, i.e., $\alpha_{d,33}/d_{33,initial}$ was negative. This could be a result of either a non-Gaussian distribution of restoring forces and/or a reduction in the number of domain walls at the triple point. As the number of random boundaries (compared to CSL boundaries) surrounding a triple point increased, the radial influence of the triple point on domain wall motion increased. The radial influence at a triple point with two CSL boundaries was 345 ± 9 nm while the radial influence at a triple point with three random boundaries was 528 ± 18 nm. Grain boundaries and triple points are shown here to have a significant effect on the extrinsic contribution to piezoelectricity in PZT films, and the density of grain boundaries should be considered in estimating the net properties of PZT films or bulk ceramics.

In many applications such energy harvesting, ambulatory sensing, and biomedical monitoring, piezoelectric microelectromechanical systems require flexibility. Chapters 2 and 3 quantified extrinsic contributions to the piezoelectric properties of films on stiff substrates. PZT films deposited on flexible substrates are expected to display different extrinsic contributions due to a relief in residual film stress. This effect was investigated by dip-coating PZT films onto five different substrates with varying thickness and coefficient of thermal expansion to examine the

dependence of dielectric and ferroelectric film properties on thermal stress. Grazing incidence XRD of these films showed that the films with higher thermal compressive stresses (PZT on a stiff nickel substrate) displayed a larger volume fraction of out-of-plane domains (~88%). Dielectric permittivity and polarization-hysteresis loop measurements of PZT films on the same type of substrate (nickel) with two different thicknesses provided evidence of preferred domain alignment by substrate clamping. The dielectric permittivity of PZT on a 500 μm thick nickel substrate displayed a 35% lower permittivity and a 12% higher remanent polarization than PZT on a 25 μm thick nickel substrate. Further, macroscopic dielectric Rayleigh analysis enabled the comparison of suppressed domain wall mobility at subcoercive fields for the films on differing substrates. It was found that PZT on flexible (25 μm thick) nickel substrates show a 56% higher nonlinear $\alpha_{\varepsilon}/\varepsilon_{initial}$ Rayleigh ratio relative to the PZT film on stiff (500 μm) substrate. It is concluded that substrate flexibility enhances irreversible domain wall and/or phase boundary motion upon PZT poling while the substrate coefficient of thermal expansion determines the initial post-fabrication domain structure.

In comparing the data for PZT films in Chapters 2 and 4, it is clear that differences in substrate, chemical solution type, film thickness, and dopant type affect the dielectric Rayleigh coefficients. Table 7.1 shows the reversible ($\varepsilon_{initial}$) and irreversible ($\alpha_{\varepsilon,initial}$) Rayleigh coefficients, along with the nonlinearity ratio ($\alpha_{\varepsilon,initial}/\varepsilon_{initial}$) for PZT films of different types. It is seen in general that the $\alpha_{\varepsilon,initial}/\varepsilon_{initial}$ increased with film thickness and was suppressed with acceptor doping. More compliant (thinner) substrates also favor high $\alpha_{\varepsilon,initial}/\varepsilon_{initial}$.

Table 7.1: Dielectric Rayleigh coefficients for PZT films of different thickness, dopant, and substrate. IMO stands for inverted mixing order (refer to Chapter 4). Data for films from Mitsubishi Materials solutions appeared in Chapter 2.

Film and substrate properties				**Rayleigh coefficients**		
PZT solution type	PZT thickness	Dopant	Substrate	$\varepsilon_{initial}$	α_ε (cm/kV)	$\alpha_\varepsilon/\varepsilon_{initial}$ (cm/kV) x10^{-3}
Mitsubishi	1.21 μm	2% Nb	500 μm Si	1430	50.0	**34.9**
IMO	~2.00 μm	2% Nb	25 μm Ni	550	19.0	**34.8**
IMO	~2.00 μm	2% Nb	25 μm Pt	740	24.6	**33.5**
Mitsubishi	1.02 μm	2% Nb	500 μm Si	1220	39.1	**32.0**
Mitsubishi	1.27 μm	2% Mn	500 μm Si	980	29.1	**29.5**
Mitsubishi	1.09 μm	2% Mn	500 μm Si	1033	30.2	**29.2**
Mitsubishi	0.78 μm	2% Nb	500 μm Si	1230	35.7	**29.0**
IMO	~2.00 μm	2% Nb	500 μm Si	1230	28.2	**22.9**
Mitsubishi	0.53 μm	2% Nb	500 μm Si	1240	28.3	**22.8**
IMO	~2.00 μm	2% Nb	500 μm Ni	330	7.4	**22.6**
Mitsubishi	0.50 μm	2% Mn	500 μm Si	1070	19.5	**18.6**

These fundamental studies on how various extrinsic contributions in PZT films affect their properties assisted in developing a flexible insole embedded PZT force sensor array. Domain wall mobility and piezoelectric polarization is enhanced away from grain boundaries, when PZT films are placed on flexible substrates with a high coefficient of thermal expansion, and when the film is doped with donor ions such as Nb^{5+}. Therefore, a Nb-doped PZT film was dip cast directly onto a 25 μm thick stainless-steel foil for analysis as a flexible force sensor. The PZT film displayed low dielectric permittivities (360 ± 10) and moderate remanent polarizations (26.3 ± 3.8 μC/cm^2) indicating a high volume fraction of out-of-plane domains in a sample with incomplete orientation. Individual platinized capacitor structures designed in an array around the surface of the film were tested for their behavior as force sensors in a "balance detection" application. The sensors showed a sensitivity of -9.76 mV/N in an applied force range of 0 to 12 N. An imitation of the "roll" that occurs during a single step from the ball of one's foot was found to activate the voltage signal from each electrode with the expected timing. An examination of the sensor response to a "heel strike" enabled the deduction of the location of center of pressure as

well. Finally, a discrete circuit prototype for multi-channel sensing, digitization, and wireless transmission of the activation signal successfully recorded, amplified, and sent the voltage output response from an applied pressure to a nearby PC. Flexible PZT films were demonstrated here to successfully operate as pressure sensing arrays.

Finally, flexoelectricity in lead-free materials was investigated. Flexoelectricity is a property found in all insulators, and the flexoelectric coefficient is improved when dielectric permittivity is increased. Here, barrier layer capacitor structures with doped silicon as the conductive region and 30 nm HfO_2 as the insulating layer was found to show a permittivity and loss tangent of 34380 ± 4260 and 0.12 ± 0.10, respectively. A cantilever beam with this material stack displayed a direct flexoelectric coefficient of 4.9 ± 0.4 μC/m. Truncated pyramid arrays were fabricated to increase the available strain gradient and reduce the possibility of cracking and device failure. Individual pyramids, with a height of 70 μm and upper square edge length of 260 μm displayed a dielectric permittivity and loss tangent of 20200 ± 1000 and 0.016 ± 0.006 at 1 Hz, respectively. The converse flexoelectric effect of a single truncated pyramid was locally probed with PFM and compared to a planar device with a similar material stack. The planar device displayed zero out of plane deflection with an applied voltage of 15 V, while the pyramid device deflected a maximum of 4 nm out of plane. The flexoelectric device which incorporated micro-sized truncated pyramids here has the potential to act as a mechanical energy harvesting device, sourcing energy from a heel-strike during a single step, to help aid in the push for “power-free” biomedical devices such as insole embedded force sensors.

7.2 Future Work

7.2.1 Automated PFM experiments for grain boundary analysis

A single nonlinear band excitation piezoresponse force microscopy measurement around defects such as grain boundaries takes around 8-12 hours to complete. Each measurement extracts information on local domain mobility and non-linear responses that can originate from multiple mechanisms. In order to obtain a better understanding of how domain walls interact with grain boundaries of varying misorientation angles and with different structures such as coincidence site lattice or random type, significantly more data is necessary. Therefore, automated experiments based on deep kernel learning (DKL) that can reduce the amount of time required for a single measurement should be considered. Liu et al., performed an automated experiment of local non-linear behavior in ferroelectric materials, which explored the correlation of nonlinearity and different PFM image channels [1]. They found that by taking exploration points, random measurements around the surface of the film, they could train the DKL model to measure neighboring points that may show similarities. Additionally, Kelley et al., demonstrated a factor of 5.8 times improvement in imaging rate by using a combination of sparse spiral scanning (see Figure 7.1) with comprehensive sensing and Gaussian processing reconstruction [2]. Although more computationally expensive, this machine learning image restoration technique enables fast scanning and complete image reconstruction.

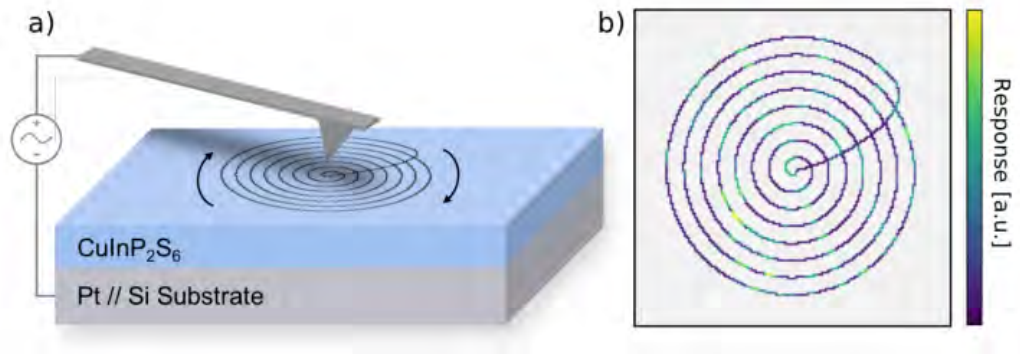

Figure 7.1: Illustration of spiral scan technique. (a) PFM spiral scanning illustration of $CuInP_2S_6$. (b) Corresponding raw data collection from spiral based scanning illustrated in a. Figure adopted from [2].

Machine learning and artificial intelligence have successfully been paired with scanning probe microscopy to enable real-time connection between domain properties and automated measurements [1–3]. This is an efficient method to map nonlinearity Rayleigh ratios across a large surface area and would expedite the nonlinear PFM measurements near grain boundaries. In theory, this method could produce enormous datasets, where every possible grain boundary orientation is mapped, measured, and recorded. This type of experiment would enable more complete understanding of domain wall behavior near grain boundary and triple point defects. Automated experiments would also allow the cluster size of correlated domain wall motion to be measured as a function of crystallite orientation, as the films investigated in Chapter 3 contained randomly oriented crystallites. Finally, the reduced scan time may enable local spectroscopic Preisach distribution analysis to complement the Rayleigh analysis. Up to this point, Preisach analysis has been too time-consuming to perform as a 100x100 pixelated map across the surface of a piezoelectric film; such high loop cycles and applied voltages damage the tip midway through experiments. Exploration point mapping or sparse spiral scanning may enable the direct measurement of the Preisach Model as a function of space, where we can directly measure the reversible and irreversible first order reversal curve (FORC) distributions.

7.2.2 What determines cluster size?

Chapter 2 presents a first of its kind quantitative analysis on the size and distribution of high-nonlinear response clusters for doped PZT films. An important, but unknown question that results from this study remains: What determines cluster size, and can it be controlled? This question may be answered by performing a similar experiment on different sample types, for example a textured 'thick film' or bulk PZT. By focus ion beam (FIB) milling bulk or thick film PZT, BE-PFM will enable cluster size measurements and analysis similar to those presented in Chapter 2. Textured PMN-PT may be measured as well, as cluster areas may depend on grain orientation. If a large enough dataset of cluster size vs grain orientation is developed, trends which may elucidate cluster size dependence may appear.

A second method to investigate what variables may affect cluster shape and size is analysis of fractal dimensions and roughness exponents. Domains and their walls have been characterized with fractal Hausdorff dimensions by comparing irregularly shaped domain wall perimeters to their areas [4]. An in-plane Hausdorff dimension ($H_{\parallel}$) between 1 and 2 was calculated for BFO and BFO-doped PZT films with a domain wall roughness dimension of ζ=0.5-0.6 [4]. This provides information on the wall dimensionality, bond disorder potential, and potential pinning sources in the system. An experiment like that performed in [5] may enable the calculation of fractal dimensions, wall roughness, and domain wall pinning potentials, and help determine how they affect overall cluster size.

Additionally, cluster analysis like that explained in Chapter 2 could be applied to Rayleigh ratio maps measured around grain boundaries and triple points in Chapter 3. Instead of using the highest K-means response as the '1' in binary plots, the lowest K-means response could be employed for each grain to simplify analysis of domain wall motion at and around grain boundaries. A systematic comparison of the grain boundary width of influence and Rayleigh ratio

minima by the existing and new methods should be conducted to assess the viability of this approach. Finally, a similar K-means method may be utilized on the $d_{33,initial}$ maps, rather than the $\alpha_{d33}/d_{33,initial}$ maps, to investigate why the piezoelectric response is high at and around triple points. One hypothesis is that reversible domain motion is enhanced at this type of defect.

7.2.3 Additional converse flexoelectric PFM and permittivity measurements

The flexoelectric barrier layer capacitor structure detailed in Chapter 6 showed an out of plane deflection when ± 15 V was applied through the thickness of a single truncated pyramid. There are several possible improvements to the converse flexoelectric PFM measurements made here on the same size pyramid, which can provide clarity on the origin of out of plane deflection. First, to confirm that the deflection was not dominated by electrostatic response between the tip and material junction, the planar device was measured. An additional measurement may include repeating the experimental procedure, but replacing the "softer" cantilever tip, which had a nominal spring constant of 0.5-9.5 N/m, with a much stiffer tip (50-100 N/m). Utilizing a stiffer tip will reduce the electrostatic contribution to out of plane deflection, and the difference in response between the two tips will verify how much, if any, of the deflection is from electrostatic contributions.

Next, the triangle voltage cycle applied between the pyramid electrodes contained a frequency of ~1 Hz, between 15 V and -15 V. By varying the frequency of applied voltage, one may determine exactly how the out of plane deflection matches the dielectric permittivity measured on a single pyramid. For example, Figure 6.13 shows a dielectric permittivity for pyramid A of 20770 at 1 Hz, 20360 at 10 Hz, 19820 at 100 Hz, and 17500 at 1 kHz. It is expected that as dielectric permittivity decreases when frequency increases, the flexoelectric out of plane deflection will decrease. Space charge permittivity dropout occurs near 1 kHz in pyramid A, so an experiment measuring the out of plane deflection at 10 kHz frequency would determine if the

out of plane deflection is a result of other mechanisms than flexoelectricity due to space charge polarizability. A third experiment, which is a follow-up of the cantilever anneal analysis in Chapter 6, would be to anneal the truncated pyramids at 50^{o}C, 100^{o}C, 200^{o}C, and 400^{o}C and repeat the PFM measurements explained in Chapter 6. The results would show whether the converse flexoelectric effect in these pyramids is enhanced when dielectric permittivity is increased by a factor between 1 and 2.7x (which was the increase in permittivity at a 400^{o}C anneal of the cantilever beams). If so, this would be an effective method to both tune the frequency dependence of the pyramids as well as maximize the flexoelectric out of plane deflection.

The dielectric permittivity temperature dependence of space charge barrier layer capacitors compared to Curie-Weiss dielectrics are one reason why this is such an exciting frontier of research. Ferroelectrics have a peak in dielectric permittivity at phase transition temperatures, which typically follows the Curie-Weiss Law. This only enables a high flexoelectric output over a narrow temperature range and is expected to significantly reduce stability in the flexoelectric performance during device operation. Space charge dielectrics are expected to show a stable dielectric permittivity within a range of temperatures. At low temperatures, the conductivity would freeze out and at high temperatures dielectric loss may become problematic. Nonetheless, temperature windows of hundreds of degrees Celsius are possible [6-8]. This measurement can be easily carried out by measuring the dielectric permittivity and loss tangent as a function of temperature, from ~4K to ~673K (where HfO_2 begins crystallizing).

No new fabrication processes are necessary for these future experiments. Samples already fabricated can be analyzed via PFM and global permittivity following these steps, and much more information on the flexoelectric response, dielectric permittivity dependence, and out of plane deflection are attainable for a better understanding of these structures.

7.2.4 Miniaturization of truncated pyramid structures

As previously stated, Očenášek et al. predict a flexoelectric size effect, where not only is the polarization improved by increasing the strain gradient in a flexoelectric structure, but the flexoelectric coefficient is improved as well [9]. To evaluate this hypothesis in barrier layer capacitor truncated pyramid structures, the pyramids can be scaled down in size. The primary variation in the fabrication procedure would be patterning the silicon nitride squares (step c and e in Figure 6.9) orders of magnitude smaller in edge length. Squares with an edge length of 10μm, 1 μm, 100 nm, and even 10 nm are possible with E-beam photolithography. The SOI wafer device layer thickness would need to be scaled down to the same effect, but the rest of the process flow would remain very similar. Standard AFM tip radii are on the order of 50 nm, so a smaller tip is necessary for a 10 nm pyramid top edge length, but this size variation (and therefore induced electric field gradient variation) could be measured with the same PFM procedure outlined in Chapter 6. Converse flexoelectric coefficients would then be compared to one another, and Očenášek's predication could be directly proved or disproved.

7.2.5 Direct flexoelectric measurements

This report did not attempt to measure the direct flexoelectric effect in micron-sized truncated pyramids. To do this, three different experimental procedures were considered. First, piezoresponse force microscopy may enable a high enough applied force to measure charge from the top and bottom electrodes. An AFM conducting colloidal probe tip with a very high stiffness would be necessary to apply a high enough pressure. A current amplifier paired to a lock-in amplifier may collect the charge and measure out of plane polarization, but the colloidal probe tip may fracture before a current output is detected. If this is true, a nanoindentation technique may be considered. Both electrodes would need to be electrically connected to a current amplifier and

lock-in amplifier. Nanoindentation would allow individual pyramids to be probed and measured for their direct flexoelectric output. If there is not enough charge output with the given strain gradient input, then a third technique may enable measurement of the direct effect.

The truncated pyramids consist of arrays, where the distance between pyramids is designed during the silicon nitride patterning step (step c, Figure 6.9). If a stiff, conductive metal plate was placed on the top and bottom surfaces of the array, a dynamic mechanical analyzer (DMA) could apply the high forces necessary to measure a current output. A significantly larger volume of material would be probed (10s of thousands to millions of pyramids), and the distance between pyramids could be changed to investigate the dependence of the strain gradient on the volume of material, for statistical analysis. These three measurements may allow direct flexoelectric coefficient measurements of an individual or an array of barrier layer capacitor truncated pyramids, which could be compared to the cantilever beam results discussed in Chapter 6.2.4.

7.2.6 Alternate flexoelectric device fabrication procedure

The fabrication procedure outlined in Chapter 6 may result in one serious problem when attempting to measure the direct flexoelectric effect: the four corners of a single pyramid are the only physically constrained regions. Because of this, pyramids may pop out of the SU8 film during an applied compressive stress, and even if they do not, the strain gradient induced within the pyramid may be very difficult to measure with this “4-corner” supported structure. To resolve this issue, a new fabrication flow is proposed, and initial results are given.

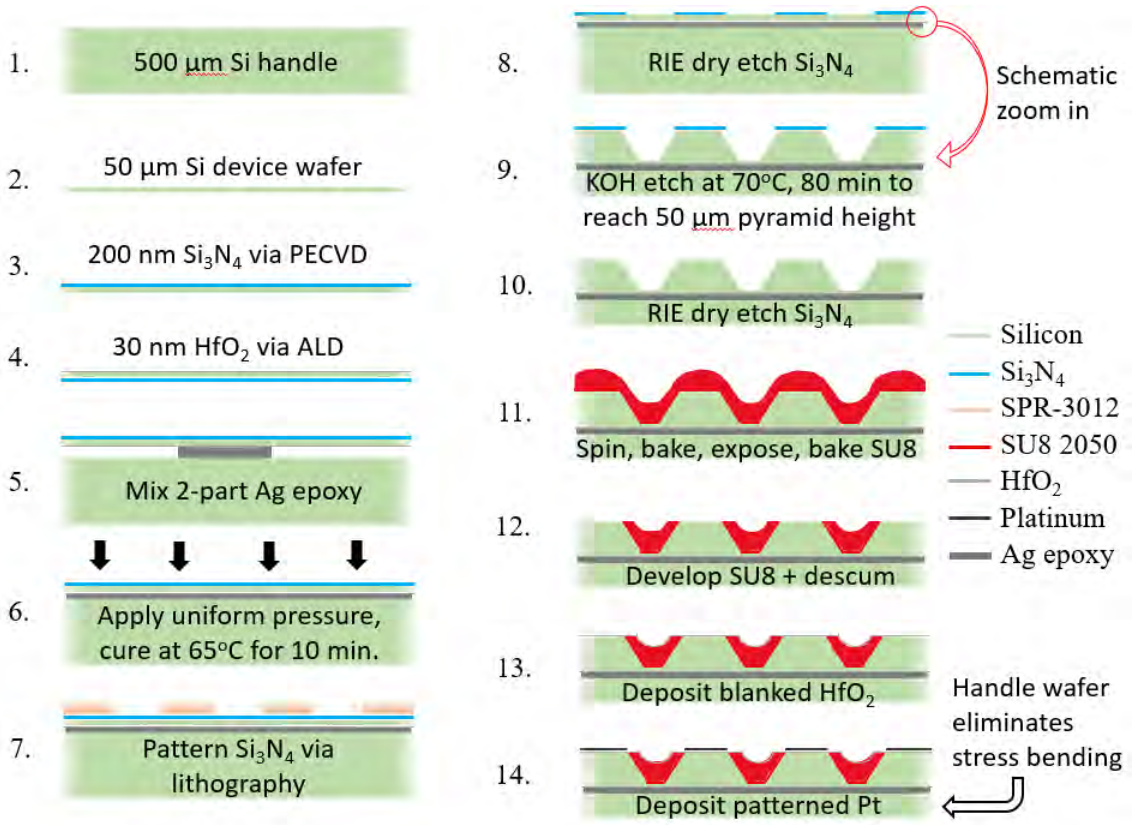

Figure 7.2: Revised flexoelectric device fabrication flow incorporating a 2-part conductive silver epoxy.

Figure 7.2 displays a revised process flow that incorporates a silver epoxy to bond a thinned wafer to a handle wafer. This method enables the deposition of HfO_2 and Pt onto the backside of a "device" wafer first, which eliminates the need to reach the backside *through* a handle wafer to deposit the HfO_2 and backside electrode. Silicon nitride was deposited via PECVD (conditions found in Chapter 6) on the top surface of a 2" diameter, 50 µm thin <100> silicon wafer (Figure 7.2 step 2), then the wafer was flipped over and 30 nm HfO_2 was deposited via ALD onto the backside (conditions found in Chapter 6). A 2-part silver epoxy (MG Chemicals 8331D silver conductive epoxy adhesive) was mixed and dispensed onto a 4" diameter, 500 µm thick silicon wafer (handle wafer) (Figure 7.2 step 5), and the HfO_2 side of the thinned wafer was pressed onto the epoxy uniformly and heated to 65°C for 10 minutes (Figure

7.2 step 6). An example of this process is displayed in Figure 7.3, and the wafer stack after cooling to room temperature is shown in Figure 7.4.

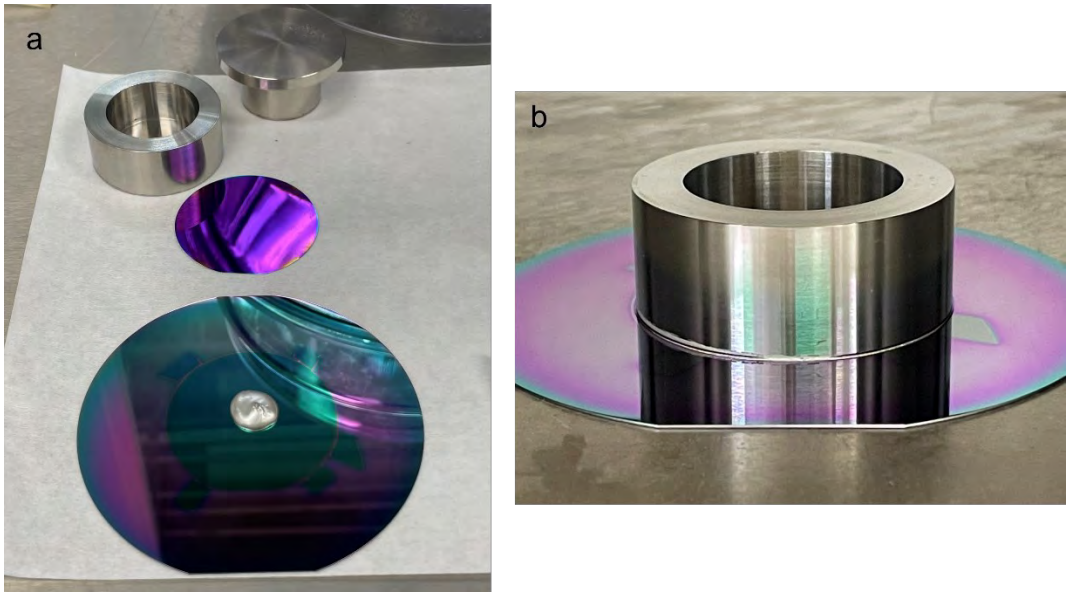

Figure 7.3: Images of the 2” diameter 50 µm thin wafer, the 4” diameter 500 µm thick wafer, and die pieces to flatten the 2” wafer onto the conductive epoxy (left). Die sitting on the 50 µm wafer/HfO_2/epoxy/500 µm stack (right).

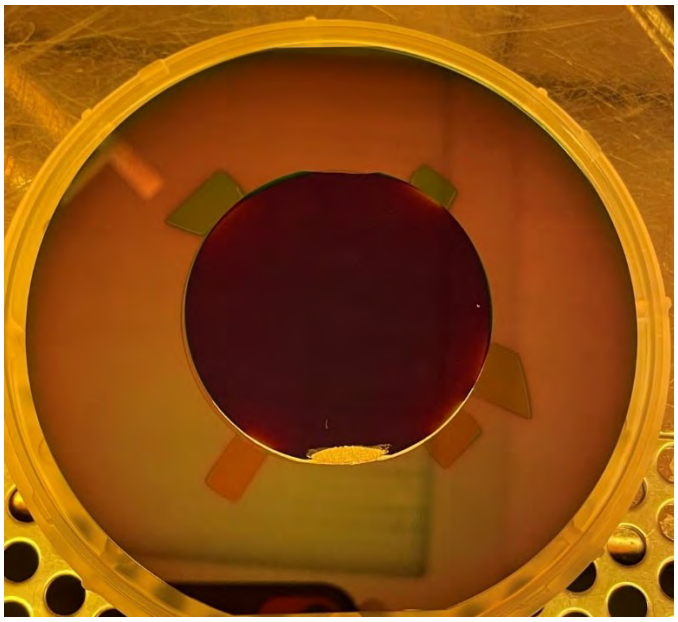

Figure 7.4: The 2” diameter wafer bonded to the 4” diameter handle wafer after the 65°C anneal step to cure the epoxy.

Steps 7-14 in Figure 7.2 were very similar to the procedure discussed in Chapter 6. Figure 7.5 shows the pyramids after a KOH etch to reach the epoxy bond (step 9 Figure 7.2) and removal of the nitride on each pyramid surface (step 10 Figure 7.2). It is important to leave a thin layer of silicon at the bottom surface so subsequent wet and dry etches do not etch the HfO_2 layer and undercut pyramids. A modification to this "wafer-bond" procedure is to replace the epoxy with a gold-gold bond between the device and handle wafer. E-beam evaporation enables low-stress Cr/Au gold layers to be deposited onto each wafer surface, then a wafer bonder can be used to bond the two gold surfaces together. This process would provide a cleaner interface between the two wafers and may hold up better in a long (70-100 minute) KOH bath.

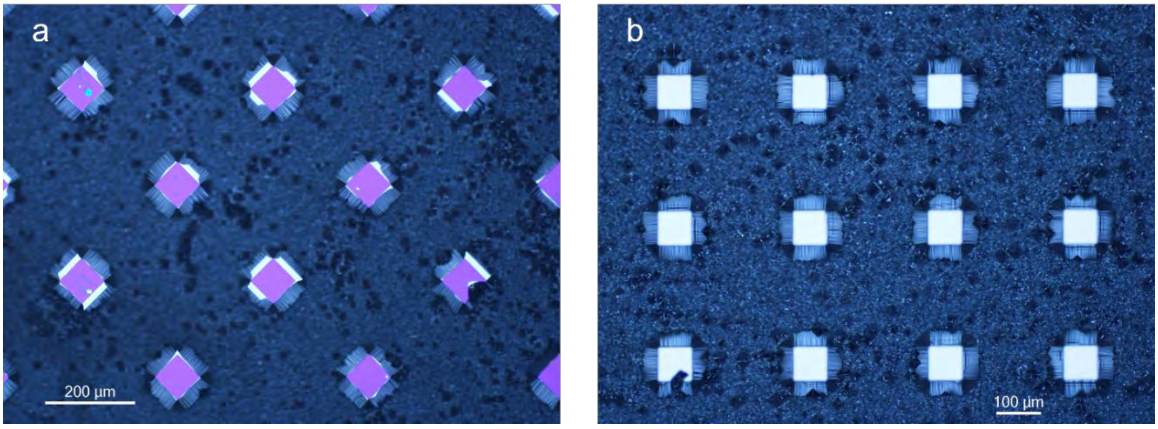

Figure 7.5: Optical microscopy images of the pyramid arrays after the KOH wet etch (a) and after a 70 second RIE to remove the silicon nitride masks (b).

7.3 References

[1] Y. Liu, K.P. Kelley, R.K. Vasudevan, W. Zhu, J. Hayden, H. Funakubo, M.A. Ziatdinov, S. Trolier-mckinstry, V. Sergei, Automated experiments of local non-linear behavior in ferroelectric materials, Small. 18 (2022).

[2] K.P. Kelley, M. Ziatdinov, L. Collins, M.A. Susner, R.K. Vasudevan, N. Balke, S. V Kalinin, S. Jesse, Fast scanning probe microscopy via machine learning: Non-rectangular

scans with compressed sensing and Gaussian process optimization, Small. 16 (2020).

[3] Y. Liu, K.P. Kelley, R.K. Vasudevan, H. Funakubo, S.S. Fields, S. Trolier-mckinstry, J.F. Ihlefeld, M. Ziatdinov, S. V Kalinin, Machine learning-driven automated scanning probe microscopy for ferroelectrics, Microsc. Microanal. 28 (2022) 2924–2926. https://doi.org/10.1017/S1431927622010972.

[4] G. Catalan, H. Bea, S. Fusil, M. Bibes, P. Paruch, A. Barthelemy, J.F. Scott. Fractal dimension and size scaling of domains in thin films of multiferroic $BiFeO_3$, PRL 100 (2008).

[5] B. Ziegler, K. Martens, T. Giamarchi, and P. Paruch, Domain wall roughness in stripe phase $BiFeO_3$ thin films, PRL 111 (2013).

[6] A.K. Rai, N.K. Singh, S.K. Lee, K.D. Mandal, D. Kumar, and O. Parkash, Dielectric properties of iron doped calcium copper titanate, J. Alloys and Compounds 509 (2011) 8901-8906

[7] D.P. Samarakoon, N. Govindaraju, and R.N. Singh, Influence of atmospheres on the dielectric properties of calcium copper titanate ceramics, J. Am. Ceram. Soc. 102 (2019) 5271-5283

[8] D.P. Samarakoon and R.N. Singh, Thickness dependent dielectric properties of calcium copper titanate ceramics measured in a controlled atmosphere, Ceramics International 45 (2019) 16554-16563

[9] J. Očenášek, H. Lu, C.W. Bark, C.B. Eom, J. Alcalá, G. Catalan, A. Gruverman, Nanomechanics of flexoelectric switching, Phys. Rev. B - Condens. Matter Mater. Phys. 92 (2015) 1–9. https://doi.org/10.1103/PhysRevB.92.035417.

APPENDIX A

Supplementary Materials for Chapter 2

Table A.1: Coercive fields (E_c) of each PZT film; each capacitor was poled at 3x the coercive voltage (V_c)

PNZT Film Thickness (nm)	Negative E_c (kV/cm)	Positive E_c (kV/cm)	Average E_c (kV/cm)	3xE_c (kV/cm)	Poled at 3xV_c (V)
288	-30.2	20.2	25.2	75.6	2.2
528	-29.3	22.7	26.0	78.0	4.1
775	-41.7	37.5	39.6	118.8	9.2
1022	-40.1	36.5	38.3	115.0	11.8
1210	-35.0	35.4	35.2	105.6	12.8
PMZT Film Thickness (nm)	**Negative E_c (kV/cm)**	**Positive E_c (kV/cm)**	**Average E_c (kV/cm)**	**3xE_c (kV/cm)**	**Poled at 3xV_c (V)**
222	-10.6	35.7	23.1	69.4	1.5
498	-9.9	43.3	26.6	79.8	4.0
773	-33.0	51.5	42.3	126.8	9.8
1085	-29.2	50.8	40.0	120.1	13.0
1265	-29.7	52.1	40.9	122.7	15.5

When the negative coercive field was greater than the positive coercive field, the DC bias positive terminal was connected to the bottom electrode and the negative terminal probe was placed on the top electrode. The opposite configuration was utilized when the positive coercive field was greater than the negative coercive field. All Nb-doped films had -Ec > +Ec, and all Mn-doped films had -Ec < +Ec

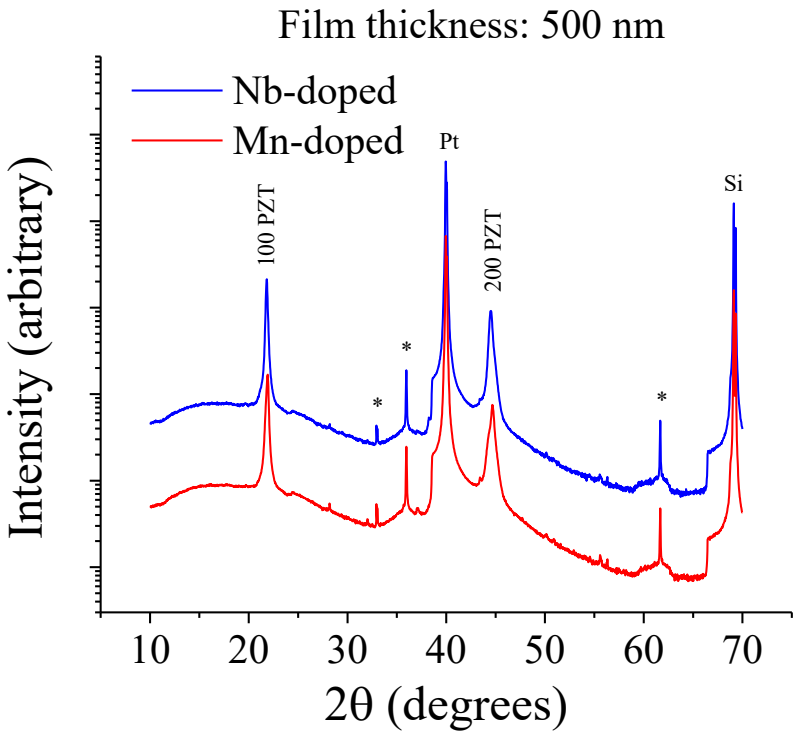

Figure A.1: Bragg-Brentano x-ray diffraction of 500 nm thick PZT films (Nb and Mn-doped) showing majority <100> orientation. Both films have a <100> Lotgering Factor of 99%.

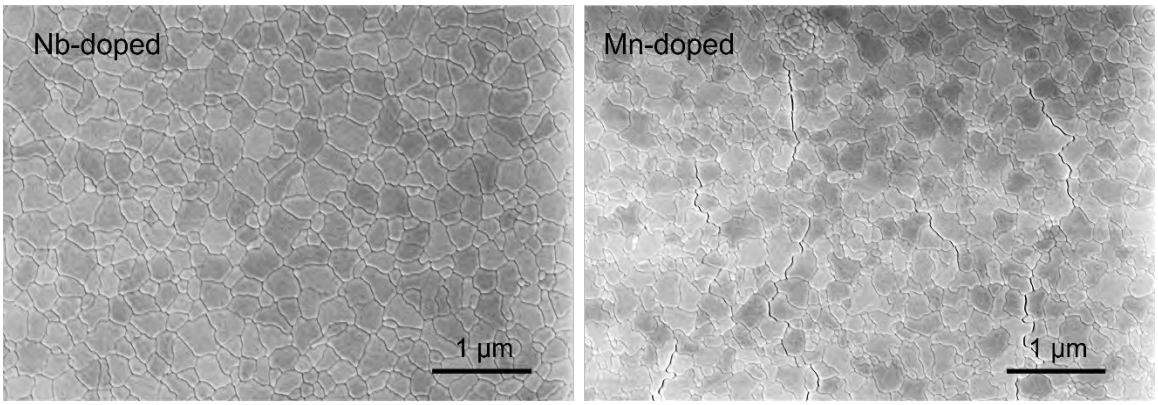

Figure A.2: Scanning electron microscopy images showing grain structure off the electrode for Nb-doped PZT (left) and Mn-doped PZT (right) 500 nm thick. Average grain size was calculated with the line intercept method and grain area was (grain size/2)^2 * 3.1415.

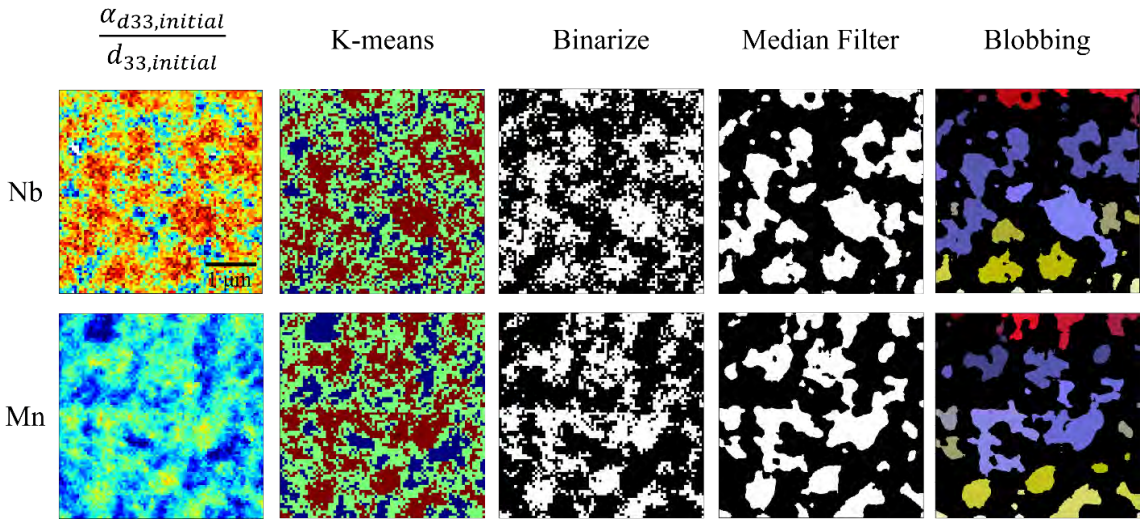

Figure A.3: Image analysis to separate and count high response clusters for 500 nm thick Nb doped (top row) and Mn doped (bottom row) films from Rayleigh ratio spectroscopic maps.

APPENDIX B

Supplementary Materials for Chapter 3

$SrTiO_3$ final polishing & anneal parameters:

The polycrystalline $SrTiO_3$ ceramics were polished with colloidal silica grit (0.05 μm) at 150 RPM sample rotator speed, 150 RPM platen speed, and 27 N of force, with water as a lubricant. The substrate was then heat treated in a rapid thermal annealer (RTA) at 700°C for 1 minute to remove organics and aid in recrystallization of the surface.

Table B.1: Deposition conditions for $SrRuO_3$ bottom electrodes on polycrystalline $SrTiO_3$ substrate stacks (100 nm $SrRuO_3$)

Composition	Chamber Pressure [mTorr]	Estimated Surface Temperature [°C]	Target-Substrate Distance [cm]	Laser Energy Density [J cm^{-2}]	Repetition Rate [Hz]	Pulses [#]
$SrRuO_3$	160	680	8	1.4	10	6,600

$SrRuO_3$ pulsed laser deposition procedure:

PLD was performed by using a KrF excimer 248 nm laser (Lambda Physik Compex Pro). The $SrTiO_3$ substrates were mounted on a Nova Pt-coated silicon wafer for PLD depositions of $SrRuO_3$ to facilitate removal of the fragile substrate from the heater block at the cost of an additional thermal barrier between the heater and surface. The $SrRuO_3$ target was obtained from AEM Deposition Co. Prior to each deposition, the target was resurfaced using sandpaper. The target surface was then pre-ablated at the desired laser energy and 20 Hz repetition rate for one minute prior to pumping down the system to a base pressure of 10^{-7} Torr. A PCI G-1 Ozone generator introduced a mixture of 90% O_2:10% O_3 into the chamber until the deposition pressure of 160 mTorr was reached. After deposition, the heater power and the laser were turned off simultaneously. The chamber was vented with air to 100 Torr, and the sample was cooled to

100°C at this pressure. For the deposition conditions in Table B.1, the $SrRuO_3$ films had an average roughness of 19.4 nm on $SrTiO_3$.

Sol-gel PZT deposition parameters:

The PZT solution was dispensed on to the substrate through a syringe with a 0.1 µm filter until the entire surface was covered. The samples were spun at 2750 rpm for 45 s using a PWM32 photoresist spinner (Headway Research, Inc., Garland, TX). The deposited layer was pyrolyzed at 100°C and 300°C on hot plates for 1 and 2 minutes, respectively, for each cycle to remove organics. The sample was RTA'd after each PZT layer at 700°C for 1 minute with a heating rate of 4°C/s and 2.0 SLPM O_2 gas ambient in the system. This process was repeated until the desired thickness (typically 1000 nm) was achieved, with each spin step sequence producing a ~80 nm layer of film for a 15 wt% solution molarity of 0.75 M.

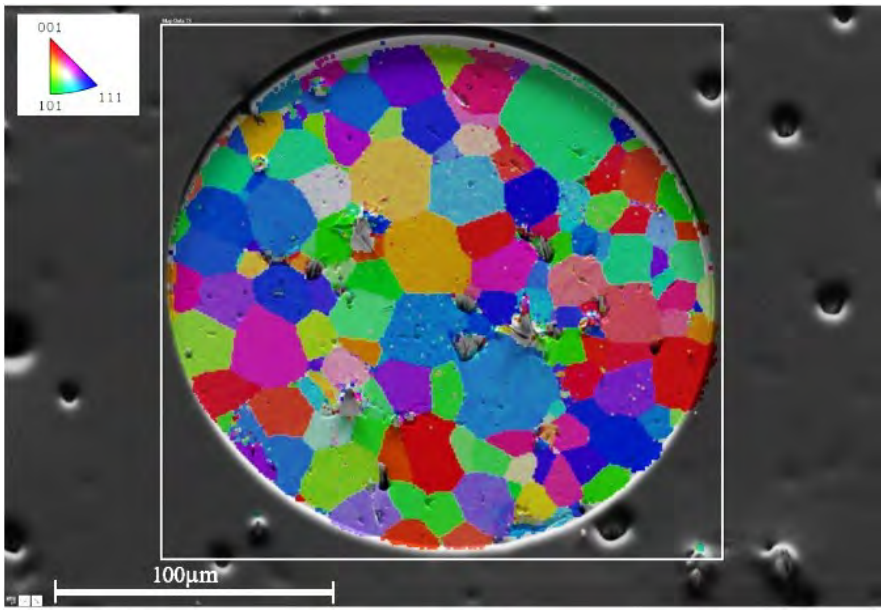

Figure B.1: EBSD scan of the exposed electrode area of 1000 nm PZT/200 nm $SrRuO_3$ on polished $SrTiO_3$ prior to platinum sputtering

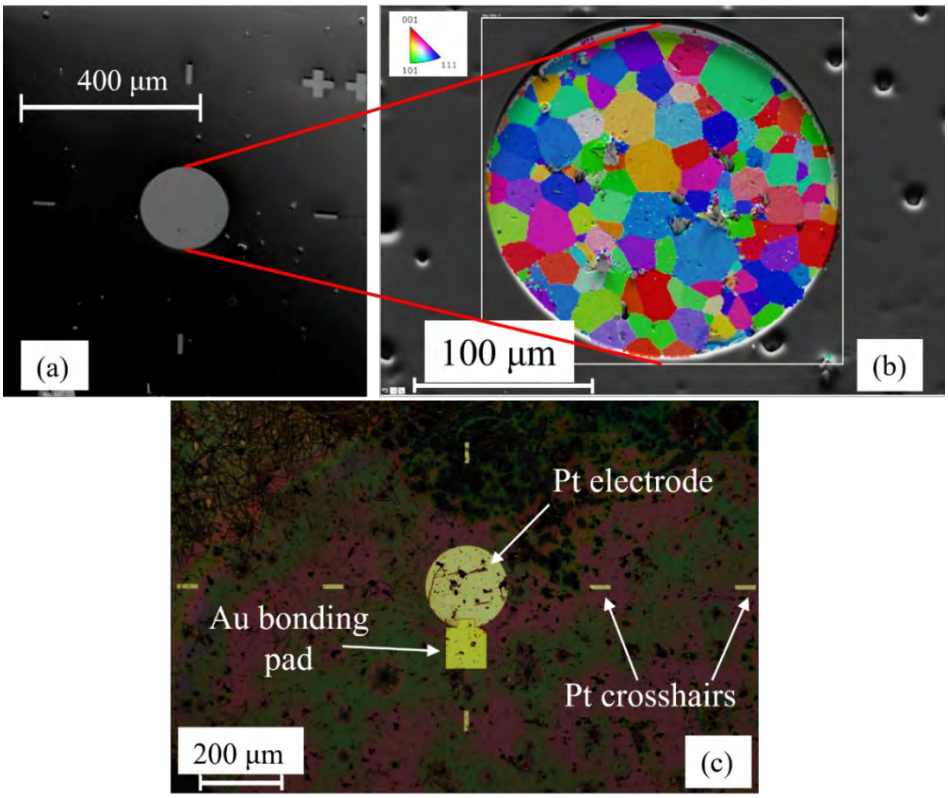

Figure B.2: (a) SEM image of patterned electrode area and alignment crosshairs with exposed PZT layer. (b) EBSD map of the same electrode area rotated with respect to PFM crosshair orientation. (c) Electrode area with patterned gold pad for electrical contact via wirebonding.

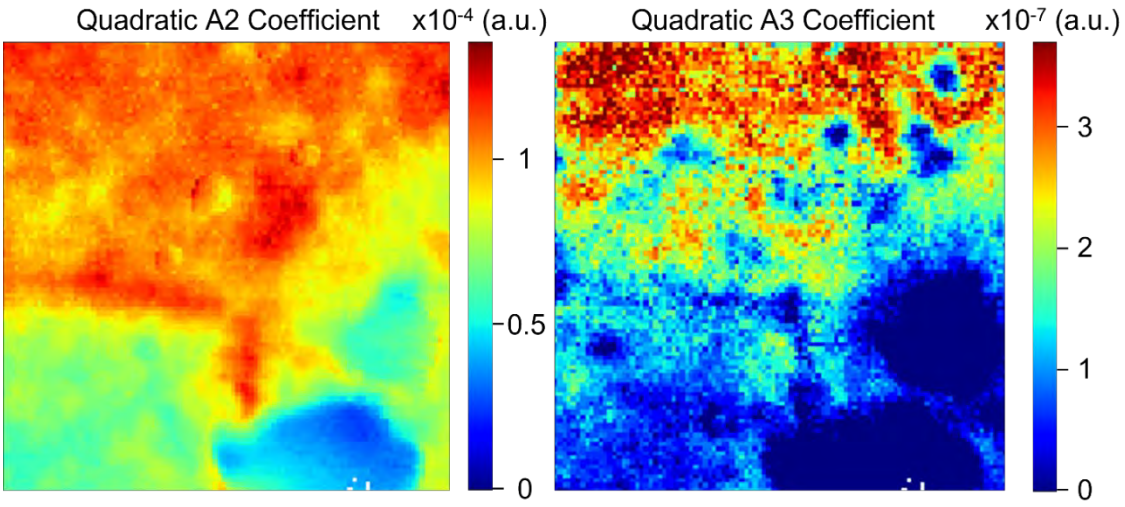

Figure B.3: Maps of A2 and A3 for the purple/pink/fuchsia triple point

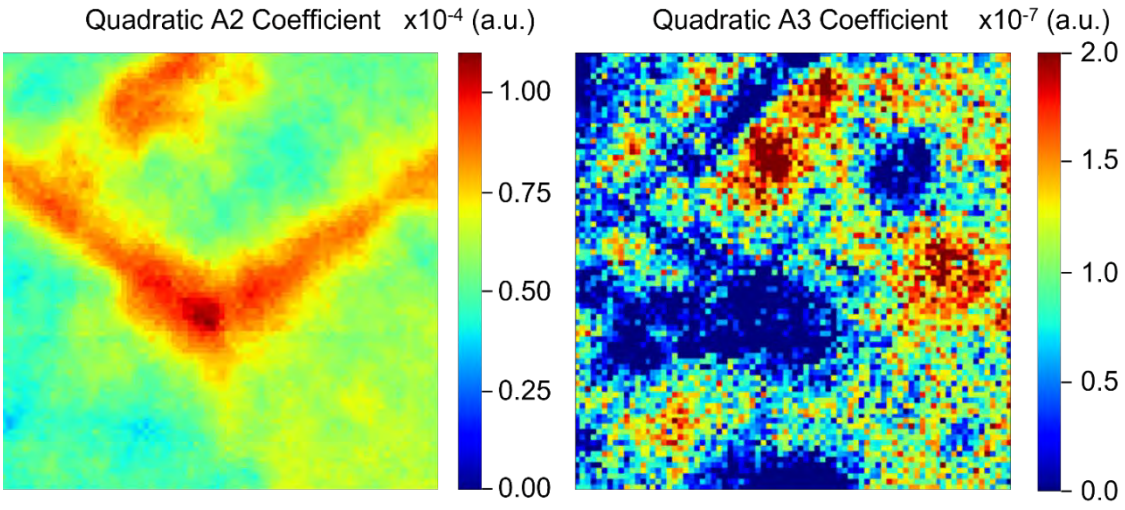

Figure B.4: Maps of A2 and A3 for the orange/dark blue/light blue triple point

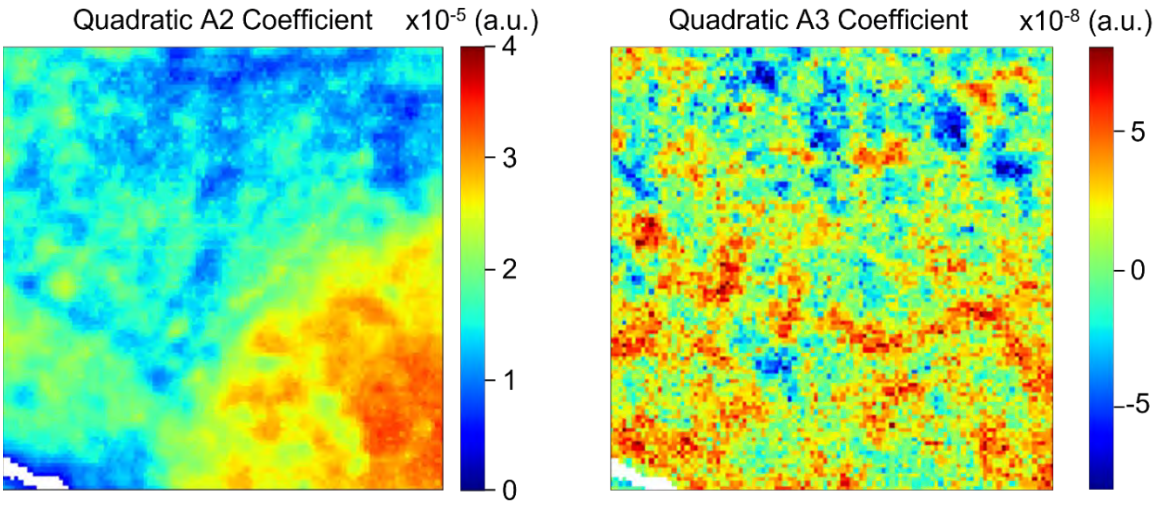

Figure B.5: Maps of A2 and A3 for the blue/pink/green triple point

APPENDIX C

Supplementary Materials for Chapter 4

Table C.1: Metal substrate polishing procedure

Elemental metal substrate	Ni (25 µm), Ni (500 µm), Pt (25 µm)		Ag (25 µm)
Step	1	2	1
Polishing Pad	Atlantis	Atlantis	Final P
Slurry	3 µm polycrystalline diamond suspension, glycol based (ALLIED)	1 µm polycrystalline diamond suspension, glycol based (ALLIED)	1 µm polycrystalline diamond suspension, glycol based (ALLIED)
Coolant	Red Lube	Red Lube	Red Lube
Sample/stage rate (rpm)	150/150	150/150	150/150
Force (lbf)	3	3	2
Time	6 minutes	2 minutes	3 minutes

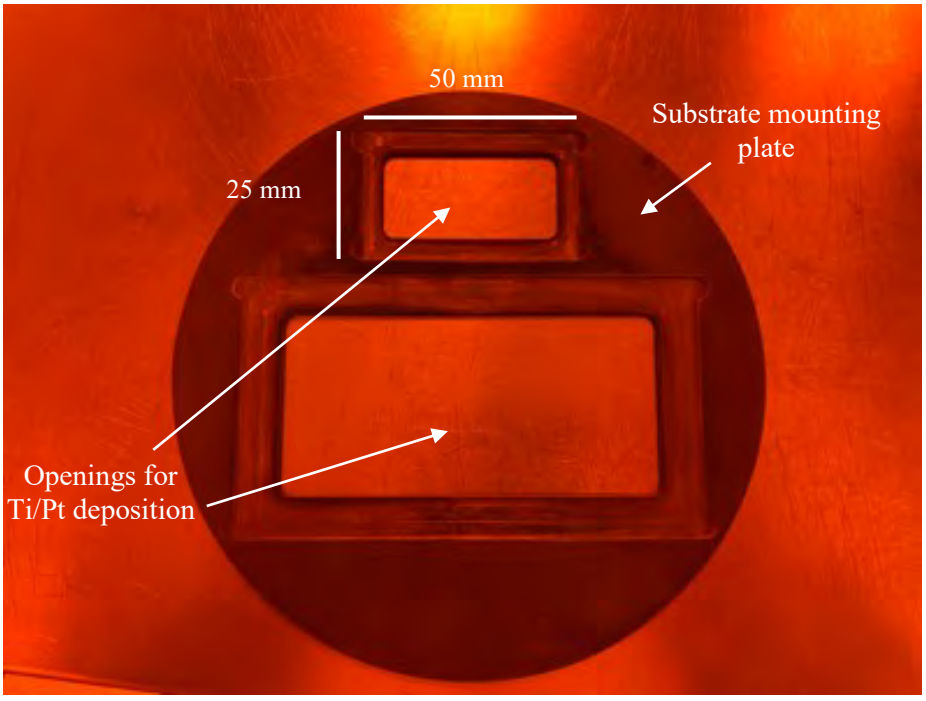

Figure C.1: Substrate mounting plate used during sputter deposition of Ti and Pt.

Table C.2: Inverted mixing order sol-gel PZT fabrication procedure

Step	
1	Pipette 7.7332 g Zr precursor into 100mL beaker
2	Pipette 4.9432 g Ti precursor, ultrasonicate for 5 minutes
3	Pipette 0.2753 g Nb precursor, ultrasonicate for 5 minutes
4	Pipette 7.2155 g acetic acid, ultrasonicate for 5 minutes
5	Add 4 mL methanol to solution
6	Add 12.8467g Pb acetate trihydrate to solution
7	Heat solution at 95ºC for 30 minutes to dissolve lead precursor, mix occasionally
8	Add 4mL methanol, 4 mL DI H_2O, and 20 mL acetic acid to achieve 0.6M

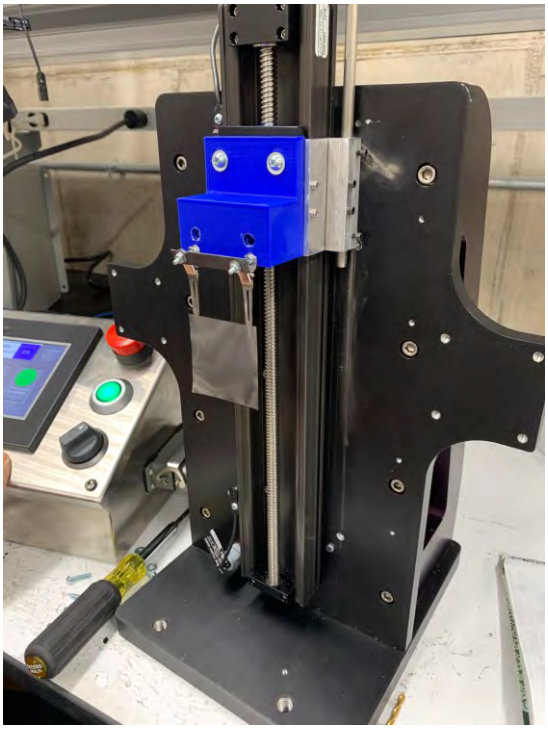

Figure C2: Dip coating setup. 3D printed substrate holder (blue) utilized with toothless alligator clips to allow for ease of substrate transfer. Automated z-control user panel interface to the left.

Table C3: Rapid thermal annealer heating and cooling script

Step	Step Function	Step time (sec.)	Ramp Rate (ºC/sec.)	Temperature (ºC)	Oxygen gas flow (SLPM)
1	Hold	5	0	200	2
2	Ramp	15	13.33	400	2
3	Hold	60	0	400	2
4	Ramp	40	6.25	650	2
5	Hold	120	0	650	2
6	Ramp	90	5	200	2
7	Hold	10	0	200	0

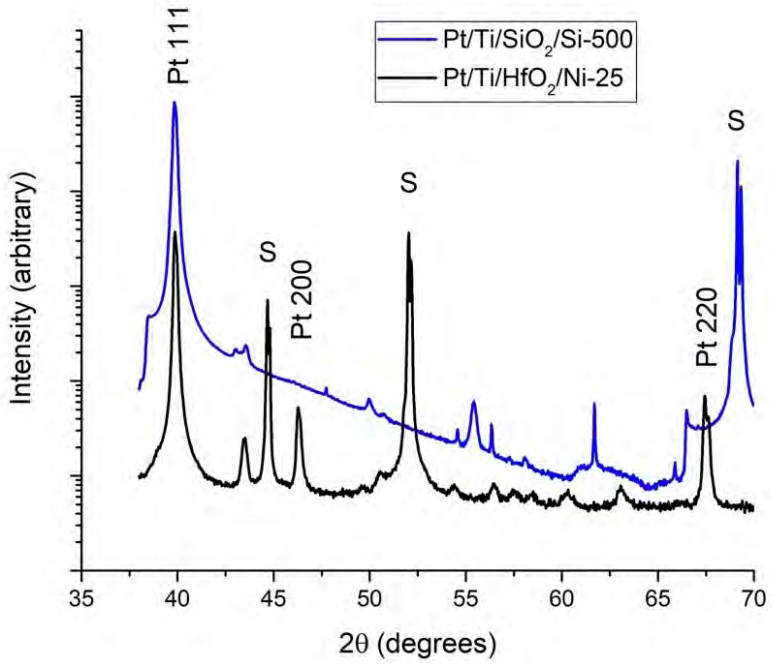

Figure C.3: Bragg-Brentano XRD measurement of Pt coated Si wafer (blue) and Pt coated 25 μm Ni foil (black). Pt on Si displays 100% (111) orientation and Pt on Ni-25 displays 85% (111) orientation.

Table C.4: Coefficients extracted from LIPRAS fit analysis of grazing incidence XRD

	PZT-Si-500		PZT-Pt-25		PZT-Ni-25		PZT-Ni-500		PZT-Ag-25	
	Value	Error	Value	Error	Value	Error	Value	Error	Value	Error
f	0.8634	0.0126	0.4770	Na	0.4936	0.0088	0.4725	0.0048	0.4999	0.0040
N1	3980	51.69	29700	136.1	36620	523.2	96230	1858	42410	863.4
x1	44.37	0.0062	44.06	0.0012	43.95	0.0043	43.82	0.0029	43.94	0.0021
a1	0.0133	0.0637	0.7509	0.0304	0.3061	0.0749	0.0587	0.0343	0.0303	0.0445
N2	-	-	12100	178.2	17640	646.5	21190	436.1	13810	1366
x2	-	-	44.46	NA	44.35	0.0061	44.28	0.035	44.45	0.0239
a2	-	-	-0.9427	0.1218	0.6567	0.2318	0.5239	0.2718	0.8679	0.5265
N3	-	-	1144	195.4	3179	276.1	3512	1912	8218	2090
x3	-	-	44.78	0.0216	44.65	NA	44.65	0.1139	44.65	NA
a3	-	-	6.675	2.298	-0.5010	0.3012	-1.1999	0.4566	0.8593	0.2867
R^2	0.9946	-	0.9998	-	0.9998	-	0.9999	-	0.9998	-
rmse	1.217	-	1.749	-	1.956	-	1.470	-	1.798	-

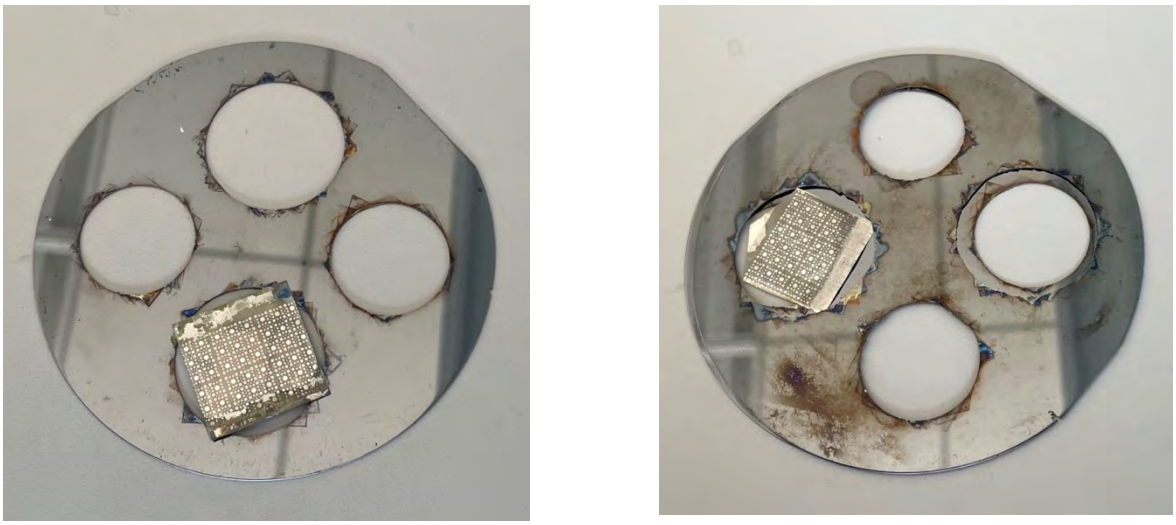

Figure C.4: Sample configuration during crystallization procedure: PZT on Si-500 and Ni-500 where one silicon carrier wafer was used below the substrate(left). PZT on Pt-25, Ni-25, and Ag-25 where a second carrier wafer was placed on top of each substrate to pin down the four corners (right).

Matlab Script to calculate the integrated intensity of each fitted peak

```
clc

clear

N=%Fit intensity of peak;

w=%Fit w value;

xv=%Fit 2-theta at peak maximum;

d=1.54/sind(xv./2) %calculate lattice parameter

g=%Fit full width half max of peak;

a=%Fit asymmetric coefficient;

b=43; %start 2-theta

c=45.5; %end 2-theta

x=linspace(b,c,100);

f = @(x) N.*((w.*(2./pi).*(1./(2.*g./(1+exp(a.*(x-xv))))).*1./(1+(4.*(x-xv).^2./(2.*g./(1+exp(a.*(x-

xv))))).^2))) + ...
```

```
((1-w).*(2.*sqrt(log(2))./(sqrt(pi))).*1./(2.*g./(1+exp(a.*(x-xv)))).*exp(-log(2).*4.*(x-
xv).^2./(2.*g./(1+exp(a.*(x-xv)))).^2)));
peak_Si_500=N.*((w.*(2./pi).*(1./(2.*g./(1+exp(a.*(x-xv))))).*1./(1+(4.*(x-
xv).^2./(2.*g./(1+exp(a.*(x-xv)))).^2))) + ...
((1-w).*(2.*sqrt(log(2))./(sqrt(pi))).*1./(2.*g./(1+exp(a.*(x-xv)))).*exp(-log(2).*4.*(x-
xv).^2./(2.*g./(1+exp(a.*(x-xv)))).^2)));
Si_500=integral(f,43,45.5)
plot(x,peak_Si_500)
```

APPENDIX D

Supplementary Materials for Chapter 5

Table D1: A comparison of existing force sensors with information on each device sensitivity, flexibility, energy requirements and applied force or pressure ranges.

Sensor type	Sensitivity	Flexible (Y/N)	Requires Energy (Y/N)	Applied force/pressure range	Reference
Capacitive	0.0007-0.008 kPa^{-1}	Y	Y	0-350 N (0-35 kPa)	[1][a]
Resistive	1.14 kPa^{-1}	Y	Y	0-5 kPa	[2][b]
Piezoresistive	840 mV/N	N	Y	0-0.008 N	[3][c]
Triboelectric	2970 mV/kPa	Y	N	0-1000 kPa	[4]
Piezoelectric	10800 mV/N	Y	N	0-0.05 N	[5][d]
Piezoelectric	4.91 mV/με	Y	N	NA	[6][e]
Piezoelectric	31.8 pC/kPa	N	Y	0-0.44 N (0-10 kPa)	[7][f]
Piezoelectric	0.34 mV/kPa	N	N	3-30 kPa	[8]
Piezoelectric	9.76 mV/N (0.03 mV/kPa)	Y	N	0-60 N (0-191 kPa)	This work

[a] indicates a sensor whose electrical output was a change in capacitance over initial capacitance, and sensitivity unit was kPa^{-1}
[b] indicates a sensor whose electrical output was a change in current over sensor current under no load, sensitivity unit was kPa^{-1}
[c] cantilever beam structure, applied pressure at sensor location unknown
[d] sensor force area not given
[e] piezoelectric strain sensor contains sensitivity units of voltage over applied strain
[f] indicates a sensor whose electrical output was charge, and sensitivity unit was output charge over applied pressure

Figure D1: Experimental setup for pyrolyzing both sides of the sample after each dip. Instead of placing the substrate directly on the hotplate, a stainless-steel bracket was created to "prop" the sample up one millimeter above the hotplate surface. A ceramic box was placed over the sample on each hotplate to improve temperature uniformity around the entire sample.

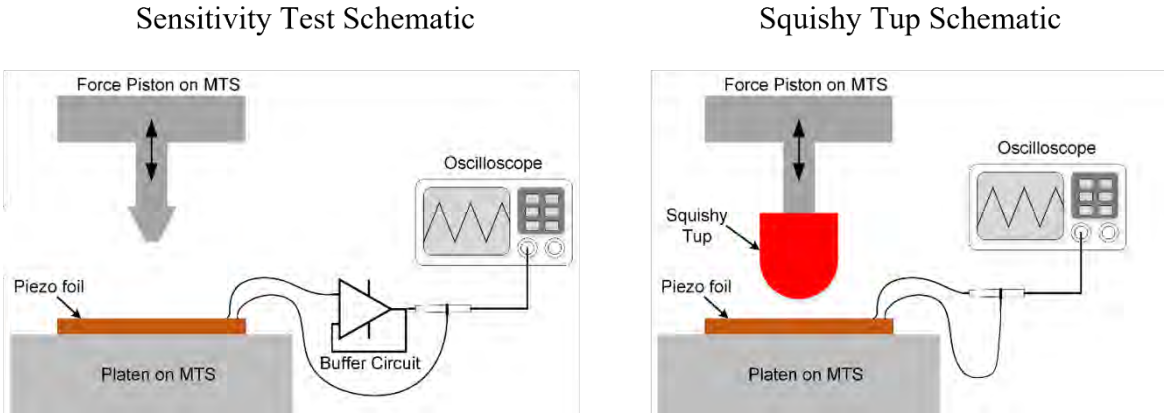

Figure D2: Schematic of the experimental setup for the sensitivity (a) and squishy tup measurements (b).

A single layer of PZT was dip-cast at 45 mm/minute on a silicon wafer with 1.5 μm SiO_2 and a 100 nm Pt top electrode. The two pyrolysis steps were performed as mentioned in the manuscript. Optical profilometry was implemented to measure the thickness variation along the

length of the dip-cast direction. The fit was performed with a Cauchy model. X-ray photoelectron spectroscopy (XPS) experiments were performed using a Physical Electronics VersaProbe III instrument equipped with a monochromatic Al Kα x-ray source (hν = 1,486.6 eV) and a concentric hemispherical analyzer. Charge neutralization was performed using both low energy electrons (<5 eV) and argon ions. The binding energy axis was calibrated using sputter cleaned Cu (Cu $2p_{3/2}$ = 932.62 eV, Cu $3p_{3/2}$ = 75.1 eV) and Au foils (Au $4f_{7/2}$ = 83.96 eV). Peaks were charge referenced to CH_x band in the carbon 1s spectra at 284.8 eV. Measurements were made at a takeoff angle of 45° with respect to the sample surface plane. This resulted in a typical sampling depth of 3-6 nm (95% of the signal originated from this depth or shallower). Quantification was done using instrumental relative sensitivity factors that account for the x-ray cross section and inelastic mean free path of the electrons. On homogeneous samples major elements (>5 atom%) tend to have standard deviations of <3% while minor elements can be significantly higher. The analysis size was ~200 μm in diameter. The sample was then annealed at 650ºC for 2 minutes in an RTA and the optical profilometry and XPS measurements were repeated in the same areas.

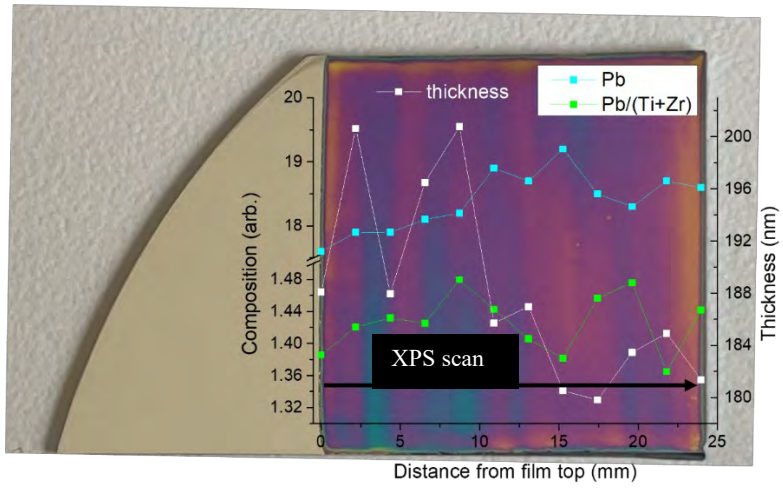

Figure D3: Top surface optical image of single layer PZT prior to crystallization step, with a dip cast withdrawal rate of 45 mm/minute. Overlaid is x-ray photoelectron spectroscopy composition measurements along the "XPS scan" arrow and film thickness measured via optical profilometry.

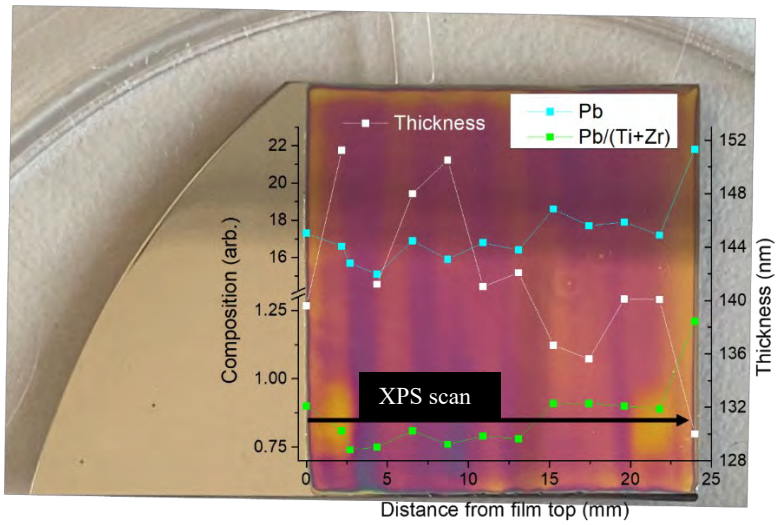

Figure D4: Top surface optical image of single layer PZT after a crystallization step. XPS and profilometry data overlaid with scanned region denoted with black arrow.

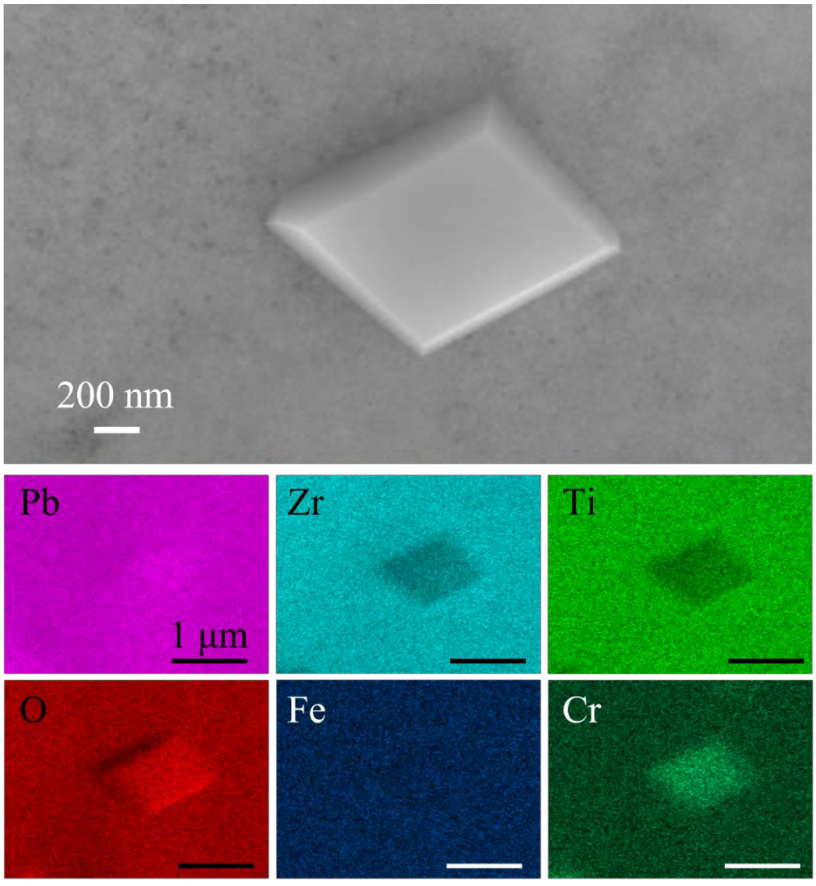

Figure D5: Energy dispersive spectroscopy analysis of lead-rich Cr_2O_3 inclusion found in scanning electron microscopy

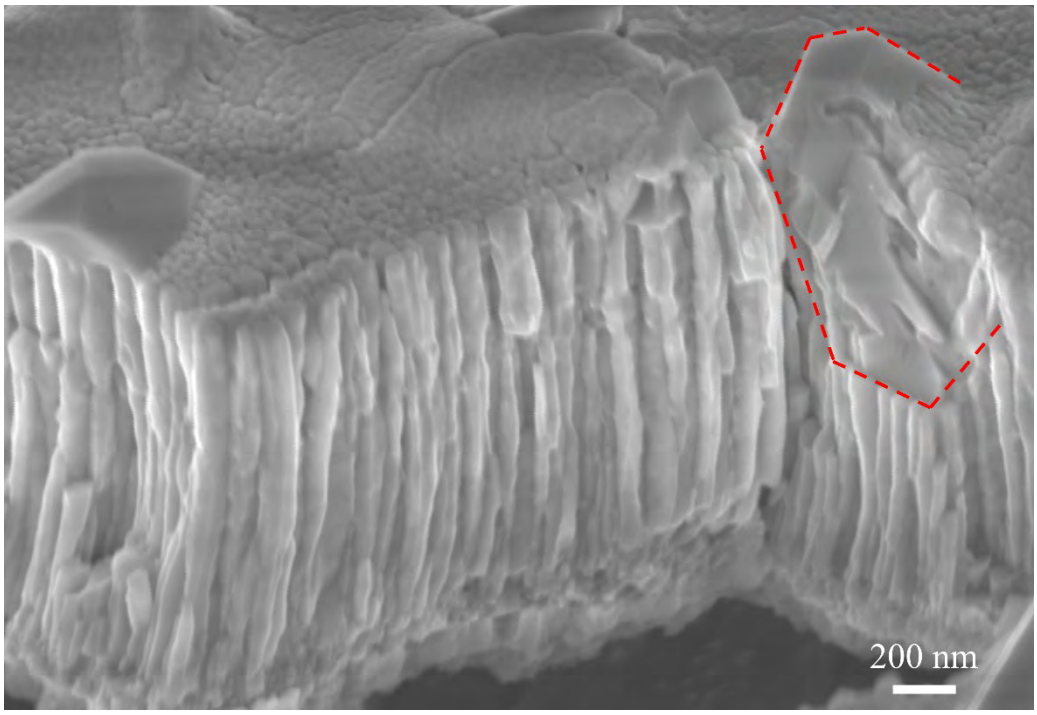

Figure D6: Scanning electron microscopy image of cross-sectional PZT on stainless steel foil. Lead-rich Cr_2O_3 inclusion outlined in red dashed lines.

Table D2: Capacitance, loss tangent and permittivity of selected electrodes, measured at 1 kHz and 30 mV AC voltage.

	Prior to BCB spin coat/cure			After BCB, Ti/Au leads				After attaching wires, poling		
	C (nF)	**tanδ**	**ε_r**	**C (nF)**	**tanδ**	**ε_r**	**Parasitic C (pF)**	**C (nF)**	**tanδ**	**ε_r**
G2	7.15	0.28	330	7.96	0.13	370	810	7.25	0.11	340
H2	7.50	0.23	350	8.18	0.13	380	680	7.34	0.12	340
K2	7.05	0.31	330	8.16	0.12	380	1110	7.26	0.12	340
L2	7.19	0.28	340	8.08	0.13	380	890	7.26	0.11	340
L1	1.60	0.47	300	2.60	0.09	490	1000	2.25	0.15	420

Ten cycles of 30 N were applied to a single force sensor to measure sensitivity and linearity. Figure D7a shows six of the ten force cycles (blue) with the corresponding voltage response (green) with respect to time. Force and piezo voltage data from each cycle were extracted. The voltage data were filtered with a 4th order low-pass Butterworth filter to remove the high frequency noise. This is displayed in Figure D7b, with the red curve as the filtered voltage signal for cycle three. The voltage response upon each force cycle displayed some drift and is shown in Figure D7c for output voltage vs. applied force for cycles two through ten. The voltage drift and high frequency noise can be attributed to the electrical measurement setup and associated electronics. The voltage drift was removed, and each voltage vs applied force measurement was overlain in Figure D7d. The python code created to analyze the sensitivity data is available on GitHub upon request.

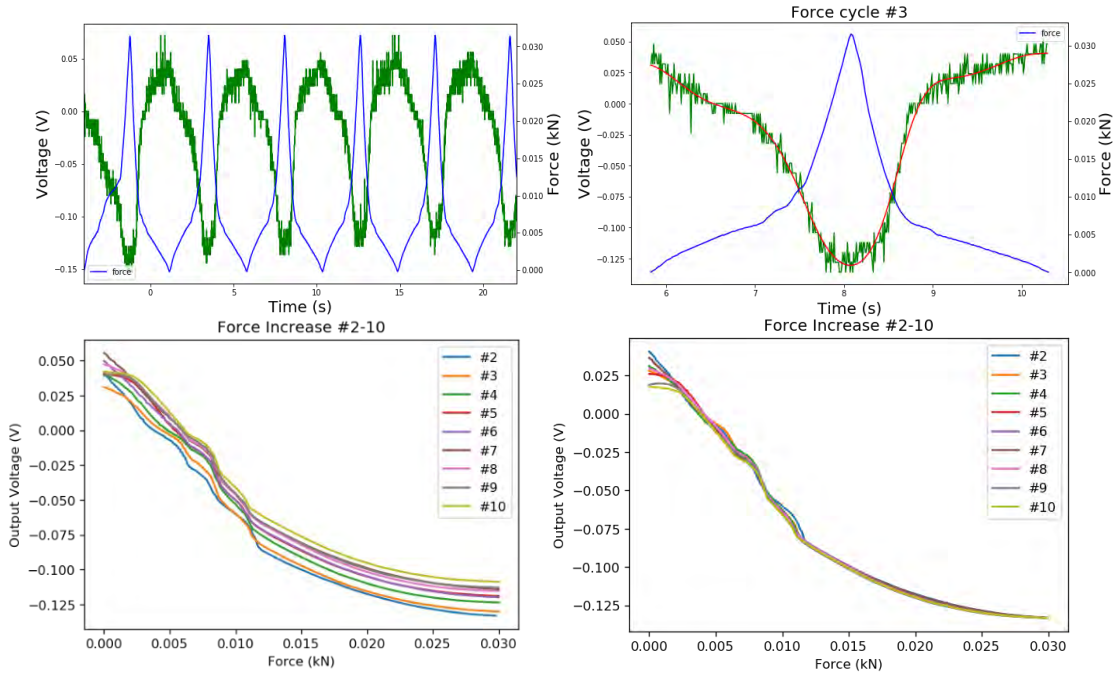

Figure D7: Voltage and force response of electrode G2 with ten 30 N force cycles. (a) Voltage response (green) and force (blue) for six of the ten force cycles. (b) Voltage response and force for cycles #3. A 4th order Butterworth filter was used to remove the high frequency noise. (c) Voltage vs applied force for force cycles two through ten. (d) When the voltage drift was removed, data for each force cycle overlap.

References

[1] M. Ntagios, S. Dervin, and R. Dahiya, “3D printed capacitive pressure sensing sole for anthropomorphic robots,” *FLEPS 2021 - IEEE Int. Conf. Flex. Printable Sensors Syst.*, pp. 1–4, 2021, doi: 10.1109/FLEPS51544.2021.9469839.

[2] S. Gong, W. Schwalb, Y. Wang, Y. Chen, Y. Tang, J. Si, B. Shirinzadeh, and W. Cheng “A wearable and highly sensitive pressure sensor with ultrathin gold nanowires,” *Nat. Commun.*, vol. 5, pp. 1–8, 2014, doi: 10.1038/ncomms4132.

[3] X. Liu, M. Mwangi, X. Li, M. O’Brien, and G. M. Whitesides, “Paper-based piezoresistive MEMS sensors,” *Lab Chip*, vol. 11, no. 13, pp. 2189–2196, 2011, doi: 10.1039/c1lc20161a.

[4] J. Yu, X. Hou, M. Cui, S. Shi, J. He, Y. Sun, C. Wang, and X. Chou,“Flexible PDMS-based triboelectric nanogenerator for instantaneous force sensing and human joint movement monitoring,” *Sci. China Mater.*, vol. 62, no. 10, pp. 1423–1432, 2019, doi: 10.1007/s40843-019-9446-1.

[5] Z. Yi, H. Yang, Y. Tian, X. Dong, J. Liu, and B. Yang, “Self-powered force sensor based on thinned bulk PZT for real-time cutaneous activities monitoring,” *IEEE Electron Device Lett.*, vol. 39, no. 8, pp. 1226–1229, 2018, doi: 10.1109/LED.2018.2846184.

[6] T. Yamashita, S. Takamatsu, H. Okada, T. Itoh, and T. Kobayashi, “Development of flexible piezoelectric strain sensor array,” *Electr. Eng. Japan (English Transl. Denki Gakkai Ronbunshi)*, vol. 204, no. 1, pp. 52–58, 2018, doi: 10.1002/eej.23084.

[7] W. Choi, J. Lee, Y. Kyoung Yoo, S. Kang, J. Kim, and J. Hoon Lee, “Enhanced sensitivity of piezoelectric pressure sensor with microstructured polydimethylsiloxane layer,” *Appl. Phys. Lett.*, vol. 104, no. 12, 2014, doi: 10.1063/1.4869816.

[8] J. Lee, W. Choi, Y.K. Yoo, K.S. Hwang, S.M. Lee, S. Kang, J. Kim, and J.H. Lee, “A micro-fabricated force sensor using an all thin film piezoelectric active sensor,” *Sensors*

(Switzerland), vol. 14, no. 12, pp. 22199–22207, 2014, doi: 10.3390/s141222199.

APPENDIX E

Flexoelectric Cantilever Beam Measurement Issues and Process Development for Flexoelectric Arrays

Flexoelectric cantilever beam measurement issues

While investigating the flexoelectric response of the $Pt/HfO_2/Si/HfO_2/Si$ cantilever stack, several issues arose which are documented here. First, the Kinetic Ceramics Piezo Driver/Amplifier is a sensitive tool. Driving beyond 15 Hz frequency was found to damage an electronic component in the internal breadboard; this entailed a long repair (several months) at Kinetic Ceramics. Secondly, it was imperative to be consistent in the clamping of the cantilever, as the clamped contact area and distance from the strain gauge should remain constant. Thirdly, it was found in practice that when an AC voltage exceeding 1.2 V was applied to the Piezo Driver/Amplifier, there is a high likelihood that the tensile stress on the backside of the beam induced fracture. If the sample were to fracture, which it often did, it was important that the lid is closed on the shielded box to prevent silicon fragments from flying around the laboratory. Fourth, it is important to monitor the temperature within the shielded box, as the piezoelectric stack heats up slightly during operation; waiting several minutes between experiments before applying a different strain to the cantilever helped, so that the starting temperature of the sample was consistent for each measurement.

The strain gauge output was consistent with the applied force, and the lock-in amplifier output voltage linearly increased with a linear increase in applied voltage to the piezo-stack. Figure E.1 shows an example of a strain gauge output with increasing applied voltage to the piezo stack. The phase angle remained constant at 0^o, as expected. When calculating the average strain gradient for each measurement, the data from 0 to ~5 minutes was removed, and the average of the remaining data resulted in the final strain.

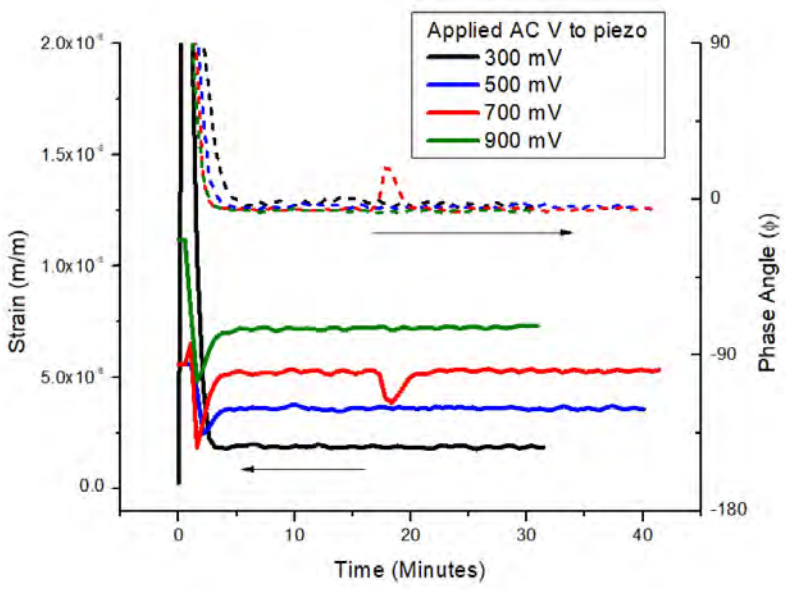

Figure E.1: Strain gauge output of flexoelectric cantilever beam with 30 nm Al_2O_3 on both surfaces.

The polarization output during cantilever beam measurements was not as reliable. An example is shown in Figure E.2 of a large variation in polarization with time during a single applied voltage to the piezo stack. Figure E.2 (left) shows the polarization and phase angle measurement during a 300 mV AC voltage applied to the piezo stack, where at ~10 minutes there is a 180° switch in phase angle, matching a jump in polarization then a subsequent decrease. Such jumps had numerous sources, such as the door of the lab opening or someone talking near the shielded box. The 500 mV applied AC measurement also took ~ 10 minutes to settle to a consistent polarization and phase angle. Figure E.2 (right) shows higher applied voltages to the piezo stack, which was expected to result in higher polarization values. The measurement at 700 mV applied to the piezo stack shows that both polarization and phase angle modulated with time, and a reliable average polarization was difficult to obtain. The 900 mV measurement shows a drop in polarization between 5 and 17 minutes then a return to the original value, while the phase angle remained the same.

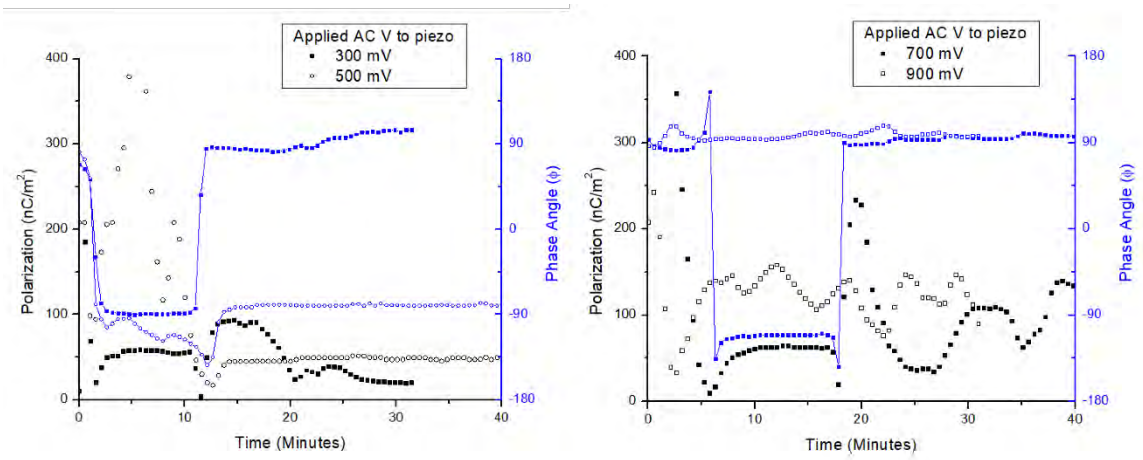

Figure E.2: Polarization output of Al_2O_3 cantilever with 300 mV and 500 mV applied to the piezo stack (left) and 700 mV and 900 mV applied (right). All measurements were at 4 Hz frequency.

Polarization and phase angle variation occurred during the measurements of the HfO_2 cantilevers as well. Figure E.3 shows the 30 nm HfO_2 beam polarization and phase angle output for 600 mV AC (left) and 1000 mV AC (right) applied to the piezo stack at 4 Hz.

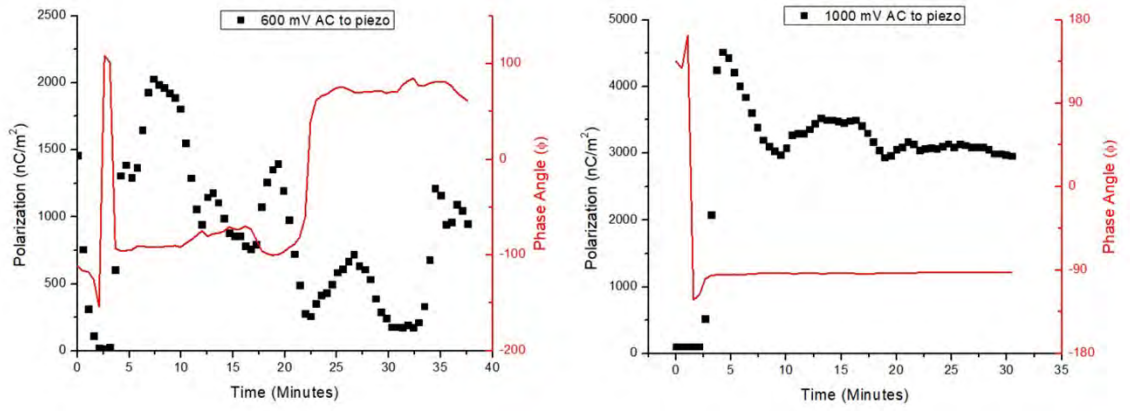

Figure E.3: Polarization output of HfO_2 cantilever with 600 mV (left) and 1000 mV (right) AC voltage applied to the piezo stack.

There was a very wide variation in both polarization and phase angle for the HfO_2 cantilever when 600 mV AC was applied to the piezo stack, but the polarization and phase angle remained relatively constant for the 1000 mV AC measurement. It is noted that higher applied voltages to the piezoelectric stack, thus higher strain gradients, resulted in more consistent

polarization and phase angle outputs. Additionally, when the door of the laboratory remained shut and movement near the shielded box was kept to a minimum, the polarization and phase angle stability were improved.

Polarization also varied with the frequency of strain applied. Figure E.4 shows the polarization output between 4 Hz, 9 Hz, and 14 Hz, where polarization decreased with increasing frequency. The measurements were relatively short and above 14 Hz the Piezo Drive/Amplifier electronic component failed, but the initial results here suggest the flexoelectric response of the barrier layer capacitors are frequency dependent even between 4 and 14 Hz.

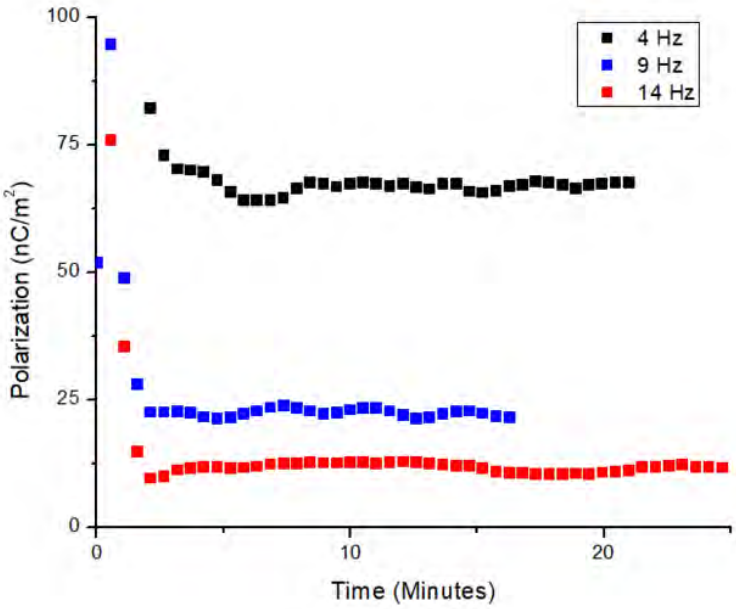

Figure E.4: Polarization output of Al_2O_3 cantilever with a variation in applied strain frequency.

Truncated pyramid array iterations for SOI wafers

Iteration #1: 6” diameter wafers

The device fabrication flow for iteration #1 is displayed in Figure E.5. Photolithography masks were designed to create pyramids of varying sizes on a 6” silicon on insulator (SOI) wafer with a device layer thickness of 70 μm oriented in the <100> direction, a BOX layer thickness of 1 μm, and a handle thickness of 500 μm. An overview of this pattern is displayed in Figure E.6, which was exposed and developed in a photoresist layer on the surface of 200 nm Si_3N_4 mask layer deposited via plasma-enhanced chemical vapor deposition. After dry etching away the silicon nitride outside of the patterned photoresist squares, a KOH+IPA anisotropic wet etch was performed at 75^{o}C for 6077 seconds, and a height of around 70 μm was expected for all pyramids, which was verified with a contact profilometer. A significant issue arose when attempting to remove the 6” SOI wafer from the 75^{o}C heated KOH+IPA bath. The handle thickness after etching was ~270 μm, and the wafer became extremely fragile. The handle was too thin to properly handle the 6” wafer and several attempted wafer removals from the bath resulted in wafer shattering. Due to this issue, six 4” SOI wafers with a device layer of 70 μm were purchased from MemsEngineering.

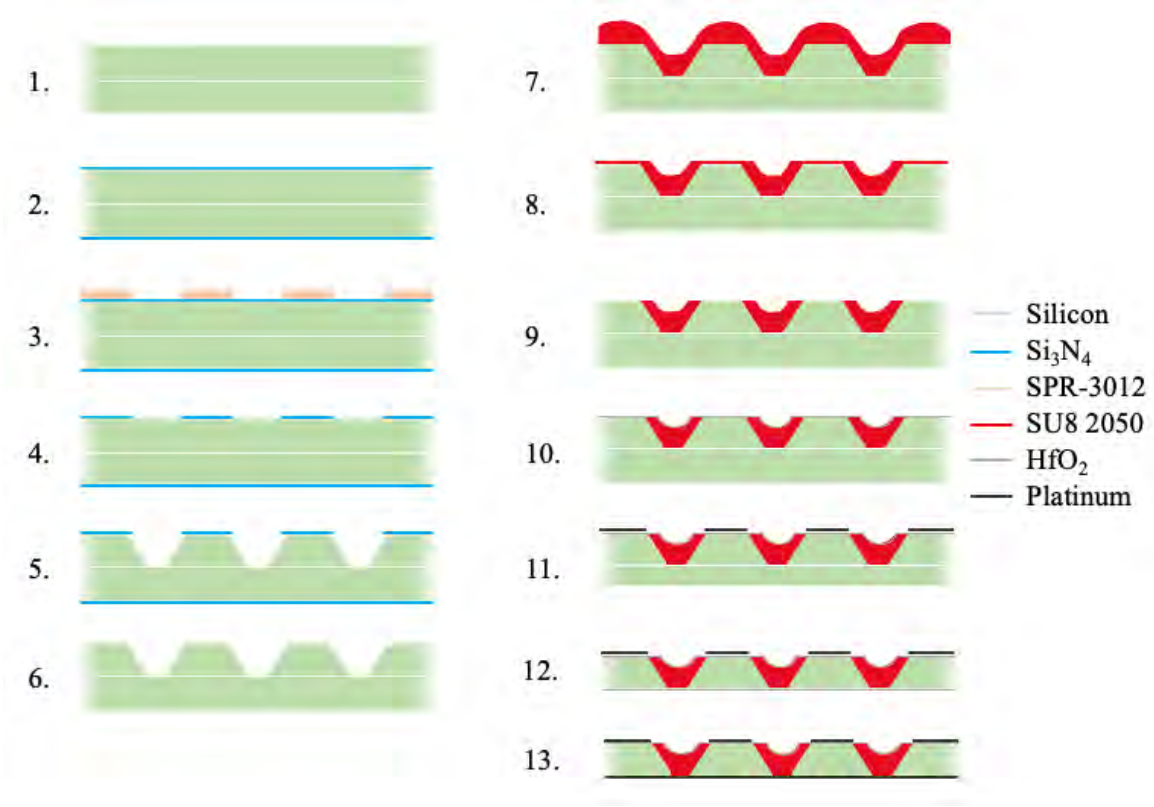

Figure E.5: Iteration #1 device fabrication flow

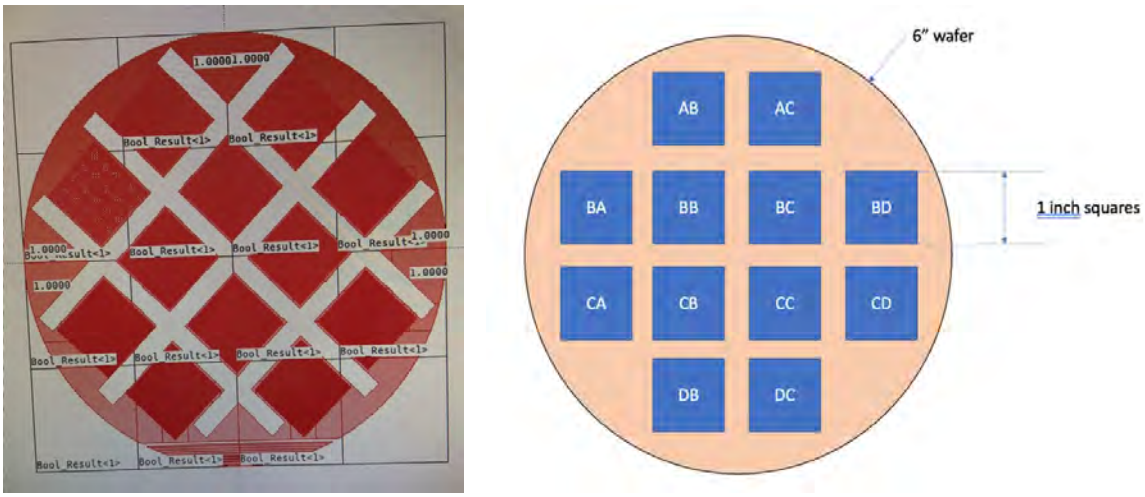

Figure E.6: Photolithographic mask design for silicon nitride patterning (step 3 in figure E.5).

Iteration #2: 4” diameter wafers, backside etching, and SU8 optimization

New 4” photolithography masks were designed and fabricated. Figure E.7 displays an updated photolithography mask for the Si_3N_4 layer for patterning prior to KOH etching. The device layer on the new 4” SOI wafers was 70 μm, so the sizes of each square and distance between neighboring squares was adjusted to optimize the pattern. Table 1 displays the 9 regions of the lithographic mask with the starting Si_3N_4 edge length (L), starting distance between squares (D), pyramid top edge length after KOH etching (L1), pyramid bottom edge length after KOH etching (L2), distance between pyramid bases after KOH etching (D1), and final heigh after etching (h).

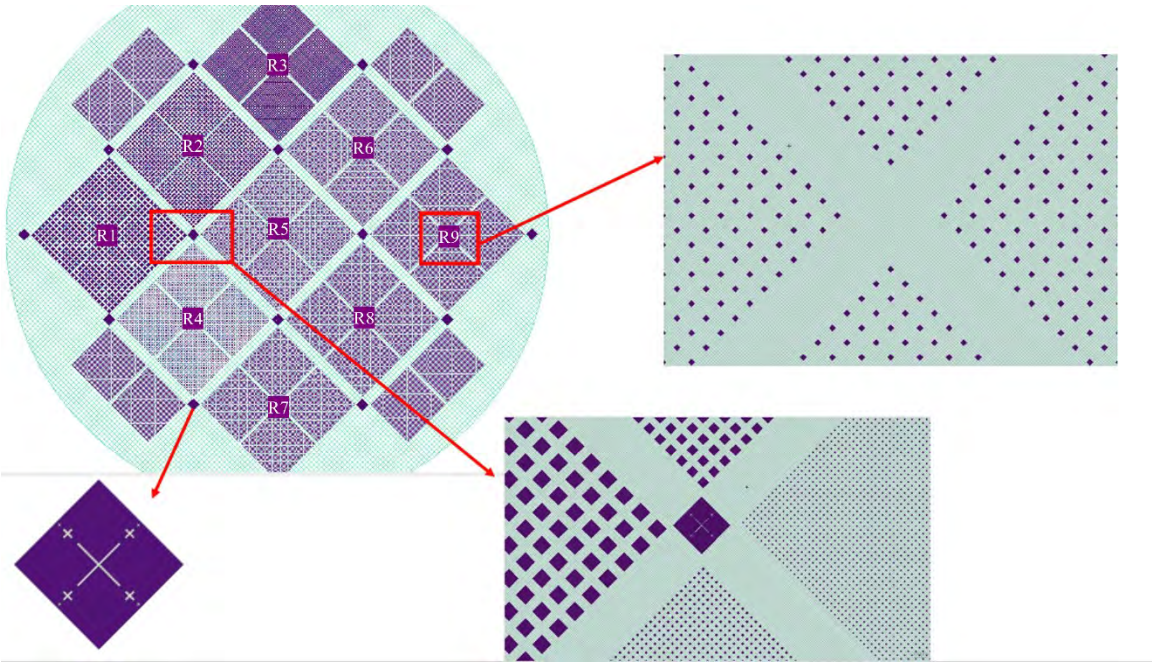

Figure E.7: Silicon nitride mask for iteration 2. Nine defined regions with varying edge length and distance. Inset images show purple squares of varying size.

Table E.1: Silicon nitride squares length (L) and distance between (D) prior to and after KOH etching to a height of 70 μm. The SU8 mask design consisted of chrome squares approximately 10 μm larger in all directions than the L1 length, which is the top pyramid surface edge length after KOH etching.

Sample Name	L (μm)	D (μm)	L1 (μm)	L2 (μm)	D1 (μm)	h (μm)	Region
FS70-micro500	500	369	464	580	290	70	01
FS70-micro300	300	269	264	380	190	70	02
FS70-micro100	100	169	64	180	90.2	70	03
FS70-micro075	75	156	39	155	77.7	70	04
FS70-micro050	50	144	14	130	65.2	70	05
FS70-micro046	46	142	9.6	126	63.2	70	06
FS70-micro044	44	141	7.6	124	62.2	70	07
FS70-micro042	42	140	5.6	122	61.2	70	08
FS70-micro040	40	139	3.6	120	60.2	70	09

The next experiment performed was to remove the backside silicon in a wet etch bath (step 11 in Figure E.5). A standard 4" <100> silicon wafer 500 μm thick was patterned with Si_3N_4 and KOH etched to 70 μm pyramid heights. The nitride was removed in an HF (49%) bath and the wafer was diced into the 9 separate regions shown in Figure E.7. SU8 2050 was spin coated at 2500 rpm for 30 seconds on Regions 09, 08, and 07, placed on a 65ºC hotplate for 10 minutes then transferred to a 95ºC hotplate for 45 minutes. Then, each region was exposed at 180 mJ/cm^2 with the SU8 mask, protecting the tops of each pyramid from being exposed, and therefore polymerized. A post-exposure bake at 65ºC for 3 minutes and 95ºC for 12 minutes was performed next. Each region was dunked in a ultrasonicating bath of SU8 developer for 12 minutes, cleaned with more SU8, IPA, DI water and N_2 dried. Gold was deposited on the surface of each region with sputter deposition to act as a hard mask to protect the pyramid top surfaces while the backside silicon was etched away. Region 09 was dunked into a KOH bath set to 85ºC to attempt to wet etch the backside silicon. After two hours, the gold delaminated from the SU8 surface, the SU8 started delaminating from the wafer piece at the edges, and there was very minimal backside silicon etched. The experimental results outlined here can be seen in Figure E.8. The conclusion

of this experiment was KOH is not an effective backside silicon etch because the topside protective layers did not withstand such long etch times.

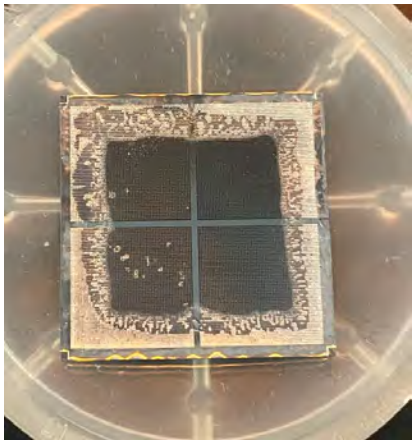

Figure E.8: SU8 delaminating on the top surface of the silicon wafer after a 2 hour KHO wet etch at 85°C. The gold protective mask fell off during the etch.

The next wet etch attempted was a 70:30 wt% HF+HNO_3 aggressive acidic solution on region 8. Figure E.9 displays the results of this etch; the gold protective mask stayed intact and displayed it was resistant to the HNO_3/HF etch. In addition, the silicon backside etched through in 6 minutes with this etch concentration with no damage to the SU8 layer. Figure E.9c shows the backside of individual pyramids still embedded in the SU8 film. This experiment showed that with the correct concentration of HF:HNO_3, the backside silicon can be quickly etched without affecting the SU8 or top pyramid features when a gold mask is employed. However, a consideration for future development steps is that the HF+HNO_3 solution will etch both Si and SiO_2, thus there would be no “etch stop” on the backs of each pyramid. This was later found to cause an issue with etch uniformity on the backside, where some pyramids began falling out of the SU8 film.

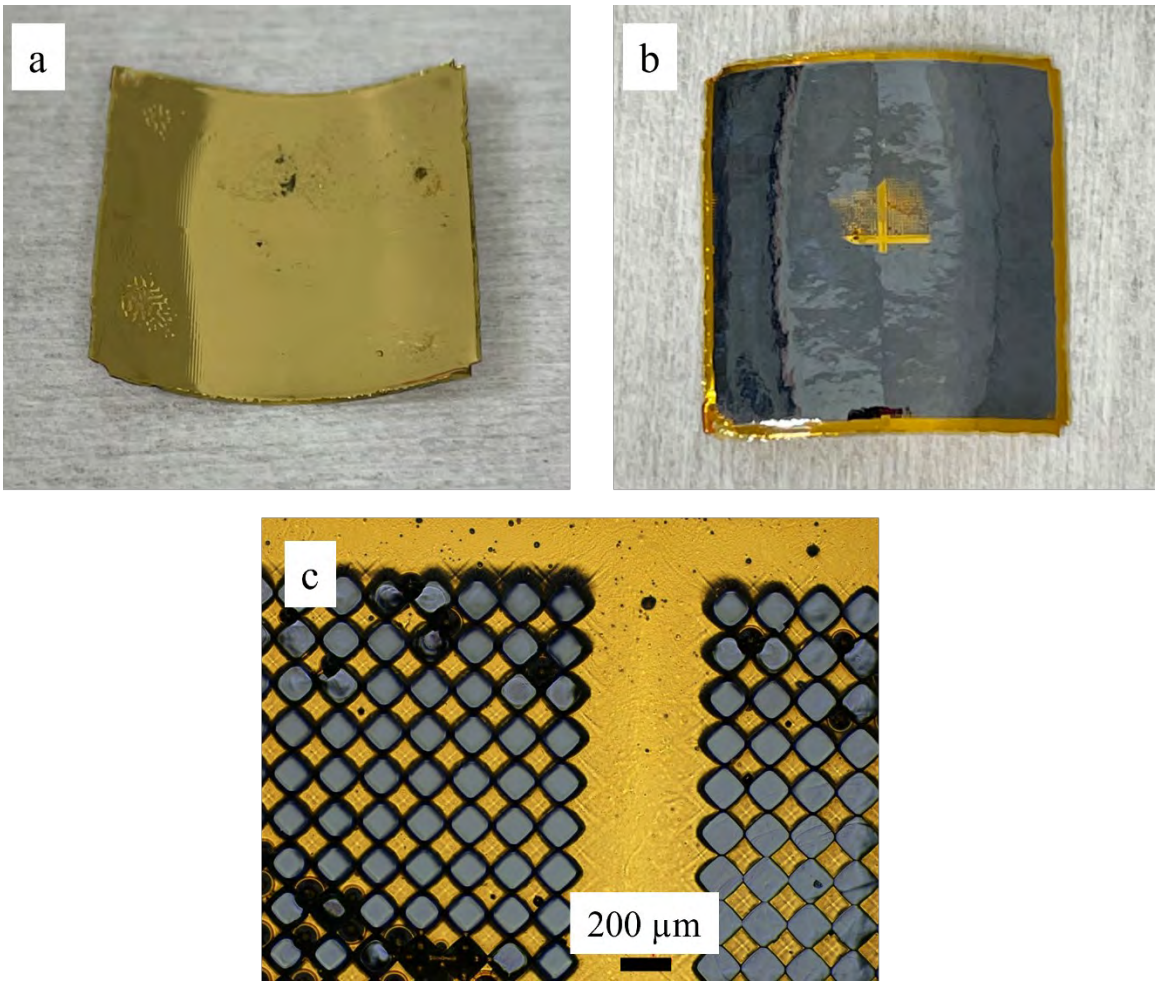

Figure E.9: Top surface displaying the Au protective film stayed intact and protected the tops of the pyramid features (top left). Bottom surface showing the silicon etched completely through the 500 µm thickness in the center of the film (top right). An optical microscopy image of the backside "etched through" region shows each silicon pyramid embedded in the SU8 film.

Next, the SU8 deposition process required optimization. Figure E.10 displays optical profilometry measurements during SU8 optimization, for a spin speed of 2000 rpm for 45 seconds (a), 3000 rpm for 45 seconds (b), and 4000 rpm for 45 seconds (c). It can be seen the SU8 profile between each pyramid surface is significantly higher than tops of each pyramid for a spin speed 2000 rpm and 3000 rpm. A spin speed of 4000 rpm for 60 seconds is displayed in Figure E.10 (d), which was found to be the optimal deposition parameters because of the small

"rabbit ears" on the pyramid edge profiles. During the SU8 develop step, cracking developed near the top of the film due to thermal stresses between film and substrate. This was repaired by placing the wafer on a hotplate set at 180ºC for 2 minutes to relieve the built-up stress.

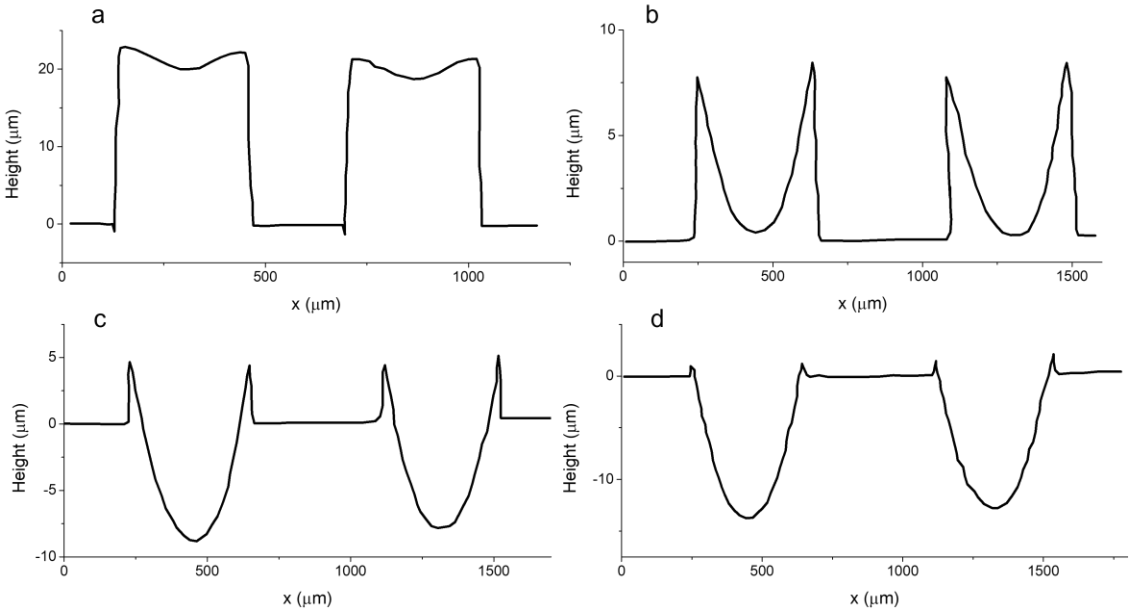

Figure E.10: SU8 profiles on Si pyramids for (a) spin speed of 2000 rpm for 45 seconds (b) 3000 rpm for 45 seconds (c) 4000 rpm for 45 seconds and (d) 4000 rpm for 60 seconds.

Iteration #3: SU8 stress and film delamination

The 4" SOI wafers were employed to begin final development stages of the process. The SOI wafers contained a 70 μm device layer, a 1 μm SiO_2 box layer, and a 500 μm silicon handle thickness. Nitride was deposited, patterned, and dry etched. The 4" wafer was immersed in the KOH+IPA bath set to 75ºC for ~80 minutes to etch the device layer into the pyramid structures. SU8 was processed according to the previous experimental parameters optimized in Iteration #2. Prior to performing the HfO_2 atomic layer deposition (step 9 in Figure E.5), optical microscopy revealed there was residual SU8 leftover on the surface of each pyramid. Figure E.11a displays what the surfaces of each pyramid looked like. An oxygen plasma descum etch was optimized to fully remove the residual SU8, and Figure E.11b displays an optical microscopy image of the pyramids after the 1.5 minute descum etch. Additionally, the descum etch removed the "bunny

ears" on the side profiles of each pyramid, displayed in the optical profilometry measurement in Figure E.11c. The SOI wafer was prepared for HfO_2 deposition and platinum electrode patterning.

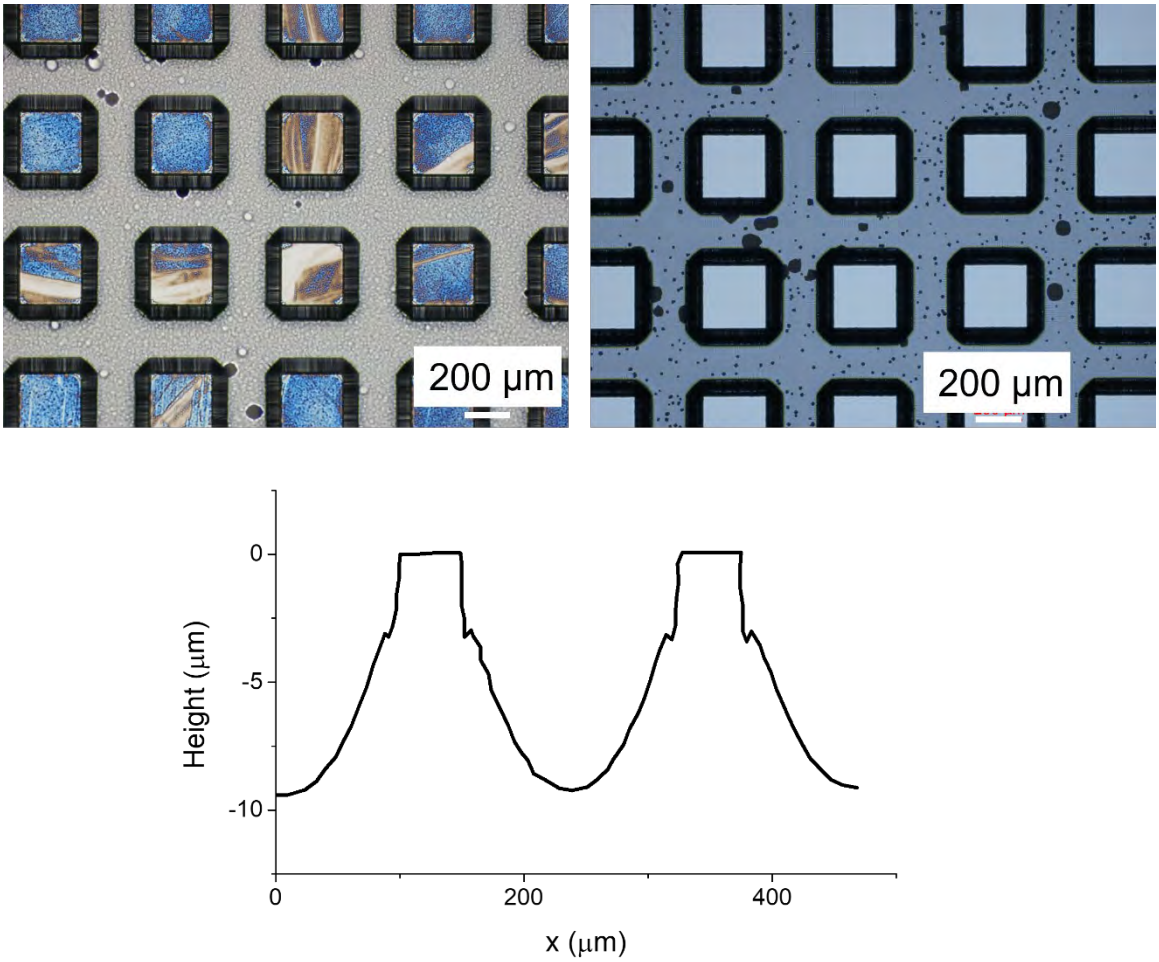

Figure E.11: Optical microscopy image of SU8 residual on the surface of each pyramid (a). Removal of the residual organic after a 90 second descum etch (b). Optical profilometry measurement of pyramid tips pointing out of SU8 film with the removal of the bunny ears after a descum etch (c).

The HfO_2 dielectric layer was deposited via ALD at 150°C for 208 cycles to reach 30 nm thickness on the top surface. Standard double layer photolithography procedures (discussed in Chapter 6) were utilized to pattern the top surface, with the exposure step using the electrode pattern photolithography mask. Platinum was sputter deposited to create the top electrodes and leads. Next, a backside silicon etch was attempted with the same 70:30 wt% HNO_3:HF

concentration in Iteration #2. Here, the gold protective film was peeled off within 30 seconds and the backside silicon etched extremely rapidly. Figure E.12a displays the resulting device after two minutes in the bath, and Figure E.12b displays the results after an additional minute in the bath. All platinum was removed from the surface, and a similar result occurred when a chrome adhesion layer was used between the gold and SU8 films. New experiments were designed to retain the top patterned surface during the wet etch by patterning the HfO_2 film; however all attempts were unsuccessful. New methods were investigated next to remove the backside silicon.

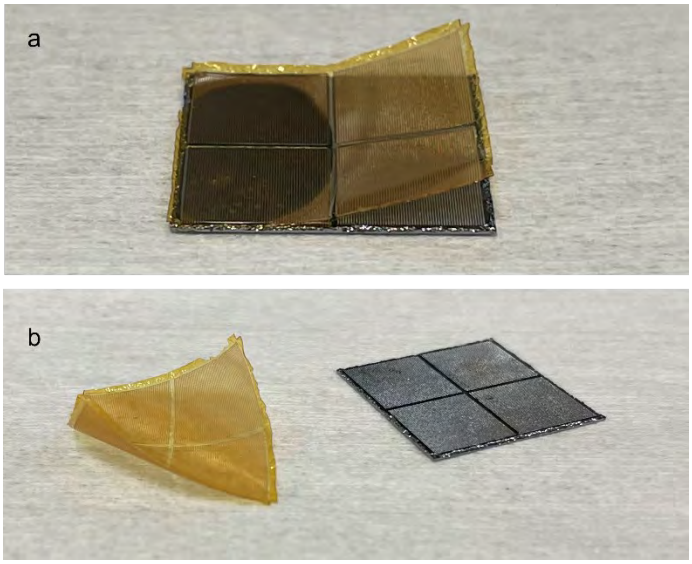

Figure E.12: SU8 film peeling off of silicon pyramids after 2 minutes in $HF:HNO_3$ bath (a). SU8 film removed from silicon surface after 3 minutes in bath (b).

Iteration #4: Bosch backside etch

A 4" SOI wafer was processed as previously described (Iteration 3). This wafer was diced into the nine individual regions, and a Bosch etch was employed to remove the backside silicon. First, region 09 of this wafer was placed face down in a reactive ion etch tool for 100 Bosch etch cycles. Figure E.13 displays the results, showing the SU8 was damaged, and the patterned top side platinum was peeled off. Next, a layer of Krytox was used as a thermal conducting layer between the patterned top side of region 08 and the carrier Si wafer with 50 nm

Al_2O_3 mask layer. The Bosch etch was performed on this region, with all four corners of the wafer piece taped down to the carrier wafer with kapton tape. Figure E.14 (a,b) displays the results after 550 Bosch cycles; the wafer was thinned down, and the thermal stress from the SU8 layer bent the remaining silicon. Next, to remove the final silicon left on the backside of the wafer, the device was dunked in a 70:30 wt% HNO_3:HF bath. The remaining handle silicon was etched to the BOX layer, and the thermal stress from the silicon was removed, flattening the entire structure. This is displayed in Figure E.14 (c,d). The backside of the silicon was successfully removed, but the frontside features were completely removed in the HF/HNO_3 bath.

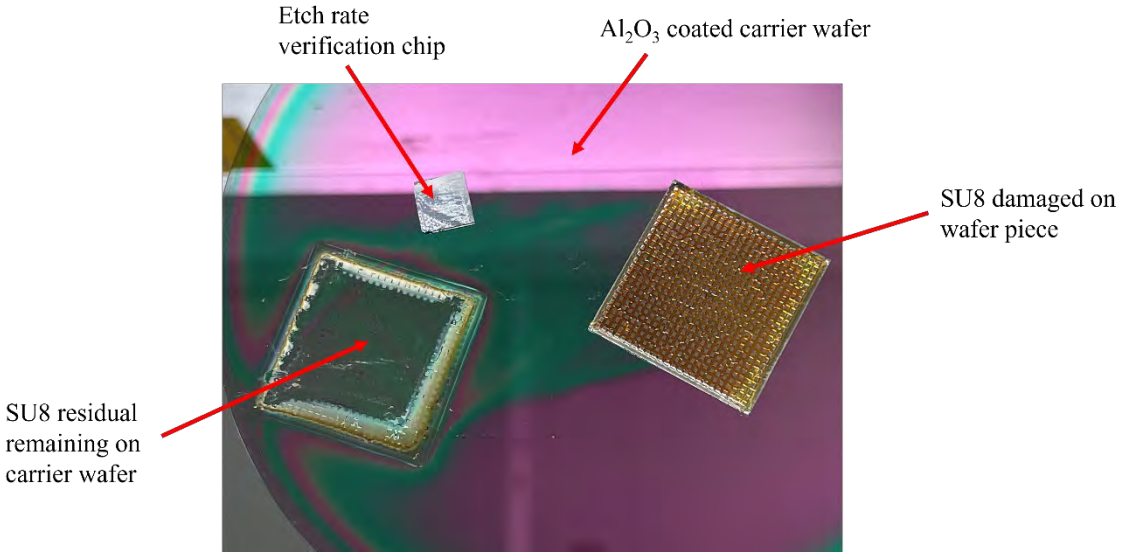

Figure E.13: Damage observed to the SU8 layer after 100 Bosch etch cycles.

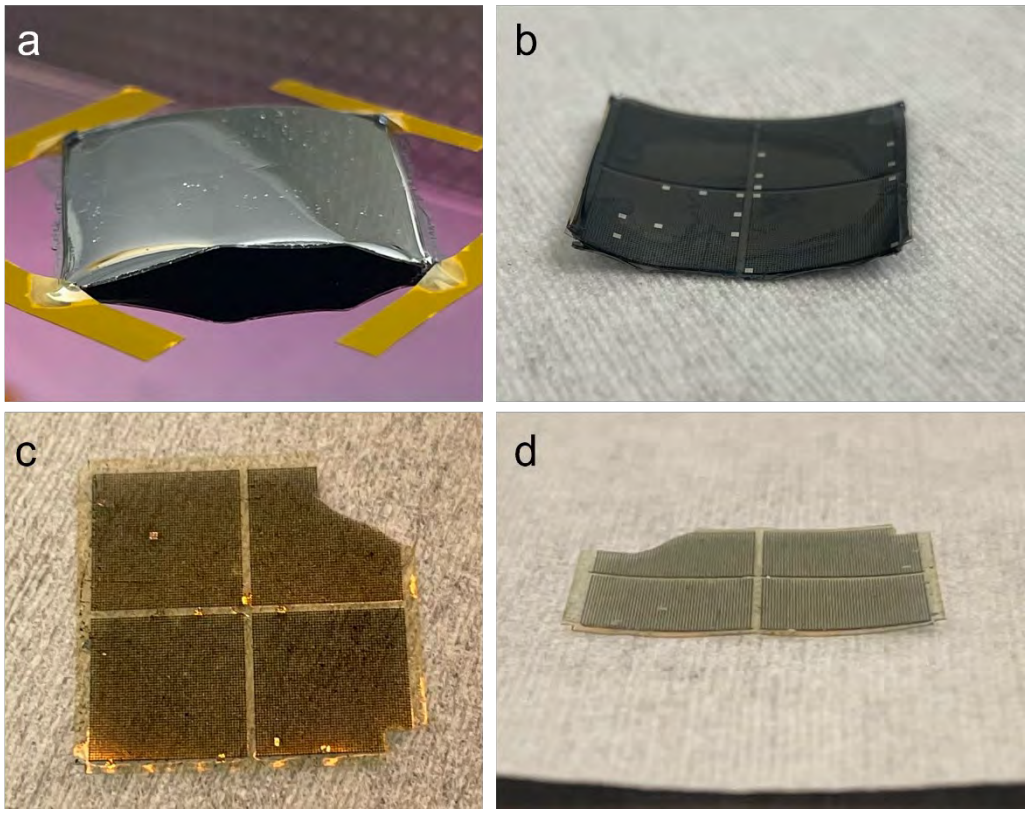

Figure E.14: Backside (a) and frontside (b) of the patterned wafer piece after 550 Bosch etch cycles. SU8 device with embedded pyramids after a 3-minute HF/HNO_3 wet etch (c,d).

Next, region 07 wafer piece was placed face down on an Al_2O_3 coat silicon carrier wafer and the corners taped down with Kapton tape. The Bosch etch was run for 600 cycles on the backside silicon, which resulted in further wafer bending but more of the silicon removed. The same procedure was repeated on region 06, this time performing the Bosch etch for 700 cycles. Figure E.15 displays the resulting features after a 600 cycle (a) and 700 cycle (b) Bosch etch. The conclusion of this experiment was that 700 cycles effectively removes all backside silicon but damages the SU8 film. The structure after 600 Bosch cycles was placed in a high state of stress and the bending was difficult to remove after etching away the rest of the backside silicon in a HF/HNO_3 bath. Parylene was utilized instead of gold as the front side mask during the HF/HNO_3 wet etch next. A 550 cycle Bosch etch was be performed, but the bending persisted.

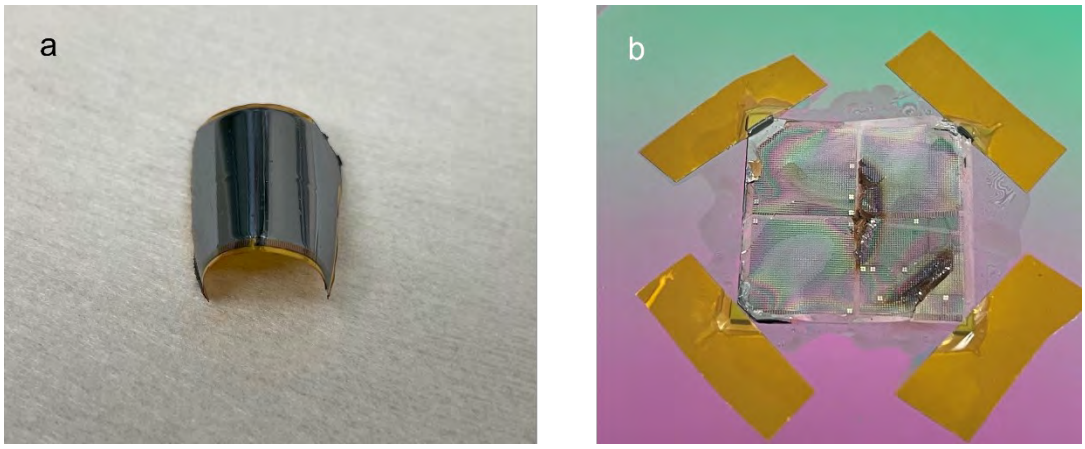

Figure E.15: Device structure after 600 Bosch cycles (a). Structure after 700 Bosch cycles (b).

After iteration #4 of the process flow, the stress induced within the SU8 as the silicon was thinned down was a problem. The help relieve some of this stress, vias were patterned in the topside SU8 film, and also Bosch etched into the backside silicon. This process flow was successful in creating a device with Pt/HfO_2/Si/HfO_2/Pt stack on each pyramid. That process flow is detailed in Chapter 6.

VITA

Travis Lee Peters

Travis Lee Peters was born in Plymouth, MI but was raised in Bryan, Ohio. Prior to beginning his doctoral degree at The Pennsylvania State University, he earned a B.S. cum laude at The Ohio State University in Materials Science and Engineering in 2018. He received his M.S. degree in Materials Science and Engineering at The Ohio State University in 2019, where his research topic was Solid-State Yttria-Stabilize Zirconia Electrochemical Sensors for Extreme Environments. Additionally, he studied as a fellowship recipient at the Oak Ridge National Laboratory for 10 months of his doctoral degree.